Matter wave interferometry in microgravity

Towards space-borne cold atomic sensors

D i s s e r t a t i o n

zur Erlangung des akademischen Grades
d o c t o r r e r u m n a t u r a l i u m
(Dr. rer. nat.)
im Fach Physik

eingereicht an der
Mathematisch-Naturwissenschaftlichen Fakultät
der Humboldt-Universität zu Berlin

von
M.Sc. Markus Krutzik

Präsident der Humboldt-Universität zu Berlin:
Prof. Dr. Jan-Hendrik Olbertz

Dekan der Mathematisch-Naturwissenschaftlichen Fakultät:
Prof. Dr. Elmar Kulke

Gutachter/innen:
1. Prof. Achim Peters, Ph.D.
2. Prof. Dr. Oliver Benson
3. Prof. Dr. Markus Arndt

Tag der mündlichen Prüfung: 22.07.14

Abstract

State-of-the-art cold atomic quantum sensors are currently about to outpace their classical counterparts in precision and accuracy, but are still not exploiting their full potential. Utilizing quantum-enhanced sensor technology such as matter wave interferometers in the unique environment of microgravity will tremendously increase their sensitivity, ultimately outperforming the most accurate ground-based systems by several orders of magnitude. Microgravity platforms such as drop towers, zero-g airplanes and sounding rockets are excellent testbeds for advanced interferometry experiments with quantum gases in space. In return, they impose demanding requirements on the payload key technologies in terms of mechanical and thermal robustness, remote control, miniaturization and redundancy.

In this work, first interferometry experiments with degenerate quantum gases in zero-g environment have been performed within the QUANTUS project. In more than 250 free fall experiments operated at the drop tower in Bremen, preparation, free evolution and phase coherence of a rubidium Bose-Einstein condensate (BEC) on macroscopic timescales of up to 2 s have been explored. To this end, a BEC interferometer using first-order Bragg diffraction was implemented in an atom-chip based setup. Combined with delta-kick cooling (DKC) techniques to further slow down the expansion of the atomic cloud, effective temperatures of about 1 nK have been reached. With an asymmetrical Mach-Zehnder geometry, high-contrast interferometric fringes were observed up to a total time in the interferometer of $2T = 677$ ms.

Keywords: Matter wave interferometry, Bose-Einstein condensates, atom chip, microgravity, drop tower, Bragg diffraction, delta-kick cooling, sounding rocket, space

Zusammenfassung

Quantensensoren auf Basis ultra-kalter Atome sind gegenwärtig auf dem Weg ihre klassischen Pendants als Messintrumente sowohl in Präzision als auch in Genauigkeit zu überholen, obwohl ihr Potential noch immer nicht vollständig ausgeschöpft ist. Die Anwendung von Quantensensortechnologie wie Materiewelleninterferometern im Weltraum wird ihre Sensitivität weiter steigen lassen, sodass sie potentiell die genauesten erdbasierten Systeme um mehere Größenordnungen übertreffen könnten. Mikrogravitationsplattformen wie Falltürme, Parabelflugzeuge und Höhenforschungsraketen stellen exzellente Testumgebungen für zukünftge atominterferometrische Experimente im Weltraum dar. Andererseits erfordert ihre Nutzung die Entwicklung von Schlüsseltechnologien, die hohe Standards in Bezug auf mechanische und thermische Robustheit, Autonomie, Miniaturisierung und Redundanz erfüllen müssen.

In der vorliegenden Arbeit wurden erste Interferometrieexperimente mit degenerieten Quantengasen in Schwerelosigkeit im Rahmen des QUANTUS Projektes durchgeführt. In mehr als 250 Freifall-Experimenten am Bremer Fallturm konnte die Präparation, freie Entwicklung und Phasenkohärenz eines Rubidium Bose-Einstein Kondensates (BEC) auf makroskopischen Zeitskalen von bis zu 2 s untersucht werden. Dazu wurde ein BEC-Interferometer mittels Bragg-Strahlteilern in einen Atomchip-basierten Aufbau implementiert. In Kombination mit dem Verfahren der Delta-Kick Kühlung (DKC) konnte die Expansionsrate der Kondensate weiter reduziert werden, was zur Beobachtung von effektiven Temperaturen im Bereich von 1 nK führte. In einem Interferometer mit asymetrischer Mach-Zehnder Geometrie konnten Interferenzstreifen mit hohem Kontrast bis zu einer Verweildauer von $2T = 677$ ms untersucht werden.

Schlagwörter: Materiewelleninterferometrie, Bose-Einstein Kondensate, Atomchip, Mikrogravitation, Fallturm, Bragg Streuung, Delta-Kick Kühlung, Höhenforschungsrakete, Weltraum

Contents

1 From quantum to cosmos - towards cold atom sensors in space

Today, there is no conclusive quantum theory of gravitation. Deep conflicts exist between General Relativity (GR) and the quantum world, describing the macrocosm classically and microscopic phenomena quantum-mechanically, respectively. Combining microscopic quantum sensors with the unique environment of space might be one of the keys to open the so far locked door of quantum gravity [1].

Quantum sensors such as optical atomic clocks and matter wave interferometers will broadly benefit from reduced gravity conditions offered by space-borne platforms and open up new possibilities to study physical models within a wide range of scientific fields. By pushing the performance beyond what is accessible on Earth, thus investigating yet unexplored parameter regimes, these devices will support important applications in the areas of Earth observation [2], navigation [3] and precision timekeeping [4]. Highly accurate on-board frequency instrumentation (e.g. space-borne optical clocks) will strongly contribute to determine the gravitational potential of our planet [5]. The metric for Earth's gravitational field will become a major subject of investigation in future quantum based geodesy [6]. Due to the availability of long distances and a low noise environment, recent proposals even suggest long baseline interferometers with matter waves in space as the next generation of low frequency gravitational wave detectors [7].

Moreover, cold atom based quantum sensors in microgravity will provide excellent possibilities to address some of the most important questions of fundamental physics and test their underlying principles with unprecedented precision [8, 9]. An environment with large spatial variations of velocity and gravitational potential is promising for implementing a versatile quantum-based testbed investigating General Relativity (GR). As one of the cornerstones of modern physics, GR is a classical theory based on the Einstein Equivalence Principle (EEP) [10]. It consists of three pillars: the Universality of the Free Fall (UFF), the Local Position Invariance (LPI) and the Local Lorentz Invariance (LLI). If these universality principles are valid, gravitational effects can be described by a space-time metric as given by the Riemannian geometry [11], for example.

UFF states that different test bodies will have the same free-fall acceleration in an external gravitational field, their trajectories only depend on initial position and velocity. Here, the infinitely long and periodic free fall in space sets promising conditions for high-precision tests of the UFF. LLI, as an underlying symmetry of all current physical theories, describes that the laws of physics of a non-gravitational experiment are independent of the velocity and orientation of frame in which it is performed. Measurements of the isotropy or velocity-independence of the speed of light aboard a space-borne instrument can potentially benefit from large velocity variations on a

highly elliptical orbit. The statement of LPI is, that the outcome of the experiment is also independent of where and when in the universe it is performed. One possible test of LPI is a measurement of the gravitational redshift, which is the difference of two frequency references placed at different heights in a static gravitational field. Thus, large potential differences offered in space are promising for highly accurate clock comparison tests.

Although being quite successful in describing phenomena in the macrocosm, EEP's classical and therefore fundamentally incomplete nature demands an extension to the quantum world [1]. The search for unification of GR with quantum mechanics is a very active research field, sometimes considered to be the holy grail of physics [12]. Several attempts or extended theories addressing this problem predict violations of the basic principles of GR [13, 14, 15].

Space-borne experiments with optical clocks and matter wave interferometers to conceive different aspects of EEP, setting new limits on, or even observing violations in given frameworks (e.g., the Standard-Model Extension (SME) [16]) will help to complete our understanding of the interplay between quantum physics and gravity — an important step towards the unification of all fundamental forces of nature. Since this obviously still is quite a long way to go, tremendous effort have been made by universities, space agencies, and private companies all over the world to develop and establish quantum technology for space applications.

From QUANTUS to cosmos - towards UFF tests based on atom interferometry

This thesis was realized within QUANTUS, a German collaboration targeting the long-term goal of studying cold quantum gas experiments on a space platform. As an important step towards realizing coherent sources for ultra-cold atom experiments under demanding conditions, this collaboration successfully demonstrated the first observation of Bose-Einstein condensation in microgravity at the Bremen drop tower [17]. The scientific and technological achievements have obviously been of great interest for both, the atomic clock and atom interferometer community. Not at least by proving that extremely sensitive laboratory equipment such as laser sources, stable optical benches, ultra-high vacuum systems and control electronics can be integrated into compact and robust payloads forming an autonomous ultra-cold matter lab within small volumes ($\leq 0.5\ \mathrm{m}^3$) and comparably low mass budgets (≤ 240 kg) [18, 19].

Independent of the general importance of the achieved results for the space-borne quantum sensor community, one of the major scientific objectives of the QUANTUS collaboration is a microgravity-enhanced test of the Universality of the Free Fall (UFF) with a dual-species matter wave interferometer. Such a measurement would lead to a direct determination of the Eötvös ratio η based on the quantum nature of particles,

$$\eta = \frac{|a_I - a_{II}|}{g} \tag{1.1}$$

determining the normalized differential acceleration of two test matter wave packets associated with individual accelerations a_I and a_{II}.

First UFF tests relying on the precision and accuracy of atom interferometric measurements have been performed by comparing a cesium fountain interferometer with a

experiment	test masses	platform	accuracy η	ref.
Cs-AI / Stanford	^{133}Cs & FG-5	lab	$7.0(7.0) \cdot 10^{-9}$	[20]
Rb-AI / Paris	^{87}Rb & FG-5	lab	$4.3(6.4) \cdot 10^{-9}$	[21]
Rb-AI / Garching	^{87}Rb & ^{85}Rb	lab	$1.2(1.7) \cdot 10^{-7}$	[22]
Rb-AI / ONERA	^{87}Rb & ^{85}Rb	lab	$1.2(3.2) \cdot 10^{-7}$	[23]
ATLAS / Hannover	^{87}Rb & ^{39}K	lab	$0.3(5.4) \cdot 10^{-7}$	[24]
10m tower / Stanford	^{87}Rb & ^{85}Rb	10 m fountain	$1 \cdot 10^{-15}$	[8]
Li-AI / Berkeley	^{6}Li & ^{7}Li	lab	$1 \cdot 10^{-14}$	[26]
CERN/ Geneve	^{1}H & $^{1}\overline{\text{H}}$	"big" lab	$2 \cdot 10^{-6}$	[41]
I.C.E / Bordeaux	^{87}Rb & ^{40}K	zero-g airbus	$5 \cdot 10^{-11}$	[42]
QUANTUS / Hannover	^{87}K & ^{41}K	drop tower	$5 \cdot 10^{-11}$	[43]
PRIMUS / Bremen	^{87}K & ^{39}K	drop tower	$5 \cdot 10^{-11}$	[44]
STE-QUEST / ESA	^{87}Rb & ^{85}Rb	satellite	$2 \cdot 10^{-15}$	[30]
QWEP / ESA	^{87}Rb & ^{85}Rb	ISS	$1 \cdot 10^{-14}$	[31]

Table 1.1: Achieved (upper part) and targeted (lower part) accuracies of cold atom interferometry based measurements of the Universality of the Free Fall (UFF).

falling corner cube [20]. In this experiment, no deviation has been reported to a level of $\eta = 7 \cdot 10^{-9}$. A similar but mobile setup even reached a slightly better agreement [21].

Pure quantum-based UFF tests in atom interferometers have been demonstrated with 10^{-7} precision [22, 23, 24], which itself constitutes a major scientific achievement. More importantly, a new generation of UFF tests is being prepared which aim for measurement accuracies comparable to classical state-of-the-art tests [25, 8, 26] and complementing them by means of possible violation parameters of the SME [16, 27].

Benchmark experiments in determining η are still given by lunar laser ranging [28] and torsion balance [29] tests, achieving precisions in the lower 10^{-13} regime. Ultimately, operating dual-species interferometer devices in space might even lead to higher performance, possibly enabling measurements of η down to an uncertainty of at least 10^{-15} [30, 9, 31].

Together with currently proposed space tests based on classical bulk matter targeting at or even beyond the 10^{-15} level [32, 33, 34], these so far unmatched precision measurements would consequently set new limits to the validity of EEP in mutual agreement or, probably more interesting, find contradictory results. Operating microscopic quantum systems at macroscopic coordinates in space-time will shed some light into yet unexplored regimes of low energy quantum phenomena [35, 14, 1] and could potentially open the door to fundamental physics at the borderline between the classical and the quantum [36, 37, 38]. In this sense, recent publications even propose antimatter for an UFF test, representing a fundamentally different testframe beyond classical theory [39, 40, 41].

Extensive research has already been undertaken aboard zero-g airplanes [45, 46] and drop towers [12, 44, 17] as pathfinder experiments towards establishing matter wave interferometers based on ultra-cold atoms in microgravity. As a next step towards space, sounding rocket experiments are in preparation [47, 48]. They all rely on the

benefits of a microgravity environment for matter wave interferometers. Before these will be highlighted in general, and specifically for dual-species operation, we will shortly introduce general applications of light-pulse interferometry and the basic measurement principle of a gravimeter.

1.1 Atom interferometry

Nowadays, atom interferometers (AI) are utilized in a variety of applications and still greatly contribute to the frontiers of precision measurements even on ground. Cooled down to only some tens of a microkelvin, near the absolute zero of temperature, cold clouds of atoms represent an ultra-sensitive and nearly perfect test matter wave for various interferometric measurements. Over the last decade, AI-based quantum sensors have been developed rapidly and different measurement schemes have been demonstrated and implemented for various high-precision measurements.

Among these, AIs are proven to be an extremely sensitive probe for inertial forces, such as accelerations and rotations. By dropping cold clouds of atoms, the local gravitational acceleration could be measured with an absolute uncertainty of $\Delta g/g \approx 3 \cdot 10^{-9}$ [49], and tiny rotations have been detected in Sagnac-type interferometers with sensitivities usually better than $10^{-6}\text{rad/s}\ \sqrt{\text{Hz}}$ [50, 51]. Gravity gradiometers have been developed to measure the gravitational difference between two locations using a common reference frame. By rejecting non-inertial accelerations, these instruments currently lead to differential acceleration sensitivities of $4 \cdot 10^{-9}$ g [2, 52].

Additional applications cover broad areas from metrology up to addressing general research in fundamental physics [8], for example, an AI-based test of the Local Lorentz Invariance [53]. Further developments of AIs led to a precise determination of physical constants. Based on atomic recoil measurements [54, 55], the fine-structure constant α has been measured with the current best relative uncertainty of $2.5 \cdot 10^{-9}$. Moreover, AIs provide an alternative method for measurements of the gravitational constant G [56, 57]. By synchronizing an oscillator to the measured value of of h/m in a self-referenced atom interferometer, it is even stated that AIs are suitable to build a novel matter wave based clock [58].

As already mentioned, another field of research are atom interferometry based tests of the Universality of the Free Fall (UFF). By tracking the free propagation of two different matter waves, the differential acceleration of quantum objects can be measured. The basic measurement principle will be summarized in the following.

The free fall of atoms measured with light-pulse interferometers

For measuring the gravitational acceleration with cold atoms of a single species, the Mach-Zehnder-type interferometer is commonly used (see Fig. 1.1, left). Here, cold clouds of atoms serve as freely falling test masses whose change in position due to gravity is read out via the interaction with appropriately designed laser waves. A simplified picture allows these waves to be seen as a nano-scale ruler to which the position of the atoms is being precisely monitored.

Consider an idealized two-level system, represented by two hyperfine ground states of an alkali atom and a freely falling ensemble of atoms initially prepared in the same

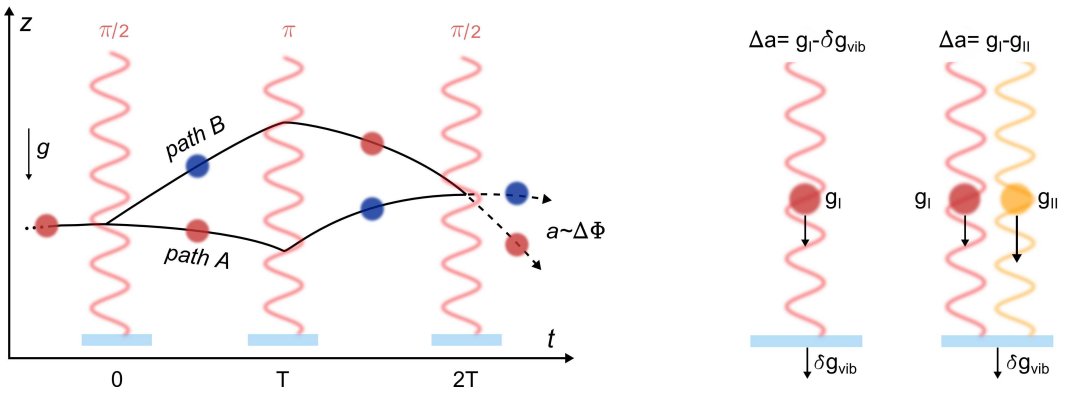

Figure 1.1: Schematic of a cold-atom based Mach-Zehnder interferometer induced by stimulated Raman transitions between two hyperfine ground states (left). In a dual-species operation (right), vibration noise of the retro-reflecting mirror cancels out in a differential measurement due to first order common-mode rejection [60, 42].

internal state. At $t = 0$ they are illuminated by a pair of counter-propagating laser beams with wave vectors k_1 and k_2, driving two-photon Raman transitions between the two hyperfine states[1]. In a gravimeter setup, they are commonly retro-reflected at a reference mirror and gravity is pointing vertically along the direction of the beams.

The first pulse constitutes an atom-optical beam splitter which, intuitively, transfers half of the atoms to the other hyperfine state and give them a momentum kick of $\hbar k_{eff}$ due to photon recoil. The transferred momentum is associated with absorption of photons from one light field and stimulated emission into the other beam ($\hbar k_{eff} = \hbar(k_1 + k_2)$). Quantum mechanically speaking, the atomic wave function is put into a coherent superposition of two internal and momentum states. The two clouds will spatially separate during an interrogation time T and propagate along path A and B, respectively (see Fig. 1.1, left).

The second pulse ($t = T$) acts as a mirror, exchanging internal and momentum states of the two atomic samples. After propagating for an additional time T, the two clouds of atoms accumulate a phase difference by propagating along the different trajectories and ideally overlap in one space-time point. Finally, a third laser pulse is applied at $t = 2T$ for coherent recombination of the two parts of the wave function.

Gravity and inertial forces in general influence the propagation of the atoms w.r.t. to the interferometer laser fields, and at each of the three interaction zones, the local laser phase is imprinted onto the atomic wave function [59]. The main contributions to the phase difference between path A and path B can be given as

$$\Delta\Phi = \Delta\Phi_{path} + \Delta\Phi_{light} + \Delta\Phi_{sep}, \tag{1.2}$$

with the free evolution phase shift along the paths $\Delta\Phi_{path}$, the phase shift resulting from the interaction with the Raman light fields $\Delta\Phi_{light}$, and a phase shift proportional

[1] A detailed description of Raman beam splitters can for example be found in [59]. Most importantly, the Raman beams feature a frequency difference that equals the energetic splitting of the hyperfine ground states.

to the separation between the center-of-mass (COM) position of the wave packets at the time of detection $\Delta\Phi_{sep}$. For a full description, see for example [20].

If we assume a homogenous gravitational field and neglect a possible separation phase difference ($\Delta\Phi_{path} \equiv 0$, $\Delta\Phi_{light} \gg \Delta\Phi_{sep}$), we can describe the resulting phase shift of an atomic gravimeter setup in first order to

$$\Delta\Phi = (k_{eff}g - \alpha)T^2 + \phi_0, \tag{1.3}$$

with the effective wave vector of the interferometer light pulses k_{eff}, the local gravitational acceleration g and the interrogation time T. We introduced α as a continuous frequency chirp of the frequency difference canceling the time-varying Doppler shift of the atoms due to their increasing velocity in free fall, and ϕ_0 as a phase offset induced by the last interferometer pulse.

This phase difference can precisely be read out by an analysis of the population of one of the two hyperfine states (e.g. $|2\rangle$) at the output of the interferometer

$$P_{|2\rangle} \sim \bar{P} + \frac{C}{2}\cos(\Delta\Phi), \tag{1.4}$$

with mean state population $\bar{P}$ and contrast C [61]. By adjusting α and ϕ_0 such that the phase difference is zero, one can determine the local gravitational acceleration g [59, 20].

The free fall of two-species matter waves and differential measurements

Using two atomic species in free fall with different masses m_I and m_{II} allows to compare two independent measurements of g. This is made possible by creating a mixture of two atomic species as an input state for the simultaneous operation of two superimposed interferometers.

In such a dual-species AI, the prepared matter wave samples of both species will be simultaneously interrogated by the same interferometer sequence. By using dilute samples of non-interacting atoms or isotopes, the center-of-mass (COM) positions of the test objects can be independently measured with high precision and subsequently brought to coincidence. Thus, two accelerations g_I and g_{II} of two independent test masses starting from exactly the same coordinate in space-time can be independently read out with high precision (see Fig. 1.1, right). Each individual acceleration measurement is limited by numerous systematic effects and noise sources such as laser phase noise and vibrational noise of the reference mirror, here shown as δg_{vib}.

However, they can be drastically suppressed in a differential measurement by using (i) the same reference mirror for both interferometers and (ii) by using the same light for coherent manipulation. Differential phase between interferometers using the same light has shown to reject common-mode noise up to large scaling factors [52, 60]. If different lasers for manipulation of the atomic test masses are necessary, e.g. different species, the two interferometers do generally not share the same sensitivity. But even in this case, it has been shown that a common-mode rejection can be achieved [42].

Before we highlight the general benefits of a microgravity environment for atom interferometric measurements, we briefly discuss the intrinsic sensitivity scaling of a Mach-Zehnder interferometer.

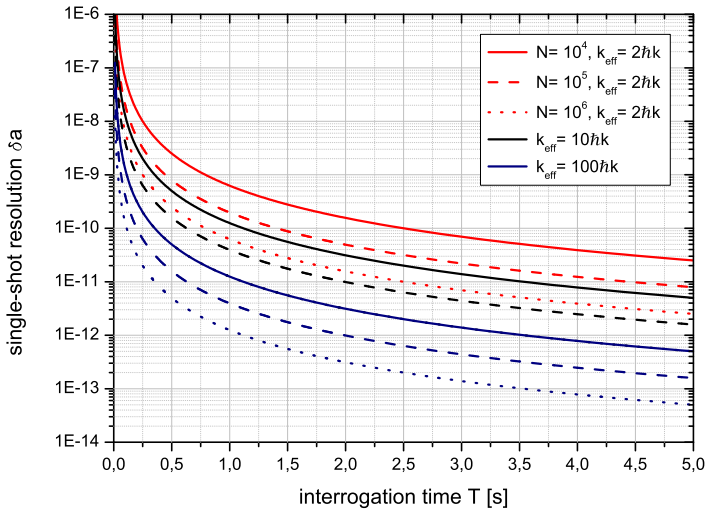

Figure 1.2: Calculation of the quantum projection noise limited single-shot resolution δa of an acceleration measurement (Mach-Zehnder configuration) for increasing interrogation time T. Neglecting other noise sources, the principal resolution per shot with $C = 1$ is given for different atom numbers N (solid, dashed, dotted lines) and effective wave vectors (red, black, blue colors) according to Eq. 1.5

Scaling of the single-shot measurement resolution

Most important for evaluating the performance of a Mach-Zehnder interferometer under space conditions is the intrinsic scaling of the measurement resolution. Therefore, we relate the single-shot resolution of the phase measurement $\delta\Phi$ as inversely proportional to the signal-to-noise ratio (SNR) of the detected fringes. Limited by quantum projection noise only [62], our acceleration resolution δa follows accordingly:

$$\delta\Phi \propto \frac{1}{SNR} \Longleftrightarrow \delta a \propto \frac{1}{C\sqrt{N}} \cdot \frac{1}{k_{eff}} \cdot \frac{1}{T^2}, \tag{1.5}$$

with the measurement contrast C, the detected atom number N, the effective wavevector k_{eff}, and the interrogation time T.

Obviously, the resolution will benefit from increasing N, enlarging the transferred beam splitter momentum associated with k_{eff} and, most importantly, enhancing the interrogation time T, which scales quadratically in the given expression. The single-shot sensitivity for different atom numbers N and effective wave vectors k_{eff} is calculated assuming interrogation times of up to $T = 5$ s (see Fig. 1.2), which is hardly to realize on ground[2]. The $1/T^2$ scaling rapidly increases the measurement resolution over several orders of magnitude. The application of higher-order beam splitters increases the resolution (see different colors), but they are more difficult to realize and to control without introducing additional systematic effects.

In the next section, we see how these parameters can be addressed by conducting the experiment in a microgravity environment.

[2] In fact, an atomic fountain with a height of about 100 m would be necessary to achieve corresponding free fall times.

1.2 Benefits of a space environment

The technology-readiness-level (TRL) of cold atom technology develops rapidly and the number of research and development programs targeting at dedicated space missions is continuously increasing. Depending on the specific experiment, space offers a multitude of advantages of which the most common ones will be described in the following.

1. **Unique environment of weightlessness**
   - Atoms can be cooled down to the lowest temperatures. One main limitation of adiabatic cooling in conservative traps is given by the gravitational field since the trapping potential must feature a gradient that is larger than the gravitational force on the trapped atoms. This limits the applicability of ultra-shallow traps for low energetic quantum ensembles on ground and will at some point lead to significant atom loss. The absence of the gravitational sag in a microgravity environment will potentially allow to surpass this restriction without the need for levitating fields [63].
   - Since mass-dependent effects on the trapping potentials are negligible, this environment should in principle allow for perfect mode match of the different types of atoms before being released for free fall. This prevents spatial separation of the dual-species mixture and density variations across the samples. Additionally, a better control over the center-of-mass (COM) of mixed two component quantum gases allows for implementation of advanced dual-species cooling methods, e.g., delta-kick cooling (DKC) [64, 65].
   - After being released from trapping potentials, the atoms will accelerate due to Earth's gravitational field but experience a free fall environment together with the ambient vacuum chamber. Thus, they will not hit the ground of the chamber or a window and remain in the observation volume for several seconds, effectively increasing the interaction times far beyond the typical limits imposed by, for example, the maximum height of terrestrial instruments. In space, interferometer times of $2T > 10$ s are certainly within the bounds of possibility. This results in an enhancement of the measurement resolution of several orders of magnitude compared to standard ground-based experiments. These are typically operating with in the regime of a few hundreds of milliseconds (see Fig. 1.2).
   - Moreover, long interrogation times can be realized even in small volumes, if the atoms themselves are cold and launched slowly enough. This is a big advantage, since the experimental apparatus can be miniaturized to a certain level, thus offering higher intrinsic stability[3].
2. **Large and predictable gradients of velocity and gravity**:
   - Regardless of the fact whether the experiments are located in satellites, free fliers, or other space vehicles, the missions can be designed in a fashion that the atomic sensor is subjected to large spatial variations of velocity and the

[3] Not to speak about reduced launch costs for a compact and lightweight payload.

gravitational potential. This depends on the specific orbit but once appropriately chosen, it allows to properly test significant constituents of GR. For example, a gravitational redshift test of the Local Position Invariance (LPI) [4] or velocity dependent forces in atom interferometers [66] to measure otherwise inaccessible parameters of the Standard Model Extension (SME) [16].

3. **Low vibration and gravity gradient noise**:
   - One major limiting factor in precision AI experiments are vibrations of the reference mirror w.r.t the freely falling atoms. Microgravity potentially offers a low-noise environment with residual vibrations at a $10^{-6}g$ level. Moreover, differential measurement schemes will additionally take advantage from high a common-mode rejection [42, 30].
   - Low background vibration will also contribute towards generating very cold samples of atoms in very weak traps, since thermal excitations can be suppressed. However, poorly designed scientific payloads and/or platforms may suffer from residual vibrations limiting the net microgravity quality.
   - Seismic surface waves induce density perturbations in the Earth which produce fluctuating gravitational forces on the AI test masses. In space as a comparably "quite location", the influence of this Newtonian noise can potentially be reduced to a negligible level.

As mentioned earlier and quantified by the measurement resolution (see Fig. 1.2), the most important advantage for AI is related to the availability of otherwise inaccessible regimes of interrogation time T. However, this is not only a question of the environment but also of the properties of the atomic source.

Especially the spatial expansion rate of a cloud of atoms (associated with an effective temperature) leads to very dilute samples of atoms after seconds of free expansion, which are challenging to detect. Moreover, the atoms may leave the detection volume, which results in a reduction of the measured signal and sensitivity ($\Delta a \sim 1/\sqrt{N}$). For laser-cooled atoms, typical temperatures of $1\,\mu$K have been reached. Evaporative cooling in conservative trapping potential was used to prepare matter waves at nK temperatures. Here, a new state of matter occurs, the Bose-Einstein condensate [67, 68, 69], whose observation was awarded with the Nobel prize in 2001.

Bose-Einstein condensates as test masses for long-time interferometry

Recently, Bose-Einstein condensates (BEC) attracted great attention as a potential atomic source for interferometry measurements. Instead of acting like millions of distinguishable point masses characterized by the classical Boltzmann distribution, ultracold atoms in a BEC loose their identity and form a single macroscopic wave function. This property makes a condensate to large extent similar to a laser in which photons coherently occupy the same mode of the electromagnetic field.

Due to the resulting properties, degenerate quantum gases are promising for applications in atom optics, atom interferometry and precision measurements. Bose-Einstein condensates feature very low momentum widths which are (i) mandatory for enhanced

signal-to-noise ratios (SNR) in interferometers with large interrogation times [12, 25] and (ii) advantageous for increased interferometric sensitivities by implementing large momentum transfer beam splitters [70]. Low velocity spreading in combination with high densities eventually making a nK cold BEC an ideal candidate to explore the full potential of microgravity.

The process of releasing condensates from conservative traps relies on carefully operating and controlling weak potentials. Due to this level of precision, BECs feature good spatial localization and predictable center-of-mass (COM) motions which are important for reliable and reproducible experiments probing, for example, the free fall of matter waves [9]. Moreover, BECs potentially enable one to surpass classical noise limits by the implementation of squeezed states with reduced quantum uncertainty, as already demonstrated in [71, 72].

The use of ultra-cold atoms was already proven to greatly enhance the measurement sensitivity in long baseline interferomety in Earth-based apparatuses and to reduce systematic errors (e.g., wave front distortions and inhomogeneous dephasing) due to the condensate's point-source character [25]. They have successfully been used in free fall experiments [17] and light-pulse interferometers [12] operated at a drop tower and are proposed sources for quantum gas experiments aboard the ISS [31] and on satellites [30].

For justifying BECs one has also to trade against the obvious disadvantages for precision measurements. Besides technical issues in building a reliable source of degenerate gases, the most commonly stated is the lower achievable flux compared to thermal or laser cooled sources. The lower the flux, the less atoms will participate in the measurement which leads to a smaller precision and more noise due to insufficient averaging. The second main downside is given by the effect of atomic interactions, causing mean-field and collision shifts due to the high densities in BECs. If not perfectly controlled or reduced in dedicated preparation protocols, these bias terms will decrease interferometric phase sensitivity and lead to systematic errors [9].

In the end, however, one can hardly omit the use of Bose-condensed sources due to their excellent properties (e.g. expansion rate) for measurements at ultra-long timescales.

1.3 Applications of atom interferometers and fundamental science in space

Several space related missions with cold atom sensors have been proposed [73, 31, 9, 7, 74] and preparatory experiments in zero-g environment have already been performed [45, 17, 46, 12] or are still under thorough investigation [42, 43]. Ultimately, a versatile and highly precise quantum-enhanced testbed investigating GR in space is envisioned in all of these mission proposals.

Besides testing the Universality of the Free Fall (UFF), the resolution enhancement of atom interferometers can be used for a variety of different applications and addressing several fundamental physics questions with unprecedented precision. In part because reduced gravity conditions allow more sensitive measurements, and in part because space allows access to unique coordinates in space, gravity and time.

The applications are truly interdisciplinary, covering diverse and important topics. In the following, some of theses applications and foundational experiments will be highlighted to emphasize the potential benefit of sending quantum sensors into space.

Precision gravity measurements

The resolution enhancement of space-borne matter wave interferometers can significantly contribute to global gravity mapping and monitoring of dynamic processes in the interplay between solid earth, ice and ocean [2, 75]. Admittedly, there have been high-class missions dedicated to precision gravity measurements such as DLR's CHAMP (Challenging Minisatellite Payload) [76] and NASA's GRACE (Gravity recovery and Climate Experiment) [77]. They are based on on-board drag-free test masses or distance measurements between two satellites, respectively. ESA's GOCE (Gravity Field and Steady-State Ocean Circulation Explorer) mission, with a payload based on precise mechanical accelerometers, provided the most precise picture of the gravitational field of the Earth so far [78].

An atom interferometer might be used for highly accurate gravity field mapping when operated in space. Atom interferometry holds great promise for new gravity mapping and monitoring capabilities, including higher measurement sensitivity, finer spatial resolution, and temporal monitoring [2, 61]. Indeed, they have their own justification, since important effects of mass on spatial and temporal determination of the geoid cannot be detected within the on-going missions [79].

To distinguish the acceleration measurement of the atoms caused by Earth from externally induced inertial effects, additional tracking information about the spacecraft's orientation is needed. In a gradiometer, differential acceleration measurements allow to cancel common mode noise induced by the microgravity platform or vibrating parts of the payload itself.[4] Here, the gravitational difference between two locations can be measured using a common reference frame, rejecting non-inertial accelerations. Two acceleration measurements are thus performed simultaneously in two atom interferometers, displaced by a distance d, but using the same Raman beams and thus only one retro-reflecting mirror. The gravity gradient induced phase shift measured by two AIs separated by the distance d along $\vec{e_z}$ is determined by

$$\frac{\Delta g}{\Delta z} = \frac{\Delta\phi_1 - \Delta\phi_2}{k_{eff} T^2 d} \tag{1.6}$$

With such a configuration, differential acceleration sensitivities of $4 \cdot 10^{-9}\ \mathrm{g}/\sqrt{\mathrm{Hz}}$ have been achieved in laboratory experiments with an interferometer separation of 1.4 m [2, 52]. Sensitivities are expected to increase in space, as pointed out, by longer interrogation times T and the use of degenerate quantum gases to longer maintain a sufficient SNR.

Measurement of fundamental constants

In quantum mechanical equations of motion such as the Schrödinger or relativistic Dirac equation, the mass of a particle is always linked to Planck's constant through

[4] It also allows to cancel all other accelerations due to the validity of Einstein's equivalence principle.

h/m. A precise measurement of this fraction would generally allow to compare quantum theories with experiment and thus contribute to the understanding of quantum mechanics.

Atom interferometers in space open up exciting prospects of high precision measurements of this fraction by a measurement of the recoil frequency $\omega_r = \hbar k^2/2m$ of atoms combined with an accurate measurement of the applied photon wavelength $\lambda = 2\pi/k$ [80]. High-precision recoil measurements are made possible due to long interrogation times, for example, in a simultaneous conjugate AI where the measured phase shift scales as $\Delta\Phi \sim \omega_r T$ [81].

Wavelength measurements on the opposite require a space-borne frequency comb which is already developed for sounding rocket applications [82], thus yielding a comparably high technology-readiness-level (TRL).

Combined with the Rydberg constant R_∞, the speed of light c, and the isotope's mass ratios m/m_e (with the electron mass m_e), this measurement can be used to determine the fine structure constant α as [83, 54]

$$\alpha^2 = \frac{2R_\infty}{c} \cdot \frac{m}{m_e}\frac{h}{m}. \tag{1.7}$$

The fine structure constant plays a significant role in fundamental physics, and its value has been determined by a variety of experiments. The precise determination of α is a prerequisite for testing quantum electrodynamics (QED), and would allow to set better limits to other dependent fundamental constants. Possible time variations of α can be investigated, which would violate metric theories of gravitation such as GR [1].

The gravito-magnetic effect

Atom interferometers which measure rotations in a Sagnac configuration might be used in a low-Earth orbit to measure geodetic effects and could potentially shed some more light into the gravito-magnetic or Lense-Thirring effect.

Predicted by GR, the orbit of a small test body orbiting around a massive, rotating mass is slightly perturbed by the rotation [84]. Freely-falling gyroscopes orbiting around Earth will thus experience this effect, also known as frame-dragging, whose precise determination would constitute a crucial test of GR. However, the effect created by a slowly rotating object such as the Earth is extremely small [85]. Recent measurements of classical gyroscopes aboard the Gravity Probe-B spacecraft could verify the predicted frame-dragging drift rate, which constitutes a major scientific achievement, but only to an accuracy of 19% [86].

Thanks to the enhancement of performance in microgravity, cold atom based gyroscopes might be considered for space-borne implementation. They have already proven to be precise in determining small rotations in ground based measurements, with sensitivities usually better than 10^{-6} rad/s$\sqrt{\text{Hz}}$ [50, 51]. In a Mach-Zehnder interferometer configuration, the induced phase shift due to rotations is given by

$$\Delta\phi_{rot} = 2\vec{\Omega} \cdot \left(\vec{k}_{\mathit{eff}} \times \vec{v}_{at}\right) \cdot T^2, \tag{1.8}$$

with rotation rate $\vec{\Omega}$, effective wave vector $\vec{k}_{\mathit{eff}}$ and the atomic velocity $\vec{v}_{at}$. The scal-

ing with T^2 again indicates the same advantages for gyroscopes of being operated in microgravity as in case of gravi- or gradiometers.

To name one prominent example, the HYPER proposal aimed at implementing a cold-atom based experiment into a drag-free environment and use this instrument as a high precision gyroscope and accelerometer [87, 73]. This proposal was the first to target at cold atom interferometers in space and would have allowed for precisely monitoring the spacecrafts orientation and differences in the expected orbit around Earth. Four atom interferometers combined to two Sagnac units to measure rotations and accelerations in two orthogonal directions would have constituted the heart of the scientific payload.

Gravitational wave detection

The detection of gravitational waves would be a fundamental breakthrough in our understanding of how the universe began. If their existence is not directly confirmed earlier [88], atom interferometry might be used to observe gravitational waves. Sources of gravitational radiation can be, for example, white dwarfs, neutron stars or black holes, which strongly radiate gravitational waves because they contain heavy stars orbiting close to proximity [89].

These waves can be detected by recording the phase shift they induce in an atom interferometric measurement by passing through the interrogation zone. Gravitational waves (GW) induce space-time strains that lead to different traveling times between the atom and the laser field and thus to a different phase shift. A cold atom based GW detector can be designed to fill the gap between space-borne laser interferometer detectors like LISA (strain sensitivity 10^{-19} @ frequency band 0.1 mHz - 0.1 Hz) [90] and ground-based instruments like LIGO (10^{-23} @ 10 Hz - 10 kHz) [91].

As mentioned earlier, competitive sensors must be based on a differential measurement scheme, since each phase shift can also be induced by vibrations and other external error sources. A possible concept might be the realization of two satellites separated by a baseline L, each housing one atomic interferometer as proposed by the AGIS-LEO mission [7]. Between the satellite, a pair of Raman laser beams oscillates back and forth, thus inducing two-photon transitions in both interferometers. Besides the noise-free environment, the great advantage of a space-borne AI based sensor is the possibility of increasing L and thus increasing sensitivity of the detector.

According to the measurement setup proposed in [7], GWs induce a phase shift between to atom interferometers separated by a baseline L along the propagation of the beam splitter light, which follows as

$$\Delta\Phi_{GW} = 8k_{\mathit{eff}}hL\sin^4\left(\frac{\omega}{T/2}\right)\left(\frac{7+8\cos\omega T}{2}\right)\sin\omega t, \tag{1.9}$$

with interrogation time T and effective wave vector k_{eff} of the interferometer and as well as strain h and frequency ω of the gravitational wave traveling at the time t. In order to observe a GW, the phaseshift must be measured during the oscillation of the GW, requiring a sampling rate at least twice the GW frequency.

As stated in [7], a strain sensitivity of 10^{-18} in the 50 mHz - 10 Hz frequency band might generally be achieved.

Microgravity-enhanced quantum physics with ultra-cold Bose-Fermi mixtures

By operating a stationary microgravity platform with an ultra-cold atom laboratory, condensates at extremely low temperatures and densities can be achieved by slowly decompressing the trap. This would lead to an enormous Fourier limited wave function as an ideal starting point for high-precision atom interferometers. Moreover, the absence of gravity is useful towards sympathetically cooling second species since microgravity will allow to relax density dependent losses [92].

Besides probing the free fall, these ultra-cold two-component condensates can be loaded in optical lattices, which, in microgravity, will feature a perfect periodicity along all three dimensions [93]. This allows for high-precision tests of spinor dynamics in Bose-Einstein condensates, which already have provided groundbreaking insight in superfluidity [94]. By precisely controlling the lattice parameters, condensed matter systems can be used to further probe quantum magnetism and exotic phases [95].

Jet Propulsion Laboratory (JPL) is developing NASA's Cold Atom Laboratory (CAL), a versatile facility for the study of ultra-cold quantum gases and mixtures on-board the ISS [74]. The scientific payload comprises an atom chip based physics package, enabling cold atom generation and versatile experiments with rubidium and potassium atoms, mostly based on commercial-off-the-shelf (COTS) hardware and subsystems. It will enable research in a temperature and force-free environment inaccessible to terrestrial laboratories, and aims for interaction times in free fall of greater than 5 s and temperatures below 100 pK [74].

The payload is designed to serve as multi-user facility and launch to the ISS is scheduled for early 2016 on a pressurized cargo vehicle in soft stowage. After integration into an EXPRESS (EXpedite the Processing of Experiments to Space Station) rack, the experiment remains operable for a nominal duration of 12 months. Within up to 5 years of extendable operation, CAL remains upgradable towards new subsystems for enabling different research with ultra-cold atoms and mixtures in microgravity.

Testing the Universality of the Free Fall

The Space Time Explorer and Quantum Equivalence Space Test (STE-QUEST) mission [9, 30] proposal was a response to the call for medium-size (M-Class) missions by ESA's Cosmic Vision plan (2015-2025). Here, a satellite is proposed which will operate in a highly elliptical orbit, hosting a a dual-species atom interferometer (ATI) operated with two different isotopes of rubidium. A microwave clock based on laser cooled cesium atoms and an optical link are considered as an optional payload.

Its scientific objectives mainly focus on testing fundamental aspects of the EEP with unprecedented precision. Using the (optional) clock on the satellite in comparison with a highly accurate ground-based network of clocks enables Earth and Sun gravitational redshift tests with fractional uncertainties of $1 \cdot 10^{-7}$ and $2 \cdot 10^{-6}$, respectively. The measurement of the differential acceleration between two different atomic isotopes (^{87}Rb and ^{85}Rb) is carried out by a dual-species atom interferometer setup.

As a source for coherent matter waves, Bose-Einstein condensates will be generated in a hybrid trap setup, consisting of an atom chip and a crossed optical dipole trap, and simultaneously interrogated by a symmetric interferometer sequence. Here, the

proposed mission duration of 5 years enables a determination of the Eötvös ratio to an accuracy of $2 \cdot 10^{-15}$ [30]. This is beyond state-of-the-art precision achieved by lunar laser ranging [28] and torsion balance measurements [29].

As another mission proposal, the Quantum Test of the Weak Equivalence Principle (QWEP) is designed to validate the technology for a matter wave sensor in space through demonstration of differential atom interferometry and gravity gradiometry [31]. It supports the investigation of the properties of condensed atomic samples in microgravity. Ultimately, it aims at performing a WEP test with a dual-species setup (^{87}Rb and ^{85}Rb) aboard the International Space Station (ISS).

1.4 Existing cold atom technology on microgravity platforms

We have seen that there are plenty of reasons to operate cold atom based interferometers in space. Obviously, they first have to be brought there which requires dedicated technology development programs as well as pioneering experiments based on terrestrial microgravity platforms.

The first experiment operating with cold atoms in space is eventually ACES (Atomic Clock Ensemble in Space) [4], which is expected to launch in 2016 [96]. It will operate aboard the International Space Station (ISS). Even though its main instrument is a cold atom based clock (PHARAO [97]) rather than an atom interferometer, we will shortly review this pioneering mission before continuing to introduce projects working on matter wave interferometry experiments aboard two established terrestrial microgravity platforms.

The latter comprise a zero-g airplane and a drop tower, both of which state demanding requirements on the payload key technologies in terms of mechanical and thermal robustness, miniaturization, and power consumption. Proper operation of these instruments manifests the necessity of quantum technological maturity and sufficiently high TRL of the key components.

ESA's ACES mission aboard the ISS

The ACES mission aims for better tests of the gravitational redshift by comparing a cold cesium (Cs) fountain clock (PHARAO) and a space hydrogen maser (SHM) aboard the ISS with a network of ground-based clocks on Earth [4]. Establishing clocks based on cold atoms in space itself represents an enormous improvement over the present level of synchronization using the Global Position System (GPS). During the planned mission duration of 18 months, the frequency stability requirement for the main instrument PHARAO is less than $3 \cdot 10^{-16}$ after one day of averaging [4].

One of the major constituents of Einstein's Equivalence Principle can be tested with accurate frequency standards in space. Local Position Invariance (LPI) states, that the outcome of any non-gravitational experiment in a local, freely-falling frame is independent of where or when the experiment is performed.

A possible test scenario of LPI is a measurement of the gravitational redshift, which is the difference of two frequency references (e.g., atomic clocks) placed at different heights in a static gravitational field. For example, a potential difference in the gravi-

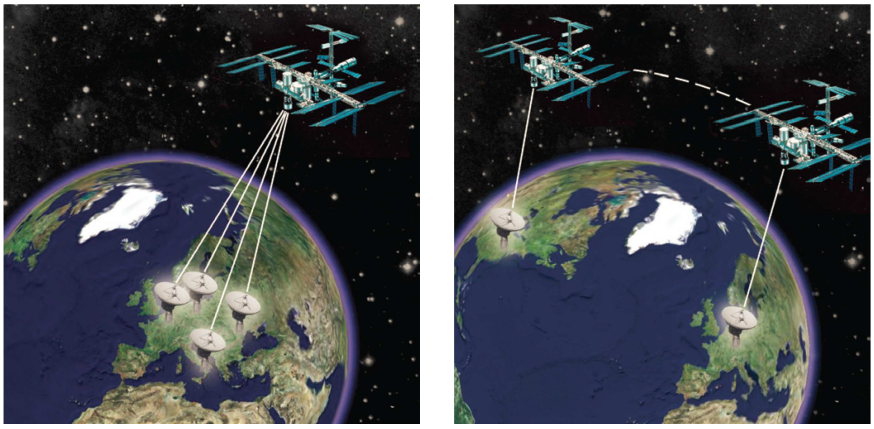

Figure 1.3: Schematic of common view (left) and non-common view (right) clock comparison test as part of ESA's Atomic Clock Ensemble in Space (ACES) mission aboard the International Space Station (ISS). Adapted from [99].

tational field of ΔU between a clock and an observer leads to a shift of the ticking rate of the clock measured by the observer of

$$\frac{\Delta\nu}{\nu} = -\frac{\Delta U}{c^2}, \tag{1.10}$$

with the speed of light c. According to EEP, this shift should be independent of the nature of clocks and/or location of the experiment. Possible deviations can therefore be parametrized with a violation parameter α as

$$\frac{\Delta\nu}{\nu} = (1+\alpha)\frac{\Delta U}{c^2}. \tag{1.11}$$

A space-borne mission with modern atomic clocks in combination with ground-based clocks has now two major advantages: (i) the accuracy and stability of cold atom based clocks itself can be improved when operated in microgravity, (ii) the potential difference between space-borne clocks and the ground network is very large and increases the strength of a possible violation signature. The first advantage is based on the fact, that the width of the measured atomic resonance in such clocks [5] is inversely proportional to the time-of-flight of the atoms, $\Delta\nu \sim 1/T$, which can reach large values in microgravity when using cold atoms.

Direct comparisons with ground-based clocks (see Fig. 1.3) at a high level of stability will be possible using both the common view (left) and the non-common view (right) technique [99]. With this, ACES aims at better tests of the gravitational redshift with 2 ppm sensitivity, time-dependance of fundamental constants (e.g., fine structure constant) at a 10^{-17} level/year and tests addressing the anisotropy of light [4, 100]. As the spacecraft turns, the direction along the microwave cavity turns and the frequency could be influenced by any spatial dependance of the speed of light.

Given the velocity variations on orbit, ACEC might even be a candidate to realize

[5] The PHARAO clock is based on Ramsey's method of separatory oscillating fields [98]

Figure 1.4: Pictures of two established multi-user microgravity facilties: The International Space Station (left) [104] and the Novespace zero-g airbus (right) [105].

a modern clock version of the Kennedy-Thorndike experiment [101].

The ISS (see Fig. 1.4, left) as an established multi-user microgravity platform will continue its service as an orbital platform until at least 2024 [102]. It has a nearly circular orbit with a varying altitude of about 250-460 km and an inclination of 51.6° to the equator [103]. Inside the station, the reduced-gravity quality is limited by quasi-steady accelerations as well as structural and acoustic vibrations.

An active rack isolation system (ARIS) was designed to isolate payloads from the external vibrations and by the same time hold them in place. With that, residual vibrations are limited to about $6 \cdot 10^{-4}$ g above 100 Hz. These conditions, must apply at certain locations inside the ISS for at least 30 continuous days, 6 times a year [103], summing up to a total time of reduced gravity of $\sim$ 180 days. Payloads are exposed to an artificial atmosphere, and can be located in one of 37 international standard payload racks (ISPR). The maximum weight of the payload is limited to 700 kg, power supplies provide 12 kW and a thermal control system (TCS) is able to dissipate up to 1200 W [103].

The suited launcher vehicles impose tight requirements to the payload robustness, including a random vibration test with 13 g_{RMS} and shock tests up to 1500 g.

CNES I.C.E. experiment on a zero-g airplane

The I.C.E. (Coherent atom interferometry for space applications) experiment is a compact and transportable atom interferometer, designed to test the Universality of Free-Fall by comparing the free fall of rubidium and potassium atoms aboard a zero-g airplane [45].

Degenerate gases of potassium (^{40}K) and rubidium (^{87}Rb) atoms will be generated by evaporative cooling in a crossed optical dipole trap. After release, they will be illuminated by a series of laser beams driving Raman transitions to form beam splitters and mirrors for both matter wave packets simultaneously. The payload has been specifically designed to withstand vibrations and temperature fluctuations in the plane, and has been validated by operating the first airborne inertial sensor [46].

The experimental apparatus operates aboard a zero-g airbus (Novespace A300–0g,

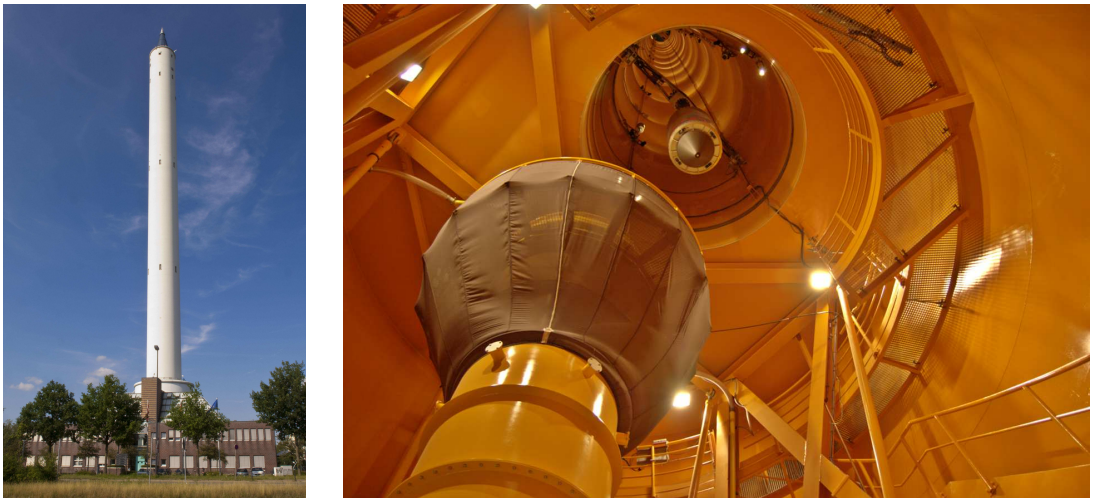

Figure 1.5: The Bremen drop tower from outside (left) and from inside along the drop tube (right). In the latter picture, the drop capsule is lifted upwards while the deceleration chamber is about to be positioned at the impact point. Copyright ZARM, Universität Bremen.

see Fig. 1.4, right) [105], taking off from Bordeaux airport in France[6]. During phases of parabolic flights which lasts for 20 s, the payload is objected to residual vibrations of about 10^{-2} g. Accelerations are moderate, typically not exceeding 2.5 g in the ascent phase or 9 g during hard landing [106]. During a flight campaign, up to 90 parabolas can be made which results in a total time of reduced gravity of about 30 minutes [45].

DLR's QUANTUS collaboration using drop tower and sounding rockets

The joint project QUANTUS is conducting research towards exploring degenerate quantum gases and mixtures under the unique conditions of microgravity. Funded by the German Space Agency (DLR), it is targeting the long-term goal of measuring the Universality of the Free Fall (UFF) with matter waves in a dual-species interferometer.

Heading towards this goal, the successful observation of Bose-Einstein condensation after 1 s of free expansion in microgravity was a major step towards realizing coherent sources for ultra-cold atom experiments in microgravity [17]. These pathfinder experiments with the first generation experiment **QUANTUS-I** have been carried out by using the high-quality microgravity environment (10^{-6} g) of a drop tower, which is operated by the Center of Applied Space Technology and Microgravity (ZARM) in Bremen, Germany (see Fig. 1.5).

The payloads have to be integrated within small capsules, which then can be used in a simple drop or an advanced catapult mode, offering 4.7 and 9.1 s of reduced gravity time, respectively [107]. Therefore, the whole drop tower has to be evacuated, which limits the repetition rate to a maximum of three drops a day. During acceleration and recapture in a deceleration chamber (see Fig. 1.5, right), mechanical loads of up to 50 g for a few hundreds of milliseconds require a proper mechanical design. The QUANTUS

[6]This airbus is also used by the German Space Agency (DLR) and the European Space Agency (ESA)

Figure 1.6: Pictures of the pre-launch preparation of TEXUS-48 in the integration hall at ESRANGE, Kiruna, Sweden (left, copyright DLR) and during ascent of TEXUS-50 launched on April 12, 2013 (right).

collaboration has for the first time shown that an entire quantum gas experiment can be integrated into compact and extremely robust payload forming an autonomous ultra-cold matter lab within small volume and comparably low mass budget [18, 17].

To continue the path towards dual-species AI in microgravity, a second generation atom-chip based experiment with ultra-cold degenerate rubidium (Rb) and potassium (K) is currently being set up. **QUANTUS-II** is capable for catapult-launch operation and aims for fundamental tests of the Universality of the Free Fall [43]. Subsystems such as vacuum chamber, control electronics or the laser system have been highly miniaturized. The latter has already been tested in the catapult mode to withstand up to 30 g shock during operation and the entire experiment is expected to operate at the drop tower in summer 2014.

As an important next stepping stone the sounding rocket mission **MAIUS** [47, 48] is planned for a launch in late 2014. The payload will comprise an atom-optical experiment able to generate BEC in space and conduct first AI tests in this environment. Here, space is considered to begin at an altitude of 100 km, above the so-called Karman line [108][7].

During the burning phase of the sounding rocket motors, high accelerations and vibrations, DC shocks and thermal loads will affect the experiment. Thus, every component and subsystem has to withstand a certain vibration spectrum, characterized by the specific motors and mechanical assembly. Another aspect of qualification are large temperature gradients, since the rocket is launched at environmental temperatures well below 0 °C until air friction heats up the outer hull to approx. 200 °C. This puts strong demands on the thermal design of the whole payload. Moreover, demanding requirements are related to the long-term stability and reliability, since the payload

[7] This was defined by the Fédération Aéronautique Internationale (FAI), whereas for NASA space begins at 50 miles above the ground [104].

should not be touched nor adapted after final integration. Usually, this is more than half a year prior to launch. Pictures of a sounding rocket payload in the integration hall at ESRANGE[8] (left, TEXUS-48) and of a similar rocket during the ascent phase after takeoff (right, TEXUS-50) are shown in Fig. 1.6.

Quo vadis?

The presented motivation, already submitted proposals and on-going activities show that there is deep scientific interest in establishing quantum sensors in space. Many studies have been conducted by several national and international space agencies (e.g., DLR, CNES, ESA, NASA) and preparatory experiments are being operated in zero-g airplanes and drop towers.

In this context, extensive research has been and currently still is undertaken towards establishing matter wave interferometers in microgravity. This includes new scientific methods as well as inevitable engineering and technological developments. Inertial sensitive atom interferometers have already been demonstrated in microgravity with moderate interrogation times ($T \leq 10$ ms) by using laser-cooled atoms [46], but so far not with degenerate gases. Given the unique properties of Bose-Einstein condensates (e.g., coherence length and slow expansion), their utilization is inevitable for matter wave interferometry at ultra-long time scales ($T > 5$ s).

1.5 Outline of this thesis

In this thesis, advanced cold atom technologies and methods have been developed to finally demonstrate the first interferometer with Bose-Einstein condensates in microgravity. This required the preparatory implementation of necessary scientific techniques as well as accompanying studies on ground which can essentially be summarized in the following three experimental prerequisites (right side):

Free-fall interferometry with Bose-Einstein condensates in microgravity (see Ch. 5)

- Atom-chip-based source of non-magnetic degenerate gases (see Ch. 2)
- ◇
- Bragg diffraction and open interferometers with degenerate gases (see Ch. 3)
- ◇
- Delta-kick cooling as a tool for long baseline atom interferometry (see Ch. 4)

Starting point for the achievements has been the QUANTUS-I setup presented in [17]. This apparatus demonstrated first Bose-Einstein condensates in microgravity and their free evolution of up to 1 s. However, anomalous expansion of atoms prepared in

[8] European Space and Sounding Rocket Range [109]

the $m_F = 2$ state led to the assumption of interactions with residual magnetic fields in the tower. During dedicated drop campaigns investigating the influence of the latter, a technical defect caused the destruction of the atom chip.

In the timeframe of this thesis, the QUANTUS-I experiment was re-assembled and characterized in detail. As one important upgrade, an RF-induced adiabatic rapid passage (ARP) was implemented on chip and optimized for the coherent transport of atoms into the $m_F = 0$ state. The new setup as well as the basic theory of Bose-Einstein condensation with atom-chips will be presented in Ch. 2.

A compact Bragg laser system for coherent manipulation was built and integrated for preparatory, ground-based matter wave interferometry experiments. Bragg diffraction was used to form open (or asymmetric) interferometers of Ramsey- and Mach-Zehnder-type, which have been operated to analyze the phase coherence of the condensate. The influence of mean-field energy on the formation of spatial fringe pattern was investigated in detail. This will be the focus of Ch. 3.

Delta kick cooling (DKC) was implemented in the atom-chip based setup to effectively reduce the expansion rate of thermal as well as degenerate atomic ensembles. We analyzed the influence of DKC on differently prepared atomic ensembles in time-of-flight series and Bragg spectroscopy measurements. For the first time, we successfully demonstrated the ground-based application of delta-kick cooled atoms in matter wave interferometers. The main results will be summarized in Ch. 4.

With this advanced setup of QUANTUS-I, over 250 free fall experiments have been carried out in dedicated measurement campaigns at the Bremen drop tower. We have been analyzing the free evolution of delta-kick cooled atoms with expansion times of up to 2 seconds. This constitutes the second largest free evolution time of cold atomic quantum object reported so far (cf. [110]). Additionally, we investigated the applicability of delta-kick cooled atoms as a coherent source for matter wave interferometry on extended timescales. To this end, an asymmetric Mach-Zehnder interferometer in microgravity was realized which led to the observation of high-contrast interferometric fringes for interrogation times of up to 677 ms. The central outcomes will be discussed in Ch. 5.

The thesis concludes with an outlook on the most recent developments and the next steps towards space-borne matter wave interferometers in Ch. 6.

Last but not least...

Operating a highly miniaturized BEC machine during free fall in a 110 m height drop tower is certainly not the task of a single person. Thus, the main results to be presented in this thesis have been achieved in a joint effort of the working Ph.D. students (H. Müntinga, H. Ahlers and A. Wenzlawski). This thesis compromises a selection of the scientific outcomes of QUANTUS-I during this time, others of which are not, or only very briefly described in this thesis since they are [111] or will be [112, 113] addressed elsewhere.

2 Atom-chip-based source of non-magnetic degenerate gases

In this chapter, the basics of Bose-Einstein condensation of dilute quantum gases will be presented and the theoretical background reviewed. Detailed studies can be found elsewhere [114, 115, 116]. The following is meant to be (i) a brief overview about the unique characteristics of a condensate and (ii) a summary on the experimental techniques, that are needed to cool down an ultra-cold atomic sample to quantum degeneracy. The latter will be described by introducing the QUANTUS-I apparatus, a compact drop tower experiment generating ^{87}Rb Bose-Einstein condensates on an atom chip. This experiment successfully demonstrated the first Bose-Einstein condensation under microgravity conditions in 2010 [17].

After a short historic overview, we start by discussing Bose-Einstein condensation of an ideal gas in a harmonic trap, and focus on important properties like the critical temperature and the fraction of atoms in the condensate (see Sec. 2.2.1). Interactions between Bosons are taken into account when formulating the Gross-Pitaevskii (GP) equation (see Sec. 2.2.2). This time-independent, non-linear Schrödinger equation can be expanded for negligible kinetic energies leading to an approximation for the density profile of a trapped gas (see Sec. 2.2.3).

Magnetic trapping of neutral atoms (see Sec. 2.3) will be briefly summarized, before we present the QUANTUS-I apparatus (see Sec. 2.4) and the experimental procedures to generate Bose-Einstein condensates on an atom- chip (see Sec. 2.5). Three important magnetic trap configurations will be characterized in ground-based measurements by evaluating the free expansion of atomic clouds and corresponding trapping frequencies induced by dipole oscillations (see Sec. 2.6). The knowledge of the main parameters of these matter wave sources are important for upcoming interferometric analysis of the phase coherence and for optimizing delta-kick cooling.

The major error source of this experiment has been the interaction of magnetically polarized atoms with residual magnetic fields during free expansion [17]. Therefore, the implementation of an adiabatic rapid passage (ARP) for coherently transferring atoms into the $m_F = 0$ state (to first order magnetically insensitive) will be discussed at the end of this chapter (see Sec. 2.7).

2.1 Bose-Einstein condensates in a nutshell

The statistical phenomenon of Bose-Einstein condensation was predicted quite some time ago in 1924. As commonly known, this was a joint effort done by Satyendra Nath Bose and Albert Einstein [117, 118]. More precisely, the Indian physicist sent a letter to Einstein in 1924, in which he showed that Planck's fundamental distribution law

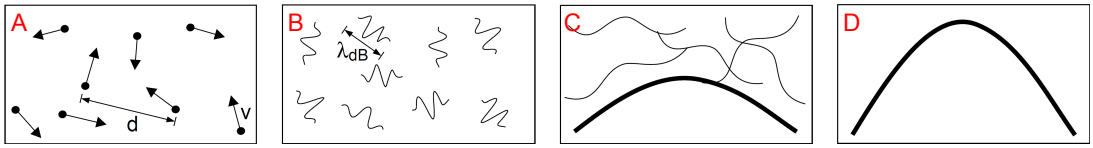

Figure 2.1: Schematic of the formation of a Bose-Einstein condensate adapted from [115]. A thermal ensemble is classically associated with point particles moving at velocity v in a volume with density $n = d^{-3}$ (A). If the temperature is lowered, they can be described as wave packets with an extension λ_{dB} (B), which start to spatially overlap at the condensate temperature $T = T_c$ (C). Approaching a temperature of absolute zero, a pure condensate is expected to form (D).

for electromagnetic radiation [119] could completely be derived from photon statistics, without the resort to the results from classical electrodynamics.

Even some time before that, Einstein confirmed Planck's assumption that the electromagnetic field itself is quantized, with light quanta or photons as the discrete energy packets. Triggered by the great importance of Boses work and inspired by the consequences of Louis de Broglies interpretation of the wave nature of particles [120], Einstein provided the full picture of quantum theory of bosonic particles in an ideal gas. He published his results in two papers [118], where he also predicted a remarkable phenomenon, the coherent condensation of atoms into one single quantum state. Since this effect only occurs because of pure quantum statistics, one has to define certain requirements for crossing the border between classical and quantum statistics.

One illustrative picture is that quantum effects need to be taken into account, when the thermal de Broglie wavelength

$$\lambda_{dB} = \sqrt{\frac{2\pi\hbar^2}{mk_BT}} \tag{2.1}$$

becomes comparable to the mean inter-particle distance $n^{-1/3}$, with n as system's density. This relation underlines one of the most fascinating prediction of quantum mechanics, that atoms should not only behave as discrete particles, but also as waves. In other words, the de Broglie wavelength characterizes the degree of position uncertainty associated with the thermal momentum distribution, which increases by lowering the temperature T. Macroscopic quantum phenomena thus arise for $n^{-1/3} \sim \lambda_{dB}$, or in other words

$$n\lambda_{dB}^3 = n\left(\frac{2\pi\hbar^2}{mk_BT}\right)^{3/2} \geq 1. \tag{2.2}$$

Fulfilling this condition leads to a spatial overlap of the particle wave functions. At this point, particles start to loose their identity, become indistinguishable, and the particle's motion cannot be associated with their classical trajectory any more.

The Bose-Einstein condensate can thus be described by one single wave function, inherently describing the properties of the whole macroscopic ensemble as one coherent quantum mechanical object. According to Pauli's exclusion principle, this is not possi-

ble for Fermions following Fermi-Dirac statistics with an anti-symmetric wave function. In terms of temperature, the above condition for Bosons can simply be rephrased to

$$T \leq n^{2/3} \left(\frac{2\pi\hbar^2}{m k_B} \right), \tag{2.3}$$

illustrating that quantum behavior is inherently coupled to low temperature phenomena. Under the normal conditions of everyday-life, the wave-like behavior is usually obscured by energetic thermal motion of particles. At high temperatures, the thermal de Broglie wavelength is small and the gas behaves classically.

However, the particle density of free electrons in metal, for example, is on the order of 10^{22} cm^{-3}. Thus macroscopic quantum properties (e.g., incompressibility and heat capacity) can be seen already at room temperature, but there might be other systems even better suited to adduce the evidence of creating that unique state of matter.

2.1.1 Degeneracy of a dilute gas of bosonic atoms

Due to the assumptions made above, cold atomic vapor systems have attracted great attention for being an ideal physical system candidate for fulfilling Bose's and Einstein's prediction.

The way towards ultra-low temperatures for quantum degeneracy was opened up with the technique of laser cooling [121, 122]. Amongst others, application and advancement of the proposed methods led to first stop an atomic beam [123], to create an optical molasses [124] and finally to confine atoms in a magneto-optical trap [125]. Cold atomic systems with temperatures in the μK regime have been investigated in laboratories ever since the 1980s (first experiments on ions even earlier [126]) and almost perfectly represent the case of a weak interacting gas. Diluteness is one of the key requirements since the formation of atomic and molecular clusters needs to be suppressed while further reducing the temperature of the gas[1]. The latter is necessary since densities and temperatures associated with laser cooling methods do not provide phase space densities below the condensation requirement (Eq. 2.2). There was a need for new scientific techniques to continue the path towards quantum degeneracy.

The first realization of a Bose-Einstein condensate has been reported in 1995 by three research groups almost at the same time [67, 68, 69]. In a ground-breaking series of experiments, researchers at the Joint Institute for Laboratory Astrophysics (JILA), at the Rice University and at the Massachusetts Institute of Technology (MIT) were able to cool down samples of dilute atomic gases to degeneracy by means of laser- and subsequent evaporative cooling in a magnetic trap. Evaporative cooling relies on the fact, that hot atoms are forced to exit the trap and subsequent re-thermalization of the remaining ensemble leads to a lower temperature. This lead to atomic gases with effective temperatures in the nK regime fulfilling the condensation requirement.

BECs of dilute atomic vapors are typically created in trapping potentials, which can be approximated as harmonic in the trapping center. This is also the case for magnetic potentials provided by an atom chip in the QUANTUS-I experiment. Thus, we now

[1] Most alkali gas BEC experiments operate at densities of about 10^{14} cm^{-3}, thus requiring temperatures well below 1 μK to reach degeneracy.

focus our discussion on the theoretical description of Bose-Einstein condensation in harmonic traps.

2.2 Bose-Einstein condensation in a harmonic trap

The properties of a Bose gas in a harmonic trap will be reviewed based on [116]. In the beginning, the treatment of an ideal gas in an anisotropic harmonic potential leads to important expressions for the density of states, transition temperature and condensate fraction.

2.2.1 Ideal Bose gas

Given a uniform non-interacting bosonic system, the occupation of states with a given temperature T according to Bose-Einstein statistics is

$$f(\epsilon) = \frac{1}{e^{(\epsilon-\mu)/k_B T} - 1}, \tag{2.4}$$

with ϵ the energy of the single particle state and the chemical potential μ. The latter can be understood as the energy equivalent, which is necessary to add an additional particle to the ensemble. The total number of atoms thus is

$$N_{tot} = \epsilon \sum g(\epsilon), \tag{2.5}$$

with g(ϵ) as the density of states. Nature sets $\epsilon_0 - \mu > 0$, since the chemical potential μ must always be lower than the ground state energy to guarantee a non-negative occupancy number of any state in the system. In the limes of an infinite number of particles (e.g., $N \to \infty$), one can rewrite the summation with an integral over the density of states $g(\epsilon)$,

$$N_{tot} = N_0 + N_{thermal} = N_0 + \int_0^\infty f(\epsilon) g(\epsilon) d\epsilon, \tag{2.6}$$

where we added the number of condensed atoms in the ground state N_0 separately. To calculate the number of atoms in the excited state, we have to derive the density of states, which is dependent on shape and dimensionality of the trapping potential.

Density of states

The density of states depends on the potential, in which the atomic ensemble is trapped. In the QUANTUS-I experiment, the Bose-Einstein condensate is formed in a magnetic trap generated by high density currents through gold wires of an atom chip (Sec. 2.4.2). Here, the three dimensional trapping potential can around its minimum be safely approximated as harmonic,

$$U_{ext}(x, y, z) = \frac{m}{2} \left(\omega_x x^2 + \omega_y y^2 + \omega_z z^2 \right), \tag{2.7}$$

with w_i the trapping frequency along the i_{th} direction. Neglecting the inter-particle interactions of this bosonic system first, the many-body Hamiltonian is the sum of the

single-particle Hamiltonians whose eigenvalues compromise the form

$$E_{n_x n_y n_z} = \left(n_x + \frac{1}{2}\right)\hbar\omega_x + \left(n_y + \frac{1}{2}\right)\hbar\omega_y + \left(n_z + \frac{1}{2}\right)\hbar\omega_z, \tag{2.8}$$

with n_i as non-negative integers. We are now able to determine the density of states $g(\epsilon)$ by calculating the number of states $G(\epsilon)$ in our harmonic trapping potential

$$G(\epsilon) = \frac{1}{\hbar^3\omega_1\omega_2\omega_3}\int_0^{\epsilon} d\epsilon_1 \int_0^{\epsilon-\epsilon_1} d\epsilon_2 \int_0^{\epsilon-\epsilon_1-\epsilon_2} d\epsilon_3 = \frac{\epsilon^3}{6\hbar^3\omega_1\omega_2\omega_3}, \tag{2.9}$$

and building

$$\frac{dG(\epsilon)}{d\epsilon} = g(\epsilon) = \frac{\epsilon^2}{2\hbar^2\omega_1\omega_2\omega_3}. \tag{2.10}$$

Transition temperature, leading order correction and condensate fraction

Based on the density of states, the number of non-condensed or thermal atoms in Eq. 2.6 follows as

$$N_{thermal} = \frac{1}{2\hbar^3\omega_x\omega_y\omega_z}\int_0^{\infty} \frac{\epsilon^2}{e^{(\epsilon-\mu)/k_BT}-1} d\epsilon. \tag{2.11}$$

In the case of particle conservation, reducing the temperature T of the system means that the chemical potential μ increases until it reaches the energy level of the ground state ϵ_0. The thermal distribution is "saturated" in the case of $\mu \to \epsilon_0$, corresponding to a critical temperature T_C. By evaluating the integral in Eq. 2.11, the number of all atoms in the thermal distribution can be given as [116]

$$N_{thermal} = N_{tot} = \frac{\Gamma(3)\zeta(3)(k_BT_C)^3}{2\hbar^3}, \tag{2.12}$$

with the Gamma function $\Gamma(\alpha)$ and Riemann's Zeta-function $\zeta(\alpha) = \sum_{n=1}^{\infty} n^{-\alpha}$. In the case of a zero ground state energy (e.g., $\epsilon \to 0$), we can find the BEC transition temperature with $\omega_{ho} = (\omega_x\omega_y\omega_z)^{1/3}$ as

$$k_BT_C = \frac{\hbar\omega_{ho}N^{1/3}}{\zeta(3)^{1/3}} \approx 0.94\hbar\omega_{ho}N^{1/3}, \tag{2.13}$$

which can be understood as the highest possible temperature associated with macroscopic occupancy of the ground sate. We see that there are two energy scales for an ideal Bose gas in a harmonic trap, the average energy level spacing $\hbar\omega_{ho}$ and the transition temperature k_BT_C. The typical level spacing in a harmonic oscillator potential for condensation (e.g., $\omega_{ho} \sim 2\pi \cdot 500$ Hz) is on the order of about a few nK, and with an average atom number of 10^4, the transition temperature T_C is expected for a few hundreds of nK.

In real systems, however, experiments are always carried out with a finite system and thus never reach the thermodynamic limit as implied above. Therefore, a correction to the critical temperature originates from the ground state energy, whose non-zero value cannot be neglected for finite particle numbers. For the three dimensional harmonic

oscillator, the ground state energy is $\epsilon_0 = \hbar/2(\omega_x+\omega_y+\omega_z)$, and the relative correction in the calculation of the critical temperature is

$$\frac{\delta T_C}{T_C} \approx 0.73 \frac{\omega_{arith}}{\omega_{ho}} N^{-1/3}, \tag{2.14}$$

with the geometric mean $\omega_{ho} = (\omega_x\omega_y\omega_z)^{1/3}$ and the arithmetic mean value $\omega_{arith} = (\omega_x + \omega_y + \omega_z)/3$ of the corresponding trapping frequencies. This correction becomes obviously more important for low particle numbers in the ensemble. Given typical trapping frequencies of the atom-chip-based QUANTUS-I experiment with about 10^4 atoms in the condensate, the correction of the transition temperature is on the order of $\delta T_C/T_C \sim 4\%$.

Having calculated the critical temperature, the number of condensed atoms in a three-dimensional harmonic oscillator potential for temperatures below T_C can be expressed as

$$N_0 = N_{tot} - N_{thermal} = N_{total}\left[1 - \left(\frac{T}{T_C}\right)^3\right]. \tag{2.15}$$

Atomic wave-function and harmonic oscillator ground state size

For $T < T_C$ atoms start occupying the lowest single-particle state, constituting the ground state of the system which can be described as a product state of the single particle wave functions ϕ_0

$$\Phi(\vec{r}_1, \vec{r}_2, ..., \vec{r}_i) = \prod_i \phi_0(\vec{r}_i). \tag{2.16}$$

The corresponding density distribution $n(\vec{r})$, reflecting the shape of the ground state wave function in the trap ϕ_0, can be calculated as

$$n(\vec{r}) = \left|\prod_i \phi_0(\vec{r}_i)\right|^2 = N|\phi_0(\vec{r})|^2. \tag{2.17}$$

For an anisotropic harmonic oscillator, the ground-state wave function can be written as [116]

$$\phi_0(\vec{r}) = \left(\frac{m\omega_{ho}}{\pi\hbar}\right)^{3/4} \exp\left[-\frac{m}{2\hbar}(\omega_x x^2 + \omega_y y^2 + \omega_z z^2)\right], \tag{2.18}$$

from which we can extract the average size of the Gaussian distribution in each dimension i, which we call the harmonic oscillator ground state size,

$$a_i = \sqrt{\frac{\hbar}{m\omega_i}}. \tag{2.19}$$

Thus, for a system of non-interacting bosons in a harmonic trap, the condensate has a Gaussian form with corresponding widths a_i. The shape of the condensates changes significantly if the atoms interact (see Sec. 2.2.3). For comparison, we consider a non-condensed, thermal ensemble of atoms in an external harmonic potential $U_{ext}(x, y, z)$.

The Gaussian width R of the classical Boltzmann distribution ($n_B \propto e^{-U/k_BT}$) is larger than a_i,

$$R = a_i \sqrt{\frac{k_B T}{\hbar \omega_i}}. \tag{2.20}$$

By calculating the Fourier transform of the ground state wave functions, we find that the momentum width of a thermal cloud is again wider than the momentum width of a BEC.

2.2.2 Interacting Bose gas and the Gross-Pitaevskii equation

Until this point, we have only considered ideal bosonic systems, but real systems are always affected by particle interactions. These will now be included and the following is based on the derivations made in [114, 127].

The grand canonical many-body Hamiltonian of N interacting Bosons under the influence of an external potential U_{ext} in second quantization is

$$\begin{aligned} \widehat{H} = &\int d\vec{r} \hat{\Psi}^\dagger(\vec{r}) \left[-\frac{\hbar^2}{2m}\Delta + U_{ext} \right] \hat{\Psi}(\vec{r}) \\ &+ \frac{1}{2} \int d\vec{r}' d\vec{r} \hat{\Psi}^\dagger(\vec{r}) \hat{\Psi}^\dagger(\vec{r}') U_{int}(\vec{r} - \vec{r}') \hat{\Psi}(\vec{r}') \hat{\Psi}(\vec{r}), \end{aligned} \tag{2.21}$$

with $\hat{\Psi}(\vec{r})$ and $\hat{\Psi}^\dagger(\vec{r})$ as bosonic field operators, which annihilate or create a particle at the position $\vec{r}$, and U_{int} as the two-body interaction potential. The field operators satisfy the Heisenberg equation of motion.

Mean-field approaches are commonly developed to overcome the problem of solving the full many-body Schrödinger equation for a large number of atoms, which in the most cases are impracticable to calculate. A common prescription is the Bogoliubov approximation, where the field operator $\hat{\Psi}(\vec{r}, t)$ is represented by a complex function $\Phi(\vec{r}, t)$ defined as the expectation value of the field operator $\langle \hat{\Psi}(\vec{r}) \rangle \equiv \Phi(\vec{r}, t)$ and a small perturbation having the physical meaning of thermal excitations like

$$\hat{\Psi}(\vec{r}, t) = \Phi(\vec{r}, t) + \delta\hat{\Psi}(\vec{r}, t). \tag{2.22}$$

$\Phi(\vec{r}, t)$ is a classical field which can be chosen as the order parameter of the system and is called the condensate's wave function with a density of $n_0(\vec{r}, t) = |\Phi(\vec{r}, t)|^2$. At very low temperatures, thermal effects and excitations can be neglected, $\delta\hat{\Psi}(\vec{r}, t) \to 0$. Here, we can derive the equation for the wave function by using the time evolution of the field operator using the Heisenberg equations of motion $i\hbar\delta/\delta t \hat{\Psi}(\vec{r}, t) = \left[\hat{\Psi}(\vec{r}, t), H\right]$, resulting in

$$\left[\frac{-\hbar^2}{2m}\Delta + U_{ext}(\vec{r}) + \int d\vec{r}' \Phi^*(\vec{r}', t) U_{int}(\vec{r} - \vec{r}') \Phi(\vec{r}', t) \right] \Phi(\vec{r}, t) = i\hbar \frac{\partial}{\partial t} \Phi(\vec{r}, t). \tag{2.23}$$

For very dilute and cold gases the particles interact only through local s-wave scat-

tering, meaning that two-body collisions play the dominant role. The interaction potential $U_{int}(\vec{r}' - \vec{r})$ can therefore be replaced by an effective contact potential in the form of

$$U_{int}(\vec{r}' - \vec{r}) = \frac{4\pi\hbar^2 a}{m}\delta(\vec{r}' - \vec{r}) = g\delta(\vec{r}' - \vec{r}), \tag{2.24}$$

where the interaction strength $g = 4\pi\hbar^2 a/m$ depends only on a single atomic parameter, the scattering length a. This approach is valid, if the mean free pathlength of an atom is much larger than the scattering length ($d \gg |a|$), or taking the mean condensate density into account, $n\,|a| \ll 1$. Using an effective contact potential here is compatible with the replacement of $\hat{\Psi}(\vec{r}, t)$ with $\Phi(\vec{r}, t)$, leading to a system which is completely described by a single wave function that fulfills the time-dependent Gross-Pitaevskii (GP) equation

$$\frac{\partial}{\partial t}\Phi(\vec{r}, t) = \left[-\frac{\hbar^2}{2m}\Delta + U_{ext}(\vec{r}) + g\,|\Phi(\vec{r})|^2\right]\Phi(\vec{r}). \tag{2.25}$$

The ground state of the time-dependent GP equation, a pure Bose-Einstein condensate, can be described by separating the wave function in a position- and time-dependent part

$$\Phi(\vec{r}, t) = \phi(\vec{r})e^{-i\mu t/\hbar}, \tag{2.26}$$

with μ as the chemical potential. Inserting Eq. 2.26 into 2.25 leads to the time-independent GP equation

$$\left[-\frac{\hbar^2}{2m}\Delta + U_{ext}(\vec{r}) + g\phi^2(\vec{r})\right]\phi(\vec{r}) = \mu\phi(\vec{r}). \tag{2.27}$$

In a given external trapping potential, the density distribution $n(\vec{r}) = \phi(\vec{r})^2$ is determined by the fraction of kinetic and interaction energy. If we neglect particle interaction again, this non-linear Schrödinger equation reduces to the usual Schrödinger equation for the single particle Hamiltonian.

GP theory based on Eq. 2.27 today is the main tool for investigating trapped BECs. The GP equation has the form of a mean-field equation where the order parameter (condensate wave function) has to be calculated in a self-consistent way. For attractive interactions, the condensates collapse, and for repulsive interaction, the GP equation can be expanded for negligible kinetic energies.

2.2.3 Thomas-Fermi approximation

For a large number of repulsive interacting atoms ($a > 0$), we can neglect the kinetic energy term completely, since the inter-atomic energy dominates the internal dynamics. This is called the Thomas-Fermi approximation and can be used to describe the density profile of the ground state according to [116] as

$$n_{TF}(\vec{r}) = \left|\Phi(\vec{r})^2\right| = \max\left\{\frac{\mu - U_{ext}(\vec{r})}{g}, 0\right\}. \tag{2.28}$$

This expression for the density profile is an inverted parabola with central density of $n(0) = \mu/g$, mirroring the shape of the external potential, which vanishes in each direction for $\mu \leq |U_{ext}(\vec{r})|$. Assuming anisotropic, harmonic potentials of the form

$$U_{ext}(x, y, z) = \frac{m}{2}\left(\omega_x x^2 + \omega_y y^2 + \omega_z z^2\right), \tag{2.29}$$

we can determine the so-called Thomas-Fermi radius, which in the i-th dimension is given by

$$R_i^{tf} = \frac{1}{\omega_i}\sqrt{\frac{2\mu}{m}}. \tag{2.30}$$

The normalization condition $N = \int d\vec{r}|\phi(\vec{r})|$ of the wave function leads to an expression for the chemical potential μ

$$\mu = \frac{\hbar\omega_{ho}}{2}\left(15Na\sqrt{\frac{m\omega_{ho}}{\hbar}}\right)^{2/5}, \tag{2.31}$$

with geometric mean of trapping frequencies $\omega_{ho} = (\omega_x\omega_y\omega_z)^{1/3}$, total number of atoms N, and scattering length a [116]. By simply combining Eq. 2.30 and 2.31, we finally obtain

$$R_i^{tf} = \left(\frac{15N\hbar^2 a}{m^2{\omega_i}^2}\right)^{1/5}. \tag{2.32}$$

Unfortunately, the TF approximation itself is not valid for analyzing the free expansion of a condensate after release from the trapping potential. Once in free fall, the internal energy is converted into kinetic energy and thus not negligible anymore. First calculations towards the expansion of a condensate by changing the trapping parameters or the external potential have been carried out by solving the GP equation numerically accompanied by comparisons with real experimental data [128].

Another approach is based on classical scaling laws. Here, the dynamic of the macroscopic wave function is described in the evolution of three scaling parameters, which are obtained by a suitable coordinate transformation [129, 130]. This method will be used to predict the free expansion of condensates in extended free fall experiments at the drop tower (Sec. 5.2).

But before we are able to analyze the temporal evolution of freely expanding condensates, we obviously have to trap atoms first. This will be discussed in the following section.

2.3 Forming a magnetic trap for neutral atoms

The magnetic dipole interaction energy U of a paramagnetic atom in a given magnetic field $\vec{B}$ is

$$U = -\vec{\mu}\cdot\vec{B} = -\mu B\cos\theta, \tag{2.33}$$

with $\vec{\mu}$ being the magnetic moment and θ the angle between the magnetic moment and the magnetic field orientation. This angle is stabilized by means of the rapid Larmor precession of $\vec{\mu}$ around the magnetic field direction with the frequency $\omega_L = \mu B/\hbar$. Quantum mechanically speaking, this becomes

$$U = g\mu_B m_F |\vec{B}|, \tag{2.34}$$

where g is the Landé factor, μ_B the Bohr magneton and m_F the magnetic quantum number associated with the projection of the total angular momentum $\vec{L} = \vec{\mu}/\mu_B g_F$ onto the direction of $\vec{B}$. In Eq. 2.34, we assume the external field to be sufficiently small, so the energy of each unperturbed magnetic sublevel is linearly shifted with respect to its hyperfine state (linear Zeeman effect).

Paramagnetic atoms therefore can be trapped making use of the interaction of the magnetic moment with a spatially varying magnetic field, causing a magnetic dipole force (Stern-Gerlach force) as

$$\vec{F}_{SG} = -\nabla U = -g\mu_B m_F \nabla |\vec{B}|. \tag{2.35}$$

Depending on the magnetic polarization of the atoms, we need to create a field minimum or maximum to trap atoms and therefore the product of the magnetic quantum number m_F and the Landé factor g_F allows to classify atoms in three distinct categories:

- $m_F g_F > 0$: **weak field seeker**, whose energy increase with increasing magnetic field strength. Therefore, the $\vec{F}_{SG}$ is pointing toward a local minimum of the external field,
- $m_F g_F = 0$: to first order **insensitive** to magnetic fields,
- $m_F g_F < 0$: **strong field seeker**, whose energy levels decreases with increasing magnetic field strength.

Since there are no magnetic monopoles as Maxwell's equations prohibit a magnetic field maximum for static current configurations in free space (Earnshaw theorem), one only can trap week field seekers in local magnetic minima. For a sufficient trapping efficiency, these minima should maintain a non-zero value in all dimension, to avoid one of the major loss channels.

Majorana losses

Atoms must maintain a given magnetic field orientation with respect to the local field, otherwise losses occur if an atom changes its state from weak field seeking to strong field seeking or even to a state with $m_F = 0$. This process in known as Majorana spin flips [131]. The trap is only stable, if the precessing atomic spin can follow the changing magnetic field direction adiabatically. In order to maintain the projection of the magnetic moment m_F, only slow changes in the projection angle θ w.r.t. to the Larmor frequency are allowed, leading to the condition

$$\frac{d\theta}{dt} < \omega_L. \tag{2.36}$$

The presence of spin flips would strongly limit the lifetime of the atoms. Static magnetic traps can be classified by the magnitude of the magnetic field in the center of the trap. Very simple magnetic traps have a zero field in the minimum, $B_0 = 0$, letting non-adiabatic Majorana transitions play a significant role, since losses occur due to unavoidable spin flips. More advanced magnetic traps show a non-zero field component in the minimum, $B_0 \neq 0$, and are usually used for cold atom and BEC experiments. Two common magnetic field configurations, representing both cases, will be introduced in the following.

2.3.1 Quadrupole trap

The Quadrupole trap provides a simple magnetic field configuration in which a local field minimum can be realized. The magnetic field scales linearly in all dimensions and may be created by a pair of coils implemented in anti-Helmholtz configuration. With an axial symmetry along the z-direction, the magnetic field can be approximated around the minimum by

$$\vec{B}(x,y,z) = B' \begin{pmatrix} x \\ y \\ -2z \end{pmatrix}. \tag{2.37}$$

Obviously, the main disadvantage of this trap configuration is a zero field in the minimum. To circumvent this, one may add a homogeneous magnetic field which is rotating in the area perpendicular to the symmetry axis of the quadrupole coils, thus forming a time-orbiting-average-potential (TOP) trap [67, 132]. Another method may be to add a repulsive, optical dipole potential (blue-detuned to the atomic resonance) which prohibits atoms from reaching the zero field [69].

2.3.2 Ioffe-Pritchard trap

A well known and extensively studied example of a magnetic trap with a local minimum is the Ioffe-Pritchard trap (IPT), first discussed by Ioffe [133] and adapted to neutral atoms by Pritchard [134, 135]. The IPT provides a quadratic confinement and has a non-zero magnetic field in the trap center. Assuming an axially symmetric case, the trapping field is given by [115, 136]

$$\vec{B}(r) = B_0 \begin{pmatrix} 0 \\ 0 \\ 1 \end{pmatrix} + B' \begin{pmatrix} x \\ -y \\ 0 \end{pmatrix} + \frac{B''}{2} \begin{pmatrix} -xz \\ -yz \\ z^2 - \frac{1}{2}(x^2+y^2) \end{pmatrix}. \tag{2.38}$$

It can be created macroscopically with a complex coil assembly [69, 67] or simply by overlapping the magnetic field of an appropriately bent, current carrying wire (e.g., atom chip) with an additional, external homogenous field (Sec. 2.4.2). Independent of the technology, the center of the trapping potential for paramagnetic atoms can be approximated as harmonic,

$$U(x,y,z) \approx \frac{m}{2}\left(\omega_x x^2 + \omega_y y^2 + \omega_z z^2\right), \tag{2.39}$$

with trapping frequencies in the axial (ω_z) and radial ($\omega_x = \omega_y \equiv \omega_{rad}$) direction of

$$\omega_z = \sqrt{\frac{\mu_B g_F m_F}{m}} \cdot \sqrt{B''}, \tag{2.40}$$

$$\omega_{rad} = \sqrt{\frac{\mu_B g_F m_F}{m}} \cdot \sqrt{\frac{B'^2}{B_0} - \frac{B''}{2}}. \tag{2.41}$$

The axial trap steepness thus scales with the curvature of the magnetic field B'' only, whereas in the radial direction additionally the gradient B' and the trap bottom B_0 need to be considered. Strongly confined atoms are favorable for high collision rates, necessary for fast re-thermalization during the evaporation process (Sec. 2.5.2).

After introducing the basics of Bose-Einstein condensation and standard principles of magnetic trapping of neutral atoms, the QUANTUS-I apparatus and the experimental sequence used to create degenerate gases with an atom chip will be presented.

2.4 The QUANTUS-I experiment

QUANTUS-I is a pathfinder experiment for exploring cold quantum gas technology under the unique conditions of microgravity. It is part of the DLR funded joint project QUANTUS[2], targeting the long-term goal of studying space-borne quantum gas experiments. As an accessible high-quality microgravity platform to perform cold atom science in free fall, the drop tower in Bremen was chosen [107]. Therefore, an experimental apparatus had to be developed and integrated into a small capsule [17, 137, 19].

A picture of the current drop capsule setup is shown in Fig. 2.2. Four aluminum stringers enclosing six intermediate platforms made of an aluminum-wood composite are fixed to the capsule bottom. From top to bottom, the scientific payload consists of a laser system including control electronics, a computer control system for the experimental sequences followed by the vacuum pump section. The heart of the experiment is an UHV chamber including atom source and atom chip, powered by low-noise current drivers. Another computer system for housekeeping data and monitoring is situated right above the batteries.

The degree of sophistication of such a setup, high enough for any BEC apparatus, is even more demanding in order to fulfill stringent requirements for operation in the drop tower environment:

- **Miniaturization.** The experiment has to fit into a drop capsule with an effective height of 1.73 m and a diameter of 0.6 m [107]. Thinking of a complete quantum gas experiment, this naturally results in a high packing density which itself is challenging regarding the construction of an UHV vacuum chamber and complex laser system assemblies, or by effectively decouple cross-talking between electrical components and ensuring sufficient thermal management.

- **Robustness.** After the free fall provided by dropping the capsule in an evacuated tube from a height of 110 m, the capsule is caught in a deceleration tube

[2]QUANTUS: Quantengase unter Schwerelosigkeit, DLR funded project which started in 2004

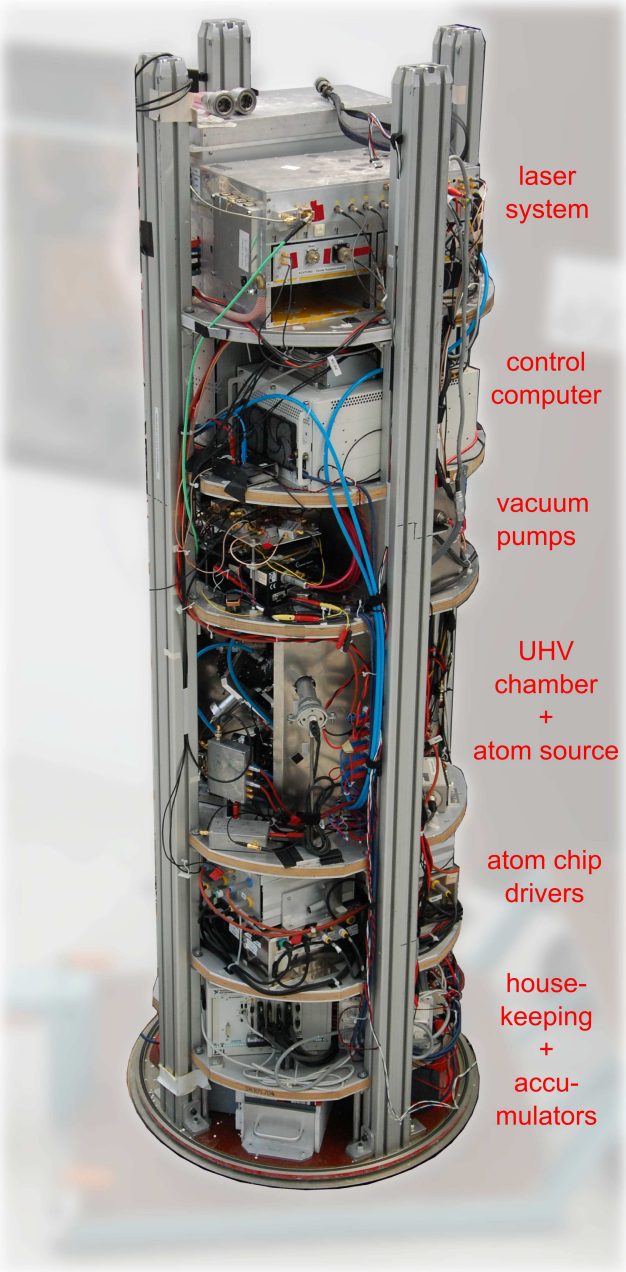

Figure 2.2: Photograph of the QUANTUS-I experiment capsule (without pressurized cover, top lid plate and nose cone [107]). Subsystems from top to bottom: laser system, NI-PXI control computer, vacuum pump section, UHV chamber with atom chip and dispensers, atom chip current drivers, NI-PXI for housekeeping data, and accumulators. This picture was taken in front of our laboratory at the ZARM in Bremen.

containing polystyrene pellets. Accelerations with peak values up to 50 g stress the mechanical structure and require a robust engineering and integration of the subsystems.

- **Temperature.** During evacuation, the vacuum-tight capsule heats up since most electronics remain switched on. Consequently cooling of sensitive parts of the payload (especially laser sources and optical bench) is required. Therefore, a dedicated thermal control system (TCS) was developed which typically limits the temperature increase to about $\sim 3°$C.
- **Mass.** Since the payload mass is limited to 234 kg, lightweight constructions had to be designed with the right choice of material and advanced engineering techniques[3].
- **Low power consumption.** The experiment has to be powered by batteries, since no power supply interface is possible during free flight. They are implemented at the bottom of the capsule, operating at 28 V DC voltage with a total stored energy of 0.56 kWh.
- **Remote control.** A computer system (NI-PXI) for housekeeping data and remote control is implemented at the bottom of the capsule. Before dropping the experiment, control sequences (LabView routines) have to be uploaded via remote control capability.

More detailed information about the drop tower requirements and the dropping procedures are given in Ch. 5, where the free fall results will be reported, or can be found elsewhere [107, 17].

During this thesis, the QUANTUS-I experiment has been fully re-assembled after destruction of the atom chip in 2010. We will now shortly review the different subsystems with focus on the atom chip and laser system, before the experimental procedures will be described. Details on the experiment hardware and the payload can be found in [137, 19].

2.4.1 Vacuum system and atom source

Ultra-cold quantum gas experiments require an ultra-high vacuum (UHV) in the 10^{-11} mbar regime. In QUANTUS-I, a compact single-chamber design made out of non-magnetic steel and based on copper seals (CF-type) was realized. The background pressure is a compromise between a fast loading rate of the MOT and a long lifetime of the BEC [19]. Here, an ion getter pump (MECA2000, 20l/s) and a passive getter (SAES) guarantee a background pressure of less than 10^{-11} mbar, ensuring sufficient long lifetimes of the BEC (~ 3 s) but limiting the MOT loading rate and therefore the experimental cycle time (~ 15 s). Additionally, a titanium sublimation pump with 3 filaments is integrated.

The atomic source are alkali metal dispensers (AMD) supplied by SAES Getters. AMDs offer an efficient and compact source for depositing alkali vapors. The evaporation rate is controlled by the amount of current sent through the wire shaped devices

[3] However, the QUANTUS-I payload already exceeds this value by roughly 100 kg

which are integrated below the atom chip. ^{87}Rb was chosen for laser cooling and trapping since it is paramagnetic, features a positive scattering length and highly mature commercial-of-the-shelf (COTS) laser diodes and electro-optical components for laser beam manipulation and switching can be used.

2.4.2 Atom chip and external magnetic fields

In QUANTUS-I, an atom chip is used to generate the field gradients necessary to cool and trap rubidium quantum gases. The use of atom chips not only leads to a compact design of UHV chambers, but generally greatly simplifies the apparatus needed to produce ultra-cold atoms or Bose-Einstein condensates [138, 139], compared to the first atom-optical experiments based on macroscopic traps [69, 67]. This miniaturization is still part of an on-going technological progress and compromises an important step towards robust application of quantum gas experiments.

Currents running through wires form magnetic field geometries which constitute versatile potential landscapes for the atoms [140]. Atom chips only require modest currents even for high field curvatures and thus high trapping frequencies, $\partial^2 B/\partial^2 r \sim 1/r^3$ which becomes large in the proximity of the chip. The distance between the wires and the atomic ensemble can be chosen to be very small, typically on the order of about 100 μm, allowing for tightly confining magnetic potentials at a low power consumption level.

Gold wires on a chip have a very good heat dissipation (which otherwise would strongly limit the maximum currents on the chip and therefore the maximum magnetic field strength) and mechanical stability. The atom chip production enormously benefits from the technology established for micro-chips, e.g. fabrication technologies, electroplating and UV lithography [136].

In combination with external fields, they allow for nearly any current distribution and magnetic field geometry that are still very hard or impossible to realize with conventional technologies. These include diverse geometries for trapping and coherent guiding of ultra-cold atoms [141], beam splitters for matter waves [142, 143], complex RF dressed potentials for on-chip BEC manipulation [144], and integrated interferometers [145, 146]. Current developments focus on integrating optical, electrical, and magnetic components into an atom chip scale subsystem for versatile fundamental and applied physics experiments.

Straight conductor configuration

Many field geometries generated with macroscopic coils can be replaced by wire structures and a uniform magnetic bias field [136]. The principle of trapping atoms with a simple straight conductor (sc), is to overlap a magnetic field arising through current send through the wire with an external, homogenous field B_{bias} in such a way, that the field amplitudes at a certain position above to the conductor cancel each other. This waveguide geometry provides a conservative potential which traps atoms in two dimensions, but allow them to move freely in the third one.

The magnitude of a *radial symmetric* field of a single, thin, infinitely long current carrying wire is [136]

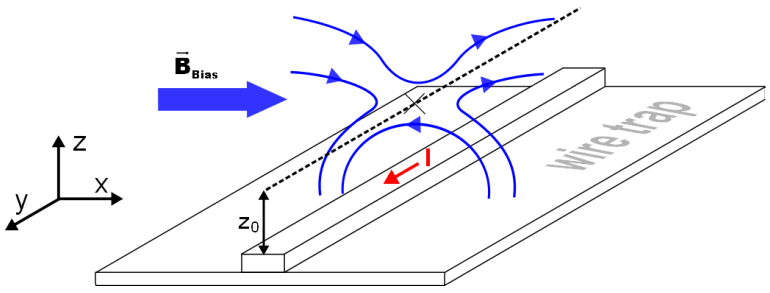

Figure 2.3: Basic configuration of a two-dimensional quadrupole field. The radial symmetric field of a straight wire (with current I) is overlapped with a homogenous bias field $\vec{B}_{bias} = B_{bias} \cdot \vec{e}_x$, giving a zero field line at distance z_0.

$$B_{sc}(z) = \frac{\mu_0}{2\pi} \cdot \frac{\mathrm{I}}{z}, \tag{2.42}$$

with the wire current I, the perpendicular distance to the straight wire z, and the vacuum permeability μ_0. Adding a homogenous magnetic bias field $\vec{B}_{bias} = B_{bias} \cdot \vec{e}_x$ perpendicular to the wire axis (see Fig. 2.3), forms a total magnetic field distribution with the following magnitude, gradient and curvature

$$B(z) = \frac{\mu_0}{2\pi} \cdot \frac{I}{z} - B_{bias}, \tag{2.43}$$

$$B'(z) = -\frac{\mu_0}{2\pi} \cdot \frac{I}{z^2}, \tag{2.44}$$

$$B''(z) = \frac{\mu_0}{2\pi} \cdot \frac{I}{z^3}. \tag{2.45}$$

In this configuration, a zero magnetic field line ($B(z_0) \equiv 0$) at the given distance

$$z_0 = \frac{\mu_0}{2\pi} \cdot \frac{I}{B_{bias}} \tag{2.46}$$

is created, and the resulting field can be approximated as a two-dimensional quadrupole in the vicinity of this line. No trapping is provided along the wire axis $\vec{e}_y$. This concept is the very basis of a 2D trap for weak field seeking atoms [147] and has been used to demonstrate atom guiding.

When superimposed with another homogenous field component (e.g. along the wire axis with $B_0 \cdot \vec{e}_y$), the initial 2D quadrupole guide is formed into an 2D Ioffe-Pritchard (IP) guide with a non-zero field in the minimum and a quadratic variation around the trap center. The position of the trap bottom (Eq. 2.46) changes with the applied bias field $\vec{B}_{bias}$ since higher fields move the trapped atoms closer to the wire.

Advanced configurations for three-dimensional trapping have been made possible by, amongst others, dimple-type traps [140], simply bending a single wire in different shapes, as explained in the following.

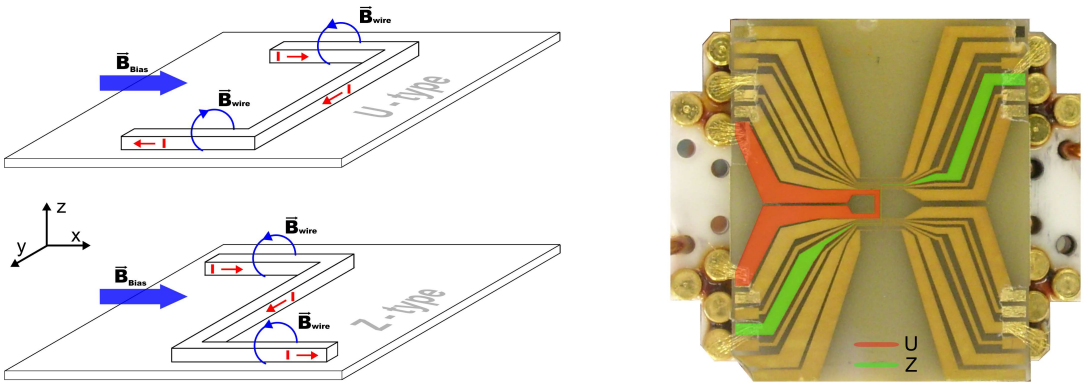

Figure 2.4: Schematic of the U-type and Z-type wire configuration (left) and photograph of the QUANTUS-I atom chip surface (right). Indicated in red and green are the wires constituting the U- and Z-type magnetic traps (in combination with a magnetic bias field $\vec{B}_{bias}$). More details in text.

U-type and Z-type wire configuration

Three-dimensional trapping by adding magnetic confinement along the direction of the straight conductor field can be realized by appropriately bending a single wire. The most common U-type and Z-type wire configuration are manifestations of a quadrupole and Ioffe-Prichtard-type magnetic trap for neutral atoms, respectively.

Here, all segments carry the same current I as depicted in Fig. 2.4 (A). The resulting magnetic field vectors are added to an additional, uniform bias field B_{bias}. In both cases, the central wire segment together with B_{bias} forms a two-dimensional quadrupole trap, whereas the bent parts (orthogonal to the central part) provide the field components for axial confinement. In Fig. 2.4 (A), x- and z-axis can be referred to as the strong axis, since the magnetic field gradient is strongest along this direction, whereas confinement in the y-direction is comparably weak.

In the case of a U-type wire, the magnetic fields of the two bent wires cancel each other at the trap center since they are pointing in opposite directions. The resulting field configuration is of 3D quadrupole type, which has a zero field at the minimum and rises linearly in the vicinity of it, and is preferably used for operating a magneto-optical trap (MOT). In the case of a Z-type trap, the magnetic field components add up to a finite value at the trap center, since they are pointing in the same direction. This configuration constitutes the chip-based version of an Ioffe-Pritchard trap and is used for magnetic trapping of atoms and subsequent BEC generation.

Both U-type (red) and Z-type (green) magnetic traps can be realized with the atom chip used in QUANTUS-I, as depicted in Fig. 2.4 (B). For details on the used atom chip see [137, 19].

External coil assemblies

Around the chamber a total number of four coil pairs are implemented. Three of them are used for generating homogeneous bias-fields (K1, K2, Bias) whereas one

	macroscopic coil pair			
	MOT	Bias (y)	K1 (x)	K2 (z)
field [G/A]	-	10	1.75	1.5
gradient [G/cm A]	1.73	-	0.5	-

Table 2.1: Induced magnetic fields and gradients of the macroscopic coil assemblies (for geometric orientation, see Fig. 2.6, right) used in the QUANTUS-I experiment [19].

pair (MOT) is used in a Anti-Helmholtz configuration (see Tab. 2.1). The latter is being used for generating a quadrupole field necessary for a macroscopic MOT, before the atoms are cooled and trapped with the magnetic field provided by the atom chip only (see Sec. 2.5.1). Their design and implementation was realized as a trade-off between proper optical access to the chamber, compactness of the overall assembly and homogeneity of the resulting field configurations [19].

The homogeneous bias fields (K1, K2, and Bias) are used for compensation of residual fields (e.g., during the molasses phase), to shift the position of the MOT (e.g., mode overlap with magnetic trap) and finally to generate the offset fields for an atom-chip-based Ioffe-Pritchard trap (Sec. 2.5.2). The geometrical configuration of these coil pairs w.r.t the atom chip and the laser beams can be extracted from Fig. 2.6 (right).

2.4.3 Miniaturized diode laser system

Besides the necessary magnetic field configurations, the second key ingredient for atom cooling and trapping is laser light. In QUANTUS-I, the laser system is based on compact and robust modules using miniaturized opto-mechanical components and distributed feedback (DFB) diode lasers as sources [137]. Within such modules (see for example right side of Fig. 2.5), the beam height is 20 mm. The housings are made from aluminum alloys with high tensile strengths and all opto-mechanical components have been designed for the highest possible mechanical stability by being (partially) adjustable at the same time. The optical interface inter-connecting the modules and the vacuum chambers is realized with polarization maintaining, single mode optical fibers (e.g. SuK PMC-850-5,1-NA013-3-APC-400-P).

A more detailed description can be found in [137], we will now shortly review the functionality of the system consisting of 4 distinct modules.

- The **reference laser** is based on a DFB diode (Eagleyard, EYP-DFB-0780-00080-1500-TOC03-0000) which is stabilized 40 MHz below the $|5S_{1/2}, F = 3\rangle \rightarrow |5P_{3/2}F' = 4\rangle$ transition of ^{85}Rb (see yellow line in Fig. 2.5). The chosen isotope has a relatively high natural abundance ($\sim 72\%$) and the particular transition additionally features the largest transition strength [148]. The error signal is generated by means of modulation transfer spectroscopy (MTS) [149]. Therefore, part of the laser beam is split into a weak probe and a strong pump beam, of which the latter is modulated with a free-space electro-optical modulator (EOM), whose resonance frequency is 7.4 MHz [137]. Both beams are overlapped in counter-propagating directions within a rubidium vapor cell. After passing the cell, the

probe beam is detected with heterodyne detection techniques. This laser module has one optical output fiber ($\sim$ 5 mW) which is guided to the switching and distribution (SD) module, where beatnotes with both, cooling and repumping lasers, are detected for offset lock stabilization.

- The module for **laser cooling** consists of a DFB-diode seeding a tapered amplifier (Eagleyard, EYP-TPL-0780-01000-3006-CMT03-0000). Such MOPA (master-oscillator power-amplifier) configurations are commonly used to reach higher output power levels by preserving the frequency characteristics of the source. Typical optical powers in the output fiber of around 140 mW are achieved. For frequency stabilization, the cooling laser light is overlapped with the master laser light in the SD module. An offset lock stabilization path regulates the frequency of the cooling laser 2-3Γ red to the $|5S_{1/2}, F = 2\rangle \rightarrow |5P_{3/2}F' = 3\rangle$ transition of ^{87}Rb. Additionally, this laser is electronically tuned to optical pumping and detection transitions (see red lines in Fig. 2.5).

- The **repumping laser** again is a single DFB diode, offset locked to the reference laser to emit laser light resonant to the $|5S_{1/2}, F = 1\rangle \rightarrow |5P_{3/2}F' = 2\rangle$ transition of ^{87}Rb (blue line in Fig. 2.5). The optical fiber output provides about 11 mW.

- The light of the above mentioned modules is provided to the **switching- and distribution** (SD) module. Besides generating the beat notes for offset lock stabilization with fast photodiodes (Hamamatsu, G4176-03), it features optics and acousto-optical modulators (AOM, Crystal Technology, 3080-125) to overlap and switch cooling and repumping light for MOT operation and optical molasses. An additional path serves for detection and optical pumping. Before coupled back into fibers, all beams pass a mechanical shutter to avoid residual light coupled into the fiber and subsequently guided to the atoms even when the AOMs are switched off.

2.4.4 Control system and housekeeping data

For experimental control, data housekeeping and monitoring two commercially available computers (National Instruments, NI) operating with a real time system are integrated within the drop capsule.

One of them is a standard equipment of the ZARM drop capsule [107], used for triggering the capsule release process and monitoring of important physical properties (e.g., temperature, pressure, acceleration) before, during and after the drop. The whole experimental sequence and the laser stabilization routines run on the second computer and are loaded into the memory via Ethernet (ground mode) or WLAN (drop mode). For a detailed description of the computer system and the used software, see [19, 112].

2.4.5 Absorption detection of ultra-cold rubidium atoms

The information we want to extract from experiments are encoded in the atoms themselves, e.g., particle number, spatial width, contrast. Therefore, the atomic cloud is detected destructively by a collimated laser beam pointing along the y-direction with

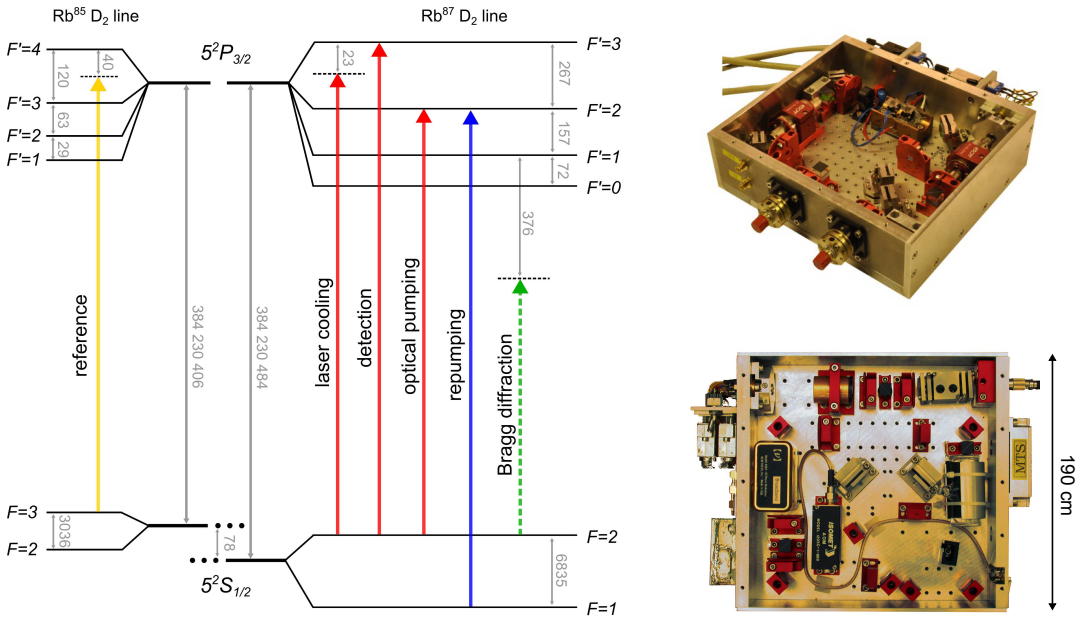

Figure 2.5: Schematic of the rubidium D_2-line hyperfine splitting and the used frequencies in the experiment (left). Frequency values correspond to MHz (grey lines), the four laser sources incl. functionality are distinguished in different colors. Exemplary pictures of a miniaturized MOPA system (upper right) and an MTS-based reference laser (lower right) as used in the QUANTUS-I experiment are given.

a diameter of 20 mm, which is resonant to the $|F = 2\rangle \rightarrow |F' = 3\rangle$ transition of ^{87}Rb. Typically, the intensity was chosen to be 20% of the saturation intensity of this particular transition, resulting in a detection intensity of less than $I_{det} = 0.5\ \mathrm{mW/cm^2}$.

In each absorption cycle, two successive images are taken with a 12 bit charge-coupled-device (CCD) camera (Hamamatsu C8484-15G), whose surface-normal is anti-parallel to the detection beam. The CCD camera features a pixel size of 6.45 μm, and the detection beam is first collimated, then partly absorbed by the atoms and subsequently imaged with an aspheric lens (Linos G322307525) onto the CCD chip. The system is designed for 1:1 imaging, but a slight magnification of M=1.03 was determined experimentally by analyzing the position of freely falling atoms.

The first picture is a shadow image of the atomic cloud and proportional to the atomic density (I_{at}). The second one is a direct beam image in the absence of all atoms, providing us with a beam intensity I_{beam}. After correction with the camera's dark image (I_{dark}), we can calculate the optical density to

$$D(x,z) = \ln\left[\frac{I_{beam} - I_{dark}}{I_{at} - I_{dark}}\right]. \tag{2.47}$$

If the detection beam is aligned along the y-direction, the number of atoms N can be calculated by integrating the optical density D along the two visible dimensions

$$N = \frac{1}{\sigma}\int D(x,z)dxdz = \int\left[\int n(x,y,z)dy\right]dxdz, \tag{2.48}$$

with the atomic density $n(x, y, z)$. To finally calculate N, we need to know the atom-light interaction cross-section given by

$$\sigma = \frac{\sigma_0}{1 + I_{det}/I_{sat} + 4\delta^2/\Gamma^2}, \tag{2.49}$$

with the resonant cross-section σ_0, the detection intensity I_{det}, the saturation intensity of the transition I_{sat}, the detuning from resonance δ and the natural linewidth Γ [150].

A typical scan of the detection frequency is given in Fig. 2.9, showing the normalized atom number dependent on the detection frequency detuning. The Gaussian part of a fitted Voigt profile has a FWHM of 13.47(72) MHz. Hence, the observed width is broader than Γ and associated with the spectral width of the detection laser (DFB-type).

In order to extract more information besides atom numbers, one can fit different distributions to the column densities (e.g., Gaussian distribution for thermal atoms, Thomas-Fermi distribution for purely condensed samples, see Sec. 2.6). Furthermore, we will introduce another type of fit-function for the analysis of spatial interference patterns, which is based on two spatially overlapping Gaussian wave packets with a modulation of the local density (Sec. 3.5.2).

But before we focus on the analysis of the spatial shape of ultra-cold clouds of atoms, we have to prepare them.

2.5 Preparing Bose-Einstein condensates in QUANTUS-I

In this section, the preparation steps for generating a condensate will be briefly described. The cycle starts by collecting atoms in a MOT, then they are transferred into a magnetic potential provided by an atom chip and evaporatively cooled down to degeneracy by means of RF-induced evaporation.

2.5.1 Two stage mirror-MOT with an atom chip

One necessary requirement to trap atoms is their motional energy to be lower than the depth of the corresponding conservative trapping potential.

Laser cooling in a magneto-optical trap (MOT) is a standard technique to trap and pre-cool atoms within a certain volume, reaching effective thermal energies limited only by the recoil shift. It relies on directed radiation pressure forces which result in viscous damping and average cooling of the sample. A magnetic field gradient (e.g., quadrupole field) ensures a position dependent force, thus providing spatial confinement [124]. Rubidium atoms enter the trap via background vapor, controlled via the current of the dispensers. They are mounted directly underneath the atom chip and are wired to electrical feedthroughs via Kapton-coated wire and crimp connectors.

In a first step, a macroscopic pair of anti-Helmholtz coils is used for generating the quadrupole field. After typical loading times of 10 s, about $1.6 \cdot 10^7$ atoms are cooled and trapped. In a second step, the field provided by the macroscopic coils is switched off, whereas current is sent through the U-type shaped wire and additional bias field coils (B_{bias}), forming a chip-based 3D quadrupole field. During magnetic field switching, the laser beams are turned of for 4 ms.

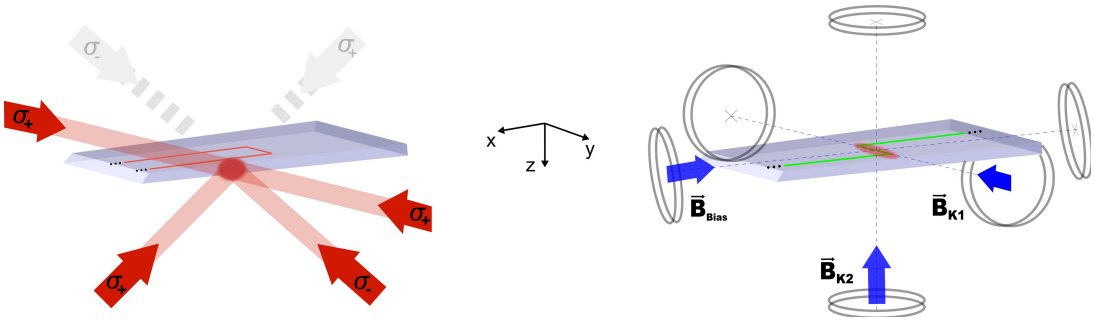

Figure 2.6: Schematic of a mirror-based magneto-optical trap (left). The laser beams are depicted as red arrows and labeled with their light helicity (σ_+ and σ_-). In this geometry and in presence of a quadrupole field, atoms see pairs of counter-propagating laser beams with orthogonal polarization in vicinity of the chip (two additional beams forming a standard six beam MOT are drafted in grey). Orientation of the compensation (K1 and K2) and bias field coils are depicted on the right side. The Anti-Helmholtz coils are not shown here for better visibility.

The chip-based field has much steeper gradients (at smaller currents) for more precise control of the trap, e.g., allowing to move the center of the chip-MOT towards the chip and to positions, which are favorable for subsequent magnetic trap loading. The prior loading in the macroscopic MOT is necessary, since the trapping volume of the chip-MOT is much smaller, not suited to efficiently load atoms from the background directly. After moving to the desired position, the chip-based MOT contains about $N \sim 1 \cdot 10^7$ atoms.

In both cases, the general principle of a mirror-MOT is used (Fig. 2.6, left). Instead of six beams on three perpendicular axes such as in standard geometries, the mirror-MOT configuration uses only four beams. Two of them (same helicity) are facing each other along the y direction whereas the other two (opposite helicity) are brought into the chamber from $+45°$ and $-45°$ in the x-z plane, respectively. In this configuration [138, 139], laser beams from the diagonal telescopes get reflected at the HR-coated dielectric layer of the surface of the atom chip and counter-propagate with each other. Since each reflection from the chip changes the helicity, atoms see pairs of counter-propagating laser beams with orthogonal polarization in vicinity of the chip, which is necessary for MOT operation.

All MOT-beams in the QUANTUS-I experiment have a diameter of 20 mm with roughly 15 mW of cooling light each, 4-5 Γ red-detuned to the cooling transition, and about 3 mW of repumping light on resonance (distributed via diagonal telescopes only).

Optical molasses

Laser cooling is based on scattering photons, and the effective limit to the lowest possible temperature which can be achieved, is $k_B T_{min} = \hbar\Gamma/2$, with the Boltzmann constant k_B and the natural linewidth of the alkali atom's cooling transition Γ. For ^{87}Rb, this leads to a Doppler limit of 145.6 μK [150].

To realize even colder temperatures for more efficient loading of the magnetic trap, a molasses phase is applied at the end of the MOT-stage [151]. Here, all magnetic fields

are switched off. The cooling laser intensity is linearly reduced to 25% of its value during MOT operation, and the frequency is further red-detuned from resonance to about $10\,\Gamma$. The repumping laser is shifted neither in intensity nor in detuning.

Low molasses temperatures can only be achieved if no ambient magnetic fields are present. Therefore, (i) a magnetic shield is foreseen to passively protect from external noise sources, and (ii) the three bias coil pairs are used to actively cancel the residual fields in all dimensions.

This allows to finally prepare a sample with $N \sim 7 \cdot 10^6$ atoms at temperatures of about $T \sim 20\ \mu$K.

2.5.2 Chip-based Ioffe-Pritchard trap

After preparation of a sufficiently cold cloud of atoms, we can load them into the Ioffe-Pritchard trap. Since the atoms are non-polarized after molasses cooling and to improve the loading efficiency, we transfer them into the $m_F = 2$ state by means of optical pumping.

Optical pumping and magnetic trap loading

Right after the optical molasses phase, optical pumping is applied to transfer the atoms to the Zeeman level with the highest magnetic moment. Therefore, the cooling laser (see Fig. 2.5) is tuned to be resonant to the $|F = 2\rangle \rightarrow |F' = 2\rangle$ transition and illuminates the atoms for a short duration of about 700 μs in the absence of all other laser beams. To obtain population trapping in the $|F = 2, m_F = 2\rangle$ state, the beam is circularly (σ_+) polarized with respect to the quantization axis given by a homogeneous magnetic field of about 8 G in the y direction.

Directly after optical pumping, the current of the Z-type trap (see. Fig 2.4) is switched on together with a bias field ($I_Z = 2$ A, $I_{bias} = 0.8$ A) to form a Ioffe-Pritchard trap. An additional homogenous field provided by K1 ($I_{K1} = 1.6$ A) defines the value of the magnetic field at the trap minimum. About $N \sim 4 \cdot 10^6$ atoms can be loaded into the cigar-shaped potential without significant heating.

Evaporative cooling

Evaporative cooling is used to reduce the temperature of atoms well below the recoil limit [69, 152, 153]. This technique adiabatically removes the hottest atoms from an ensemble, by ensuring re-thermalisation due to elastic scattering at all times, thus lowering the effective temperature. This is necessary to further increase the phase space density until condensation occurs

$$\rho = n\lambda_{dB}^3 \geq 2.613. \tag{2.50}$$

In our chip-based magnetic trap, we use an RF field, which selectively induces spin flips between trapped and untrapped states. As described in Sec. 2.3, trapping is a result of the Zeeman splitting of the hyperfine ground state. Once trapped, atoms with high kinetic energy can reach regions with high potential and thus experience a larger energy shift due to $\Delta E = m_F g_F \mu_B |\vec{B}|$.

	Δt [ms]	I_z [A]	I_{bias} [A]	I_{K1} [A]	ω_{rad} [Hz]	ν_{rf} [MHz]
z-trap 1	0	2	0.8	1.6	$2\pi \cdot 260$	-
z-trap 2	20	2	$0.8 \rightarrow 2.7$	1.6	$2\pi \cdot 1300$	-
	290	2	$2.7 \rightarrow 6.5$	1.6	$2\pi \cdot 7600$	
evap. 1	230	2	6.5	1.6	$2\pi \cdot 7600$	$40 \rightarrow 4$
	20	2	$6.5 \rightarrow 5.5$	1.6	$2\pi \cdot 5500$	
evap. 2	300	2	$5.5 \rightarrow 5$	1.6	-	$4 \rightarrow 2.3$
evap. 3	100	2	$5 \rightarrow 3.55$	1.6	$2\pi \cdot 2500$	$2.3 \rightarrow 1.99$
evap. 4	300	2		1.6		$1.99 \rightarrow 1.83$
condensate generation						
decomp.	152	$2 \rightarrow 1.2$	$3.55 \rightarrow 0.6$	1.6	$2\pi \cdot 130$	$1.83 \rightarrow 3$
h-trap	250	1.2	$0.6 \rightarrow I_{bias,h}$	1.6	$\omega_{rad,h}$	-
condensate release						

Table 2.2: Evaporation sequence with corresponding IP trap current configuration (I_Z, I_{bias}, and I_{K1}), step duration Δt, radial trapping frequencies ω_{rad} [137] and radio frequency ν_{RF} for forced evaporation. Differently shaped current ramps are used for the specific steps [19], the RF ramps are linear.

The frequency of the RF radiation is chosen to be resonant with the most energetic atoms near the edge of the trap and drives spin transitions of $\Delta m_F = 1$, therefore $h\nu_{RF} = 1/2 g_F \mu_B |\vec{B}|$. Atoms are repelled from the trap, when they end up in a high-field seeking state. To continuously cool down the sample, the RF frequency is chirped with decreasing temperature. With this run-away-evaporation, the phase space density can be increased even with occurring losses in atom number [69, 152, 116].

The steepness of the trap determines the rate of inter-atomic collisions and therefore places a fundamental limit on how fast the evaporation can be realized. This is crucial for conducting experiments within the timescale of a drop experiment, which in the case of QUANTUS-I is limited to about 4.7 s. Higher elastic scattering rates

$$\tau_{el} = n \sigma_{el} \bar{v} \sqrt{2}, \tag{2.51}$$

with density n, s-wave scattering cross section σ_{el}, and mean relative velocity $\bar{v}$ of the gas, are favorable for fast re-thermalisation.

This is the reason for initial compression of the trap. On the other hand, the probability of inelastic collisions will increase with higher density ($\sim n^2$) and particle losses become more important, making the evaporation process inefficient. Therefore, the density is controlled and balanced by smoothly opening the trap during the evaporation process. By keeping the z-wire current at a constant value, the bias field can be ramped down to decompress the trapping potential and to move the atoms further away from the chip.

2.5.3 Experimental sequence for BEC generation

The actual experimental sequence of condensate generation by means of forced RF evaporation is given in Tab. 2.2. If not indicated differently, all current ramps are adiabatic w.r.t. the atomic motion and the RF sweeps are linear in time.

After the atoms are initially trapped in z-trap 1 ($I_z = 2$ A, $I_{bias} = 0.8$ A, and $I_{K1} = 1.6$ A) which is directly switched on after optical pumping, the trap is immediately compressed in a first step lasting $\Delta t = 20$ ms by ramping up the current of the bias coils ($I_{bias} = 0.8 \rightarrow 2.7$ A). The atoms are now trapped in z-trap 2 with $\omega_{rad} = 2\pi \cdot 1300$ Hz.

With the beginning of the first evaporation ramp ($\nu_{rf} = 40 \rightarrow 4$ MHz), a second compression follows ($I_{bias} = 2.7 \rightarrow 6.5$ A) which leads to maximum trapping frequencies along the fast axis of about $2\pi \cdot 7.6$ kHz. In the last 20 ms of evaporation ramp 1, we already start to decompress the trap ($I_{bias} = 6.5 \rightarrow 5.5$ A) to $\omega_{rad} = 2\pi \cdot 5.5$ kHz.

Evaporation ramp 2 ($\nu_{rf} = 4 \rightarrow 2.3$ MHz) is executed synchronous to a smooth adiabatic decompression for $\Delta t = 300$ ms, ending up with $I_{bias} = 5$ A. During the last two ramps, which in total last for $\Delta t = 400$ ms, the trap is further opened ($I_{bias} = 5 \rightarrow 3.55$ A). Finally, BEC is reached ($\nu_{end} \cong 1.83$ kHz) in a cigar-shaped potential with radial trapping frequencies of $2\pi \cdot 2500$ Hz. The overall duration of magnetic trapping and evaporative cooling to degeneracy sums up to 1240 ms.

After BEC generation, the RF frequency is ramped up again to reject any residual thermal atoms while the trap is further decompressed[4] ($I_{bias} = 3.55 \rightarrow 0.6$ A). Finally, the atoms are smoothly transferred into a final holding trap (h-trap) by only changing the bias current to a distinct value $I_{bias,h}$. From here, the atoms can be released by switching off all currents ($I_{bias,h} = I_z = 0$) except a homogeneous quantization field, provided by the coil pair K_1. In this thesis, the following three holding traps are used in most experiments:

- **Shallow trap**: decompressed trapping potential resulting in the slowest expansion in ground-based experiments with $\omega_{rad,h} \sim 2\pi \cdot 40$ Hz ($I_{bias,h} = 0.36A$). Gravitational sag losses and trapping potential deformation occur for further reduction of the bias field.

- **Steep trap**: fast expansion and fast conversion of mean-field energy, advantageous for interference experiments with $\omega_{rad,h} \sim 2\pi \cdot 130$ Hz. This trap is generated using $I_{bias,h} = 0.6A$

- **Lens trap**: very fast expansion with $\omega_{rad,h} \sim 2\pi \cdot 350$ Hz used for preparatory experiments on delta-kick cooling in ground-based experiments, realized with $I_{bias,h} = 1A$.

Independent of the final trap geometry, generated condensates in this experiment contain roughly $N = 10^4$ atoms, which is about one magnitude lower than state-of-the-art atom-chip experiments [154, 141].

[4] However, we typically end up with condensate fractions of 65% only.

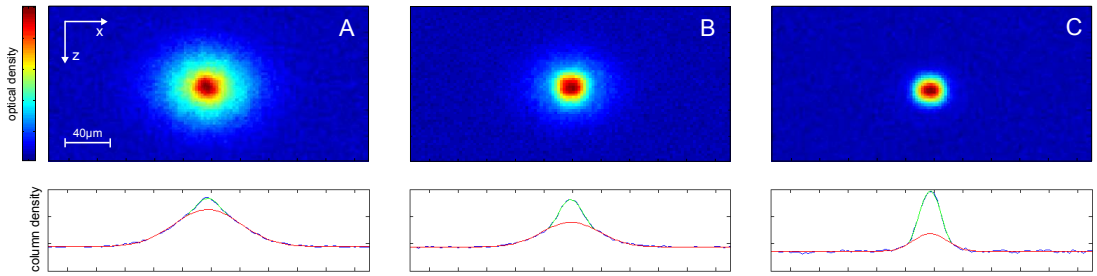

Figure 2.7: Exemplary measurement of the condensate fraction for different effective temperatures. From A-C, the condensate fractions N_c/N have been measured to be $6\%, 34\%$, and 62% corresponding to end frequencies of evaporation ν_{end} of 1.875 MHz, 1.850 MHz, and 1.830 MHz. The integrated column density along the z-direction has been fitted with a bi-modal function consisting of a Gaussian part (red lines) and an inverted parabola (green lines).

Proof of condensate formation

The evidence of creating a condensate emerges from analyzing the expansion of the atomic cloud via time-of-flight measurements, thus detecting the velocity distribution of the expanding gas by means of absorption imaging.

By ramping down the effective expansion temperature of the ensemble, a sharp non-Gaussian peak (inverted parabola) occurs both in the density and velocity distributions super-imposed on the broader thermal (Gaussian) background, signalizing the phase transition to a Bose-Einstein condensate. By further reducing the effective ensemble temperature, the height of the condensate peak increases while the tails of the thermal distribution are reduced until they completely vanish for a entirely pure condensate.

Such a typical evaporation process is depicted in Fig. 2.7. For different evaporation end frequencies, the fraction of condensed to thermal atoms is evaluated by fitting a bi-modal distribution based on the sum of a Gaussian (red line) and a Thomas-Fermi (green line) function to the column density. Based on this fit, we extract the atom number of the condensed and non-condensed part, respectively. We start with a RF-frequency well above the transition frequency and continuously decrease to three distinct final values. From A-C, the condensate fractions N_c/N have been measured to be 6%, 34%, and 62% corresponding to evaporation end frequencies ν_{end} of 1.875 MHz, 1.850 MHz, and 1.830 MHz.

Magnetic trap lifetime measurements

Once transferred into the conservative trapping potential, collisions with background atoms and three-body interactions result in an average heating of the ensemble and lead to effective losses in atom number. This fundamentally limits the lifetime in the magnetic trap. Especially for experiments on macroscopic timescales, a sufficient UHV environment is necessary whose quality next to the atom chip is best approximated by the magnetic trap lifetime.

Such lifetime measurements can be realized by detecting the number of atoms after a certain time-of-flight for different trapping times. An example of such a measurement

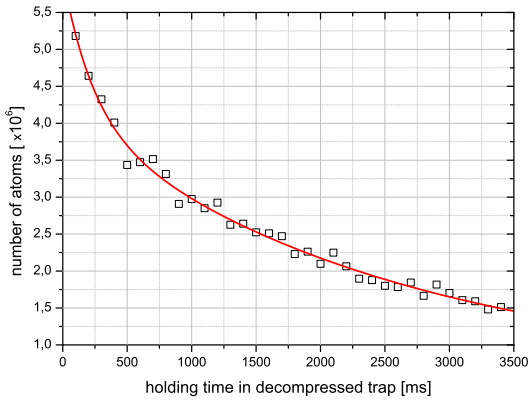

Figure 2.8: Typical measurement of the lifetime in a decompressed trap giving a two-body loss dominated lifetime of $t_{2b} = 3.49(19)$ s.

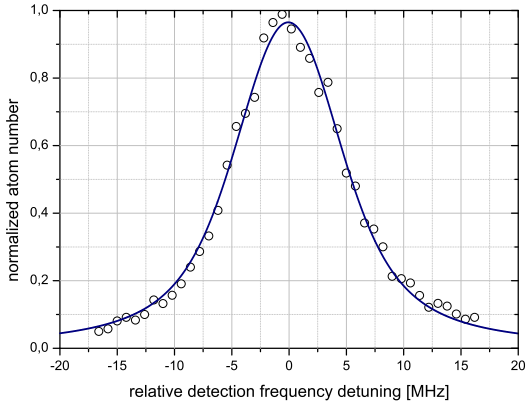

Figure 2.9: Scan of the detection frequency. The Gaussian part of the fitted Voigt profile gives a FWHM of 13.47(72) MHz.

is shown in Fig. 2.8 for the decompressed trap after BEC generation with $\omega_{rad} = 2\pi \cdot 130$ Hz (see Tab. 2.2).

The atom number shows an exponential decay with two loss rates. Three-body collisions clearly dominate the lifetime measurements in the beginning, whereas the second timescale is characterized by two-body losses (e.g., collisions with background atoms). Fitting a double exponential decay rate results in a two-body loss dominated e^{-1} lifetime of $t_{2b} = 3.488(187)$ s, which is comparable with other atom-chip-based experiments and sufficient for BEC generation including subsequent free fall experiments at timescales of a drop experiment (see Sec. 5.1).

2.6 Characterizing magnetic trap configurations

If a trap is adiabatically opened, energy from a well isolated quantum system is extracted by means of a thermodynamic process. Consequently, very shallow trapping potentials contain extremely cold clouds of atoms which expand much slower than a gas released from a steep potential corresponding to high trapping frequencies.

With the QUANTUS-I atom chip setup, one can control the steepness of the trap along the fast axis with the magnetic bias field I_{bias} (see Sec. 2.4.2) and already used during the evaporation process (see Sec. 2.5.3). The trap minimum is also shifted, which is not considered now but will be of importance later on (see Ch. 4).

The exact knowledge of the trapping frequencies and corresponding expansion rates is important for preparing experiments with interfering Bose-Einstein condensates and for the implementation of magnetic delta-kick cooling. As already mentioned, three different holding traps (shallow, steep, lens) will be of importance in the experiments of this thesis. Hence, we will measure the temperatures of different atomic ensembles emerging from these traps and the corresponding trapping frequencies.

2.6.1 Effective temperatures of expanding atomic clouds

In a classical gas, there is a direct link between momentum distribution and temperature. An approximation of the temperature of an evolving cloud of atoms can thus be realized by evaluating a series of absorption images for different expansion times. From each picture of such a time-of-flight measurement, the width σ of a thermal cloud can be evaluated. By fitting

$$\sigma(t) = \sqrt{\sigma_0^2 + \sigma_v^2 t^2} \tag{2.52}$$

to the measured temporal evolution, we can approximate the size of the cloud σ_0 right after the release [115].

More importantly, the velocity width σ_v can be extracted, which allows to calculate the temperature in each dimension i according to

$$k_B T_i = m\sigma_{v,i}^2, \tag{2.53}$$

with the mass of atoms m and the Boltzmann constant k_B.

For characterizing condensed sources, the shape of the spatial wings of the distribution ascribed to the thermal cloud (assuming not a pure condensate) is evaluated and associated with the ensemble temperature. Therefore, a bi-modal distribution is fitted to the column density to obtain the velocity width σ_v of the Gaussian part. This will be done in the next section for differently prepared atomic ensembles.

Comparison of the shallow, steep, and lens trap configuration

Clouds of atoms released from the three trap configurations (shallow, steep, and lens) are evaluated by time-of-flight series with expansion times from $T_{tof} = 4$ - 32 ms. For each trapping potential, we additionally vary the temperature of the trapped gas by means of forced RF evaporation. By changing the end-frequency of the last evaporation ramp ν_{end}, six different ensembles between a purely thermal cloud ($\nu_{end} = 2$ MHz), and the purest achievable condensate[5] ($\nu_{end} = 1.830$ MHz) have been analyzed in time-of-flight measurements. The results are given in Fig. 2.10.

In each graph for the shallow trap (upper left), steep trap (upper right) and lens trap (lower left), the Gaussian widths in x- (squares) and z-direction (circles) of the clouds are given for the six values of ν_{end} (different colors). Eq. 2.52 is separately fitted to the widths along x- (solid line) and z-direction (dashed line) and from the fits we obtain the velocity width σ_v and the initial cloud size σ_0 in each direction. This method is reliable in determining σ_v, which obviously dominates the expansion for long time-of-flights. For short expansion times, however, cloud sizes are generally on the order of the resolution limit of our detection system, which can be approximated to about 15 μm. This consequently limits the accuracy of σ_0, which therefore should be calculated using the trapping frequencies (see Eq. 2.20).

Since the detection beam is oriented along the weak axis of an assumable cigar-shaped potential, we expect nearly isotropic distributions. This could be verified for

[5] Here, the condensate fraction is about 60% (cf. Fig. 2.7). A typical measurement of the condensate fraction in dependence of ν_{end} is also given in Fig. 3.22.

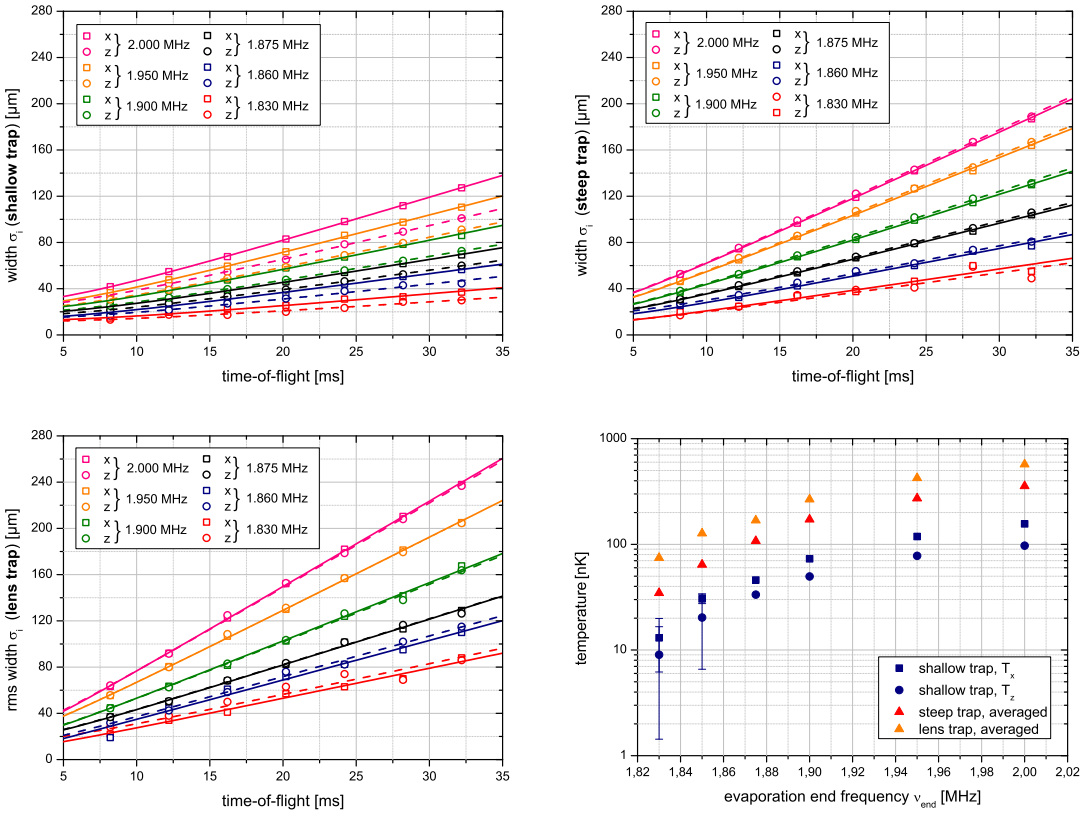

Figure 2.10: Time-of-flight measurements of partially condensed clouds (evaporation end frequencies ν_{end} scanned from 1.830 - 2.000 MHz) released from three different holding trap potentials. The shallow trap is the standard laboratory trap and generates our coldest ground based BEC (upper left). The steep trap is used to generate BECs, which converts mean-field energy much faster for interferometry experiments (upper right). The lens trap yields the fastest expansion and is used for our experiments with atom-chip-based delta-kick cooling (lower left). The given widhts σ_i are rms values of the Gaussian part and corresponding temperatures are summarized in the lower right graph. More details in text.

the steep and lens trap. For the shallow trap, our measurements indicate different expansion rates in x- and z-direction. The comparably weaker potential shows a clear asymmetry and is probably already deformed by gravity or other residual fields. This will be verified by direct measurements of the trapping frequencies (see Sec. 2.6.2).

Temperature estimation

The velocity widths σ_v of the different ensembles have been extracted from the fits and used in Eq. 2.53 to calculate the temperature. The results are plotted versus the evaporation end-frequency in the lower right graph of Fig. 2.10. Temperatures for the steep (red triangles) and lens (orange triangles) trap have been averaged over x- and z-direction, since nearly isotropic temperatures have been determined from the time-of-flight series. For the shallow trap, however, temperatures for both visible

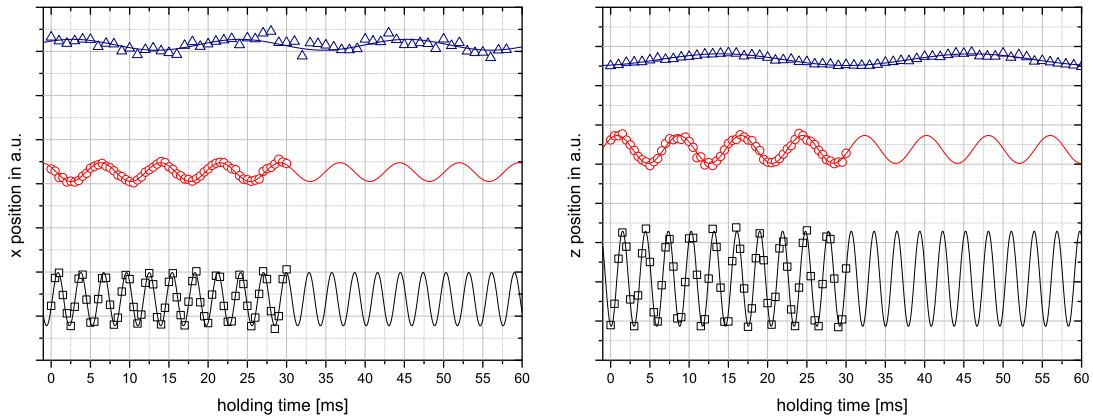

Figure 2.11: Measurement of the trapping frequencies in x- and z-direction for the shallow (blue triangles), steep (red circles) and lens (black squares) trap. The COM position of the condensates (in a.u.) is given for different holding times in the corresponding trap. A sinusoidal function is fitted to each data set to extract the oscillation frequency.

dimensions are depicted separately since they differ independently of the evaporation end frequency ν_{end} by a fraction of $T_z/T_x \cong 0.66$ (blue squares and circles).

The Statistical error of σ_v consequently leads to temperature errors, only given if exceeding the size of the data points. This is the case for our coldest clouds of atoms emerging from the shallow trap ($\nu_{end} = 1.830 - 1.860\,\mathrm{MHz}$), the resulting error in temperature is on the order of 40%, mainly caused the resolution limit of the detection system as mentioned earlier.

By increasing the evaporation end frequency ($\nu_{end} \to 2.0\,\mathrm{MHz}$), all evaluated temperatures increase proportional to the trapping frequencies of the holding traps. For the steep and lens trap, the averaged temperatures increase isotropically for both dimensions to final values of $T_{ave} \approx 355\,\mathrm{nK}$, and $T_{ave} \approx 570\,\mathrm{nK}$, respectively. The derived expansion temperatures for the shallow trap again visualize the asymmetry with final values of $T_x \approx 156\,\mathrm{nK}$ and $T_z \approx 97\,\mathrm{nK}$.

Another approach for temperature determination and cross-check of the observed asymmetries of the shallow trap is based on the knowledge of the trapping frequencies. The basic measurement principle of these will be introduced in the next section.

2.6.2 Direct measurement of the trapping frequencies

A simple method to measure trapping frequencies is to induce dipole oscillations of the BEC in the trap and observe the center-of-mass (COM) position after different holding times by taking images after a fixed time-of-flight [115]. The oscillations in the trap are directly transferred into a COM displacement. Another method would be parametric heating induced by AC field driven losses or other excitations in the trap [155].

Fig. 2.11 shows the COM position in x- and z-direction of BECs released from the three trap configurations (shallow, steep, lens) after different holding times. For the steep and lens trap, the holding time is scanned from $t_{hold} = 0 - 30\,\mathrm{ms}$, which has to be increased to $t_{hold} = 0 - 60\,\mathrm{ms}$ for the shallow trap to be able to observe a clear

trap configuration	$\omega_x/2\pi$ [Hz]	$\omega_z/2\pi$ [Hz]	$\omega_y/2\pi$ [Hz]
shallow ($I_{bias} = 0.36\,A$)	46.56(1.32)	31.29(31)	17.8(1.1)
steep ($I_{bias} = 0.6\,A$)	131.48(45)	126.9(4)	17.6(9)
lens ($I_{bias} = 1.0\,A$)	343.46(36)	343.88(38)	48.9(5.3)

Table 2.3: Direct measurement of trapping frequencies by induced dipole oscillations in three different magnetic traps. For x- and z-direction, the values are extracted from the fits in Fig. 2.11. The values for the y-direction correspond to an individual measurements, not shown here.

oscillation. The images are taken after a time-of-flight of $T_{tof} = 31$ ms, where the clouds already have sizes well above the resolution limit.

We extract the value for the trapping frequency by fitting a sine-function to the evaluated COM positions in x- and z-direction. The results of three averaged measurements are summarized in Tab. 2.3 and directly mirror the observations of the time-of-flight measurements. The approximation of a cigar-shaped potential with $\omega_x \approx \omega_z \equiv \omega_{rad}$ is only valid for the steep and lens trap configuration. The shallow trap shows an asymmetry of $\omega_z/\omega_x \cong 0.67$, corresponding to the already measured fraction of the expansion temperature ($T_z/T_x \cong 0.66$).

For detecting dipole oscillations in the y-direction, the detection system had to be rebuilt. This individual measurement is not shown here, however the values for the trapping frequency are given for completeness.

Temperature revisited

By measuring the trapping frequencies directly, the temperature of a freely expanding cloud of atoms can be calculated with just one additional data point giving the width at one single point in time [115]. With the Boltzmann constant k_B, the temperature in the i-th dimension follows as

$$k_B T_i = m\sigma_i^2(t)\frac{\omega_i^2}{1+\omega_i^2 t^2}. \tag{2.54}$$

This expression can now be used as an alternative approach and to cross-check the temperature values based on time-of-flight measurements. With the evaluated spatial widths σ_i after a time-of-flight of 32.2 ms for all configurations, temperatures derived with Eq. 2.54 typically agree within better than 10% to the temperatures derived via the expansion method and given in Fig. 2.10.

We now can prepare cold and ultra-cold clouds of atoms with various expansion temperatures and predict their thermal expansion in ground-based measurements. Until now, the atoms are prepared in the $m_F = 2$ state, which is necessary for efficient trapping and fast evaporation. However, these atoms are likely to interact with residual magnetic fields.

To reduce the influence of these stray fields (especially at ultra-long timescales of free expansion), an adiabatic rapid passage (ARP) as a coherent process to transfer atoms into the $m_F = 0$ state will be discussed next.

2.7 Coherent on-chip transfer of atoms to a non-magnetic state

Our previous expansion studies of Bose-Einstein condensates in microgravity showed that residual magnetic fields in the drop tower interact with spin polarized atoms and disturb the otherwise "free" evolution [17]. Center-of-mass (COM) motion as well as the spatial width in one dimension did clearly not correspond to the theoretical predictions, indicating external forces acting on the atoms. In order to verify the influences of inhomogeneous magnetic fields, comparative expansion studies with atoms much less sensitive to the stray fields (e.g., $m_F = 0$) would be beneficial.

Therefore, we implemented an adiabatic rapid passage (ARP), a method to coherently transfers atoms between the Zeeman sublevels. Specifically, we optimized a sequence to reliably transfer up to 90% of the atoms into the $m_F = 0$ state.

2.7.1 Adiabatic rapid passage in the dressed state picture

An adiabatic rapid passage (ARP) is a very robust technique for coherent population transfer between quantum mechanical states, e.g., Zeeman sublevels. Here, electromagnetic radiation is tuned above or below the resonance frequency of a particular transition, and subsequently swept through the resonance. Alternatively, the radiation frequency can be kept constant and the eigenenergies of the atomic states itself can be tuned. An ARP process can be explained in the adiabatic frame of a dressed atom picture, in which the Hamiltonian is given by

$$\hat{H} = \frac{\hbar}{2}\begin{pmatrix} -\epsilon(t) & \Omega_0(t) \\ \Omega_0(t) & \epsilon(t) \end{pmatrix}, \tag{2.55}$$

where $\Omega_0(t)$ corresponds to the Rabi frequency of the particular transition and $\epsilon(t)$ is the effective detuning from resonance. This Hamiltonian yields the new eigenenergies

$$E_{1,2} = \pm\hbar/2\sqrt{\epsilon^2 + \Omega^2}, \tag{2.56}$$

and the corresponding eigenvectors are linear combinations of the unpertubed states $|1\rangle$ and $|2\rangle$ coupled with a transition strength Ω_0 [137, 156]

$$\phi_\pm = \frac{\epsilon \pm \sqrt{\Omega_0^2 + \epsilon^2}}{\sqrt{\Omega_0^2 + \left(\sqrt{\Omega_0^2 + \epsilon^2} \pm \epsilon^2\right)}} |1\rangle + \frac{1}{\sqrt{1 + \left(\frac{\sqrt{\Omega_0^2+\epsilon^2}\pm\epsilon^2}{\Omega_0}\right)^2}} |2\rangle . \tag{2.57}$$

An atom initially prepared in state $|1\rangle$ for positive detuning $\epsilon(t) > 0$ transforms to state $|2\rangle$ if the detuning is scanned to negative values $\epsilon(t) < 0$. If the detuning again is scanned from negative to positive values, we observe coherent re-population of $|1\rangle$. An equal superposition state can be prepared for $\epsilon = 0$.

The fraction of Rabi frequency Ω_0 and effective detuning ϵ can be expressed by an mixing angle

$$\tan(2\theta) = \Omega_0/\epsilon, \tag{2.58}$$

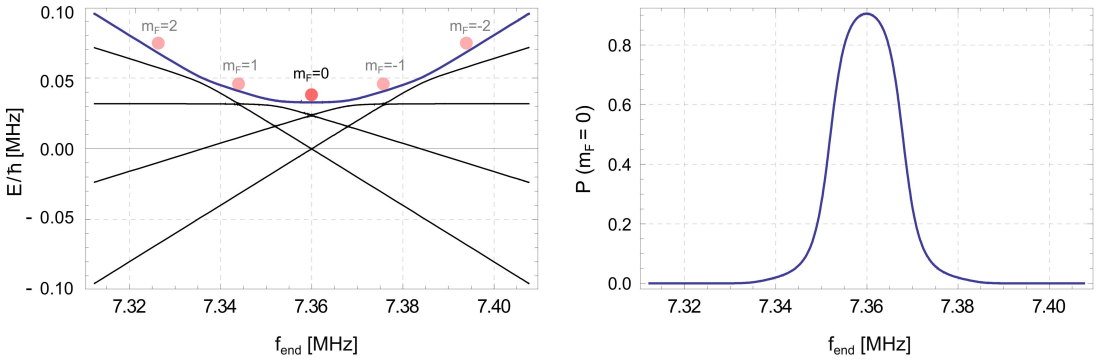

Figure 2.12: Simulation of dressed states and avoided crossings for the $|F = 2\rangle$ manifold of ^{87}Rb (left). These are calculated with an offset field of 10.5 G and an applied RF field of $\Omega_0 = 2$ kHz [157]. Here, different slopes correspond to different m_F states to which the atoms can be transferred to by scanning f_{end} (indicated with red circles). With the given parameters, the probability to find an atom in the $m_F = 0$ state is about 85% (right).

and this expression now allows us to rewrite the eigenvectors of the coupled system as

$$|\phi_+\rangle = \cos(\theta)\,|1\rangle + \sin(\theta)\,|2\rangle\,, \tag{2.59}$$

$$|\phi_-\rangle = -\sin(\theta)\,|1\rangle + \cos(\theta)\,|2\rangle\,. \tag{2.60}$$

The ARP process has to happen on carefully chosen timescales. It should be fast enough compared to decoherence and system-related relaxation and at the same time slow enough to fulfill the condition of adiabaticity. Especially optically induced ARPs suffer from excitation leading to decoherence, which can be neglected for RF passages between Zeeman sublevels of an atomic ground state.

Perfect efficiency is thus given if the condition of adiabaticity is fulfilled,

$$\sqrt{\Omega^2(t) + \epsilon^2(t)} \ll |\dot{\Theta}(t)|, \tag{2.61}$$

with the phase angle $\Theta(t) = \tan^{-1}(\epsilon(t)/\Omega(t))$. This means, that the angular frequency of the torque vector has to be smaller than the angular frequency of the Bloch vector.

Implementation in an atom chip experiment

After laser cooling ^{87}Rb atoms in a chip-MOT configuration, the atoms are optically pumped into the $|F = 2, m_F = 2\rangle$ for magnetic trapping. In this state, the condensate is generated. The implementation of an ARP should thus be able to coherently transfer atoms from $|F = 2, m_F = 2\rangle$ to $|F = 2, m_F = 0\rangle$ with low intrinsic losses. Therefore, the atoms are released from the final magnetic trap and after some expansion time being exposed to (i) a strong magnetic bias field and (ii) to a specifically designed RF frequency chirp.

A strong homogenous magnetic field lifts the degeneracy between the different Zeeman sublevels, which are again coupled via the present RF field. For generating the

bias field, compensation coils (K1) are used which are otherwise dedicated to control and adapt the trap bottom of the chip-based IP-trap. For the RF sweep a 16 Bit arbitrary waveform generator is used (PXI 5421) with 100 MS/s sampling rate and 43 MHz analog bandwidth, coupled to the z-wire of the atom chip, which is used as an on-chip antenna to radiate RF.

Calculation of the ARP parameters

The specific choice of the magnetic bias fields determines the frequency range of the RF sweep. The linear Zeeman splitting of the five sublevels of $|F = 2\rangle$ in a homogenous magnetic field B can be approximated to [150, 156]

$$\Delta E_{lin}(m_F) \approx m_F \cdot \hbar\omega_{lin}, \tag{2.62}$$

with $\omega_{lin} = 0.6998$ MHz/G, Bohr magneton μ_B, Lande-factor g_F and the Zeeman quantum number. Following that, an applicable offset field of about 10.5 G requires an RF chirp around 7.36 MHz to be on resonance with neighboring m_F states, which is easily accessible with our RF source. The quadratic Zeeman effect now shifts the splittings between adjacent magnetic sublevels due to

$$\Delta E_{quad}(m_F) \approx (4 - m_F^2)\hbar\omega_{quad}/4, \tag{2.63}$$

with $\omega_{quad} = 286\,\mathrm{Hz/G^2}$ so that we can use the arising asymmetry to address the resonances with carefully tuned RF chirps.

Fig. 2.12 (left) shows a simulation of the dressed states and avoided crossings for the $|F = 2\rangle$ manifold of ^{87}Rb. The calculations are done for an 10.5 G offset field and an RF field coupling the m_F states with a Rabi frequency of $\Omega_0 = 2$ kHz. The different Zeeman sublevels correspond to different slopes. To end up in the (to first order) magnetic insensitive $m_F = 0$ state, two avoided crossings ($m_F = 2 \rightarrow m_F = 1$, and $m_F = 1 \rightarrow m_F = 0$) need to be passed when the atoms are initially prepared in the $|F = 2, m_f = 2\rangle$ state.

For the given parameters, the probability to find atoms in the $m_F = 0$ state can be calculated to about 85% for an end frequency of $f_{end} = 7.36$ MHz (Fig. 2.12, right). In this graph, the transfer probabilities to the other Zeeman sub levels are not shown for better visibility.

Transfer efficiencies in QUANTUS-I

The experimental results of ground-based measurements with the QUANTUS-I apparatus are shown in Fig. 2.13. The condensate is released from the shallow trap with $\omega_i = 2\pi \cdot (46, 18, 31)$ Hz and expands freely for 4 ms. During this expansion, a homogenous magnetic field is ramped up, generated by the K1 coils. Given the magnetic coil conversion factors (see Tab. 2.1), we applied a current of $I_{K1} = 6$ A to meet the previously simulated offset field of about 10.5 G. In the next 3.8 ms the RF sweep is applied, until the bias field is again ramped down within 1 ms, closing the ARP sequence with a total cycle time of about 9 ms.

The RF sweep started at a frequency of $f_{start} = 7.7$ MHz, which is well below any

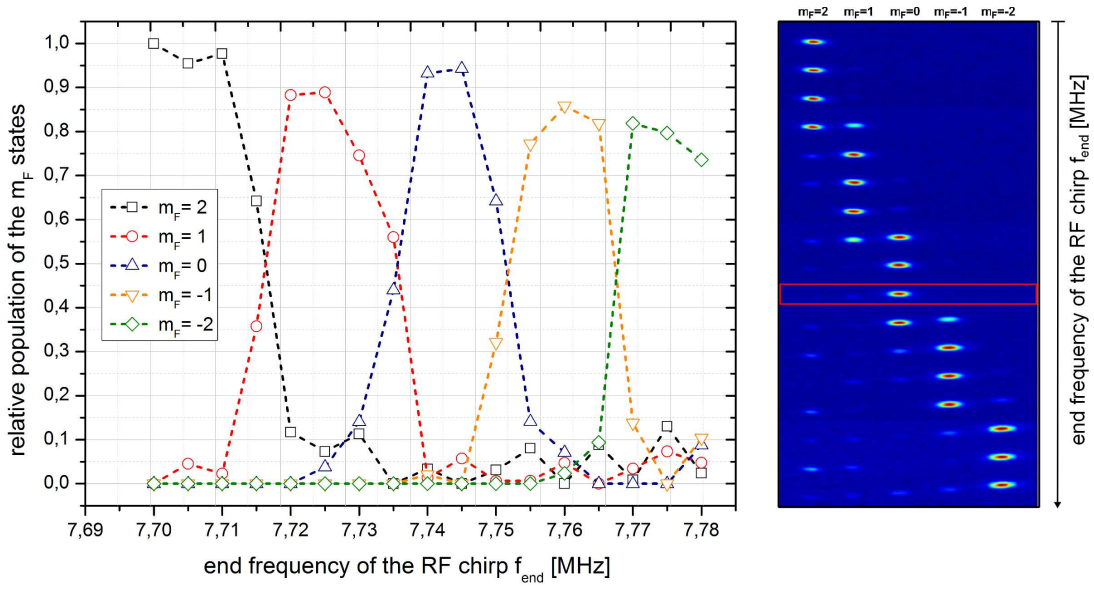

Figure 2.13: On-chip ARP between Zeemann sublevels of $|F = 2\rangle$. Shown is the transfer efficiency into the different Zeeman states in dependence of the end frequency of the RF chirp f_{end} (left). Between the data points, dashed lines are added to guide the eye and different colors represent the different m_F states. The applied magnetic bias field was 10.5 G and the duration of the RF sweep was 3 ms. The corresponding absorption images given for each different f_{end} (right) have been taken 25 ms after applying a Stern-Gerlach field to spatially separate the different Zeeman levels. They are individually normalized and based on a region-of-interest (ROI) which is adapted for better illustration. Highlighted in the red box is the coherent transfer of 92% in the $m_F = 0$ state.

resonance, and was smoothly chirped to variable final values of 7.7 MHz $\leq f_{end} \leq$ 7.8 MHz at a constant RF amplitude[6].

Coherent population transfer is observed for RF frequencies which are somewhat larger than previously calculated for the given magnetic field configuration. The results indicate an effectively higher bias field on the order of $\Delta B/B \approx 5\%$ which might be ascribed to residual offset fields at the atoms position or an inaccuracy in the conversion factor for the K1 magnetic coil assembly taken from [19].

To evaluate the population transfer efficiency for each f_{end}, we normalized the number of atoms in the particular m_F state to the total atom number (see open symbols in Fig. 2.13). This is done by performing a Stern-Gerlach experiment right after the ARP sequence. Therefore, we switch on the magnetic coils generally used for generating the field gradient for the macroscopic MOT. The different Zeemann states spatially separate and allow for state-dependent atom number analysis. Transfer efficiencies are typically $> 80\%$ in any of the Zeemann sublevels, but specifically we optimized the population of the $m_F = 0$ state with an efficiency of $\sim 90\%$.

On the right side of Fig. 2.13, corresponding absorption images are shown for dif-

[6]Before and after the 3.8 ms lasting RF sweep, the effective amplitude is linearly ramped up/down within a duration of 0.1 ms

bias field K1 [A]	$f_{m_F=2}$ [MHz]	$f_{m_F=1}$ [MHz]	$f_{m_F=0}$ [MHz]	$f_{m_F=-1}$ [MHz]	$f_{m_F=-2}$ [MHz]
10.5	$\leq$ 7.7047(8)	7.7252(5)	7.7443(4)	7.7597(4)	$\geq$ 7.7752(6)
5.60	$\leq$ 4.1214(2)	4.1288(1)	4.1342(1)	4.1392(1)	$\geq$ 4.1450(3)
2.60	$\leq$ 2.0669(4)	2.0680(3)	2.0694(2)	2.0708(3)	$\geq$ 2,0723(3)

Table 2.4: Experimentally determined RF end frequencies f_{end} for an on-chip adiabatic rapid passage between the Zeeman sublevels of $|F = 2\rangle$ for different magnetic bias fields 10.5 G, 5.6 G, and 2.63 G. The corresponding transfer efficiencies in the $m_F = 0$ state are 90%, 74%, and 56%, respectively.

ferent f_{end}. Each absorption image is taken 25 ms after applying a Stern-Gerlach field and individually normalized. The region-of-interest (ROI) has been adapted for better illustration.

After additionally scanning the population transfer for lower K1 bias fields of 5.6 G and 2.6 G, the center frequency for maximum population transfer into each sublevel was approximated by fitting a Gaussian to the relative population distribution. The results are given in Tab. 2.4. Obviously, the adressability of the sublevels for smaller offset field suffers due to a smaller energetic splitting, such that the resonances overlap in the frequency domain. Thus, for the offset fields of 5.6 G and 2.6 G, reduced transfer efficiencies to the $m_F = 0$ state of 74% and 56% occur.

2.8 Summary

In this chapter, the basics of Bose-Einstein condensation in harmonic traps generated by the magnetic fields of an atom chip have been presented. This included the main theoretical tools accompanied by a step-by-step description of the specific experimental techniques to generate condensates with about 10^4 atoms in QUANTUS-I.[7].

Moreover, the setup has been characterized with an emphasis on three important magnetic trap configurations. The knowledge of the main parameters of which are important for the upcoming interferometric analysis of the phase coherence and for the optimization of delta-kick cooling.

As a major upgrade compared to the first setup of the QUANTUS-I payload described in [17], an RF-induced adiabatic rapid passage (ARP) was implemented on chip. Typically, up to 90% of the atoms could be coherently transferred into the $m_F = 0$ state. In earlier runs of this experiment, the interaction of magnetically susceptible atoms ($m_F = 2$ state) with residual magnetic fields have been suspected to be the main reason for anomalous expansion and center-of-mass (COM) motion of the condensates.

With the succesful implementation of the on-chip ARP, we thus met one of the essential requirements for unperturbed matter wave interferometers on extended time scales in the drop tower:

[7]Note: A technical defect caused the destruction of the atom chip at the beginning of this thesis. Thus, the atom chip had to be replaced and the QUANTUS-I experiment to be re-assembled first.

Free-fall interferometry with Bose-Einstein condensates in microgravity (see Ch. 5)

- Atom-chip-based source of non-magnetic degenerate gases
- ◇
- Bragg diffraction and open interferometers with degenerate gases (see Ch. 3)
- ◇
- Delta-kick cooling as a tool for long baseline atom interferometry (see Ch. 4)

The next chapter will introduce optically-induced Bragg diffraction as a technique to form matter wave beam splitters. After a theoretical description of light-matter interactions leading to the important parameters of Bragg diffraction as a coherent two-photon processes, a miniaturized, drop tower capable Bragg laser system will be presented. The main part of the chapter will then focus on preparatory ground-based studies of the phase coherence and mean-field interactions of the condensates manipulated in open interferometers of Ramsey- and Mach-Zehnder type.

3 Bragg diffraction and open interferometers with degenerate gases

Ultra-cold clouds of atoms in the $m_F = 0$ state are promising for unperturbed free expansion and microgravity-enhanced matter wave interferometry at targeted timescales of about a second. But before we move to microgravity, a coherent manipulation technique has to be implemented in the experiment, which can be used to form beam splitters and combiners for matter waves. In principle, two types of beam splitters have been commonly used in light-pulse atom interferometry, which are usually referred to be of Bragg- or Raman-type [158, 159].

In both cases, the atomic cloud gets illuminated with an optical lattice and interacts via two-photon Raman transitions. The initial wave function is placed into a coherent superposition of different quantum states, and the major difference is given by the nature of the addressed states. In Bragg diffraction, different momentum states (of the same internal state) are coupled [160], whereas Raman diffraction is typically implemented via two different hyperfine ground states [59]. In both cases the coupled parts of the wave function spatially separate due to photon recoil, which can be used to form interferometers based on the wave nature of particles.

Interferometers based on Bragg diffraction have the advantage of atoms remaining in the same internal state. Differential effects such as AC Stark shifts and couplings to residual electro-magnetic fields are negligible or highly suppressed. Multi-photon transitions are possible [161], which lead to a higher momentum splitting and therefore paving the way for long baseline interferometers [162] and high-resolution spectroscopy [163].

On the other hand, they require atomic sources whose momentum width is smaller than the transferred momentum of the Bragg resonance in order to obey spatial overlapping. This is mandatory for detection, since no state labeling can be used to differentiate between the coupled states as usually done in Raman interferometry [59]. The velocity distribution of a BEC is largely smaller than the recoil velocity, making condensed samples of atoms an ideal matter wave source for Bragg interferometry.

Bragg diffraction of condensed sources has been studied and used in a variety of applications, i.e. to manipulate atomic samples in interferometers [164], for realizing coherent frequency shifts [165] or amplification [166] of matter waves. Therefore, BECs can be accelerated towards a standing light wave [167] or stationary condensates can be diffracted by a moving lattice of near-resonant laser light [160]. It has been established in spectroscopic applications to analyze the momentum distribution of degenerate gases [168] and for measurements of the coherence length of condensates in the presence of phase fluctuations [169].

After an intuitive description of Bragg diffraction in the momentum picture (see Sec. 3.1), a simplified model of the atom as a discrete two-level system in a coherent

electro-magnetic field is described to study the basic dynamics (see Sec. 3.2). From that, a stimulated two-photon transition will be derived and important properties discussed (see Sec. 3.2.2) before we present the implementation of Bragg scattering and preparatory ground-based experiments in QUANTUS-I (see Sec. 3.4). In particular, we discuss momentum-width related loss mechanisms in the scattering process and Bragg spectroscopy, before the last section will focus on the realization of open interferometers (see Sec. 3.5). These will be used to probe the phase evolution of freely expanding condensates, for measurements of the coherence length and studies of the mean-field driven influences on the emerging interference patterns.

3.1 Bragg scattering of atoms in the momentum picture

Back-scattering processes of the newly discovered x-rays from three dimensional crystalline structures were first observed in 1912 [170]. In the same year, W.H. Bragg and W.L. Bragg developed a theory for the diffraction of electromagnetic radiation off periodic structures [171], which was honored with the Nobel prize in 1915. The periodic spacings of the crystals have been similar to the wavelength of the x-rays, and scattered radiation constructively interfered for specific angles of incidence θ_b fulfilling the Bragg condition

$$n\lambda_x = 2d_{crys}\sin(\theta_b), \tag{3.1}$$

with diffraction order n, wavelength of the electromagnetic radiation λ_x and periodic crystal spacing d_{crys}.

Such as electromagnetic waves can be scattered from solid crystalline structures, atomic matter waves can be scattered from the periodic structure of a standing light wave, i.e. cold atoms interacting with periodic optical potentials. Bragg diffraction of atoms was first observed by a mono-energetic beam of sodium atoms scattered off a standing light wave in 1988 [172].

Manipulating atoms in the same way as we manipulate light with optical elements is usually called *atom optics*. The light crystal as an atom-optical element can be realized by interfering two laser beams with wavelength λ_L at the position of the atoms, resulting in a one-dimensional averaged intensity distribution

$$I(x) = 2c\epsilon_0 E_0^2 \cos^2(kx), \tag{3.2}$$

with the speed of light c, the permittivity ϵ_0 and the electric field's amplitude E_0. The aforementioned spacing of the crystal d_{crys} now has to be replaced with the spacing of an optical lattice ($d_{light} = \lambda_L/2$). For atoms with mass m and velocity v, we have to use the thermal de Broglie wavelength $\lambda_{dB} = 2\pi\hbar/mv$. The new resonance condition therefore follows as

$$n\lambda_{dB} = \lambda_L \sin(\theta_b), \tag{3.3}$$

which, for example, can be fulfilled by accelerating atoms towards a standing wave. But in most cases of cold atomic physics experiments, the atoms are at rest while being exposed to the optical lattice. Here, we have to introduce a moving, optical lattice by

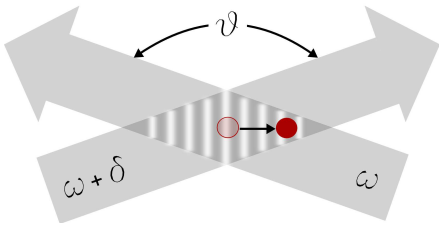

Figure 3.1: Schematic of Bragg diffraction in the particle picture. Atoms interact with photons from two laser beams with frequency ω and $\omega + \delta$ enclosing a crossing angle ϑ. They can be coherently diffracted from momentum state $|p_0\rangle = |0\hbar k\rangle$ to $|p_r\rangle = |2\hbar k \sin(\vartheta/2)\rangle$ if the energy difference of the laser beams fulfills $\hbar\delta = p_r^2/2m$.

interfering two laser beams with a frequency difference δ, resulting in a time-dependent intensity distribution

$$I(x) = 2c\epsilon_0 E_0^2 \cos^2(kx - \delta t/2). \tag{3.4}$$

In a simplified picture, an atom now absorbs one photon from one of the laser beams and subsequently gets coherently stimulated down to the ground state by interacting with a photon from the other laser beam (see Fig. 3.1). In this stimulated two-photon Raman process, the scattered atom will finally have a momentum of $p_r = 2\hbar k \sin(\vartheta/2)$ relative to the unscattered atoms in the BEC, when the laser beams with wave vector $k = 2\pi/\lambda_L$ ($k_\omega \approx k_{\omega+\delta} \equiv k$, since $\delta \ll \omega$) are aligned with a crossing angle of ϑ.

To obey energy conservation during this Bragg diffraction process, the two laser beams need to have a specific frequency difference δ, which is determined by the effective energy difference between the two coupled ground states

$$\Delta E = \frac{p_r^2}{2m} = \frac{(2\hbar k \sin(\vartheta/2))^2}{2m} = \hbar((\omega + \delta) - \omega) = \hbar\delta. \tag{3.5}$$

In case of a non-zero center-of-mass (COM) motion, atoms with initial momentum p_0 lead to a modification of the above condition as

$$\Delta E = \frac{(p_r + p_0)^2 - p_0^2}{2m} = \frac{(2\hbar k \sin(\vartheta/2) + mv_0)^2 - m^2 v_0^2}{2m} = \hbar\delta. \tag{3.6}$$

From Eq. 3.6, we finally get an expression for the frequency difference δ of the Bragg laser beams

$$\delta = 4\omega_r \sin^2(\vartheta/2) + 2kv \cdot \sin(\vartheta/2), \tag{3.7}$$

with the recoil frequency $\omega_r = \hbar k^2/m$. In the QUANTUS-I setup, the angle of incidence is $\vartheta = 180°$, thus laser beams are aligned anti-parallel. To fulfill the resonance condition for a first-order Bragg diffraction process with resting ($p_0 = 0$) ^{87}Rb atoms, the necessary frequency difference is $\delta = 4\hbar k^2/m = 4\omega_r = 2\pi \cdot 15.08$ kHz.

3.2 Semi-classical description of Bragg diffraction

Treating Bragg diffraction in a simplified particle picture led us to define necessary conditions for diffraction of matter waves off periodic light crystals. Now, to derive useful expressions for the dynamics between photons and atoms, we first introduce the simple case of an idealized two-level atom in a mono-chromatic electromagnetic field. In a second step, we extend this treatment towards a coherent two-photon transition.

3.2.1 An electromagnetic field and a two-level atom

Let us assume a discrete two-level atom which is exposed to electromagnetic radiation with frequency ω and an arbitrary phase ϕ, which we treat as a classical field (*semi-classical* approach). To make predictions about the dynamics of the two-level system, it is important to calculate the temporal evolution of the probabilities of an atom being in state $|1\rangle$ or $|2\rangle$.
We start by writing down the Hamiltonian, neglecting coupling to the vacuum causing decoherence due to spontaneous emission processes,

$$\hat{H}(t) = \hat{H}_0 + \hat{H}_{AL}(t). \tag{3.8}$$

The unperturbed part of the Hamiltonian $\hat{H}_0 = \hbar\omega_2|2\rangle\langle 2| + \hbar\omega_1|1\rangle\langle 1|$ describes the atomic energy levels. The light-matter-interactions perturbing the eigenfunctions of $\hat{H}_0$ are given by the time-dependent part $\hat{H}_{AL}(t)$. A particle with a given dipole moment $\vec{d} = -q\vec{r}$ (electrical charge q) in an external electrical field $\vec{E}$ has a potential energy of

$$U = -\vec{d}\cdot\vec{E}. \tag{3.9}$$

The wavelength of light is usually much larger than the size of an atom, $\lambda \gg a_0$. Assuming the position of the atom $\vec{R}$ is kept constant during the interaction time, variations of the phase are small and the amplitude of the electric field is uniform over the size of the atom. This electrical dipole approximation thus neglects spatial variations of the electric field, $E(\vec{r},t) \approx E(\vec{R},t) \equiv \vec{E}(t)$.

With the polarization $\vec{\alpha}$, the electric field amplitude E_0 and the frequency of the light field ω_L, the oscillating field at the atoms' position therefore follows as

$$\vec{E}(t) = \vec{\alpha}E_0\cos(\omega_L t), \tag{3.10}$$

which determines the resulting interaction Hamiltonian to $\hat{H}_{AL}(t) = -\vec{d}\cdot\vec{E}(t)$. The total Hamiltonian of the system can now be written as

$$\hat{H}(t) = \hat{H}_0 + \hat{H}_{AL}(t) = \hbar\omega_2|2\rangle\langle 2| + \hbar\omega_1|1\rangle\langle 1| - \vec{d}\cdot\vec{E}(t). \tag{3.11}$$

Time-dependent Schrödinger equation

The temporal evolution of the two level system can be described by a time-dependent Schrödinger equation with the following ansatz for the wave function

$$i\hbar\frac{d}{dt}|\Psi(t)\rangle = i\hbar\frac{d}{dt}\left(c_2(t)|2\rangle + c_1(t)|1\rangle\right) = \hat{H}|\Psi(t)\rangle, \tag{3.12}$$

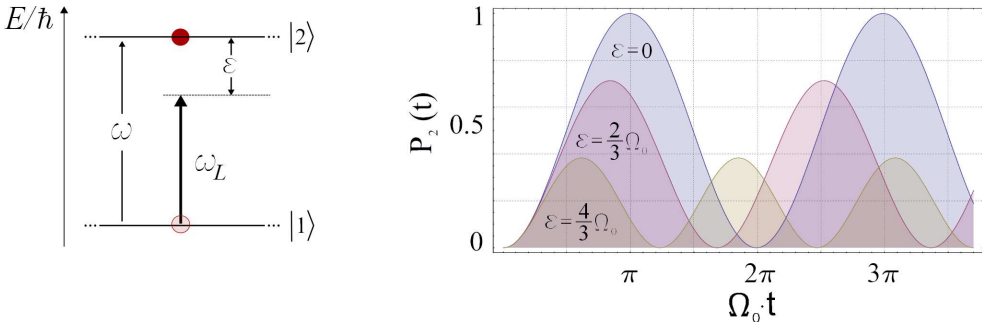

Figure 3.2: Schematic of a discrete two-level system under the presence of a non-resonant light field $\omega_L = \omega - \epsilon$ (left). Given a resonant Rabi frequency Ω_0 and interaction time t, calculations of the temporal occupation probability $P_2(t)$ for different values of the detuning ϵ are given (right). Details in text.

where normalization requires $\langle\Psi|\Psi\rangle = |c_2(t)|^2 + |c_1(t)|^2 = 1$.

With a frequency of the driving field ω_L and $\omega_2 - \omega_1 \equiv \omega$ (see Fig. 3.2, left), Eq. 3.12 determines a system of coupled equations for the coefficients $c_{1,2}$ [159],

$$\begin{aligned}\frac{d}{dt}c_1(t) &= i\frac{\left[\langle 1|\vec{d}|2\rangle\right]\vec{\alpha}E_0}{\hbar}\exp(-i\omega t)\cos(\omega_L t)c_2(t),\\ \frac{d}{dt}c_2(t) &= i\frac{\left[\langle 2|\vec{d}|1\rangle\right]\vec{\alpha}E_0}{\hbar}\exp(-i\omega t)\cos(\omega_L t)c_1(t).\end{aligned} \tag{3.13}$$

The coupling strength of a particular transition is given by the dipole matrix element, e.g., $\vec{d}_{12} = \langle 1|\vec{d}|2\rangle$, whose projection on the polarization of the light field we use to introduce the Rabi frequency $\Omega_{12} \equiv \langle 1|\vec{d}\vec{\alpha}|2\rangle E_0$. With that, Eq. 3.13 can be rewritten as

$$\begin{aligned}\frac{d}{dt}c_1(t) &= i\frac{\Omega_{12}}{2}\left(\exp(i(\omega_L-\omega)t) + \exp(-i(\omega_L+\omega)t)\right)c_2(t),\\ \frac{d}{dt}c_2(t) &= i\frac{\Omega_{21}}{2}\left(\exp(-i(\omega_L-\omega)t) + \exp(i(\omega_L+\omega)t)\right)c_1(t).\end{aligned} \tag{3.14}$$

We now define a detuning of the driving light field from the two-level resonance $\epsilon = \omega_L - \omega$ (see Fig. 3.2, left), which is typically small compared to the transition frequency itself, $\epsilon \ll \omega$. Regarding the two level dynamics, the fast oscillating terms in Eq. 3.14 can be neglected in the rotating wave approximation (RWA). Thus, our set of equations simplifies with $\Omega_{12} = \Omega_{21} \equiv \Omega_0$ to

$$\begin{aligned}\frac{d}{dt}c_1(t) &= i\frac{\Omega_0}{2}\exp(-i\epsilon t)c_2(t),\\ \frac{d}{dt}c_2(t) &= i\frac{\Omega_0}{2}\exp(i\epsilon t)c_1(t).\end{aligned} \tag{3.15}$$

Here, we (i) eliminate the time dependance of the exponential function and (ii) transform the equations in a rotating system whose rotation frequency coincides with the eigenfrequency ϵ of our atomic system [173]. This finally results in an expression with new coefficients $a_{1,2}$ and a time-independent Hamiltonian

$$\frac{d}{dt}\begin{pmatrix} a_1(t) \\ a_2(t) \end{pmatrix} = \frac{i}{2}\begin{pmatrix} -\epsilon & \Omega_0 \\ \Omega_0 & \epsilon \end{pmatrix}\begin{pmatrix} a_1(t) \\ a_2(t) \end{pmatrix}. \tag{3.16}$$

AC Stark shift

The energy shift of the eigenstates of the time-independent Hamiltonian in the presence of a light field is called AC Stark shift

$$\begin{aligned} \Delta E_1 &= \frac{\hbar}{2}(\epsilon - \Omega_0), \\ \Delta E_2 &= \frac{\hbar}{2}(\Omega_0 - \epsilon). \end{aligned} \tag{3.17}$$

Here, the energy shift of the so-called dressed states is symmetric and can be expanded in terms of Ω_0/ϵ (for $\epsilon \gg \Omega_0$),

$$\Delta E_1 = -\Delta E_2 = \frac{\hbar}{2}\left(\epsilon - \Omega_0\right) = \frac{\hbar}{2}\left(\epsilon - \epsilon\sqrt{1 + (\Omega_0/\epsilon)^2}\right) \approx -\hbar\frac{\Omega_0^2}{4\epsilon}. \tag{3.18}$$

In the case of a stimulated two-photon transition (see Sec. 3.2.2), the AC Stark shift is not symmetric anymore, which leads to a differential energy shift.

Rabi oscillations

We can now prepare a two level system, where all atoms are in one state at the beginning (e.g., $a_1(t=0) = 1$ and $a_2(t=0) = 0$) and derive the probability to find an atom in state $|1\rangle$ or $|2\rangle$,

$$\begin{aligned} P_1(t) = |a_1(t)|^2 &= \frac{\Omega_0^2}{\Omega_\epsilon^2}\cos^2\left(\frac{\Omega_\epsilon}{2}t\right) = \frac{\Omega_0^2}{2\Omega_\epsilon^2}\left[1 + \cos(\Omega_\epsilon t)\right], \\ P_2(t) = |a_2(t)|^2 &= \frac{\Omega_0^2}{\Omega_\epsilon^2}\sin^2\left(\frac{\Omega_\epsilon}{2}t\right) = \frac{\Omega_0^2}{2\Omega_\epsilon^2}\left[1 - \cos(\Omega_\epsilon t)\right], \end{aligned} \tag{3.19}$$

with the non-resonant Rabi frequency

$$\Omega_\epsilon = \sqrt{\Omega_0^2 + \epsilon^2}. \tag{3.20}$$

These equations show the dynamics of an idealized two-level atom in an external electromagnetic field. Without taking spontaneous emission effects into account (this is the case for $\Omega_0 \gg \Gamma$), the atom oscillates between the two states and we have to distinguish between

- **resonant interaction** ($\epsilon = 0$): the transition probability has a maximum amplitude and oscillates between 0 and 1, and

- **non-resonant interaction** ($\epsilon \neq 0$) : the transition probability is reduced and the oscillation frequency itself is always higher than the resonant frequency according to $\Omega_\epsilon = \sqrt{\Omega_0^2 + \epsilon^2}$.

These Rabi oscillations are depicted in Fig. 3.2 (right). A pulse area can be defined where the population of the system in the case for $\epsilon = 0$ is completely inverted, $\Omega_0 \cdot \tau = \pi$. This is called a π-pulse. By realizing a pulse area of $\Omega_0 \cdot \tau = \pi/2$, a so called $\pi/2$-pulse, the atoms are equally distributed between both states. For $\epsilon \neq 0$, the pulse areas are specified using Ω_ϵ.

Momentum of the atoms

If we now consider the atoms to have a certain momentum $\vec{p}$, the spatial variation of the electromagnetic field has to be considered, $\vec{E}(\vec{r},t) = \vec{\alpha} E_0 \cos(\vec{k}\cdot\vec{r} - \omega t)$ and consequently the Hamiltonian must to be complemented with the kinetic energy term as

$$\hat{H} = \hbar\omega_2 |2\rangle\langle 2| + \hbar\omega_1 |1\rangle\langle 1| - \vec{d}\cdot\vec{E} + \frac{\vec{p}^2}{2m}. \tag{3.21}$$

With a new set of eigenstates, $|1,\vec{p}\rangle$ and $|2,\vec{p}+\hbar\vec{k}\rangle$, the dynamics of the system with external degrees of freedom are described by the wave function [174]

$$\begin{aligned} |\psi(t)\rangle = {} & c_{1,\vec{p}}(t)|1,\vec{p}\rangle \exp\left[-i\left(\omega_1 + |\vec{p}|^2/2m\hbar\right)t\right] \\ & + c_{2,\vec{p}+\hbar\vec{k}}(t)|2,\vec{p}+\hbar\vec{k}\rangle \exp\left[-i\left(\omega_2 + |\vec{p}+\hbar\vec{k}|^2/2m\hbar\right)t\right]. \end{aligned} \tag{3.22}$$

In this new basis, the non-resonant Rabi frequency has to be calculated taking the Doppler shift $\vec{p}\cdot\vec{k}/m$ and the photon recoil $\hbar|\vec{k}|^2/2m$ into account. This leads to an effective detuning ϵ_{eff}, which is now to be calculated as

$$\begin{aligned} \epsilon_{\mathit{eff}} &= \omega_L - \left[\frac{\vec{p}\cdot\vec{k}}{m} + \frac{\hbar|\vec{k}|^2}{2m}\right] \\ &\equiv \omega_L - \bar{\omega}. \end{aligned} \tag{3.23}$$

3.2.2 A stimulated Raman process between two momentum states

The derived expressions for the two-level dynamics in the previous section are based on the assumption of negligible spontaneous processes. The involved states $|1\rangle$ and $|2\rangle$ have to have sufficiently long lifetimes τ, which at least are longer than the interaction time with the driving laser fields. However, if $|2\rangle$ is associated with an excited state, the population will rapidly decay ($\tau \sim$ ns) into the ground state by randomly emitting photons.

We now want to adapt this treatment to derive important quantities of a two-photon process between long-living ground states. When a coherent transition between two momentum states of the same ground states is realized, we call it Bragg diffraction

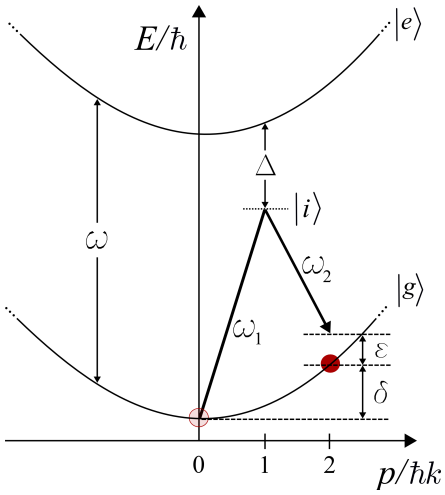

Figure 3.3: Schematic of first-order Bragg diffraction as a two-photon Raman process coherently coupling two momentum states $|0\hbar k\rangle$ and $|2\hbar k\rangle$ of the same ground state $|g\rangle$. Two light fields (ω_1 and ω_2) are detuned from the excited state $|e\rangle$ and effectively couple the momentum states via a virtual level $|i\rangle$. Both ground states lie on the dispersion relation curve of a free particle, hence determining $\hbar\delta = p_r^2/2m$.

[172, 160]. Transitions between two different atomic states (e.g., hyperfine ground states of an alkali atom) will be referred to as Raman diffraction [59, 175].

In the QUANTUS-I experiment, Bragg diffraction will be implemented, a basic schematic of which is given in Fig. 3.3. Here, one lattice beam couples the ground state $|g, 0\hbar k\rangle$ with a virtual level $|i, 1\hbar k\rangle$, the second laser beam couples that virtual level again with the ground state $|g, 2\hbar k\rangle$. Since the absolute detuning Δ w.r.t the excited level is sufficiently large, the population of $|e\rangle$ as well as spontaneous emission and scattering processes leading to decoherence can both be neglected.

We treat our problem as an idealized atom with two energy levels $|g, 0\hbar k\rangle \equiv |1\rangle$ and $|g, 2\hbar k\rangle \equiv |2\rangle$, an effective two-level system whose energy difference is supposed to be $\Delta E = \hbar\delta = p_r^2/2m$ (see Sec. 3.1). The latter determines the dispersion relation to be of parabolic shape. Compared to the single-photon treatment, the atom now interacts with an electromagnetic field composed of two frequencies,

$$\vec{E}(t) = \vec{E}_1(t) + \vec{E}_2(t) = \vec{\alpha} E_1 \cos(\omega_1 t) + \vec{\alpha} E_2 \cos(\omega_2 t). \tag{3.24}$$

For Bragg diffraction the ratio of relative detuning between the laser frequencies and their absolute frequency is negligibly small, $\delta/\omega \approx 0.01$ ppb. To calculate the eigenenergies, we approximate the laser fields to have the same wave vector norm as $|\vec{k_1}| \approx |\vec{k_2}| \equiv k$. This results in the following eigenenergies of the two momentum states

$$\begin{aligned} E_{|1\rangle} &= \hbar\omega_g, \\ E_{|2\rangle} &= \hbar\omega_g + \frac{(p_0 + 2\hbar k)^2}{2m} \equiv \hbar\bar{\omega}_g. \end{aligned} \tag{3.25}$$

The Hamiltonian has to consider interactions with both laser fields (see Fig. 3.3). By neglecting three-photon processes [176], it can be written as

$$\begin{aligned}\hat{H} &= \hat{H}_0 + \hat{H}_{AL} \\ &= \hbar\omega_g \left|g,0\right\rangle \left\langle g,0\right| + \hbar\bar{\omega}_g \left|g,2\hbar k\right\rangle \left\langle g,2\hbar k\right| \\ &+ \hbar\omega_1 \left|i,\hbar k_1\right\rangle \left\langle i,\hbar k_1\right| + \hbar\omega_2 \left|i,\hbar k_2\right\rangle \left\langle i,\hbar k_2\right| - \vec{d}\cdot\vec{E}.\end{aligned} \tag{3.26}$$

Analogously to Sec. 3.2.1, a superposition state can be used as an ansatz to solve the time-dependent Schrödinger equation,

$$\begin{aligned}\left|\Psi(t)\right\rangle = c_1(t)\left|g,0\right\rangle + c_2(t)\left|g,2\hbar k\right\rangle + c_{i,1}(t)\left|i,\hbar k_1\right\rangle \\ + c_{i,2}(t)\left|i,\hbar k_2\right\rangle .\end{aligned} \tag{3.27}$$

The resulting system of rate equations obtained in RWA can again be transformed in a time-independent set of equations [174]. For the starting parameters $c_1(t=0)=1$ and $c_2(t=0)=0$, the populations of both states can be expressed as

$$\begin{aligned}P_1(t) &= \frac{\Omega_{\mathit{eff}}^2}{\Omega_{\mathit{eff}}^2 + (\epsilon_{\mathit{eff}} - \delta_{AC})^2}\cos^2\left[\sqrt{\Omega_{\mathit{eff}}^2 + (\epsilon_{\mathit{eff}} - \delta_{AC})^2}\cdot t/2\right], \\ P_2(t) &= \frac{\Omega_{\mathit{eff}}^2}{\Omega_{\mathit{eff}}^2 + (\epsilon_{\mathit{eff}} - \delta_{AC})^2}\sin^2\left[\sqrt{\Omega_{\mathit{eff}}^2 + (\epsilon_{\mathit{eff}} - \delta_{AC})^2}\cdot t/2\right].\end{aligned} \tag{3.28}$$

We now discuss the important parameters of the equations given above.

- **Effective Rabi frequency:** $\Omega_{\mathit{eff}} = \frac{\Omega_{1,1}\Omega_{2,2}}{2\Delta}$, which is the resulting coupling strength of the coherent two-photon transition $\left|1,0\hbar k\right\rangle \rightarrow \left|i,1\hbar k\right\rangle \rightarrow \left|2,2\hbar k\right\rangle$. The detuning of the laser beams w.r.t to the excited state $\left|e\right\rangle$ is given by Δ.
- **Single photon coupling strength:** $\Omega_{l,m} = -2\left\langle i\right|\vec{d}\left|l\right\rangle E_m/\hbar$, with $l \in (1,2)$ being one of the two ground states, i the virtual level and $m \in (1,2)$ indicating the two laser beams generating the optical lattice. Given the linewidth Γ of the $5S_{1/2} \rightarrow 5P_{3/2}$ transition in ^{87}Rb and laser beam intensity I_m, one can calculate the resonant single photon Rabi frequencies as $\Omega_{l,m} = \sqrt{6\pi c^2\Gamma I_m/\hbar\omega_m^3}$.
- **Effective two-photon transition detuning:** $\epsilon_{\mathit{eff}} = \omega_{\mathit{eff}} - \left[\frac{\vec{p}\cdot\vec{k}_{\mathit{eff}}}{m} + \frac{\hbar|\vec{k}_{\mathit{eff}}|^2}{2m}\right] \equiv \omega_{\mathit{eff}} - \bar{\delta}$, with frequency difference of the lattice beams $\omega_{\mathit{eff}} = \omega_1 - \omega_2$, effective wave vector $\vec{k}_{\mathit{eff}} = \vec{k}_1 - \vec{k}_2 \approx 2k$, initial momentum $\vec{p}$ and mass m of the atoms.
- **AC Stark shift of $\left|g,0\hbar k\right\rangle \equiv \left|1\right\rangle$:** $\Omega_{\left|1\right\rangle}^{AC} = \frac{|\Omega_{1,1}|^2}{4\Delta} + \frac{|\Omega_{1,2}|^2}{4(\Delta-\bar{\omega})}$, caused by the interaction of state $\left|1\right\rangle$ with both laser beams,
- **AC Stark shift of $\left|g,2\hbar k\right\rangle \equiv \left|2\right\rangle$:** $\Omega_{\left|2\right\rangle}^{AC} = \frac{|\Omega_{2,1}|^2}{4(\Delta+\bar{\omega})} + \frac{|\Omega_{2,2}|^2}{4\Delta}$, caused by the interaction of state $\left|2\right\rangle$ with both laser beams,

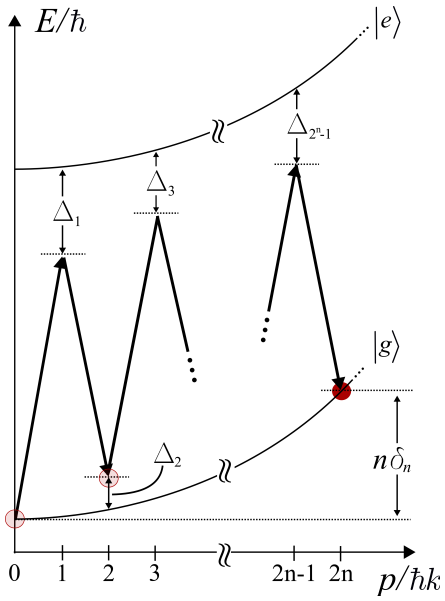

Figure 3.4: Schematic of n-th order Bragg diffraction as a stimulated 2n-photon Raman process. Energy conservation requires $\hbar n\delta_n = (2n\hbar k)^2/2m$ to coherently couple the momentum states $|0\hbar k\rangle$ and $|2n\hbar k\rangle$. The energy levels are labeled by their transverse momentum states which are displayed in units of $\hbar k$. The corresponding detunings to ground and excited state are given by Δ_i.

- **differential AC Stark shift:** $\delta_{AC} = \Omega^{AC}_{|2\rangle} - \Omega^{AC}_{|1\rangle}$.

Two-photon Raman transitions will give rise to Rabi oscillations with a Rabi frequency of Ω_{eff}, for example a π-pulse will ideally transfer all of the population from one momentum state to the other. For Bragg diffraction $\omega_{\mathit{eff}}/\Delta \approx 0.01$ ppb, which allows to approximate the effective Rabi frequency to

$$\Omega_{\mathit{eff}} = \frac{\Omega_{1,1}\Omega_{2,2}}{2\Delta} \approx \frac{\Omega^2}{2\Delta}, \tag{3.29}$$

with $\Omega_{1,1} = \Omega_{2,2} \equiv \Omega$ as the single photon Rabi frequency. In the case of a resonant interaction ($\epsilon_{\mathit{eff}} = 0$), Eq. 3.28 now simplify to the basic expressions

$$\begin{aligned} P_1(t) &= \cos^2[\Omega_{\mathit{eff}} \cdot t/2] = \frac{1}{2}[1 + \cos(\Omega_{\mathit{eff}} \cdot t], \\ P_2(t) &= \sin^2[\Omega_{\mathit{eff}} \cdot t/2] = \frac{1}{2}[1 - \cos(\Omega_{\mathit{eff}} \cdot t]. \end{aligned} \tag{3.30}$$

Higher-order Bragg diffraction

In a momentum picture, the above depicted process is described by an atom undergoing a two-photon Raman process with corresponding momentum transfer of $p_r = 2\hbar k$. We call this first-order Brag diffraction. It is also possible to transfer even higher momentum, i.e. $2n\hbar k$, which is called n-th order Bragg diffraction. For this process, again

an effective Rabi frequency can be derived [177]

$$\Omega_{eff}^{nth} = \frac{\Omega^{2n}}{2^{1n-1}\Delta_1\Delta_2...\Delta_{n-1}}, \tag{3.31}$$

where Ω_0 is the single-photon Rabi frequency and Δ_i are the detunings from any virtual level as indicated in Fig. 3.4. Here, an atom prepared in momentum state $|g, 0\hbar k\rangle$ interacts via a 2n-photon transition, involving 2n-1 virtual levels, and will subsequently end up in $|g, 2n\hbar k\rangle$. Energy and momentum conservation of a moving atom with initial momentum p_0 leads to the following resonance condition

$$\Delta E = \frac{(np_r + p_0)^2 - p_0^2}{2m} = \frac{(2n\hbar k \sin(\vartheta/2) + mv_0)^2 - m^2v_0^2}{2m} = \hbar n\delta_n \tag{3.32}$$

With the recoil frequency $\omega_r = \hbar k^2/m$, the frequency difference between the laser beams for n-th order Bragg diffraction results in

$$\delta_n = 4n\omega_r \sin^2(\vartheta/2) + 2kv \cdot \sin(\vartheta/2), \tag{3.33}$$

thus scaling linearly with diffraction order n. To give an example, for $\vartheta = 180°$ (counter-propagating laser beams), a third order Bragg pulse for resting ^{87}Rb atoms ($p_0 = 0$) would need an optical lattice with a frequency difference of $\delta_3 = 12 \cdot \omega_r \cong 2\pi \cdot 45.24$ kHz.

3.3 Bragg spectroscopy of atomic momentum distributions

Up to now we only assumed single atoms in the Bragg diffraction process. If the detuning δ fulfills the resonance condition, resonant Rabi oscillations occur and the atom can in principle be transferred into a final momentum state with a probability of 100%. But even a sub-recoil BEC has a non-vanishing expansion rate associated with an effective momentum spread Δp_{rms}. As a result, some atoms of the corresponding distribution remain non-resonant by application of a Bragg lattice with fixed δ, and would therefore oscillate with a reduced amplitude between the coupled states (see Eq. 3.28).

This momentum selectivity can be used to individually address different velocity classes of an atomic distribution by carefully adjusting δ. For Bragg diffraction with $n = 1$ and $\vartheta = 180°$, Eq. 3.32 allows to formulate a resonance condition for atoms with initial momentum p_0,

$$p_0(\delta) = \frac{m\hbar\delta}{p_r} - \frac{p_r}{2} = m\left[\frac{\delta - 4(\hbar k^2/2m)}{2k}\right]. \tag{3.34}$$

In a simplified picture, atoms fulfilling Eq. 3.34 get diffracted and spatially separate from the un-diffracted part of the cloud, if the initial momentum spread of the cloud is narrower than the value of transferred momentum ($\Delta p_{rms} < p_r$). In that case we can scan δ, measure the diffraction efficiency for a certain momentum class and analyze the obtained distribution in momentum space. This is called Bragg spectroscopy (BS).

BS was demonstrated as a versatile instrument for investigating the evolution of

condensate wave functions [168, 160]. It has been used for measurements of the coherence length or phase fluctuations of trapped degenerate gases [169, 178], as well as to analyze their excitation spectrum [179]. In this thesis, BS will be used to measure the momentum width of freely expanding condensates released from differently steep atom chip traps (see Sec. 3.4.3).

The observed spectrum in momentum space is given by the spectral response function of the condensate [180, 168]. In other words, the shape of the measured distribution is a convolution of the atomic clouds momentum distribution with the Fourier distribution of the applied Bragg pulse. We will shortly discuss and quantify the implication of finite Bragg pulses to the momentum selectivity in the next section.

3.3.1 Momentum selectivity and finite pulse duration

In order to realize specific pulse areas for controlled light-matter-interactions (see Sec. 3.2.2) or to perform Bragg spectroscopy, the interaction time of atoms with the Bragg lattice oscillating at δ is usually limited to finite pulse durations of τ. By a Fourier transformation of the temporal intensity profile $I(t)$ applied to the atoms, we get the spectral distribution $\tilde{I}(\omega)$ of the Bragg pulse. For example, the intensity profile $I(t)$ of a Gaussian pulse is given as

$$I(t) = I_0 \exp\left(-4\ln 2 \frac{t^2}{\Delta\tau^2}\right) \tag{3.35}$$

with $\Delta\tau$ as the FWHM width. Fourier transformation of I(t) yields

$$\tilde{I}(\omega) = \int I(t) \cdot \exp(-i\omega t) dt = \tilde{I}_0 \exp\left(\frac{-\Delta\tau^2\omega^2}{4\ln 2}\right). \tag{3.36}$$

This can in principle be done for any envelope and leads to the formulation of the time-bandwidth product (TBP)

$$[\Delta\omega \cdot \Delta\tau]_{FWHM} \geq 4\ln 2, \tag{3.37}$$

with the temporal FWHM of the pulse $\Delta\tau$ and the corresponding spectral width of the pulse $\Delta\omega = 2\pi\Delta\nu$ [1]. This limitation is essentially a property of the Fourier transform of the Bragg pulse envelope. Since there are other sources of broadening, the TBP is often used for indicating how close a pulse is to the transform limit.

By using the definitions of the rms width for Gaussian shaped pulses, the TBP is given as

$$[\Delta\omega \cdot \Delta\tau]_{\sigma} \geq 1. \tag{3.38}$$

A finite pulse duration thus determines a spectral width $\Delta\omega \equiv \Delta\delta$ which according to Eq. 3.34 can directly be translated into a momentum uncertainty of the Bragg resonance. Let the atomic momentum distribution be characterized by a momentum width Δp_{at}. In the limiting case of very long pulses ($1/\tau \ll \Delta p_{at}$), a narrow velocity

[1] For rectangular shaped pulses, the TBP is limited by $\Delta\omega \cdot \Delta\tau \geq 2.783$ [181], indicating a slightly larger spectral width compared to equally long Gaussian shaped pulses

class can be scattered out of the initial atomic cloud. This is mandatory for Bragg spectroscopy (BS) since only in this limit the scanned spectrum would properly reflect the momentum distribution of the condensate. In the other limit of very short pulses ($1/\tau \gg \Delta p_{at}$), the spectral width broadens such that, for example, all atoms of a condensate can be diffracted at once. Here, BS would now measure the pulse width.

Ultimately, even shorter pulse durations will lead to scattering in neighboring momentum states, if the spectral width exceeds the resonance frequencies of higher-order diffraction (see Eq. 3.33). This is called Raman-Nath scattering [182]. Since there is no sharp transition between the Bragg and the Raman-Nath regime, and it might be useful to approximate the pulse duration ensuring scattering in the Bragg regime. For first-order (n=1) Bragg diffraction of ^{87}Rb atoms, the energy uncertainty should not exceed $\Delta\tilde{E} = \hbar\Delta\delta = 2\hbar\omega_r$. Assuming Gaussian shaped pulses with rms width $\Delta\tau$, this results in a lower bound for the pulse duration of $\Delta\tau \geq 1\Delta\delta \approx 21\ \mu$s to safely operate in the Bragg regime.

3.4 Implementation of Bragg diffraction in QUANTUS-I

The QUANTUS-I experiment constitutes an atom-chip-based source of non-magnetic degenerate gases with sub-recoil momentum distribution, an ideal starting point for Bragg diffraction experiments. A drop-tower capable Bragg laser system based on a distributed feedback (DFB) laser diode will be presented as well as ground-based experimental results of

- Rabi oscillations to determine the basic performance of the system and to optimize the beam splitting and mirror pulses for matter wave interferometry (see Sec. 3.4.2),
- Bragg spectroscopy to study the momentum width evolution of condensates emerging from different magnetic trap configurations (see Sec. 3.4.3),
- open (or asymmetric) interferometers (e.g., Ramsey-type and Mach-Zehnder type) to probe the phase evolution of freely expanding condensates (see Sec. 3.5.1), for measurements of the coherence length (see Sec. 3.5.3) and studies of the mean-field influence (see Sec. 3.5.4), and
- pulsed optical levitation of atoms as a proof-of-principle experiment for measuring the local gravitational acceleration (see Sec. A).

These experiments were done in preparation of drop campaigns demonstrating the first interferometer with Bose-Einstein condensates in microgravity (see Sec. 5).

In Fig. 3.5, a schematic of the used coordinate system is given. The BEC is generated in the magnetic chip trap, has an initial momentum p_0 (most of the cases $p_0 \approx 0$) and after release accelerates towards Earth in the z-direction. After an expansion time T_0, two anti-parallel laser waves traveling along the x-direction are switched on for a duration τ to induce Bragg diffraction ($\tau \ll T_0, T_{sep}$). In the case of only one Bragg pulse, an absorption image is taken after spatial separation of the momentum classes $|p_0\rangle$ and $|p_0 + 2\hbar k\rangle$ during T_{sep}. The detection axis (y-direction) is oriented perpendicular to the lattice beams.

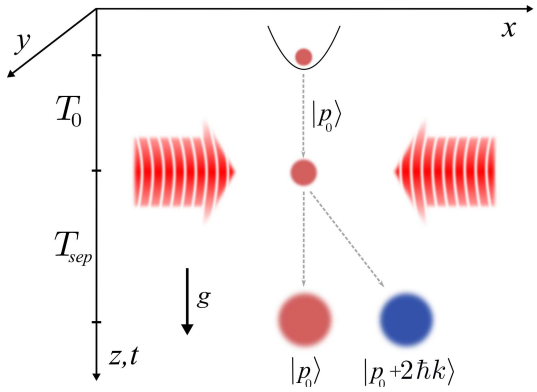

Figure 3.5: Schematic of first-order Bragg diffraction in the QUANTUS-I experiment. The atom chip is located in the x-y plane and the released BEC is accelerated towards Earth in the z-direction. After an expansion time T_0, the Bragg laser beams form a one-dimensional optical lattice in the x-direction for a pulse duration τ with $\tau \ll T_0, T_{sep}$. The momentum states spatially separate for T_{sep} until an absorption image is taken along the y-direction after a total time-of-flight of $T_{tof} = T_0 + T_{sep}$.

3.4.1 Bragg laser system for drop tower operation

Stringent mechanical requirements are imposed on the laser system, since it will be objected to critical thermal and mechanical loads (see Sec. 5.1). The other main requirement is obviously given by the capability of driving two-photon transitions between different momentum states of ^{87}Rb.

For anti-parallel Bragg beams and a perfect resting point source, first-order Bragg diffraction is resonant at a detuning of $\delta = 2\hbar k^2/m = 2\pi \cdot 15.08\,\text{kHz}$. Since this is only an ideal case, the frequency difference δ should be a variable parameter to compensate any shifts of the resonance. Continuously illuminated atoms undergo Rabi oscillations between the coupled momentum states. Therefore, the Bragg pulse duration τ obviously needs to be tunable to optimize the beam splitter efficiency. The effective Rabi frequency (see Sec. 3.2.2), can be calculated as

$$\Omega_{eff} = \frac{3\pi c^2 \Gamma I}{\Delta \hbar \omega^3}. \tag{3.39}$$

Therefore, the absolute intensity I of the beams as well as the detuning Δ to the $|5S_{1/2}, F = 2\rangle \rightarrow |5P_{3/2}F = 3\rangle$ transition of ^{87}Rb should be an adjustable parameter. We now want to focus on the technical realization. A schematic and a photograph of the assembled Bragg laser system are given in Fig. 3.6.

Distributed feedback (DFB) diode laser source

The light source is a distributed feedback (DFB) laser diode, based on a III-V compound semiconductor (GaAs) integrated into a hermetic TO_3 housing filled with a technical gas (Eagleyard, EYP-DFB-0780-00080-1500-TOC03-0000). It features a Bragg grating which is implemented by a periodic variation of the index of refrac-

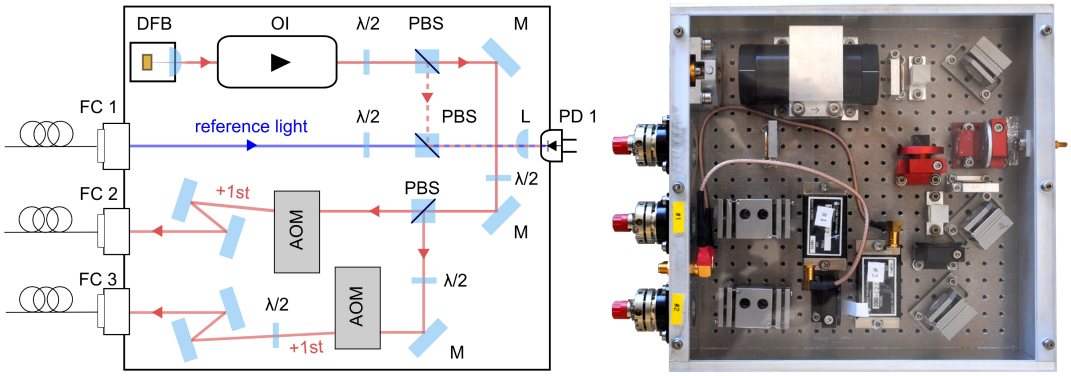

Figure 3.6: Miniaturized Bragg laser system for drop tower operation. The system is based on a distributed feedback (DFB) diode laser, miniaturized optics and opto-mechanics mounted onto an 270 x 310 mm^2 aluminum breadboard with M3 threads (1 cm spacing). Further details in text.

tion and extends over the total length of the semiconductor resonator[2]. The grating narrows the linewidth of the emission and guarantees single frequency emission by selecting a single longitudinal laser mode. Tuning of the emitted light is accomplished by modulating either the diode's current ($d\lambda/dI \approx 0.003$ nm/mA) or temperature ($d\lambda/dT \approx 0.06$ nm/K), the latter of which is possible since the chip is soldered onto a thermoelectric cooler (TEC).

Due to the absence of any critical opto-mechanical component, DFB diodes compromise a monolithic structure and permit high long-term stability and reliability. The maximum forward current and corresponding optical output power given by the manufacturer are $I_{max} = 200$ mA and $P_{max} \approx 100$ mW. The laser threshold and slope have been measured to be $I_{th} = 37$ mA and $S = 0.74$ W/A, respectively. The emission spectrum reached the D_2-line of ^{87}Rb for a temperature of 22.0°C. Standard specifications are summarized in Tab. 3.1.

Opto-mechanical design and beam paths

The light emitted by the DFB diode (see Fig. 3.6) is collimated with an aspheric lens ($f = 2.2$ mm) and passes an optical isolator (OI, 30 dB isolation), whose transmission was measured to be 0.78. In this module, the used opto-mechanical components (mirror mounts, optics holders) are self-made constructions, mostly based on aluminum alloys and stainless steel.

After passing a half-wave plate ($\lambda/2$), the beam is split into two paths at a polarization beam splitter cube (PBS). One path is used for absolute frequency stabilization. A fraction of Bragg laser light is overlapped with reference light (emerging from fiber collimator (FC) 1) using another PBS. As a reference, we use the cooling laser (see Sec. 2.4.3), stabilized to the $|5S_{1/2}, F = 2\rangle \rightarrow |5P_{3/2}F = 3\rangle$ transition of ^{87}Rb. The

[2] Another laser type with an integrated Bragg grating is the distributed Bragg reflector (DBR) diode laser. Here, the grating is not situated in the vicinity of the active medium but implemented aside the gain section acting as a local reflector.

parameter	unit	min.	typ.	max.
spectral width (FWHM) $\Delta\nu$	MHz		2	
temperature coefficient $d\lambda/dT$	nm/K	0.06		
current coefficient $d\lambda/dI$	nm/mA	0.003		
typ. Output power @ $I = 180$ mA	mW	80		
slope efficiency S	W/A	0.6	0.8	1
threshold current I_{th}	W/A			70

Table 3.1: Specifications of the DFB-diode used in the Bragg laser system at the begin of life, adapted from [183]. Remark: By using the QUANTUS-I laser electronics, we usually measured FWHM linewidths of about $\Delta\nu \approx 5$ MHz.

beat signal is detected with a fast GaAs-based photodetector (Hamamatsu G4176-03).

The other path is used to generate the optical lattice and therefore the beam is again split into two paths, each passing an acousto-optical modulator (AOM). These devices (Crystal technology, 3080-122) are switchable on a ns-timescale and driven with 80 MHz and 80 MHz + δ, respectively. In this way, they generate the required frequency difference δ for the two beams. After passing the AOMs, the light is coupled into polarization maintaining single-mode optical fibers (SuK, PMC-850-5,1-NA013-3-APC-400-P) with commercial, miniaturized laser beam couplers (SuK 60SMS series, 8° polished), and finally guided to the experiment.

The light from both fibers is collimated to a Gaussian beam with a diameter of 0.65 cm (FWHM) using a single-lens telescope each, attached at opposites sides of the vacuum chamber and pointing along the x-direction (see Fig. 3.5). Both beams are equally linearly polarized, thus forming an optical grating at the position of the atoms. Fiber-coupling and AOM diffraction efficiencies (cw) are both around $\eta = 70\%$, resulting in typical values of total optical power for the Bragg lattice of about $P_{typ} =$ 10 mW (cw) @ $I_{typ} = 100$ mA.

To verify the mechanical stability of the whole setup, the laser system was successfully tested in a self-built mini drop tower providing a drop altitude of approximately 1 m (designed and built by K. Moehle during a research assistant period in 2008). This tower consists of a platform, on which laser test assemblies can be mounted and which is identical to the used platforms in the drop capsules [107]. It is guided via two stainless steel metal rods and can be elevated by a mechanical winch to a height of 1 m and subsequently be dropped from that distance. At the bottom, a combination of foam sheets decelerates the assembly with typical loads of up to 50 g which are comparable to the expected ones for the QUANTUS-I apparatus in the Bremen drop tower.

Stabilization and Switching electronics

To prevent excitations and atom losses which lead to decoherence, the absolute laser frequency of the Bragg beams has to be sufficiently detuned from atomic resonances. This is realized by an offset lock stabilization, as depicted in Fig. 3.7 (top).

The detected beat signal (G4176-03) between Bragg and cooling laser is typically around $\Delta = 640$ MHz. It is first amplified (ZJL-7G), passes a directional coupler

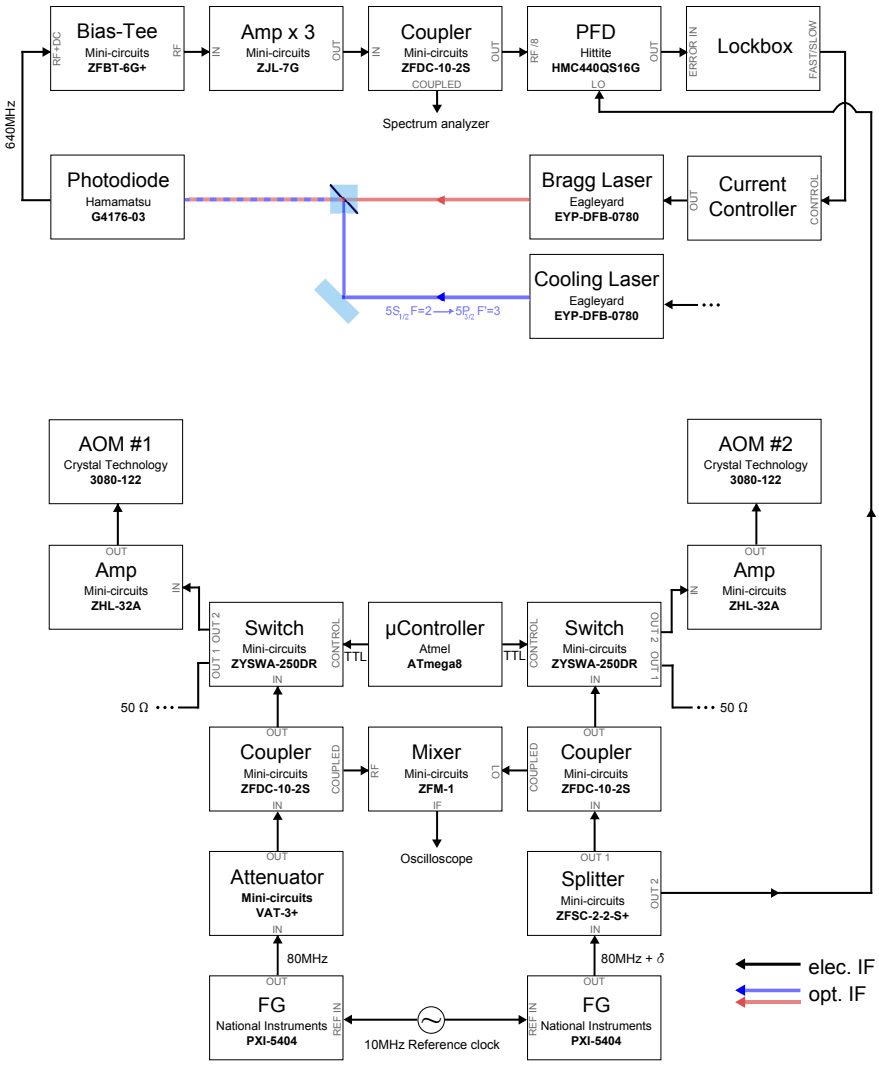

Figure 3.7: Stabilization path of the Bragg laser system in QUANTUS-I. Details in text.

(ZFDC-10-2S), then divided by a programmable divider and compared with a stable reference oscillator (PXI-5404, 80 MHz) in a digital phase frequency detector (HMC 440QS16G). Subsequently, an error signal is fed into a lockbox which generates a control signal for the current controller driving the Bragg laser diode. In this way, the frequency of the Bragg laser source can be stabilized to a fixed detuning Δ, which can be adjusted by changing the LO frequency or the divider scaling.

The electronics for driving the AOMs are depicted in Fig. 3.7 (bottom). Here, two frequency generator cards (PXI-5404), phase-locked to a 10 MHz internal reference, are used to drive one AOM each. The PXI-5404 is a 100 MHz frequency generator with a 1.07 μHz frequency and 12 Bit vertical resolution. By following the right path, the 80 MHz + δ output passes a power splitter (ZFSC-2-2-S+) from which one output (OUT 2) is used as the LO for offset lock stabilization. On the left-hand side, the 80 MHz output has to be attenuated (VAT-3) such that both RF signals remain at the

same amplitude for subsequent amplification.

They pass a directional coupler (ZFDC-10-2S) and are fed into one RF switch each (ZYSWA-2-50DR), capable of switching times of about 20 ns (10 − 90%). A microcontroller (Atmel ATmega8) generates a TTL signal to simultaneously trigger both switches with μs resolution. This device controls our Bragg pulse duration. Finally, each output is amplified to about 1 W (ZHL32A) and fed into the AOMs (3080-122).

In a later stage of the experiment, we exchanged this pulse generation concept with a state-of-the-art timing processor (PulseBlaster DDS-II-300), providing two independent analog output channels ranging in frequency from 5 kHz to 100 MHz with sub-Hertz resolution. Various envelopes can now be programmed with 300 MHz sampling rate and 14 Bits sampling precision[3]. This board gets triggered from the experimental sequence (LabView routine) and is programmed via USB.

3.4.2 Rabi oscillations of condensates released from an atom chip

With the above described setup, Rabi oscillations between the coupled momentum states $|0\hbar k\rangle$ and $|2\hbar k\rangle$ have been measured. In Fig. 3.8, the diffraction efficiency as the number of diffracted atoms versus total atom number,

$$\frac{N_{2\hbar k}}{N_{tot}} \sim A \cdot \left(1 - e^{-\tau/t_0} \cos(\Omega_{\mathit{eff}} \cdot \tau)\right), \tag{3.40}$$

is plotted for increasing duration of square-shaped pulses τ and two different initial expansion times T_0. In contrast to the previous theoretical description, damping (with decay constant t_0) is considered mainly due to the momentum selectivity of the Bragg pulses (see Sec. 3.3.1). Excitations and atom losses can be neglected since the total atom number was measured to be constant during the Rabi cycles.

The condensate was released from the shallow trap ($\omega_x = 2\pi \cdot 46$ Hz) and transferred into the $m_F = 0$ state by means of an ARP. The Bragg beams were $\Delta = 2\pi \cdot 640$ MHz red-detuned w.r.t the cooling transition and we optimized the frequency difference between the laser beams to be in resonance with the center of the atomic momentum distribution ($\delta \approx 2\pi \cdot 15$ kHz).

The duration τ in Fig. 3.8 was scanned from 0 - 880 μs for two different expansion times T_0 of 4 ms (red circles) and 19 ms (blue squares). After application of the Bragg pulse, we waited for $T_{tof} = T_0 + T_{sep} = 33$ ms to let the ensembles spatially separate before detection. By fitting Eq. 3.40 to both data sets (solid red and blue lines), we can extract π-pulse durations of $\tau_\pi^{19ms} = 90$ μs and $\tau_\pi^{4ms} = 180$ μs with diffraction efficiencies of about 0.80 and 0.72, respectively. With that, effective Rabi frequencies and corresponding beam intensities at the position of the atoms can be calculated using

$$\tau_\pi = \frac{\pi}{\Omega_{\mathit{eff}}} = \frac{\pi\hbar\Delta\omega^3}{3\pi c^2 \Gamma I}, \tag{3.41}$$

resulting in $\Omega_{\mathit{eff}}^{4ms} = 2\pi \cdot 2.83$ kHz and $\Omega_{\mathit{eff}}^{19ms} = 2\pi \cdot 5.54$ kHz. The Bragg lattice intensity at both positions therefore follows as $I^{4ms} = 3.3$ W/m^2 and $I^{19ms} = 6.5$ W/m^2.

[3] This enabled the generation of Gaussian-shaped pulses in the time-domain

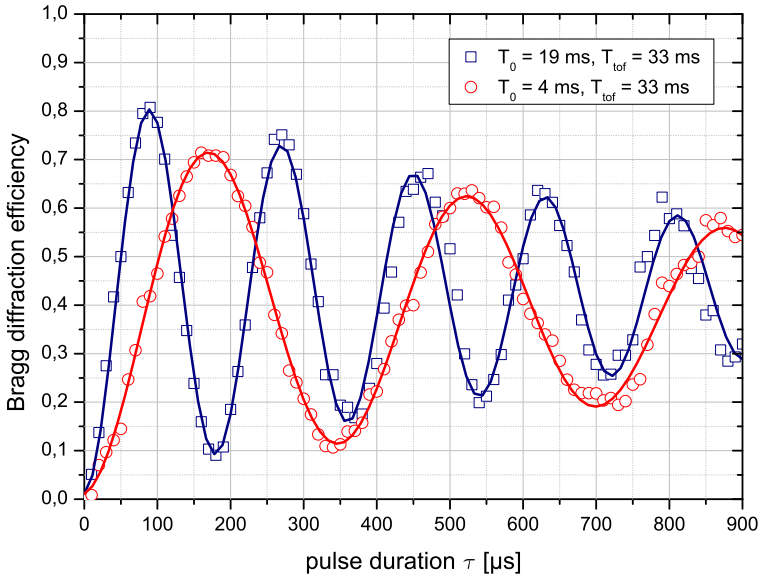

Figure 3.8: Rabi oscillations of a Bose-Einstein condensate between $|0\hbar k\rangle$ and $|2\hbar k\rangle$ after $T_0 = 4$ ms (red circles) and $T_0 = 19$ ms (blue squares) of free expansion. The solid lines correspond to fits of a damped, periodic function (see Eq. 3.40).

The observed differences are predictable and occur because during expansion, the condensate are accelerated towards Earth and experience different local intensities due to the Gaussian beam profile of the Bragg lattice. This spatial dependance was independently measured by scanning the expansion time T_0 prior application of a weak Bragg pulse with

$$\Phi \cdot \tau < \pi \,\forall\, T_0, \tag{3.42}$$

The results are plotted versus the corresponding vertical distance from the holding trap position (see blue triangles in Fig. 3.9). The Gaussian fit (red line) indicates that the free fall trajectory of the released atoms is not exactly perpendicular to the wave vector of the Bragg lattice. The angle is dependent on the orientation of the drop capsule which is usually (e.g. in-between of two drop campaign) not perfectly aligned w.r.t gravity while standing in the lab. This causes a Doppler-shift (typically on the order of a few kHz) which will be addressed in upcoming Bragg spectroscopy experiments (see Sec. 3.4.3) but might be neglected here due to the broader spectral width of the used pulses ($\Delta\omega \approx 2\pi \cdot 12.5$ kHz). Hence, we can approximate the Gaussian intensity maximum to be centered about $d_{z_0} \approx 4.3$ mm below the position of the holding trap.

This position of the beam center is actually desired to reduce reflections of the Bragg light at the HR coated atom chip surface. Stray light or interferences of the beams in the vicinity the atom chip surface lead to a complex intensity distribution and a deformed wavefront. They obviously complicate an accurate prediction of what the Bragg lattice below the chip actually looks like, which is important for experiments targeting at high-precision interferometry measurements with atom-chip-based condensates [9, 43]. However, this geometry yields high asymmetries of the pulse durations in

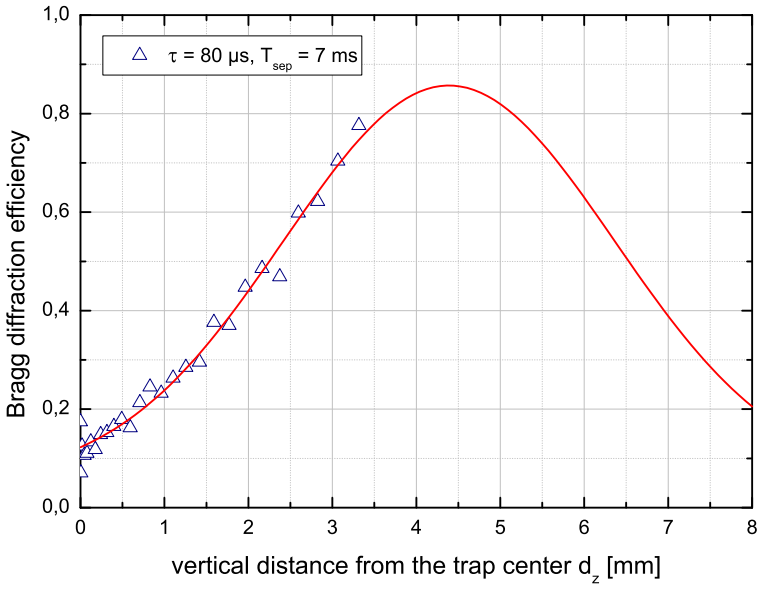

Figure 3.9: Spatial dependence of the Rabi frequency. The diffraction efficiency of a Bragg pulse is measured versus the vertical position of the atoms. The observed spatial dependence is modeled by a Gaussian profile (red line) to approximate the center position of the Bragg lattice at $d_{z_0} \approx 4.3$ mm

ground-based measurements and more generally less effective Bragg pulses compared to the available power. Given the measured beam profile of Fig. 3.9, we are using less than 30% of the available peak intensity during the first 20 ms ($d_z \leq 2$ mm) of free expansion.

Taken this systematic into account does still not entirely explain our measured Rabi frequencies Ω_{eff}^{4ms} and Ω_{eff}^{19ms}, which are about a factor of 2 smaller compared to the calculated ones (Eq. 3.41) using typical power values in the Bragg fibers of $P_{cw} = 10$ mW (see Sec. 3.4.1). Reasons for that are related to (i) reduced efficiency of AOMs in pulsed mode, (ii) non-perfect polarization and overlapping of both beams, (iii) transmission losses at the non-AR coated entry windows of the vacuum chamber and (iv) losses in the Bragg beam telescope assembly.

Nevertheless, beam splitter efficiencies can be increased by the use of Gaussian-shaped pulses in the time-domain as well as a higher effective Rabi frequencies (more optical power or less detuning) to realize shorter pulse durations[4]. Gaussian-shaped pulses feature a slightly narrower spectral distribution compared to rectangular shaped pulses with the same duration [181], vice versa the same frequency width is achieved for effectively longer pulses. Additionally, the spectral representation of rectangular shaped pulses ($\tilde{I}(\omega) \sim \mathrm{sinc}(\omega \cdot \tau/2)$) features side lobe peaks, which is not the case for a Gaussian beam which remains a Gaussian after Fourier transform (see Sec. 3.3.1). These will limit the diffraction efficiency for the main Bragg order in resonance and can lead to spurious scattering in unwanted momentum states.

[4] Already demonstrated in our setup with Bragg diffraction efficiencies of about $\sim 90\%$

Finite momentum width of the atom source

The Rabi oscillation measurement with $T_0 = 19$ ms is compared to numerical simulations in Fig. 3.10. On the right hand side, a stack of absorption images is given where each picture corresponds to one pulse duration of the measurement cycle. The aspect ratio of the pictures has been adapted in order to better visualize the condensates finite momentum width in the beam splitter direction, which is displayed in units of $\hbar k$.

On the left, numerical simulations are shown where the momentum of the atoms (also given in units of $\hbar k$) is plotted versus the pulse area $\Phi = \Omega\tau$. The simulations are based on the theoretical model described in [184]. It relies on a partitioned representation of the wave function in momentum space, where each interval is defined as

$$\Delta k_n : (n - 1/2)|2\hbar k| < k_x \leq (n + 1/2)|2\hbar k|. \tag{3.43}$$

By now only considering first-order Bragg diffraction in the non-interacting case, we represent the atomic state $\Psi(k_x, t)$ in two momentum zones Δk_0 and Δk_1 as

$$\Psi(k_x, t) = \phi_{k_x} \cdot \begin{pmatrix} c_0(k_x, t) \\ c_{2\hbar k}(k_x, t) \end{pmatrix}, \tag{3.44}$$

with the wave function in momentum space ϕ_{k_x}, the time-dependent coefficients representing the amplitudes of both diffraction orders c_0 and $c_{2\hbar k}$, and the atomic momentum in beam splitter direction k_x.

The temporal evolution of the coefficients $c_i(k_x, t)$ is determined by the Gross-Pitaevskii equation in momentum space. By considering the Bragg lattice as a plane-wave classical field, the dynamics in the non-interacting case are given by

$$i\frac{\partial}{\partial t}\begin{pmatrix} c_0(k_x, t) \\ c_{2\hbar k}(k_x, t) \end{pmatrix} = \begin{pmatrix} \frac{\hbar k_x^2}{2m} & \frac{\Omega_{eff}}{2} \\ \frac{\Omega_{eff}}{2} & \frac{\hbar}{2m}(k_x + 2k)^2 - \delta \end{pmatrix} \cdot \begin{pmatrix} c_0(k_x, t) \\ c_{2\hbar k}(k_x, t) \end{pmatrix} \tag{3.45}$$

with the effective Rabi frequency Ω_{eff}, wave vector of the beam splitters k and the detuning δ. We now can assume the atomic distribution as a Gaussian wave packet in momentum space, the modulus squared of which is given as

$$|\phi(k_x)|^2 = \frac{1}{\sqrt{2\pi}\sigma_{k_x}} \exp\left(-\frac{k_x^2}{2\sigma_{k_x}^2}\right). \tag{3.46}$$

In the simulation, the atoms are considered as a Gaussian wave packet with a momentum width of $\sigma_{k_x} = 0.13\hbar k$. This is an approximation based on Bragg spectroscopy of freely expanding of atoms from the shallow trap with $\omega_x = 2\pi \cdot 46$ Hz at $T_0 = 10$ ms (see Sec. 3.4.3).

Assuming the laser beams to be tuned to the two-photon resonance for resting atoms, the effective detuning is only a result of the Doppler-width of the atomic cloud. The time-dependent Rabi amplitude in momentum zone Δk_1 can hereby be calculated to

$$|c_{2\hbar k}(k_x, t)|^2 = \frac{\Omega_{eff}^2}{\Omega_{eff}^2 + (2\hbar k k_x/m)^2} \sin^2\left(\sqrt{\Omega_{eff}^2 + (2\hbar k k_x/m)^2} \cdot \tau/2\right), \tag{3.47}$$

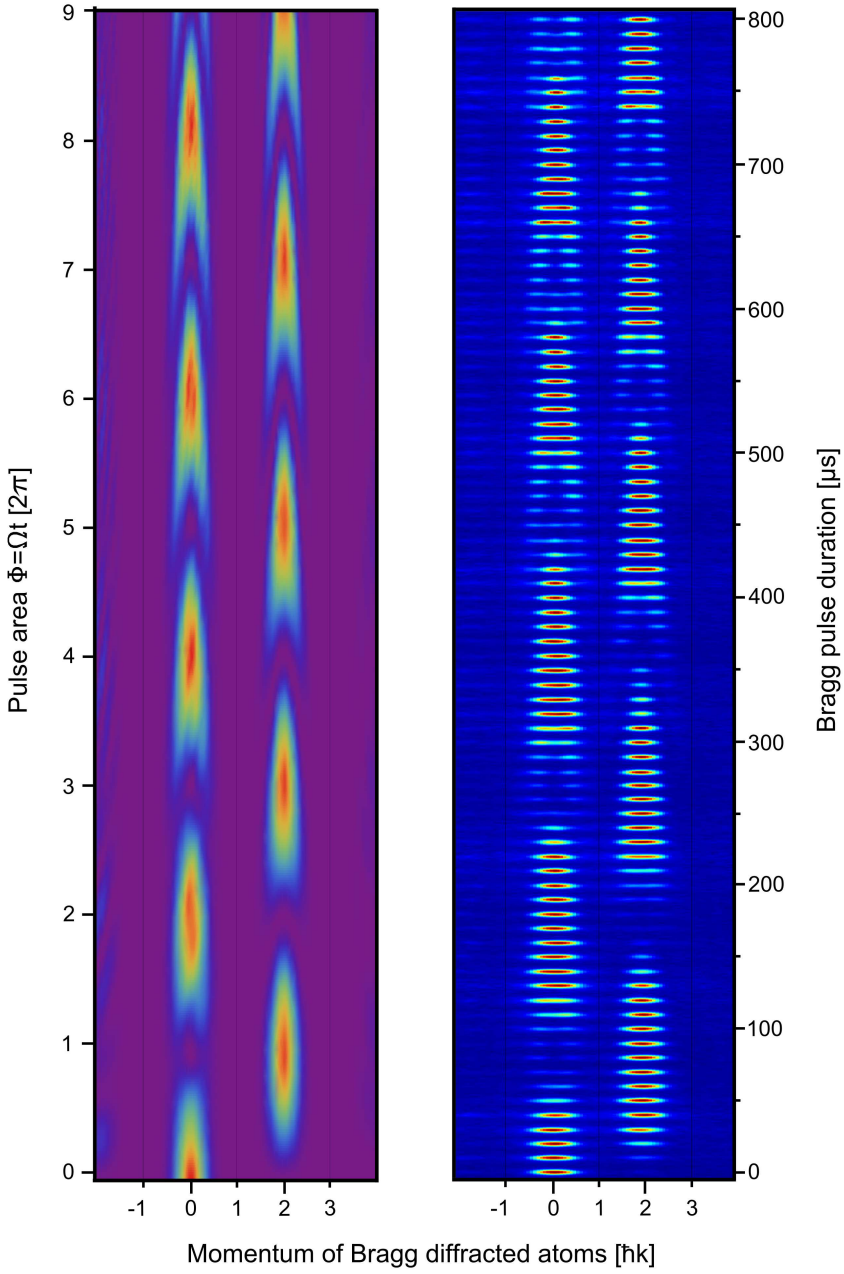

Figure 3.10: Comparison of simulation (left) and experiment (right) of Rabi oscillations induced by first-order Bragg diffraction. The condensate is released from the shallow trap ($\omega_x \approx 2\pi \cdot 50$ Hz) and expands for $T_0 = 10$ ms until the beam splitter is applied. The effective Rabi frequency was measured to be $\Omega_{eff}^{19\,\mathrm{ms}} = 2\pi \cdot 5.54$ kHz. For the calculation, we assumed the atoms to evolve as a Gaussian wave packet with an rms width of $\sigma_{k_x} = 0.13\ \hbar\mathrm{k}$.

where we can plug in the value for Ω_{eff} from our previous measurement. The expectation of value of the wave function $\Psi_{2\hbar k}$ after beam splitter operation then follows as

$$|\Psi_{2\hbar k}(k_x, t)|^2 = |\phi(k_x)|^2 \cdot |c_{2\hbar k}(k_x, t)|^2. \tag{3.48}$$

Oscillations of off-resonant atoms ($\epsilon_{eff} \neq 0$) are faster, but occur with a smaller amplitude. The smaller the initial momentum width of the atomic distribution, the more homogenous is the Rabi frequency over the ensemble which will increase the beam splitter efficiency. Another possibility would be to increase the Rabi frequency which leads to a power broadened Rabi amplitude and enables the application of short pulses.

An approximation for an effective π-pulse can be made based on the comparison of the atomic distribution width and the width of the Rabi amplitude $c_{2\hbar k}(k)$ [184]. The latter decays to $P = 0.5$ for $(2\hbar k \cdot k_x/m)^2 \equiv \Omega_{eff}^2$, and we can define a FWHM of the distribution (range of k_x about the Bragg resonance point for which the probability of momentum transfer exceeds 1/2) as

$$\sigma_{c_{2\hbar k(k)}} = m\Omega_{eff}/2\hbar k, \tag{3.49}$$

which increases linear with the effective Rabi frequency Ω_{eff}. The Rabi cycling behavior of the whole wave packet now depends on the fraction of the power broadened $\sigma_{c_{2\hbar k(k)}}$ and the momentum width of the initial state σ_{k_x}. Efficient mirror pulses are expected for $\sigma_{c_{2\hbar k(k)}}/\sigma_{k_x} > 1$ [184], if we assume an idealized two system without losses. In real systems, however, scattering in other momentum states occurs which limits the diffraction efficiency in the target state. For a Gaussian wave packet with rms momentum width of $\sigma_{k_x} = 0.13$, the fraction can in our case be calculated to

$$\frac{\sigma_{c_{2\hbar k(k)}}}{\sigma_{k_x}} = \frac{m \cdot \Omega_{eff}}{2\hbar k \cdot 2\sqrt{2 \ln 2}\sigma_{k_x}} \approx 1, \tag{3.50}$$

which matches to our observed diffraction efficiency of 81% (see Fig. 3.8) considering moderate losses of a real system and rectangular shaped beam splitter pulses. This exemplary study shows the interplay between condensate width (approximated as a Gaussian distribution) and power broadening of the Bragg beams. As already pointed out, higher diffraction efficiencies were achieved with increased optical power and thus shorter pulse durations. Another possibility is given with the application of delta-kick cooling, which effectively reduces the velocity width of the matter wave source and therefore σ_{k_x} (see Sec. 4.3.2).

The diffraction efficiency is limited due to the spectral selectivity of the Bragg pulses. This is not only a disadvantage since it can be used to directly analyze the momentum distribution of a freely evolving condensate, which is presented in the next section.

3.4.3 Bragg spectroscopy of expanding Bose-Einstein condensates

We can analyze the momentum distribution of the Bose-Einstein condensate using Bragg spectroscopy [168]. Atoms are diffracted by interacting with Bragg beams whose mutual detuning δ determines the momentum component which is diffracted out of the

condensate (e.g. in resonance). A typical measurement performed for a condensate released from a steep trap ($I_{bias} = 0.7$ A, $\omega_x \approx 2\pi \cdot 150$ Hz) is shown in Fig. 3.11.

After $T_0 = 10$ ms of free expansion, we probe the condensate with a $\tau = 5$ ms lasting first-order Bragg pulse (rectangular shaped). The intensities are chosen to be in resonance for first-order processes only, moreover, they have been reduced in order ensure pulse areas of $\Phi \cdot \tau \ll \pi$. The beams are $\Delta \approx 640$ MHz red detuned below the cooling laser frequency. After a separation time of $T_{sep} = 17$ ms, we detect the diffracted and un-diffracted cloud of atoms in dependence of the frequency detuning δ between the Bragg beams.

Typical absorption images for the different detunings ($\delta = 6 - 17$ kHz) and corresponding column densities are given in Fig. 3.11. In contrast to the expected resonance for first-order Bragg diffraction of resting atoms at $\delta \approx 15$ kHz, the center is shifted by about $\Delta\delta \approx 3$ kHz. Large crossing angles ϑ between the Bragg beams potentially shift the resonance (see Sec. 3.1), but are prohibited due to the geometry of the vacuum chamber and the beam telescopes. The observed deviation is related to the fact, that the drop capsule itself (e.g., in-between of two drop campaigns) is not perfectly aligned w.r.t gravity while standing in the lab. This causes a non-zero velocity component v_x of the freely falling atoms along the wave vectors of the Bragg beams. In our case, the Doppler shift Δf_d of the Bragg laser light can be approximated to $\Delta f_d \approx v_x \cdot 1.258$ kHz/(mm/s) [150], leading to a fractional error of the effective detuning $\Delta\delta/\delta_0 \approx 3/15$ for velocities v_x on the order of 1.2 mm/s. For example, such velocities already occur at an expansion time of $T_0 = 10$ ms, if the angle between wave vector of the Bragg lattice and gravity exceeds only $\alpha_{\vec{k},\vec{g}} \approx 1°$.

The sensitivity is limited by the stability of δ during the pulse duration time $\tau = 5$ ms. As long as the Doppler-shift is constant, this would only absolutely shift the spectrum but has no influence on the width. Another systematic is given by the spatial dependence of the Rabi frequency due to the Gaussian beam profile, which we neglect since $\Phi \cdot \tau \ll \pi$.

Influence of the trap steepness

From each picture in Fig. 3.11, the Bragg diffraction efficiency can be calculated and displayed versus the difference to the center resonance $\Delta\delta$ to achieve a spectrum in momentum space. This has been done to evaluate the momentum width of condensates expanding from four differently steep holding traps (see open symbols in Fig. 6.3.1, left). The corresponding trapping frequencies in the beam splitter direction were $\omega_x \approx 2\pi \cdot (50, 100, 150, 350)$ Hz.

A Gaussian was fitted to the central peak of each spectrum (solid lines) to approximate the Bragg resonance rms width $\sigma_{\Delta\delta}$ of the evolving condensates[5]. The obtained rms width of the four data sets are then used to calculate the momentum width of the atomic distribution as

$$\sigma_{k_x} = \frac{m \cdot \sigma_{\Delta\delta}}{2k}, \tag{3.51}$$

[5]This was done by either fitting a double-Gaussian distribution to the spectrum or by manually subtracting the thermal background.

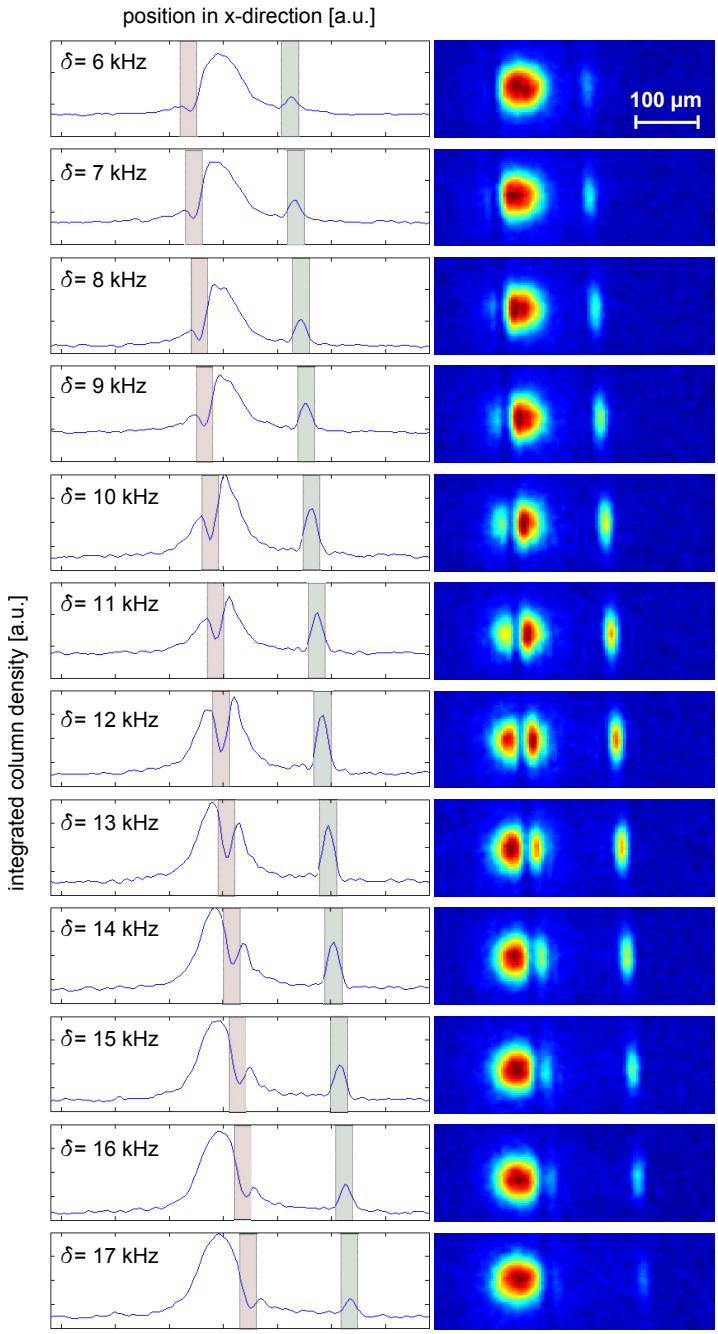

Figure 3.11: Bragg spectroscopy as a tool to measure the momentum distribution of a freely expanding Bose-Einstein condensate. In each picture from top to bottom, the pulse duration of the box-shaped Bragg pulses is kept constant at $\tau = 5\,\mathrm{ms}$ and the detuning is scanned from $\delta = 6\,\mathrm{kHz} - 17\,\mathrm{kHz}$. After application of the Bragg pulse, we let the distribution expand for 22 ms before taking the image. Diffracted atoms are indicated with the green box, the resulting hole in the initial distribution is marked red. More details in text.

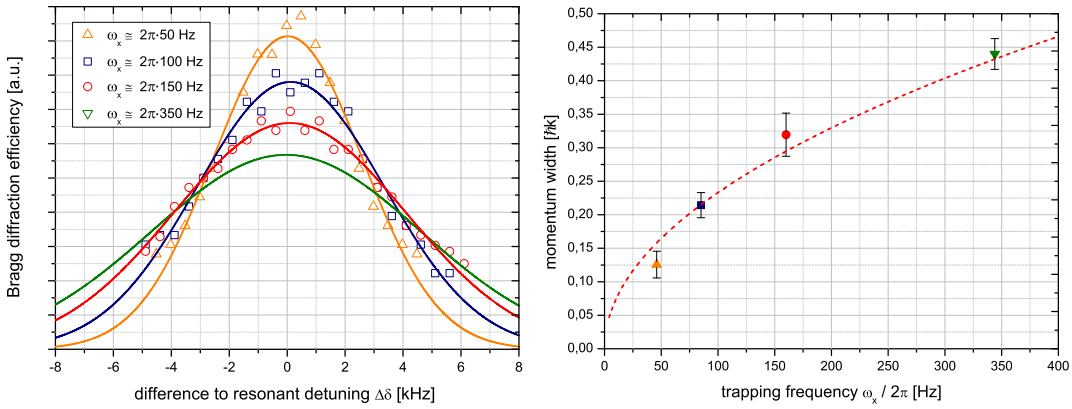

Figure 3.12: Bragg spectroscopy of Bose-Einstein condensates released from differently steep magnetic traps with $\omega_x \approx 2\pi \cdot (50, 100, 150, 350)$ Hz. The observed spectra in momentum space are fitted with a Gaussian function (left). The extracted rms width is plotted versus the trapping frequency and fitted with $A \cdot \sqrt{\omega_x}$ (right).

with mass of the atoms m and wave vector of the Bragg beams k. The resulting width in units of $\hbar k$ are separately displayed as a function of the trapping frequency of the holding trap (full symbols in Fig. 6.3.1, right). In a classical gas, the momentum width is proportional to the square root of temperature T of the expanding cloud (see Sec. 2.6.1). In a harmonic trap, the temperature dependents linearly on the trapping frequency, we thus expect the Bragg resonance to evolve as $\sigma_{k_x} \sim A \cdot \sqrt{\omega_x}$, of which a corresponding function is fitted to the data (solid red line).

Mean-field expansion from the shallow trap

Bragg spectroscopy can also be used to analyze the mean-field driven expansion of a condensate. Therefore, we prepared our BEC in the shallow trap ($\omega_x \approx 2\pi \cdot 50$ Hz) and probed the momentum distribution after different free expansion times (see Fig. 3.13). Here, pulse durations of 3 ms (blue squares) and 5 ms (red triangles) were applied.

Directly after release, the width of the Bragg resonance increases immediately due to mean-field acceleration and asymptotically reaches a finite value in the far-field, which is expected for entirely converted mean-field energy. The resonance width σ_k can be translated into a velocity width σ_v. The dashed red line is a theoretical prediction of the latter using the measured trapping frequencies of Sec. 2.6.2 in a scaling law approximation for cigarre-shaped condensates in the Thomas-Fermi regime [168, 130].

This data shows, that mean-field contributions are still present for expansion times of $T_{tof} \leq 10$ ms, which is expected for shallow traps (see Sec. 3.5.2). The non-linear expansion of matter wave packets will play an important role as a systematic error in interference experiments and therefore addressed in detail in Sec. 3.5.

Scattering in the Raman-Nath regime

Scattering in the Bragg regime occurs if the interaction time of the atoms with the optical lattice beam is long enough, to fulfill the criteria of a thick grating. The atomic

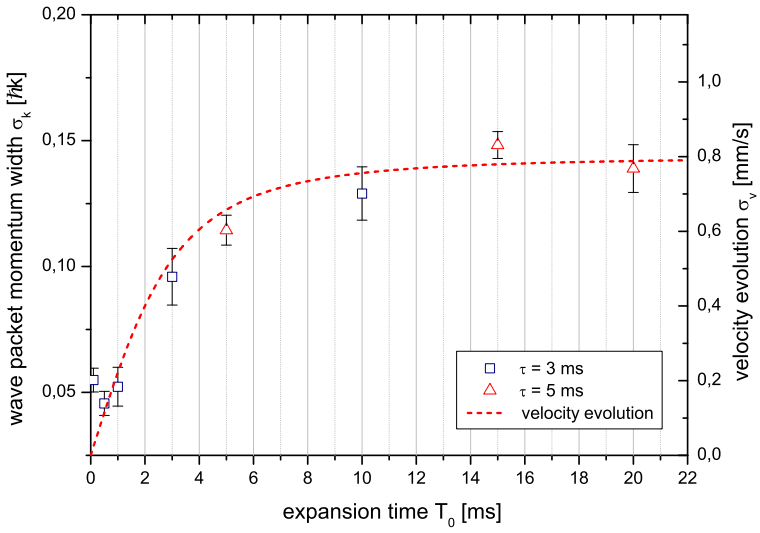

Figure 3.13: Mean-field acceleration of a Bose-Einstein condensates released from a shallow magnetic trap ($\omega_x \approx 2\pi \cdot 50$ Hz), depicted by the increase of the Bragg resonance width during free expansion of the sample. The dashed red line corresponds to the calculated velocity evolution $v_x \sim v_{inf}\omega_x t/\sqrt{(1+(\omega_x t))^2}$ [130, 168].

waves scatter from all layers of the diffraction plane and add constructively in a single order diffraction process, as previously used in first-order Bragg diffraction and Bragg spectroscopy experiments.

Very short pulse durations instead broaden the resonance and lead to scattering in neighboring momentum states, which is called Raman-Nath scattering [182, 172, 158]. Due to the comparably short interaction time, the optical lattice can be seen as a stationary wave, imprinting a sinusoidal phase distribution at the wave function due to the AC Stark shift, which develops into a Bessel-type distribution in the far field [161].

To find an approximation for the transition to the KD regime, we assume a cloud of atoms which is exposed to a standing wave ($\delta = 0$) and adapt the description of power broadening of the Rabi amplitude for multi-order scattering (see Eq. 3.4.2). If the Rabi amplitude is on the order of the effective detuning to the neighboring momentum states as

$$\Omega_{eff} \approx \frac{\hbar}{m}\left(4nk^2 - 2k\sigma_{k_x}\right), \tag{3.52}$$

multi-order scattering will occur [184]. For example, simultaneous diffraction of a Gaussian wave packet (released from the shallow trap) in ± 2 momentum states would for our parameters results in $\pi-$pulse durations of about

$$\tau_{\pm 2} = \frac{\pi}{\Omega_{eff}} \approx \frac{m \cdot \pi}{\hbar(8k^2 - 2k(0.13\hbar k))} \approx 8.6\ \mu\text{s}, \tag{3.53}$$

In Fig. 3.14 (left), the realization of multi-order Bragg scattering is shown. The condensate is adiabatically released from the shallow trap ($\omega_x \approx 2\pi \cdot 50$ Hz) and expands for $T_{tof} = 13$ ms. Then, a short pulse is applied with a duration of $\tau = 8$ μs and an in-

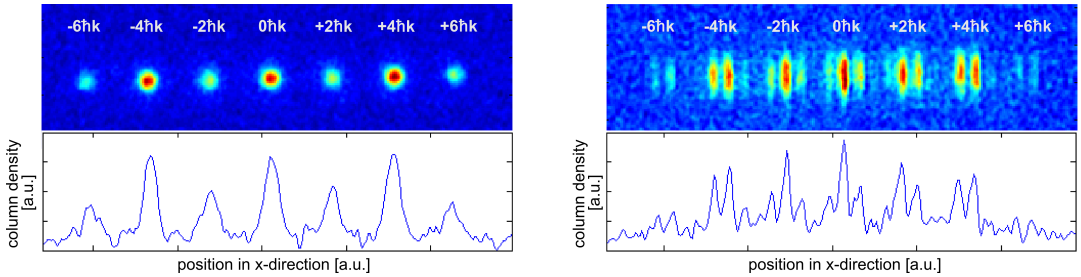

Figure 3.14: Diffraction in the Raman-Nath regime. The initial condensate ($0\,\hbar k$) is simultaneously scattered in $\pm$ 3 momentum states after application of a pulse with $\tau = 8\ \mu$s (left). The application of two successive multi-order beam splitters, separated by about 100 μs, leads to a multi-order interference pattern (right).

tensity of $I_{KD} \approx 10\ \mathrm{W/m^2}$. The sub-recoil momentum distribution of the condensate allows to distinguish between the different momentum states in the absorption images, where atoms are mainly scattered from $0\hbar k$ order into $\pm 4\hbar k$ with a less significant occupancy of $\pm 2\hbar k$ and $\pm 6\hbar k$.

If we after application of the first Raman-Nath beam splitter wait for an interrogation time of about 100 μs and subsequently apply a second beam splitter, we observe spatial interference patterns in each of the outputs associated with the diffraction order (see Fig. 3.14, right). The interference pattern can be clearly seen in the absorption image as well as in the integrated column densities[6]. We will discuss the reason for the formation of such interference patterns in the next section.

3.5 Interference experiments with Bose-Einstein condensates

Once released from the confining potential, Bose-Einstein condensates can be seen as a giant matter wave expanding in free space with a periodicity associated with the thermal de Broglie wavelength λ_{dB}. One of the striking manifestations of the condensate's wave nature is the observation of a spatial interference pattern in the overlapping region of initially separated clouds. The first interference experiment demonstrating the wave nature of a BEC was performed at MIT in 1997 [185]. The results clearly indicated the self-interference of one BEC as well as the interference of two separately generated BECs described by two distinct wave functions.

In the first case, degeneracy was reached by evaporatively cooling sodium atoms in a magnetic trap. After passing the phase transition, the ultra-cold cloud has been coherently split with the repulsive force of a blue-detuned light sheet - a single wave function with two density peaks. The second case corresponds to a double-well configuration where two independent clouds of atoms where first trapped in separate sites, and then simultaneously cooled down to quantum degeneracy - two individual condensate wave functions with a random phase distribution. In both cases, switching off the trap caused the wave packets to expand and interfere during time-of-flight such that

[6] Here, the BEC was released from the steep trapping potential ($\omega_x \approx 2\pi \cdot 130$ Hz) for a better visibility of the fringe pattern

spatial interference fringes have been observed in the overlapping region.

These pioneering results demonstrated the first-order coherence of a condensate wave function and opened the way to a manifold of new experiments exploring the wave nature of degenerate quantum gases. As one of the most fundamental properties, the global phase coherence of condensates attracted great attention for applications in enhanced atom interferometry. However, BECs suffer from mean-field interactions which causes the phase distribution to evolve non-linear. The latter of which can be modeled with scaling factors (λ-matrix formalism [130]) for time-dependent trap configurations in the Thomas-Fermi limit.

In the next sections, we will address this important aspect in operating different open interferometer concepts based on Bragg diffraction [160, 164]. To this end, the implication of mean-field driven acceleration on the formation of the fringe pattern in light-pulse atom interferometers will be investigated [186].

3.5.1 Open Ramsey-type interferometer (ORI)

Different approaches such as the mentioned double-well potential or spatial splitting due to repulsive optical dipole forces have been studied to coherently prepare wave packets with an initial separation for subsequent interference experiments.

Another common method has been realized in the QUANTUS-I experiment and is based on two successive Bragg pulses. In a simplified scheme (see Fig. 3.15), the condensate is adiabatically released from an atom-chip-based trap and evolves freely for an expansion time T_0. Then, a first beam splitter ($\pi/2$) is applied to coherently prepare a superposition of two momentum states which separate with twice the recoil velocity ($2v_r = 2\hbar k/m \approx 11.8\,\mathrm{mm/s}$ [150]). After an interrogation time T_{int}, the different momentum classes of the wave function have a spatial displacement of $\delta x = 2v_r \cdot T_{int}$. Now, a second $\pi/2$ pulse again recombines the two different momentum classes. During an additional separation time T_{sep}, the output ports spatially separate until an absorption image is taken after a total time-of-flight of $T_{tof} = T_0 + T_{int} + T_{sep}$. Such a beam splitter sequence generates two output ports with two partially overlapping condensates each (red and blue clouds).

Complementary fringe patterns will appear in the two output ports, which can be Fourier analyzed to extract contrast and fringe spacing [187, 188]. In this way, global phase fluctuations in each experimental cycle can be filtered out, which would result in a shifted fringe pattern perpendicular to the direction of the interferometer beams.

Bose-Einstein condensates are an excellent matter wave source for this type of experiment because they have been demonstrated to be phase-coherent over the whole cloud size for modest aspect ratios [186, 179]. The interference pattern of overlapping condensates is expected to be spatially uniform and equidistant. This is a direct result of the quadratic phase profile of freely expanding clouds of atoms which we want to discuss in the next section.

Phase evolution of a Bose-Einstein condensate

The scaling approach for time-dependent potentials allows to calculate the temporal evolution of freely expanding condensates [130]. For harmonic potentials with trapping

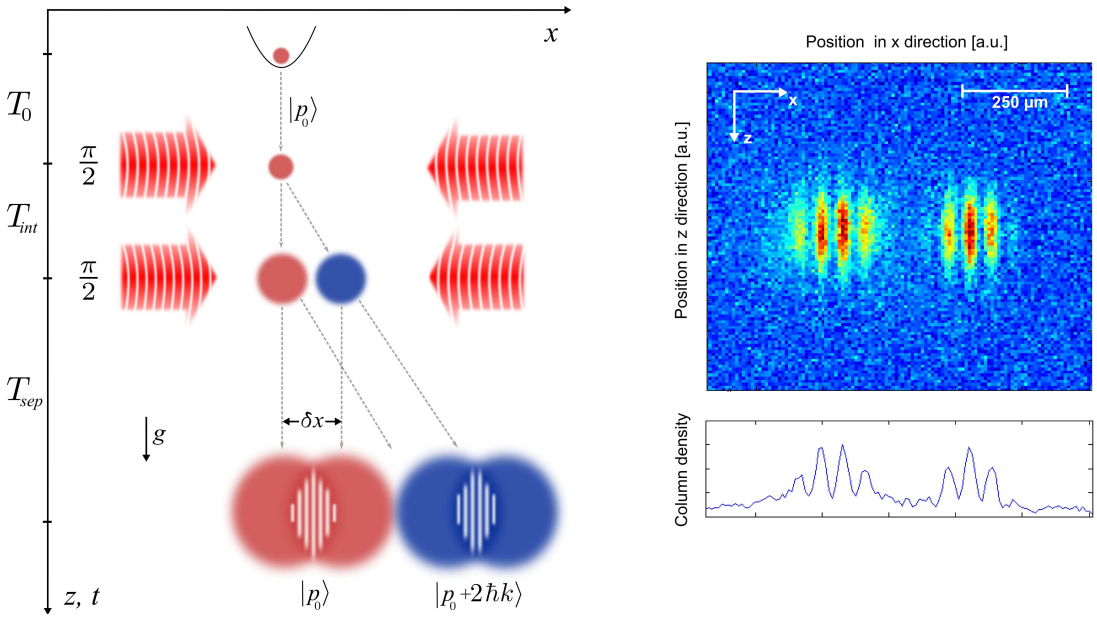

Figure 3.15: Schematic of an open Ramsey-type interferometer (ORI) with Bose-Einstein condensates (left). After a free expansion time T_0, a first $\pi/2$ pulse coherently splits the wave function into two momentum classes. An interrogation time T_{int} later, where the density peaks feature a spatial displacement of δx, a second $\pi/2$ pulse again recombines the two momentum classes. The output ports separate with twice the recoil velocity during T_{sep}, until they are detected by means of absorption imaging (right). A spatial interference pattern emerges in the overlapping zone of the expanding wave packets. More details in text.

frequencies ω_i in the Thomas-Fermi regime, the scaling factors λ_i are determined by a system of coupled differential equations (see Sec. 2.2.3)

$$\ddot{\lambda}_i = \frac{\omega_i^2(0)}{\lambda_i \prod_j \lambda_j} - \omega_i^2(t)\lambda_i. \tag{3.54}$$

Based on this approximation, a common expression for the velocity field dependent on λ_i can be derived [130]

$$v_i(\vec{r}, t) = r_i \frac{\dot{\lambda}_i(t)}{\lambda_i(t)}. \tag{3.55}$$

The velocity can also be given in terms of the derivative of the wave function's phase distribution [116], leading to

$$v_i(\vec{r}, t) = \frac{\hbar}{m} \frac{\partial}{\partial_i} \phi(\vec{r}, t). \tag{3.56}$$

In Thomas-Fermi (TF) approximation, Bose-Einstein condensates show a quadratic density profile. The phase evolves proportionally to the density in free space, so we can assume a quadratic phase profile of a generic wave function $\psi \sim e^{i\phi}$ (simplified to

a 1D treatment[7]), with

$$\phi(x) = \frac{\alpha}{2}x^2 + \beta x, \tag{3.57}$$

where $\alpha = \nabla^2\phi$, and β corresponds to the center-of-mass (COM) motion of the condensates causing an additional linear phase evolution. With Eq. 3.55 and 3.56 we can now derive an expression for α in terms of the scaling parameters

$$\frac{\hbar}{m}\alpha(t) = \frac{\hbar}{m}\frac{\partial^2\phi}{\partial x^2} = \frac{\partial v_x}{\partial x} = \frac{\dot{\lambda}_x(t)}{\lambda_x(t)}. \tag{3.58}$$

Spatially interfering matter waves

The interference pattern emerges in the overlapping zone of expanding wave packets with initial spatial separation δx. After the second beam splitter (see Fig. 3.15), the two wave packets can generally be described as $\psi_1(x) = \sqrt{n_1(x)}\cdot\exp(i\phi_1(x))$ and $\psi_2 = \sqrt{n_2(x+\delta x)}\cdot\exp(i\phi_2(x+\delta x))$.

By assuming that interactions between the atoms in the different condensates are negligible, therefore not affecting the dynamics during expansion and spatial overlap, the one dimensional interference pattern in the overlapping region can be derived by calculating the local density

$$\begin{aligned} n(x) &= |\psi_1(x) + \psi_2(x+\delta x)|^2\,, \\ n(x) &= |\psi_1(x)|^2 + |\psi_2(x+\delta x)|^2 + 2\,\mathrm{Re}\left[\psi_1^*(x)\psi_2(x+\delta x)\right]. \end{aligned} \tag{3.59}$$

The interference pattern is a consequence of the last term, caused by the spatially dependent phase evolution of the two expanding ensembles. The particle density at any point is thus given by the densities of the single wavepackets and the interference term.

Let us isolate the interference term of the density ($n_i(x)$) and evaluate it with the already derived phase distribution of a condensate (see Eq. 3.57). For the general situation of two wave packets with a non-zero relative velocity, the two phase profiles have an opposite sign in the linear term ($\phi_{1,2} = \alpha/2x^2 \pm \beta x$). This results in

$$\begin{aligned} n_i(x) &= 2\sqrt{n_1(x)n_2(x+\delta x)}\,\mathrm{Re}\left[\exp[i(-\phi_1(x)+\phi_2(x+\delta x)]\right], \\ n_i(x) &= 2\sqrt{n_1(x)n_2(x+\delta x)}\cos\left[\alpha/2(x+\delta x)^2 + \beta(x+\delta x) - (\alpha/2x^2 - \beta x)\right], \\ n_i(x) &= 2\sqrt{n_1(x)n_2(x+\delta x)}\cos\left[\kappa\cdot x + \phi_0\right]. \end{aligned} \tag{3.60}$$

The argument of the cosine-function consists of a constant phase shift $\phi_0 = \alpha/2(\delta x)^2 + \beta\delta x$ and a spatial fringe frequency $\kappa = \alpha\delta x + 2\beta$, which is proportional to the separation δx. By considering a fully phase coherent condensate, the interference pattern

[7] Analogously for other dimensions. In principle, we reduce the BECs displacement to a scalar δx.

shows up as straight fringes, uniformly spaced:

$$d(x) = \frac{2\pi}{\kappa}. \tag{3.61}$$

Lines of constant phase are perpendicular to the separation vector $\delta\vec{x}$ between the COM of both wave packets. The separation here is induced by two temporally separated beam splitters in a so-called open Ramsey-type interferometer (ORI). This nomenclature is reasonable since there are obvious analogies to a standard Ramsey interferometer (or to Ramsey spectroscopy) which will be illustrated shortly before we continue with the calculation of the fringe pattern based on the scaling law formalism.

Analogy to Ramsey's method of separated oscillatory fields

In a simplified picture of Ramsey's method of separated oscillatory fields [98], a thermal beam or a cloud of cold atoms crosses two separated interaction zones where phase-locked microwaves are applied to the atoms. In the first zone, a coherent superposition of two internal states is generated with a $\pi/2$ pulse, whose relative phase is oscillating at the eigenfrequency ω_0 of the transition. After an interrogation time T_{int}, the projection of the atoms quantum state at the second interaction zone now depends on the accumulated phase difference between the atomic superposition state and the microwave phase as $\Delta\omega = (\omega_0 - \omega_\mu) \cdot T$.

This experiment can be seen as a T-lasting phase comparison measurement between the local microwave oscillator and the induced quantum beat. By carefully scanning the frequency ω_μ around the atomic transition ω_0, a periodic resonance curve is obtained which can be approximated as

$$I(\omega) \propto \cos\left(\Delta\omega \cdot T_{int}\right) = \cos\left(\left(\omega_\mu - \omega_0\right) \cdot T_{int}\right), \tag{3.62}$$

and whose central peak is usually used in atomic clocks for stabilization of an local oscillator to an atomic transition. The longer the interrogation time, the narrower the resonance width. Generally, ultra-cold clouds of atoms are promising for this application, since they allow for comparably high SNR after longer interrogation times due to smaller momentum widths.

However, in an open Ramsey-type interferometer with Bragg diffraction, a coherent superposition of momentum states is generated and the relative phase is oscillating at the energy difference of the coupled states. In an ORI with expanding condensates, this is a function of distance since the energy difference at each position x (see Eq. 3.34) is determined by

$$\hbar\delta(x) = \frac{(2\hbar k + p_0(x))^2}{2m} - \frac{p_0(x)^2}{2m} = 4\left(\omega_r - \frac{p_r p_0(x)}{2m\hbar}\right). \tag{3.63}$$

Let the the frequency difference of the applied Bragg lattice be resonant to resting atoms ($\delta_0 = 4\omega_r$). The resonance curve in this case can be written as

$$I(\delta) \propto \cos\left(\left(\delta(x) - \delta_0\right) \cdot T_{int}\right) = \cos\left(\frac{2p_r p_0(x) \cdot T_{int}}{m\hbar}\right). \tag{3.64}$$

The momentum distribution $p_0(x)$ is dependent on the phase profile $\phi(x)$ of a condensate (Eq. 3.56 and 3.57) and can be approximated as

$$p_0(x) = \hbar \frac{\partial}{\partial x} \phi(x) = \hbar \alpha x + \beta \tag{3.65}$$

Assuming no relative velocities between the interfering wave packets ($\beta = 0$), our measurement signal as being an absorption image proportional to the atomic density, can be expressed as

$$I(\delta) = n_i(x) \propto \cos\left(\alpha \frac{2p_r}{m} \cdot T_{int} \cdot x\right) \equiv \cos\left(\gamma \cdot x\right). \tag{3.66}$$

By a comparison of Eq. 3.66 and 3.60, we see that $\gamma = \kappa$ which justifies our nomenclature of the applied ($\pi/2$ - $\pi/2$) beam splitter sequence as an open Ramsey-type interferometer (ORI). We now come back to the calculation of the fringe spacing for interfering condensates based on the λ-matrices formalism

3.5.2 Evolution of the fringe spacing

By neglecting the linear contribution of the phase evolution as $\beta = 0$ (i.e. no relative velocity between the wave packets) in Eq. 3.60, the periodicity of the fringe spacing (distance between two local maxima/minima) is given by

$$d(t) = \frac{2\pi}{\alpha \delta x} = \frac{\lambda_x(t)}{\dot{\lambda_x}(t)} \cdot \frac{h}{m \delta x}. \tag{3.67}$$

Hence, we can predict the temporal evolution of the fringe pattern for a given separation δx by calculating $\lambda/\dot{\lambda}$. In QUANTUS-I, the confining potentials of the chip-based Ioffe-Pritchard trap in ground-based experiments can be approximated as cigar-shaped ($\omega_x = \omega_z \equiv \omega_{rad} \gg \omega_y$). For a sudden opening of the trap at $t = 0$, the solution for the scaling factors is [130]

$$\lambda_{rad}(\tau) = \sqrt{1 + \tau^2}, \tag{3.68}$$

$$\lambda_y(\tau) = \left(1 + \epsilon \left(\tau \arctan \tau - \ln \sqrt{1 + \tau^2}\right)\right), \tag{3.69}$$

with the dimensionless variable $\tau = \omega_{rad} \cdot t$ and the fraction of radial and axial trapping frequency $\epsilon = \omega_y/\omega_{rad}$.

The Bragg beams are aligned along the x-direction and the interference pattern will emerge with lines of constant phase along the y-direction (see Fig. 3.5). The dynamics of the fringe spacing can thus be discussed by evaluating the temporal evolution of the fraction $\dot{\lambda}_{rad}/\lambda_{rad}$ (see Fig. 3.16). Here, the scaling factors are calculated for three different initial radial trapping frequencies of $2\pi \cdot (50, 100, 150)$ Hz.

The temporal evolution of the radial Thomas-Fermi radii of expanding BECs is proportional to λ_{rad} (see Sec. 5.2.1), which for long timescales increases linearly in time and trapping frequency ($\lambda_{rad} \sim \omega \cdot t$). Here, most of the mean-field energy is converted into kinetic energy which causes the expansion velocity to asymptotically reach a constant value ($\dot{\lambda}_{rad} \sim \omega$). The stepper the trap, the faster the condensate expands due

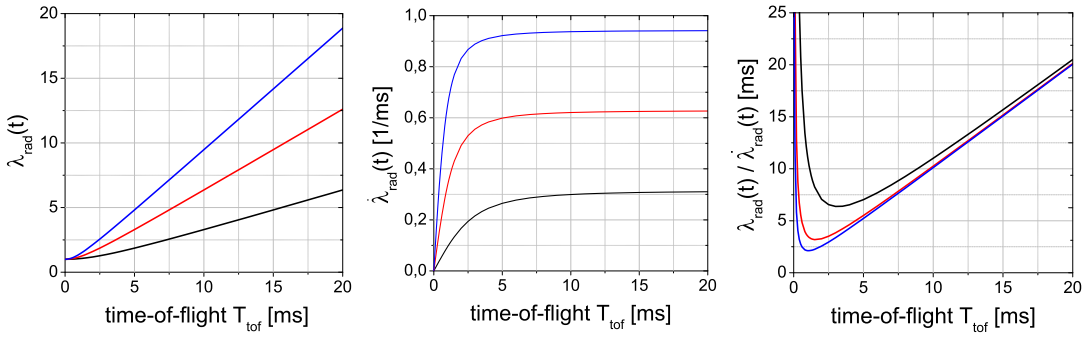

Figure 3.16: Calculation of the temporal evolution of the radial scaling factor $\lambda_{rad}(t)$ (left), the first derivative $\dot{\lambda}_{rad}(t)$ (center) and the fraction of $\lambda_{rad}(t)/\dot{\lambda}(t)$ (right) for trapping frequencies of $2\pi \cdot 50$ Hz (black lines), $2\pi \cdot 100$ Hz (red lines) and $2\pi \cdot 150$ Hz (blue lines).

to density-dependent mean-field conversion. For comparison, the steepest trap shown here ($\omega_{rad} = 2\pi \cdot 150$ Hz), converts 95% of the mean-field within an expansion time of $T_{150\,Hz,mean} \approx 3.25$ ms, whereas the corresponding conversion time for the shallow trap ($\omega_{rad} = 2\pi \cdot 50$ Hz) is significantly larger with $T_{50\,Hz,mean} \approx 9.5$ ms. We will review the influence of mean-field accelerated expansion on the emergence of a fringe pattern in upcoming interferometry experiments. The fraction of $\dot{\lambda}_{rad}/\lambda$ determines the temporal evolution of the fringe spacing and seems to converge towards a fixed slope for large timescales.

In the far-field ($t \gg T_{mean}$), the fraction $\lambda/\dot{\lambda}$ can be approximated as

$$\frac{\lambda_{rad}(t)}{\dot{\lambda}_{rad}(t)} = \frac{\sqrt{1+\omega_{rad}^2 \cdot t^2} \cdot \sqrt{1+\omega_{rad}^2 t^2}}{\omega_{rad}^2 t} \approx t. \tag{3.70}$$

This result combined with Eq. 3.67 and $t \equiv T_{tof}$ yields the far-field approximation of the fringe spacing

$$d(T_{tof}, \delta x) = \frac{h \cdot T_{tof}}{m \cdot \delta x}, \tag{3.71}$$

which increases linearly with expansion time T_{tof}. In Fig. 3.16 (right), this would correspond to a straight line emerging from the origin with a slope of 1, which differs from the the scaling law approach due to the disregard of density dependent mean-field conversion and finite size of the condensate.

To analyze the temporal evolution of interference pattern in experiment, we first have to image it and evaluate the important properties with a suitable fit function.

Detection of the fringe pattern

As described earlier (see Sec. 2.4.5), we can calculate the optical density D of a camera image to

$$D \equiv \left[\frac{I_{beam} - I_{dark}}{I_{at} - I_{dark}} \right]. \tag{3.72}$$

In QUANTUS-I, the atomic clouds are detected destructively and spatial information is obtained by fitting different distributions to the obtained column densities. With the resonant cross section σ, the atomic column density follow as $n = D/\sigma$. For analyzing the spatial interference pattern, we integrate the density along the dimension perpendicular to the interferometer beams (z-direction) and evaluate the 1D density profile (x-direction) by fitting the following distribution to the column densities

$$n^{1D} = n^{1D}_{max} \sum_{n=1}^{2} \left[1 + C \sin\left(\frac{2\pi}{d}(x - x_n) + \phi_n \right) \cdot \exp\left(-\frac{(x - x_n)^2}{2\sigma^2} \right) \right] + n^{1D}_0. \quad (3.73)$$

With constant background n^{1D}_0 and amplitude n^{1D}_{max}, this function describes the center of the output ports at positions x_1 and x_2 with a Gaussian density profile. To consider interference, it is multiplied by a periodic function with fringe spacing d and phases ϕ_1 and ϕ_2. Most important for interferometry studies of the condensates phase coherence and related systematics are fringe spacing d and the contrast C.

In Fig. 3.15 (right), a typical absorption image and the integrated 1D column density are given for ORI performed on ground. The positions x_1 and x_2 correspond to the output ports with momentum classes $p_1 = 0\hbar k$ and $p_2 = 2\hbar k$ at the time of detection.

In a first set of experiments, we start by analyzing the fringe pattern and discussing the temporal evolution by scanning either T_{tof} or the separation distance δx of the interfering matter waves in an ORI.

Linear scaling of the fringe pattern with time-of-flight

In Fig. 3.17, the linear scaling of a fringe pattern with increasing T_{tof} is shown. There, the condensate is released from a steep potential with $\omega_{rad} \approx 2\pi \cdot 350$ Hz, to be able to observe several fringes within the overlapping region and to minimize mean-field effects. After switching-off the trapping potential, it evolves freely for a total expansion time of $T_0 = 10$ ms until the first beam splitter $(\pi/2)$ is applied with durations of typically $\tau \approx 100$ μs. During an interrogation time of $T_{int} = 240$ μs, the two coupled parts of the wave function separate to a maximum distance of only $\delta x = 2v_r \cdot T_{int} \approx 2.6$ μm. The second beam splitter $(\pi/2)$ thus recombines still overlapping clouds and generates two complementary output ports. As already mentioned, we use rectangular-shaped pulses in the time-domain and the interrogation time T_{int} is approximated by the distance between the temporal centers of each pulse.

In the case of a Ramsey-type interferometer with first-order Bragg pulses, the fringe spacing d_{ori} in the far field can be re-written as

$$d_{ori} = \frac{hT_{tof}}{m\delta x} = \frac{\pi \cdot T_{tof}}{k \cdot T_{int}}, \quad (3.74)$$

with wave vector $k = 2\pi/\lambda$ of the Bragg beams. An absorption image is taken after an additional separation time T_{sep} which was scanned to realize different total time-of-flight between release of the matter waves and detection of $T_{tof} = T_0 + T_{int} + T_{sep}$.

Error bars in Fig. 3.17 depict 1σ confidence bounds of the fitted parameters. Since the interrogation time T_{int} is kept constant, the fringe spacing (blue circles) evolves

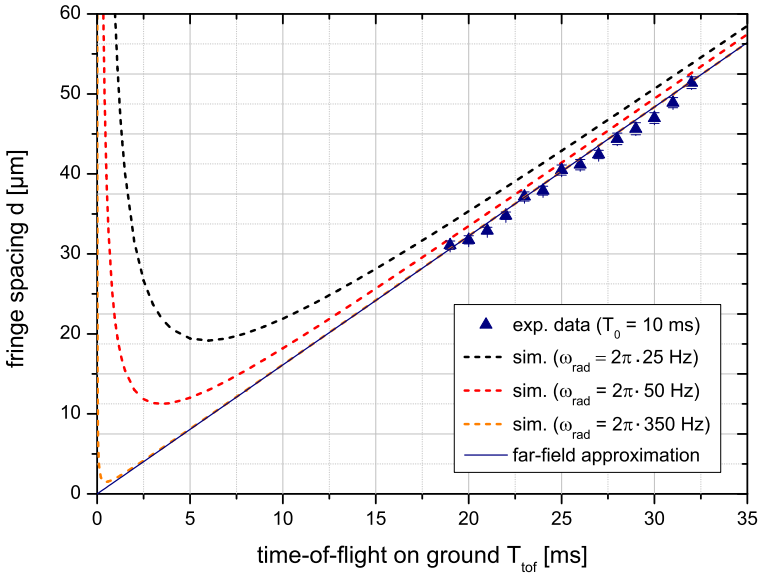

Figure 3.17: Temporal fringe spacing evolution of a ground-based ORI with constant interrogation time $T_{int} = 240$ μs. The interferometer is applied $T_0 = 10$ ms after release of the condensate from a steep trap ($\omega_{rad} \approx 2\pi \cdot 350$ Hz). Scaling law calculations for the fringe spacing of differently steep radial-symmetric traps (dashed lines) and the far-field approximation (solid line) are given for comparison.

linearly in time which fits well to the scaling law calculation using the corresponding trapping frequency (dashed orange line). The far-field approximation coincides with the numerical calculation after a few ms (solid blue line), which confirms our measurement to be operated in the linear regime. A gallery of absorption images of this measurement is shown as a temporal sequence in Fig. 3.20 (left).

For comparison, the scaling law calculations of $d(t)$ for more shallow initial traps are given (dashed red and black lines). These correspond the the most shallow trap operable in ground-based measurements ($\omega_{rad} \approx 2\pi \cdot 50$ Hz) and the holding trap used in microgravity experiments ($\omega_{rad} \approx 2\pi \cdot 25$ Hz, see Sec. 5.2.2). As expected, the presence of mean-field acceleration would shift $d(t)$ to larger values.

Scanning the wave packet separation

Another method to analyze the fringe spacing evolution and to verify the validity of Eq. 3.74 has been demonstrated by scanning the interrogation time T_{int} for a fixed time-of-flight T_{tof}. This changed the separation of the interfering wave packets δx. In Fig. 3.18, two experimental data sets of condensates released from a steep trap ($\omega_{rad} \approx 2\pi \cdot 350$ Hz) are shown for which the initial expansion time T_0 is different. Red circles show the fringe spacing for an ORI immediately applied after release of the condensate ($T_0 = 0$ ms), whereas blue circles correspond to a sequence applied during the linear expansion phase ($T_0 = 10$ ms).

The total time-of-flight T_{tof} between both data sets is slightly different, which is why two dashed lines (red and blue) are calculated for the expected fringe spacing in

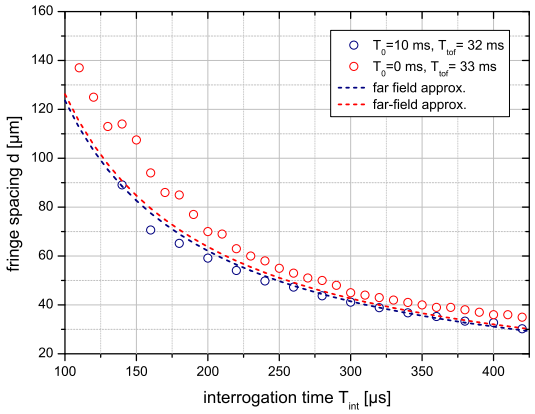

Figure 3.18: Fringe spacing for increasing interrogation time T_{int} ($\widehat{=}$ wave packet separation) in an ORI.

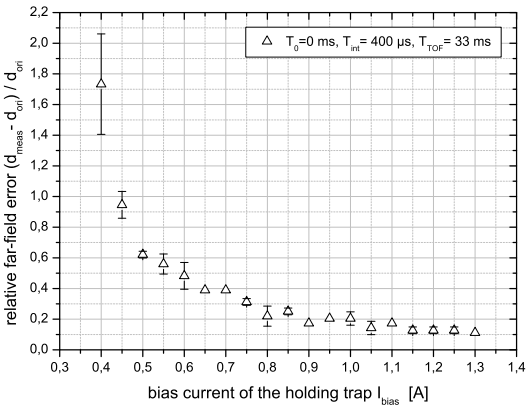

Figure 3.19: Influence of the trap steepness on the relative far-field approximation error in an ORI.

far-field approximation. Error bars are on the same order as compared to Fig. 3.17, but not given here for better visibility. A gallery of absorption images for the measurement with $T_0 = 10$ ms is shown as a temporal sequence in Fig. 3.20 (right).

The fringe spacing is expected to decrease as $1/\delta x \sim 1/T_{int}$, which could be verified for $T_0 = 10$ ms. Large discrepancies between experiment and far-field approximation occur for the data with $T_0 = 0$ ms. During the first 400 μs after release, 73% of mean-field energy is converted into kinetic energy, given the dynamics of $\dot{\lambda}_{rad}$ for the used trapping potential. The acceleration of the condensate during the ORI is therefore strongly mean-field driven. If now a beam splitter is applied, the wave function is split into a coherent superposition of two momentum states with bisected density. The wave packets expansion rate $\dot{\lambda}$ will therefore reach its asymptotic value earlier and changes the slope of $\alpha \sim \dot{\lambda}/\lambda$. The observed discrepancy may thus be a consequence of slowing down the mean-field conversion process.

Based on this assumption, the relative error w.r.t the far-field approximation should decrease for even steeper trapping potentials which lead to a faster mean-field conversion.

Influence of the trap steepness

If we prepare the condensate in more steeper traps, they expand much faster leading to almost entirely converted mean-field energy even at timescales of a few hundreds of μs. An ORI with a fixed interrogation time of $T_{int} = 400$ μs is applied to condensates directly after release. After $T_{tof} = 33.1$ ms, the fringe pattern is detected and the spacing evaluated for different I_{bias}, which determines the steepness of the holding trap (the trapping frequency roughly scales as $\omega_{rad} \sim I_{bias}^{3/2}$, see Sec. 2.4.2).

The relative error between the measured fringe spacings and the far-field approximation

$$\frac{d_{meas} - d_{ori}}{d_{ori}} \tag{3.75}$$

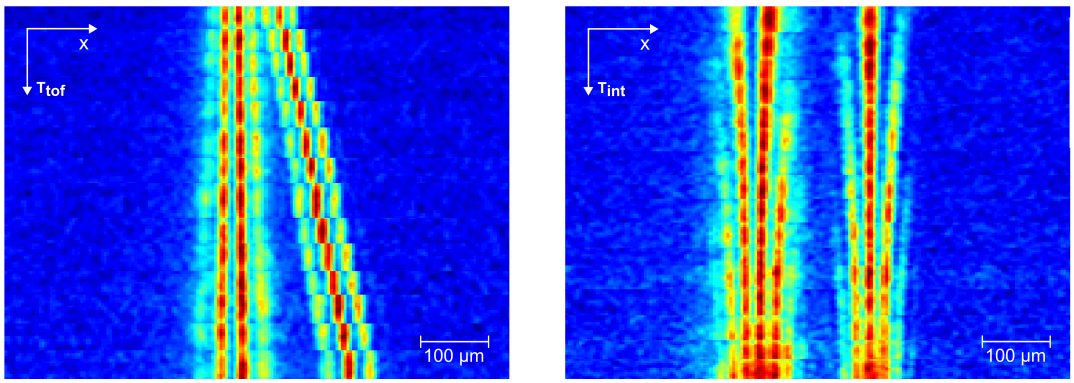

Figure 3.20: Temporal sequences of absorption images for an ORI with Bose-Einstein condensates. Every picture corresponds to a single measurement from the data sets evaluated in Fig. 3.17 and 3.18, respectively. For a fixed interrogation time ($\widehat{=}$ distance δx between the interfering wave packets), the fringe spacing increases linear with the time-of-flight T_{tof} (left). If the T_{tof} is constant and the interrogation time T_{int} is increased (right), the fringe spacing decreases as $1/T_{int}$. In these pictures, the condensate widths exceed the applied separation δx by about a factor of ~ 25, thus leading to a fringe pattern over the whole envelope. More details in text.

is given in Fig. 3.19. The error bars correspond to the standard deviation of two independent measurement cycles. At the beginning, the dominating mean-field acceleration of dense ensembles emerging from shallow traps (lower values of I_{bias}) yields comparably high discrepancy of the measured fringe spacing d_{exp} w.r.t. to the far-field approximation. For steeper traps ($I_{bias} \to 1.3$ A), most of the mean-field is converted and the measured fringe spacing slowly converges to the corresponding values given by the far-field approximation.

Until now, we implemented an ORI with an atom-chip-based BEC and investigated the fringe spacing evolution under influence of mean-field driven acceleration. With the same setup, a coherence length measurement of the condensate will be presented next.

3.5.3 Autocorrelation measurement to study phase coherence

Contrast measurements of the fringe pattern for different separations δx allow the study of the decay of the first order spatial correlation function $C^1(\delta x)$ [169]

$$C^1(\delta x) = \int d^3\vec{r}\psi_0^*(\vec{r}\cdot\vec{e}_x)\psi_0(\vec{r}+\delta x\cdot\vec{e}_x). \tag{3.76}$$

The decay of the density correlation is particularly interesting for determining the coherence length L_c of a degenerate sample and the ratio of this value compared to the spatial extension (e.g., Thomas-Fermi radius). In other words, this value determines how well the wave function of an initially trapped BEC represents a minimum uncertainty state w.r.t Heisenberg's position-momentum relation [168].

Moreover, phase fluctuations due to thermal excitations, background collisions and

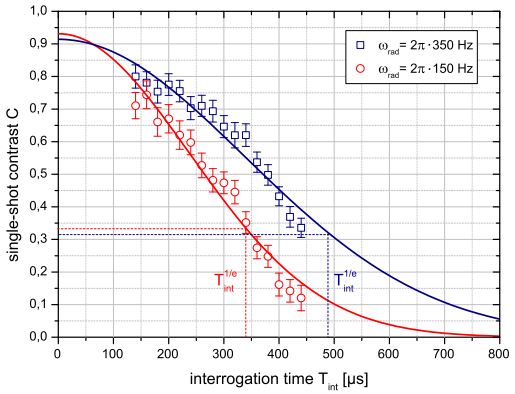

Figure 3.21: Single-shot contrast of an ORI as a function of the interrogation time T_{int}, fitted by a Gaussian (straight lines).

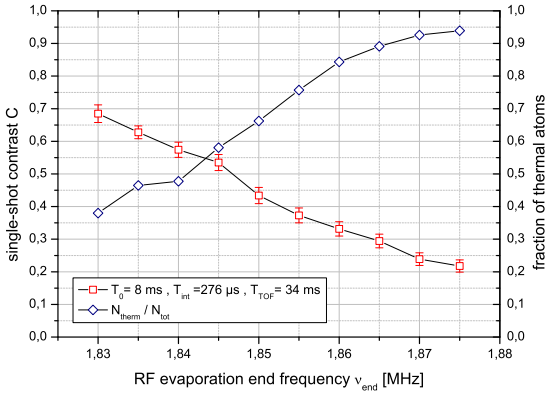

Figure 3.22: Single-shot contrast of an ORI for different condensate fractions by scanning of the evaporation end frequency ν_{end}.

other decoherence processes can be analyzed in this setup. These influences need to be thoroughly investigated since they fundamentally limit the phase coherence of a matter wave source.

The evolution of the contrast is obtained by fitting the fringe patterns of interfering BECs after an ORI sequence with $T_0 = 10$ ms for different interrogation times T_{int}. In Fig. 3.21, we compare the decay of the single-shot contrast for condensates released from two differently steep trapping potentials with $\omega_{rad,1} \approx 2\pi \cdot 150$ Hz (red circles) and $\omega_{rad,2} \approx 2\pi \cdot 350$ Hz (blue squares). The depicted results (incl. standard deviation) correspond to one measurement cycle each, where both output ports have been analyzed independently.

The correlation function is expected to decay as a Gaussian [169], which is fitted to both data sets (solid lines). In order to extract quantitative information, a coherence length L_C can be defined as the $1/e$-width $T_{int}^{1/e}$ of the measured correlation curve

$$L_c = 2v_r \cdot T_{int}^{1/e}, \tag{3.77}$$

resulting in $L_{c,1} = 4.0(2)$ μm and $L_{c,2} = 5.6(2)$ μm for the shown contrast evolution, respectively.

These values can now be compared with the size of the condensate at the time of the interferometer. For a fully phase-coherent condensate, the decay of the first order correlation function directly reflects the width of the density profile [163]. However, our current RF evaporation strategy typically leads to condensate fractions of only about 60%, which already signalizes a limited phase coherence due to the presence of thermal atoms in this case.

The Thomas-Fermi radius at the time of the interferometer can be approximated by calculating the size of the condensate in the trap multiplied by the solution of the scaling law for the radial component

$$R^{tf}(t) = R_0^{tf} \cdot \sqrt{1 + \omega_{rad}^2 \cdot t^2}, \tag{3.78}$$

with initial size of the condensate in the trap (see Sec. 2.2.3)

$$R_0^{tf} = \left(\frac{15N\hbar^2 a}{m^2 {\omega_{rad}}^2} \right)^{1/5}. \tag{3.79}$$

For $N = 10^4$, $a = 100\, a_b \approx 5.3 \cdot 10^{-9}$ m and the given trapping parameters, the TF radius of the BEC after expansion of $T_0 = 10$ ms can be calculated to $R_{TF}^1 \approx 32\ \mu$m and $R_{TF}^2 \approx 51\ \mu$m, for $\omega_{x,1} = 2\pi \cdot 150$ Hz and $\omega_{x,2} = 2\pi \cdot 350$ Hz. With that, the fractions of L_C/R_{tf} are given by 0.13 and 0.11, respectively.

This measurement indicates that phase coherence of our matter wave source is limited independent of the steepness of the trap. Previous calculations and interference pattern analysis have shown that this measurement is operated in the linear regime. Besides wavefront distortions, which should be negligible due to the timescales of T_{int}, one major limitation arises from the thermal background. The presence of thermal atoms may wash out the contrast and thus lead to a faster decay rate. This correlation will now be shortly presented in a direct measurement.

Limitations in contrast due to thermal background

The influence of the thermal background on the measured contrast is exemplary depicted in Fig. 3.22. In this graph, the obtained single-shot contrast (red squares) for an ORI ($T_0 = 8$ ms, $T_{int} = 260\ \mu$s, $T_{tof} = 34$ ms) is plotted versus the end frequency of the final evaporation ramp ν_{end}. The latter determines the fraction of thermal to total atoms N_{therm}/N_{tot} of the released ensemble (see also Sec. 2.5.3), which is additionally given as blue squares in the plot. Lines are added to guide the eye and we see that larger fractions of thermal atoms in the cloud lead to a reduced contrast. This is mainly a result of the incoherent background washing out the contrast even for the longest possible time-of-flight in ground based measurements (~ 34 ms). As already pointed out, our currently best evaporation strategy still leads to about 40% of thermal atoms in the investigated clouds.

This contrast limitations will again be addressed in dedicated drop experiments. The absence of a thermal background after sufficiently long time-of-flights (e.g., $T_{tof} \geq 100$ ms) will essentially lead to an improved contrast of about $C \approx 1$ (see Sec. 5.3).

3.5.4 Asymmetric Mach-Zehnder interferometer (AMZI)

Another interferometer scheme to measure the evolution of the quantum-mechanical phase of an expanding Bose-Einstein condensate is the so-called asymmetric Mach-Zehnder interferometer (AMZI) [186], a scheme of which is given in Fig. 3.23. At first, the condensate is released from the atom chip's trapping potential. The wave function evolves for a time T_0 until it is split into a coherent superposition of different momentum states ($\pi/2$ -pulse) by means of a first-order Bragg pulse. After an interrogation time T, the wave packets get redirected with a π -pulse. The timing of the last recombination pulse ($\pi/2$) at $T - \delta T$ can now be adjusted in a way the different momentum states of the wave function are subjected to a variable spatial displacement $\delta x = 2v_r \cdot \delta T$. This again results in the formation of complementary fringe patterns in two output ports, which separate with twice the recoil velocity.

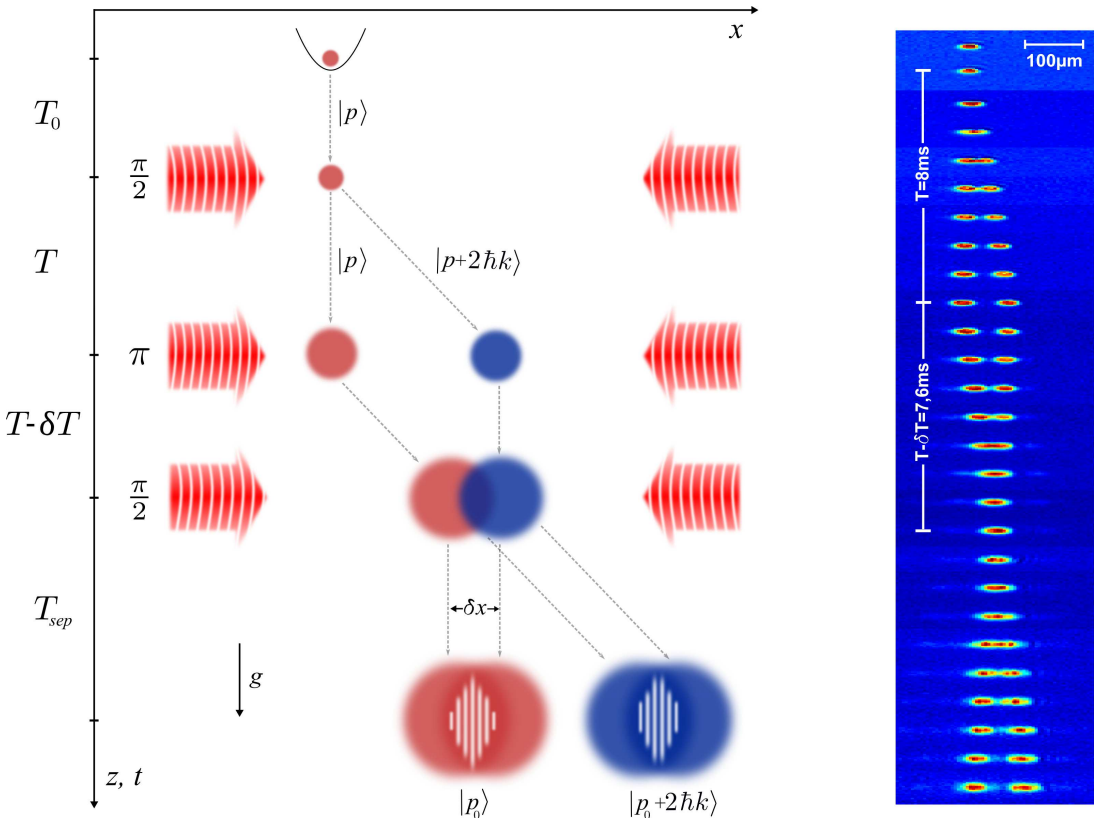

Figure 3.23: Schematic of an asymmetric Mach-Zehnder interferometer (AMZI) with Bose-Einstein condensates (left) and a temporal sequence of absorption images on ground (right). An AMZI is characterized by non-overlapping condensates at the interferometer output ports due to different interrogation times between the three optical pulses. The wave packets separate during a first interrogation time T, a π pulse then redirects the center-of-mass trajectories. After a second interrogation time $T - \delta T$, a $\pi/2$ pulse finally recombines two partially overlapping condensates in two output ports. A time T_{sep} later, an absorption image is taken.

In comparison to the ORI sequences, this scheme is not limited by finite pulse durations of the interferometer beams, thus allowing for very small spatial displacements δx. Auto-correlation measurements can be performed by using a broader regime of parameters enabling a more precise evaluation of the phase evolution. By using sub-recoil sources such as BECs and increasing the interrogation time T between the beam splitter pulses, we can ensure that the two superimposed states of the wave function get entirely separated in space before recombination. We will highlight this fact in drop tower experiments with an AMZI in microgravity, described in Sec. 5.

Fringe spacing approximation in the far-field

A spatial interference pattern emerges in the overlapping regions whose fringe spacing is inversely proportional to the phase profile $\phi(x)$ of the wave function. Like in Ramsey-

type interferometers, larger asymmetries δx lead to larger wave packet separations and thus narrower fringe patterns.

The fringe spacing in the far field d_{amzi} can here be approximated to

$$d_{amzi} = \frac{hT_{tof}}{m\delta x} = \frac{\pi \cdot T_{tof}}{k \cdot \delta T}, \tag{3.80}$$

with $T_{tof} = T_0 + T + T - \delta T + T_{sep}$ and the asymmetry δT, which is precisely controlled by the timing of the beam splitter pulses and independent of their duration.

Quadratic and linear phase evolution of a condensate - revisited

The spatial interference fringes of two overlapping Bose-Einstein condensates arise because of the quadratic phase profile and a relative velocity between the wave packets' center-of-mass. The latter has been neglected so far but will be in focus from now on. In Sec. 3.5.1, the interference term of the density was derived

$$n_i(x) = 2\sqrt{n_1(x)n_2(x+\delta x)}\cos\left[\kappa \cdot x + \phi_0\right], \tag{3.81}$$

with n_1, n_2 being the local densities of the two wave packets and δx the spatial displacement. Neglecting global phase fluctuations due to vibrations or laser phase fluctuations ($\phi_0 = 0$), this expression predicts a one-dimensional interference pattern with a spatial fringe frequency

$$\kappa(\delta x) = \alpha\delta x + \frac{m\delta v}{\hbar}, \tag{3.82}$$

where the mean-field expansion of the wave packet is characterized by its phase curvature α. The positive scattering length of ^{87}Rb causes an additional phase shift due to mean-field repulsion between the overlapping wave packets, which can be measured as a small repulsion velocity δv. For a chosen separation of $\delta x_0 = -m\delta v/\alpha\hbar$, the fringe frequency yields $\kappa(\delta x_0) = 0$ and the pattern disappears. Here, the contribution to the global phase difference due to the quadratic phase evolution of an freely expanding BEC is equalized by the contribution of the repulsion velocity.

For $\delta x = 0$, however, a fringe pattern has to occur because of the influence of the mean-field induced δv as

$$\kappa(0) = \frac{m\delta v}{\hbar}. \tag{3.83}$$

By scanning the separation δx of the interfering wave packets from negative to positive values, both contributions to the condensate's phase profile can be simultaneously read out. In the next section, we measure the phase curvature α and repulsion velocity δv of a condensate for different expansion times T_0.

3.5.5 Measurement of phase curvature and repulsion velocity

To image the phase of a freely evolving Bose-Einstein condensate, we first release it from a moderately steep trapping potential ($\omega_{rad} \approx 2\pi \cdot 130$ Hz). Roughly 10^4 atoms

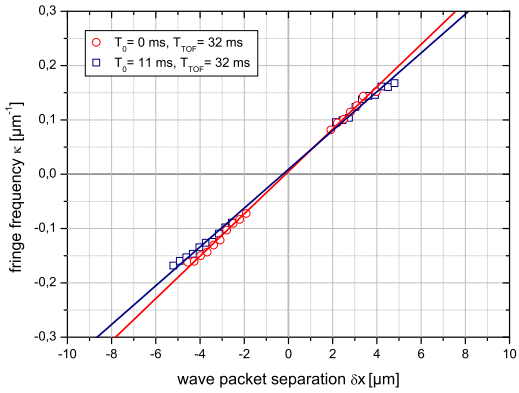

Figure 3.24: Measurement of the linear dependance of the spatial fringe frequency κ from the initiated wave packet separation δx.

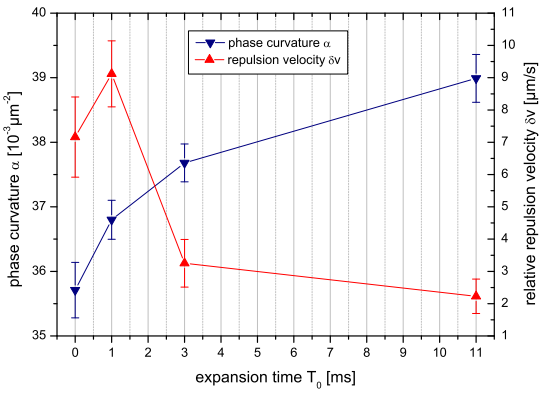

Figure 3.25: Evolution of the phase curvature α and the relative repulsion velocity δv for different initial expansion times T_0.

expand for different expansion times $T_0 = [0, 1, 3, 11]$ ms until they are subjected to an AMZI.

Here, beam splitter durations for a $\pi/2$ pulse have typically been $\tau \sim 100$ μs. The first interrogation time was fixed to $T = 3$ ms, whereas the second one $T = 3$ ms $- \delta T$ was scanned with asymmetries from $\delta T_{start} = 700$ μs to $\delta T_{end} = -700$ μs. Positive values of δT determine the condensates are led to interfere before they entirely overlap, negative values indicate that the clouds' center-of-mass have already crossed before recombination. After a separation time of $T_{sep} = 32$ ms $- T_0 - T - (T - \delta T)$, we image the output ports.

Fringe pattern and fringe frequency

Exemplary measurements of $|\kappa| = 2\pi/d_{meas}$ are shown in Fig. 3.24 for different wave packet separations δx. They correspond to an initial expansion time of $T_0 = 0$ ms (red circles) and 11 ms (blue squares), and have been fitted by a straight line, as predicted by Eq. 3.82. The observed fringe pattern evolves proportional to $1/\delta x$ (Eq. 3.82), and diverges for $\delta x = 0$. Moreover, no fringe frequencies are given for induced separations δx from -2 μm to 2 μm. Here, fitting the fringe spacing gets more challenging since d_{amzi} first reaches the size of the interfering clouds itself.

The slopes of κ correspond to the phase curvature α and the intercepts are proportional to the repulsion velocity δv. In this way, the values for α and δv for all four expansion times have been extracted from the corresponding fits (incl. error) and separately illustrated in Fig. 3.25 (with lines to guide the eye).

In this graph, the time-dependent phase evolution of a condensate is depicted. Directly after release, the BEC has a uniform phase ($\alpha = 0$) and expands mainly driven by strong mean-field repulsion (see Sec. 3.5.2). The measured non-zero value for α at $T_0 = 0$ ms is related to the fact, that the condensate already evolves during the interferometer and until detection.

In general, the temporal evolution of α (blue triangles) is proportional to the fraction

of a wave packet's rate of velocity and size, $\alpha \sim \dot{\lambda}_{rad}/\lambda_{rad}$. At early times when the mean-field energy is converted to kinetic energy, $\dot{\lambda}_{rad}$ increases rapidly and α increases as well. At later times, when most of the mean-field energy has been converted, the increase of $\dot{\lambda}$ gets substantially slowed down, effectively leading to a constant α. Ultimately, α will even start to decease again since $\dot{\lambda}_{rad} = const.$ for $t \gg 0$, but the wave packet still expands.

The data in Fig. 3.25 indicates that α is still, but only slowly increasing at the investigated timescales. A more clear signature could have possibly been measured for shorter interferometer times $2T - \delta T$ and earlier detection of the output ports [186]. However, the latter would have generally led to smaller fringe spacings ($d_{amzi} \sim T_{tof}$) which we would have not been able to detect anymore.

Even with the given restrictions of this setup, a repulsion velocity δv between the overlapping wave packets could be measured. The observed dependance of δv on the expansion time T_0 is given as red triangles in Fig. 3.25. Obviously, the more dense the samples are at short expansion times, the higher is their relative mean-field induced velocity. After some expansion time, the densities of the clouds are reduced due to mean-field expansion and this effect gets less significant.

3.6 Summary

In this chapter, an overview about the basic interactions of light and matter was given which led to the description of Bragg diffraction as a coherent two-photon process between two momentum states. These transitions have been used to form beam splitters and combiners for the matter waves emerging from our atom-chip-based source.

In this context, a miniaturized Bragg laser system was built and qualified for drop tower application. After implementation of the system, the optical properties of the Bragg beams in the vicinity of the atom chip have been directly analyzed with the condensate itself as a sensitive probe. Resulting systematics on the spatial dependance of the Rabi frequency have been analyzed in preparation of the drop experiments.

To identify a convenient source for matter wave interferometry, Bragg spectroscopy was implemented as a tool to measure the momentum width of freely expanding condensates released from different magnetic trap configurations. In a next step, the phase evolution of differently prepared condensates has been probed with open light-pulse interferometer geometries.

The temporal evolution of contrast and fringe spacing of interfering condensates in an open Ramsey-type interferometer (ORI) has been investigated and compared with the theoretical predictions. The single-shot contrast usually exceeded $C = 0.6$, which is on the order of the condensate fraction of our matter wave source. In the linear expansion regime, the observed fringe spacing evolution was proven to follow the predictions of the far-field approximation. However, we explored the border to the non-linear regime as we probed the influence of residual mean-field energy on the quadratic and linear term of the condensate's phase. This was done in ORI geometries as well as with an asymmetric Mach-Zehnder interferometer (AMZI), the latter of which was finally used to probe the phase coherence of the condensate in our drop experiments.

After the successful implementation of an atom-chip-based source of non-magnetic

degenerate gases (see Ch. 2), we now have reached the second milestone towards the demonstration of a microgravity-enhanced matter wave interferometer at the Bremen drop tower:

Free-fall interferometry with Bose-Einstein condensates in microgravity (see Ch. 5)

- Atom-chip-based source of non-magnetic degenerate gases (see Ch. 2)
- ◇
- Bragg diffraction and open interferometers with degenerate gases
- ◇
- Delta-kick cooling as a tool for long baseline atom interferometry (see Ch. 4)

In principle, we would be ready for dedicated drop campaigns. But before conducting experiments with QUANTUS-I in extended free fall, we will demonstrate an atom-chip-based method to further reduce the expansion energy of freely evolving condensates.

As a matter of fact, it is the application of a technique known as delta-kick cooling (DKC) which allowed for the observation of condensates after 2 s time-of-flight and the demonstration of an asymmetric Mach-Zehnder interferometer at timescales of half a second.

4 Delta-kick cooling as a tool for long baseline atom interferometry

If a harmonic trap containing atoms is adiabatically opened, energy from the quantum system is extracted as long as the atoms are sufficiently isolated from the environment. The trap can be assumed as a conservative (magnetic or optical) potential in well shielded ultra-high vacuum (UHV) chambers. The main limitation of adiabatic cooling is given by the gravitational field since the trapping potential must feature a gradient that is larger than the gravitational force on the trapped atoms. This limits the applicability of ultra-shallow traps for low energetic quantum ensembles at some point. For example, the gravitational sag restricts the lowest reachable trapping frequencies in ground-based experiments with our apparatus to $\omega_i = 2\pi \cdot (46, 18, 31\,\mathrm{Hz})$. However, this corresponds to temperatures of the released ensembles in the lower tens of nK (see Sec. 2.6.1).

Ultra-cold clouds of atoms released from such shallow traps clearly feature a sub-recoil velocity distribution. Amongst others, this was verified in Bragg spectroscopy measurements (see Sec. 3.4.3) and in experiments to image the phase evolution of a BEC with a matter wave interferometer (see Sec. 3.5.5). Here, the density peaks of the condensate wave function are split into a coherent superposition of momentum states which separate faster than they expand. In a matter wave interferometer based on Bragg diffraction, this allows for resonant detection of both momentum states after relatively short separation times. Quantitatively, the interferometer times in our ground-based measurements can already be chosen such that the spatial distances between the interfering paths exceed the width of the condensate by a factor of ~ 2. From this point of view, there is no immediate reason to further cool down the sample.

For microgravity experiments with ultra-long evolution times, the situation is different. Here, the expansion of even the coldest condensates will lead to dilute clouds of atoms, since $N = 10^4$ atoms spread over areas of about a few square millimeters. This is a challenge for absorptive detection methods and will at some point limit the accessible expansion time [17, 12]. If the condensates expand to such macroscopic sizes, they might also start to interact with the dielectric coating of the atom chip via van-der-Waals forces, or even get adsorbed by the surface. To circumvent this and achieve the highest possible signal-to-noise ratio (SNR), the expansion energy has to be further reduced which increases the density of the atomic ensemble.

If beam splitter pulses are applied to form interferometers, the SNR will additionally suffer from imperfect pulses and inherent atom losses. The finite velocity spread of the atomic sample will lead to a Rabi frequency distribution over the cloud. Each velocity class will oscillate at its own frequency which might limit the pulse efficiency. Assuming a sufficiently broad Fourier distribution of the Bragg pulses $I(\omega)$, another loss channel is given by the Bragg lattice intensity, which should be as homogenous

as possible to address all atoms from the ensemble with the same cycle time. Up to now, our coldest sources in microgravity typically feature Thomas-Fermi radii of about 1 mm after 1 s of free expansion (see Sec. 5.2.3). Measurements in microgravity indicate a COM velocity away from the chip surface, which after 1 s accumulates to a vertical distance from the atom chip of about 2 mm. At this specific position and by considering a Gaussian beam profile of the Bragg beams with diameter of 0.65 cm, this leads to a Rabi frequency variation of 15% over the whole cloud (see Sec. 3.4.2). Thus it is worth to investigate even colder sources.

Moreover, interferometric measurements rely on a precise determination of the phase difference between the interfering paths. If the imprinted wavefront changes from pulse to pulse due to non-negligible center-of-mass (COM) motion or fast expanding samples, a measurable phase error will occur. Point-source interferometry [110] overcomes these issues by assuming the condensate's expansion rate to be much smaller than the change of the phase curvature. This can be realized by either using wide beams or extremely cold sources.

Adiabatic decompression may be a convenient method to further decrease the kinetic energy of an atomic sample in microgravity. The adiabatic decompression criteria is given by

$$\frac{d\omega}{dt} \ll \omega^2, \tag{4.1}$$

where the rate of change of the trapping frequency has to occur slowly compared to the oscillation frequency in the trap, allowing the condensate to adiabatically follow the changes of the potential. With this method, atoms could already be cooled down below 500 pK using a weakly confining gravito-magnetic trap[1] [63]. To prepare such an ensemble with thermal temperatures of a few hundreds of picokelvin requires to adiabatically reduce the mean trapping frequencies to about $2\pi \cdot 1$ Hz. Such a cooling process would last for some seconds and besides limitations in the lifetime of the magnetic trap due to background collisions, adiabatic expansion in ultra-weak traps would also requires an exceptional level of control over magnetic stray fields. Both is not feasible for QUANTUS-I with free fall durations of less than 5 s, the given magnetic coil assemblies and only one single layer of μ-metal shield.

If it had been possible though, ultra-cold temperatures by adiabatic decompression would come along with another disadvantage. The mean-field conversion of extremely shallow traps is slow compared to steeper ones as the velocity scaling factor evolves as

$$\dot{\lambda}_{rad}(t) = \frac{\omega_{rad}^2 t}{\sqrt{1 + \omega_{rad}^2 t^2}} \tag{4.2}$$

for the radial component of a condensate [130]. The velocity field approximately reaches its final value for the characteristic time $t \geq 1/\omega_{rad}$, which for a $2\pi \cdot 1$ Hz trap would be about a second. Before that, the expansion is mean-field driven which influences the phase evolution of the condensate and therefore needs to be considered for the interpretation of the interferometer's read-out (see Sec. 3.5.2).

[1] However, this was a ground-based experiment which required a levitating field since otherwise the atoms would have dropped out of the weak trap due to the gravity.

An idea leading to a shortcut to adiabaticity was presented 20 years ago [64]. It relies on an appropriately applied momentum kick to the freely expanding ensemble. This so-called delta-kick cooling (DKC) technique was first demonstrated by using magnetic fields to apply momentum kicks on expanding clouds of thermal atoms and thus reducing their velocity spread. The significant reduction of the velocity spread consequently leads to lower temperatures and increased densities of freely expanding clouds. Moreover, it has the advantage of being considerably faster than adiabatic expansion [189, 65], as we will see in the upcoming sections.

After a short introduction into the basic principle of DKC (see Sec. 4.1), we implement this method in our atom-chip based apparatus (see Sec. 4.2). The influence of spatial displacements between the DKC trap center and the condensates center-of-mass (COM) due to inappropriate timing or wrong trap parameters will be discussed (see Sec. 4.2.2). We analyze the cooling effect for thermal and condensed sources, which will be proven to be independent of the condensate fraction in the investigated regime. This is verified with a series of free expansion (see Sec. 4.3.1) as well as with measurements of the beam splitter efficiency (see Sec. 4.3.2). In this thesis, the first application of DKC on Bose-Einstein condensates as a source for matter wave interferometry is realized. To this end, we investigate the influence of DK-cooled condensates on the fringe spacing and the contrast of an open Ramsey-type interferometer (see Sec. 4.4).

4.1 Delta-kick cooling (DKC) with harmonic traps

The technique of delta-kick cooling (DKC) can be used to overcome the time-dependent restrictions of adiabatic expansion into very weak trapping potentials. DKC relies on a position dependent force, which matches the momentum-space distribution of an expanding sample. Classically speaking, the atoms convert kinetic energy into potential energy during expansion in the DKC potential. In an ideal 1D model, the duration of the kick can be chosen such that all atoms reach their reversal point immediately before the switch-off. This reduces the expansion rate after DKC manipulation to nearly zero.

4.1.1 DKC in momentum space

Let us assume a 1D cloud of non-interacting atoms being released from a harmonic atom-chip based trap and allowed to expand freely in the ballistic regime. After a time T_0, atoms with velocities v_i, which had been at position $x_{i,0}$ directly after switch-off, will now have individual positions as

$$x_i = v_i \cdot T_0 + x_{i,0} \approx \frac{p_i \cdot T_0}{m}. \tag{4.3}$$

To bring the atoms to rest, a position-dependent momentum kick of

$$F(x) \cdot \tau_{dkc} = p_i = \frac{x_i m}{T_0} \tag{4.4}$$

has to be applied, which requires a linear restoring force. The fastest atoms need to get the greatest momentum kick. We therefore expose the atomic cloud to a 1D harmonic

potential with frequency ω_x,

$$U_{dkc}(x) = 1/2 m\omega_x^2 x^2 \tag{4.5}$$

for a short duration of τ_{dkc}, such that the sinusoidal acceleration of the atoms in the trap can be linearized. Each individual atom with mass m will now experience a position dependent momentum kick as

$$F(x) \cdot \tau_{dkc} = -\frac{\delta U_{dkc}}{\delta x} \cdot \tau_{dkc} = -m\omega_x^2 x_i \cdot \tau_{dkc}. \tag{4.6}$$

If we now engineer the delta-kick potential such that the harmonic frequency of the confining potential and the duration of kick fulfill

$$T_0 \cdot \tau_{dkc} = 1/\omega_x^2, \tag{4.7}$$

the kinetic energy of each individual atom can theoretically be reduced to zero (cf. Eq. 4.4 and 4.6). We can define the strength of the delta-kick $S = 1/T_0 = \omega_{dkc}^2 \cdot \tau_{dkc}$, in analogy to the power of an optical lens. This is why delta-kick cooling is often referred to as a magnetic lens for matter waves.

4.1.2 DKC in phase space

In the phase space picture, exposing an atomic distribution to a harmonic potential leads to a rotation of the distribution. At the beginning, all atoms are confined in an external potential and show a Gaussian (thermal atoms) or Thomas-Fermi (BEC) distribution in momentum and position space (Fig. 4.1, left). After releasing the atoms from the trap and allowing them to freely expand, the distribution spreads in the x-direction (Fig. 4.1, center). The atoms propagate according to their momentum, which means that the fastest atoms are further away from the center than colder ones.

A carefully designed delta-kick with a harmonic potential can rotate the tilted elliptical phase-space distribution onto the x-axis (Fig. 4.1, right). DKC operation converts position into momentum and vice versa. Besides the kick duration itself, the fidelity is dependent on the mode-match between the applied harmonic oscillator potential and the momentum-position correlation of the atomic distribution. Optimized DKC minimizes the expansion energy of the atomic ensemble by increasing its spatial spread, thus the sample will remain with precisely the same phase-space density as before the kick.

DKC tolerances and trap anharmonicites

In our experiment, the delta-kick cooling is realized with atom-chip based magnetic potentials. Mode mismatching thus can arise due to errors in the strength of the magnetic fields, their spatial distribution and anharmonicities, as well as in the timing of the delta-kick.

The momentum imparted at a final position x_f is given by $p = m\omega_x^2 x_f \cdot \tau_{dkc}$, and the ideal delta-kick condition follows as $\omega^2 \tau_{dkc} = 1/T_0$. After such an ideal kick, the tolerance of the delta-kick momentum transfer should be less than the final momentum

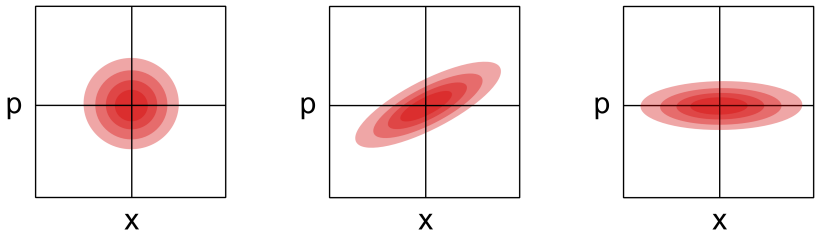

Figure 4.1: Phase-space diagram for harmonic-force delta-kick cooling (DKC). In the trapping potential, the atoms show a Gaussian or Thomas-Fermi distribution in momentum and position space (left). After some expansion time the cloud has expanded in space (x-direction), which leads to an elongated and tilted phase-space distribution (center). The application of an appropriate delta-kick will rotate the distribution onto the x-axis. In this manner, the remaining momentum spread of the atoms is reduced while simultaneously the spatial spread is increased (right). This preserves the phase-space density of the initial cloud.

spread after the kick

$$\delta p = p_i \delta(\omega^2 \tau_{dkc} T_0) < p_f = x_i p_i / x_f. \tag{4.8}$$

From Eq. 4.8 we get the expression for tolerable fractional errors

$$\frac{\delta(\omega^2)}{\omega} + \frac{\delta\tau_{dkc}}{\tau_{dkc}} + \frac{\delta T_0}{T_0} < \frac{x_i}{x_f} \sim \sqrt{\frac{T_f}{T_i}}, \tag{4.9}$$

with T_f/T_i as the ratio of the final and initial temperature of the ensemble.

For achieving extremely low temperatures, high expansion rates are necessary which put tight restrictions on the tolerance of the delta-kick strength. Since harmonic magnetic traps are discussed here, we can set $\delta(\omega^2)/\omega = \delta(B^{(2)})/\sqrt{B^{(2)}}$ with $B^{(2)}$ as the curvature of the magnetic field. Perfectly harmonic potentials do not exist. However, if we only focus on the center of the trapping potential we can approximate the influence of trap anharmonicities and set restrictions to allowable trap anharmonicities. Taylor expansion of the magnetic field around the center gives

$$B(x) = B^{(0)} + \frac{1}{2}B^{(2)}x^2 + \frac{1}{6}B^{(3)}x^3 + ... + \frac{1}{n!}B^{(n)}x^{(n)}. \tag{4.10}$$

The effective force acting on the atoms is proportional to the gradient of the magnetic field ($F(x) = g\mu_B m_F \nabla B(x)$), with Landé factor g, the Bohr magneton μ_B and the magnetic quantum number m_F. For an ideal delta-kick, the magnetic curvature should fulfill $g\mu_B m_F B^{(2)} x_f \tau_{DKC} = p_i$ and aberrations caused by higher harmonic terms should be smaller than the final momentum spread

$$F(x) \cdot \tau_{dkc} < p_f, \tag{4.11}$$

$$g\mu_B m_F \cdot \sum_{n\geq 3} \left(\frac{1}{(n-1)!} B^{(n)} x^{(n-1)} \right) \cdot \tau_{dkc} < p_f. \tag{4.12}$$

The resulting condition for n-th order error in anharmonicities follows as [93]

$$\frac{B^{(n)}}{B^{(2)}} < \frac{x_i}{x_f}\frac{(n-1)!}{x_f^{n-2}}. \tag{4.13}$$

Another problem is generally related to dimensionality and the goal to achieve the lowest temperatures in all three dimensions simultaneously. Elongated atom-chip based potentials feature an asymmetry. Thus the restoring force of a delta-kick is not isotropic, which prevents an optimization of cooling in all directions such that a trade-off has to be made. Once an appropriate trapping potential is found, the remaining optimization parameters are the initial expansion time T_0 and the kick duration τ_{dkc}.

Before we start with an analysis of some of the mentioned error sources and their influence on the measurement, we will first discuss the general implementation of DKC on chip in the the next section.

4.2 Implementation of on-chip DKC

To realize DKC, the atomic cloud should be exposed to an appropriately designed harmonic trap, which is switched on for a short duration. We simply use our atom-chip structures to produce a suitable magnetic potential. The condensate is first generated in the $m_F = 2$ state, then released from the holding trap and expands freely (see Fig. 4.2, left). After some free expansion time T_0, a chip-trap is switched on again for a duration of τ_{dkc} (typically a few hundreds of microseconds) which ideally fulfills the cooling condition $T_0 \cdot \tau_{dkc} = 1/\omega^2$. The application of a short harmonic potential will rotate the elongated distribution in phase-space and ideally convert the entire velocity width into a position width. Considerably fast switching times for the delta-kick are possible thanks to the microscopic structures of the atom chip. Between initial release and DKC, the bias field generated by macroscopic coils is continuously present (additional offset field to K1, see Sec. 2.4.2) and within a ms ramped to the final value for DKC, whereas the actual kick is realized by a brief current pulse through the z-current. To transfer the atoms in the $m_F = 0$ state for subsequent experiments, an adiabatic rapid passage (ARP) is typically applied a few ms after DKC operation.

In microgravity experiments, we can use the same trap parameters for the holding trap and the DKC potential since in the first ms after release the condensate will hardly move w.r.t the initial center position. More importantly, the COM velocity ($\sim 1.2\ \mu$m/ms) during the kick (~ 2 ms) can be neglected in microgravity. This not only simplifies the experimental sequence but constitutes an ideal environment to test the fundamental limitations of delta-kick cooling. The cooling effect can be investigated just by observing the cloud after sufficiently long expansion times while optimizing the DKC parameters T_0 and τ_{dkc}.

Due to the influence of gravity in ground-based measurements, however, the condensate's COM is accelerated away from the chip surface and thus from the initial position of the holding trap. Hence, measurements in 1 g require an adaption of the currents to guarantee a sufficient mode overlap between the condensate and the DKC trap. As already discussed in Sec. 2.4.2, the trap center r_0 of a chip-based Ioffe-Pritchard trap

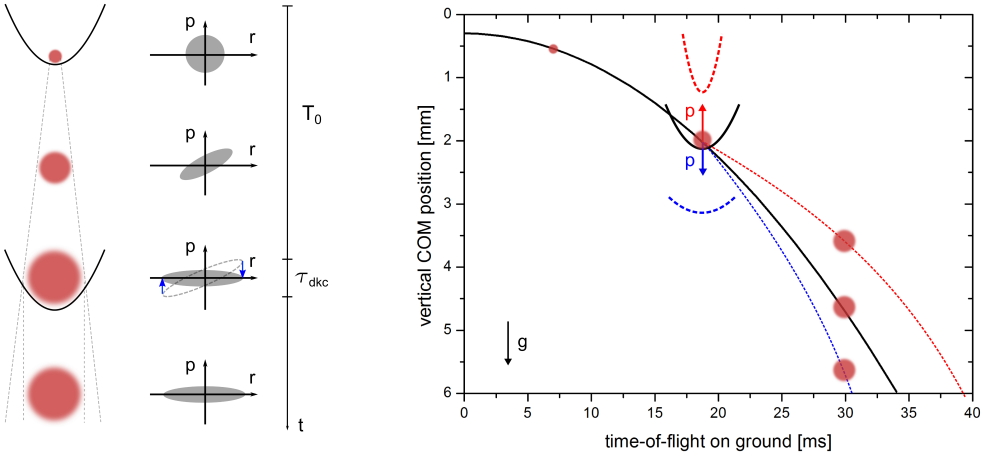

Figure 4.2: Schematic of delta-kick cooling (DKC) in a temporal sequence (left). The atoms are released from a harmonic trap and expand for T_0 until a mode-matched trap is switched on for a short duration τ_{dkc}. Ideally, the tilted elliptical phase-space distribution is hereby exactly rotated onto the x-axis. A spatial mismatch between the condensates COM and DKC trap position will lead to an additional velocity kick (right).

(IPT) can be shifted perpendicular to the chip surface as

$$r_0(z) = \frac{\mu_0}{2\pi} \cdot \frac{I_z}{B_{bias}}, \tag{4.14}$$

with the z-wire current I_z, the vacuum permeability μ_0, and the bias field B_{bias}. However, the further away we move the trap center, the less steep the potential becomes in radial direction [19, 136]

$$\omega_{rad} \approx \sqrt{\frac{\mu_B g_F m_F}{m} \cdot \frac{B'^2}{B_0}} \propto \frac{B_{bias}^2}{I_z}, \tag{4.15}$$

with the Landé factor g, the Bohr magneton μ_B and the magnetic quantum number m_F. An appropriate source for ground-based DKC demonstration and the influence of a mismatch between condensate's position and DKC potential will be discussed in the next section.

4.2.1 An appropriate source for ground-based DKC demonstration

Effective delta-kick cooling (DKC) requires an atomic ensemble which features a linear position-momentum distribution. In case of a degenerate source, the expansion dynamics will be driven by strong mean-field interactions, a regime where the derived expressions of Sec. 4.1.1 are not applicable, or only to some extend. Consequently, one has to wait until the condensates correlation of momentum and position is linearized. However, the validity of this approximation for the wave packet expansion in the far-field depends on the condensate's preparation in the holding trap. As an example for the QUANTUS-I experiment, condensates released from the shallow trapping potential

($\omega_{rad} \approx 2\pi \cdot 50$ Hz) still feature significant non-linear dynamics for expansion times on the order of 10 ms (see Sec. 3.5.2). The application of a controlled delta-kick would therefore be restricted to timescales between release and DKC operation of $T_0 \geq 10$ ms, determined by the mean-field conversion of the cloud.

However, shifting the IPTs harmonic center to positions which coincide with the COM position of the condensate after 10 ms comes at the cost of shallower traps. This is an inherent feature of the atom-chip physics, and leads to longer durations τ_{dkc} of the delta-kick compared to condensates which are closer to the surface[2]. Moreover, the condensates COM will develop a certain velocity and propagate through the DKC potential. Time-dependent DKC potentials will additionally influence the dynamics and have essentially to be modeled within the λ-matrix formalism. They do not correspond to the assumed ideal case anymore (see Sec. 4.1.1) and may lead to systematic errors.

Based on these assumptions, the most appropriate source for demonstration of on-chip DKC in ground-based measurements would be a condensate prepared in a steep holding trap. Here, the mean-field is entirely converted after a few ms, which allows us to apply DKC earlier than for shallow potentials. An earlier application means that errors due to the condensates COM velocity will be reduced and the magnetic field curvatures are larger which allows for high trapping frequencies and consequently short pulse durations. The faster expansion as compered to shallow traps leads to a larger wave packet spread at the time of DKC operation which is favorable for reaching lower temperatures (Eq. 4.9). Thus, for most of the upcoming experiments, the condensate will be released from a holding trap with a radial trapping frequency of $\omega_{rad} \approx 2\pi \cdot 350$ Hz.

For this source, different DKC configurations have been investigated to find the right parameters for a significant reduction of the expansion energy and negligible influences on the COM motion. This optimization process foremost has been realized by the variation of one of the following parameters for the DKC kick:

- Current of the z-wire I_z
- Magnetic bias field B_{bias}
- Free expansion time prior to the magnetic pulse T_0
- Duration of the DKC pulse τ_{dkc}

In the next subsections, we show exemplary measurements which investigate the influence of these parameters on the position of the DKC center as well as the net cooling effect. Major attention will be payed on the consequences of a mismatch between the harmonic trap center for DKC and the condensates position.

4.2.2 Position of the DKC trap center

Mismatches between the COM position of the atomic cloud and the center of the DKC potential during the kick will lead to an additional linear force acting on the atoms

[2] Again, the ideal case is given by a microgravity environment, where the condensates COM motion can be brought to negligible values for DKC operation.

(see Fig. 4.2, right). For now, we neglect possible displacements in the horizontal plane (x- and y-axis) due to the symmetry of the setup. Moreover, the fact that gravity is pointing along the vertical direction (z-axis) makes the setup more sensitive to position-dependent errors in this direction. The condensate is released from the holding trap and follows an unperturbed, parabolic trajectory (black line). After expansion time T_0, a DKC trap is shortly switched on. We assume it to be perfectly mode-matched, such that the atomic cloud expands in the center of a harmonic trap during the kick. In this case, insignificant deviations of the trajectory compared to free expansion will occur and the atoms can be detected with negligible spatial displacements compared to free expansion without DKC.

If the DKC trap center is not overlapped with the condensate, an effective linear force points in the direction of the DKC trapping center during the application time. This can either be the case for atoms which already passed the DKC trap center (red lines) or for traps at a position which is still to be passed (blue lines). Both situations will influence the effective trajectory which can be studied quantitatively in time-of-flight series.

Especially in the context of atom interferometric measurements, additional COM velocities and inherent uncertainties in velocity and position of the matter waves would strongly affect the phase extraction. Therefore, arising systematics need to be well understood and controlled at a sufficiently high level. To obtain a first understanding of this error source, we study the influence of a DKC trap displacement by choosing a fixed expansion time of the condensate T_0 and vary the DKC trap positions with I_z and B_{bias}. We can also fix the DKC parameters and scan the T_0 prior to the magnetic pulse. Results of both approaches will be presented in the next subsections.

Influence of the atom-chip current

In this experiment, we shift the DKC trap center by scanning the z-wire current I_z for a given configuration of the bias field B_{bias}. After application of the lens, the spatial displacement for a fixed time-of-flight of $T_{tof} = 34.3$ ms is measured. After release, the condensate expands for $T_0 = 6$ ms before DKC with $B_{bias} = 6.5$ G and a duration of $\tau_{dkc} = 300$ μs is applied to the atoms. An absorption image is taken and the COM position extracted from a Gaussian fit.

We scanned I_z and calculated the displacement for positions with and without application of DKC (see Fig. 4.3, left). The atomic motion is reduced to a 1D trajectory in z-direction, and in case of no DKC, the atomic position is characterized by z_{at} at the time of detection. For a perfectly timed (and sufficiently short) kick, the COM position is ideally not affected ($z_{at,dkc} - z_{at} \approx 0$), which in this experiment can be fulfilled for a chip current of roughly $I_z = 1.4$ A.

If the center position of the harmonic potential during the kick is already passed by the atoms, a linear force is acting on the atoms which points towards the trap center and therefore against gravity (see red trap in Fig. 4.2, right). This pulsed levitation arises for currents 1.0 A $< I_z <$ 1.4 A and leads to observed displacements of $z_{at,dkc} - z_{at} < 0$. For $I_z < 1$ A the gradient seems to be constant independent on the current value. Here, the trap may not be approximated as harmonic anymore.

For the investigated chip currents between 1.4 A $< I_z <$ 1.9 A, the DKC trapping

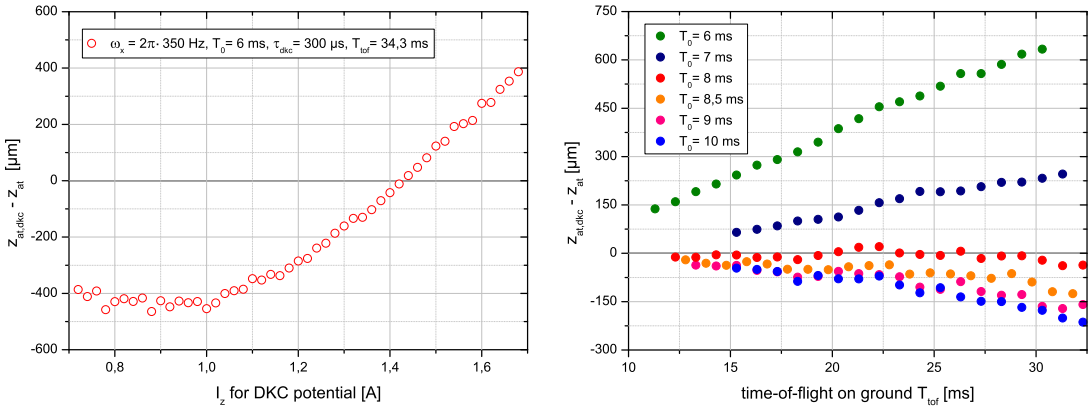

Figure 4.3: Influence of a mismatch between the condensates COM position and the center of the DKC trap during the magnetic pulse. For a given set of parameters, the vertical displacement between atoms manipulated with DKC and freely expanding atoms $z_{at,dkc} - z_{at}$ is measured for different DKC trap chip currents I_z (left) and by varying time T_0 prior to DKC (right). More details in text.

center is not yet reached by the atoms. Consequently, they get accelerated towards the center which leads to an additional velocity kick in the direction of gravity ($z_{at,dkc} - z_{at} > 0$). In the linear regime between 1.0 A $< I_z <$ 1.9 A, the additional velocity kick in the z-direction (for these specific DKC parameters) can be approximated as

$$\delta\vec{v}_{dkc} = 41.4(6)\ \frac{\mu\text{m}}{\text{ms}\cdot\text{A}} \cdot (I_z - 1.4\ \text{A}) \cdot \vec{e}_z. \tag{4.16}$$

Influence of the free expansion time prior to DKC

Once an appropriate DKC potential is found, a position mismatch between the condensate and the DKC trap center still can occur for an incorrect timing between release and application of the kick. Again, this yields a systematic velocity kick $\delta\vec{v}_{dkc}$ which was investigated in a dedicated experiment.

We measured a time-of-flight series of a condensate released from the steep trap without application of DKC. The obtained reference positions are then subtracted from the COM positions of condensates manipulated with DKC. Here, the clouds expand for a certain free expansion time T_0 until a DKC potential with $I_z = 1.8$ A and $B_{bias} = 5.25$ G was applied for $\tau_{dkc} = 300\ \mu$s. The measured vertical displacements $z_{at,dkc} - z_{at}$ are calculated for different expansion times prior to DKC and plotted as colored, full circles in (see Fig. 4.3, right). Here, we can again distinguish between three regimes:

- expansion times where the atoms already passed the trap center ($T_0 > 8$ ms), which leads to $z_{at,dkc} - z_{at} < 0$,
- expansion times for which a sufficient spatial overlap is achieved which leads to a nearly unperturbed COM velocity ($T_0 \approx 8$ ms), and

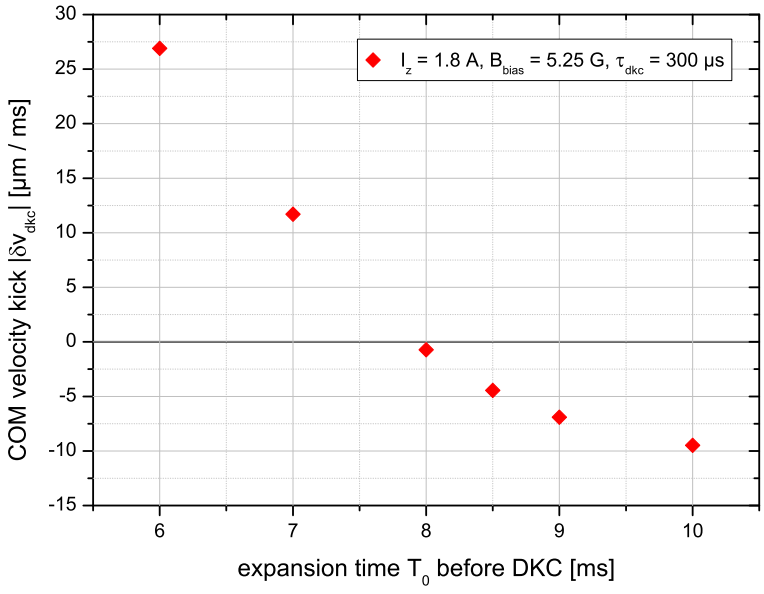

Figure 4.4: Additional COM velocity $|\delta\vec{v}_{dkc}(T_0)|$ based on a straight line fit of the data in Fig. 4.3 (right). For the given DKC trap configuration ($I_z = 1.8$ A, $B_{bias} = 5.25$ G and $\tau_{dkc} = 300\ \mu$s), the mismatch between condensate's COM and DKC trap center is modeled by an inappropriate timing of T_0.

- expansion times where an additional momentum kick in direction of gravity is observed ($T_0 < 8$ ms), since $z_{at,dkc} - z_{at} > 0$.

Moreover, the observed value of $|\delta\vec{v}_{dkc}|$ (given by each slope) is larger for shorter free expansion times ($T_0 < 8$ ms). From that we can conclude that the gradient must be stronger, which can be explained by the asymmetry of the radial shape of the IPT potential. Due to the $1/z$ dependence of the magnetic field strength perpendicular to a single wire (see Sec. 2.4.2), it is usually steeper in the direction of the atom chip surface [138, 140]. The observed additional COM velocities $|\delta\vec{v}_{dkc}(T_0)|$ based on a straight line fit of the data in Fig. 4.3 (right) are depicted in Fig. 4.4 (here, the statistical errors are negligible).

Influence of the bias field

According to Eq. 4.14, the position of the atom-chips's trap center r_0 is also dependent on the value of the bias field B_{bias}. We measured again the displacement $z_{at,dkc} - z_{at}$ of the atoms COM for a fixed time-of-flight of $T_{tof} = 23.3$ ms for various configurations of I_z and B_{bias} (see Fig. 4.5). The reference position of the condensate without application of delta-kick cooling was measured previously and is subtracted from the obtained data with DKC manipulation.

In this experiment, the condensate is released from the steep trap and expands for $T_0 = 2$ ms before a delta-kick with a duration of $\tau_{dkc} = 300\ \mu$s is applied. Within T_0, the condensate only moves for about 20 μm and we consequently can use trap configurations which are closer by the atom chip's surface.

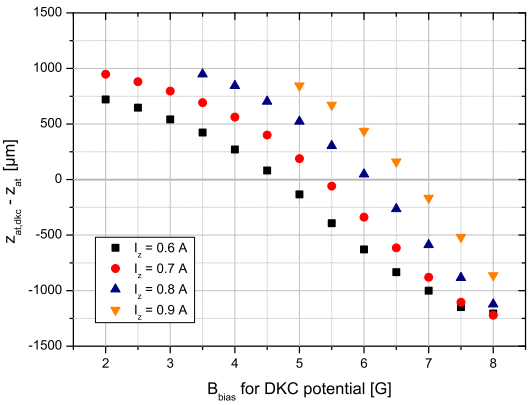

Figure 4.5: Vertical displacement of the COM position for a fixed timing $T_0 = 2$ ms but different bias currents B_{bias} for the DKC trap.

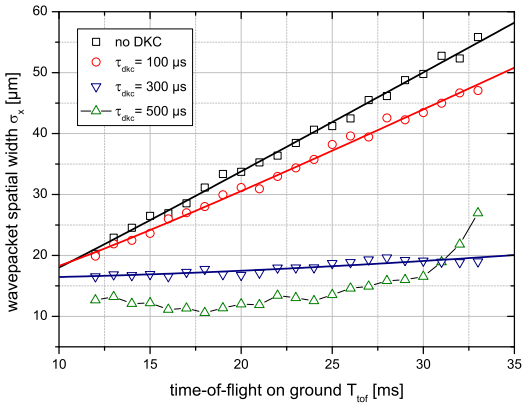

Figure 4.6: Influence of the kick duration τ_{dkc} onto the wave packet rms width σ_x for a given DKC trap configuration.

For each I_z, we can find a bias field $B_{bias,0}$ for which the DKC trap center and the condensate's COM position sufficiently coincide ($z_{at,dkc} - z_{at} = 0$). The measured values are summarized in Tab. 4.1 and correspond to the expected evolution of the trap center position as $r_0(z) \sim I_z/B_{bias}$ (see Eq. 4.14). Starting from here, a further increase of the bias field ($B > B_{bias,0}$) means that the DKC trap center is moved towards the chip surface and thus leads to displaced COM positions with $z_{at,dkc} - z_{at} < 0$. In the other direction ($B < B_{bias,0}$), the condensate gets an additional kick in direction of gravity which leads to observed positions after DKC application as $z_{at,dkc} - z_{at} > 0$.

If we approximate the observed dependencies as linear in the regime for $z_{at,dkc} - z_{at} \in \{-500\ \mu\text{m}, 500\ \mu\text{m}\}$, we can fit a straight line and extract the slopes determining $\delta\vec{v}_{dkc}$ around each $B_{bias,0}$. With each slope $m_{\delta v}$ given in Tab. 4.1, the velocity kick in the z-direction can be calculated to

$$\delta\vec{v}_{dkc} = m_{\delta v} \cdot (B_{bias} - B_{bias,0}) \cdot \vec{e}_z. \tag{4.17}$$

From Eq. 4.17 and Tab. 4.1, we see that DKC traps with a higher $B_{bias,0}$ (and consequently higher I_z to remain at the same position) feature an increased linear restoring force. This can be explained by the higher magnetic field curvatures at the condensate's position for the chip-based IPT which evolves as $\omega_{rad} \sim B_{bias,0}^2/I_z$ (see Sec. 4.2).

4.2.3 DKC pulse duration and cooling effect

Since we are now able to identify a trap for DKC which coincidences with the COM position of the condensate, we can additionally vary the pulse duration τ_{dkc}. In combination with the expansion time prior to the DKC pulse T_0 and the effective trapping frequency of the DKC trap ω_{dkc}, the right choice of the duration τ_{dkc} will ideally stop the expansion for $T_0 \cdot \tau_{dkc} = 1/\omega_{dkc}^2$. If we scan the timing parameters, the fidelity of the cooling effect is best approximated by a measurement of the spatial width of the

manipulated wave packets in a time-of-flight series.

The condensate is again released from the steep trapping potential and after a free expansion time of $T_0 = 8$ ms, we switch on the DKC trap. The absorption images are fitted with a Gaussian function and as a measure for the wave packet expansion, the rms widths are exemplary given for the x-direction (see Fig. 4.6). The corresponding error bars are on the order of the size of the data points and are omitted for better visibility. In this measurement, we used a chip current of $I_z = 1.9$ A for the DKC trap. We started with a slightly off-center trap ($B_{bias} = 3.5$ G) from which we know its center is still to be passed by the atoms, and a comparably short duration of 100 μs to observe a small cooling effect at first. Now, we can both improve the position of the DKC trap (and with that the effective restoring force) and the pulse duration τ_{dkc} in parallel until focusing occurs. Once this point is reached, a thorough optimization can be started to find the right parameters for a minimized width by preserving the aspect ratio of the cloud before DKC application.

For now we only focus on the width in the x-direction, and as a rough measure for the cooling effect, an expansion temperature can be approximated by fitting

$$\sigma(t) = \sqrt{\sigma_0^2 + \sigma_v^2 t^2} \tag{4.18}$$

to the data and calculating $T = m\sigma_v^2/k_B$. Without DKC (black squares), a temperature of $T = 47(3)$ nK is obtained from the fit. With a short kick of $\tau_{dkc} = 100$ μs (red circles), a small fraction of the expansion energy can be extracted which results in $T = 41(2)$ nK.

The next example (blue triangles) constitutes a nearly ideal combination of pulse duration ($\tau_{dkc} = 300$ μs) and bias field ($B_{bias} = 5.7$ G) for the given parameters, which reduces the expansion rate of the wave packet to effectively zero on the investigated timescales ($T \approx 5(5)$ nK, 10-fold reduction of the expansion rate). Here, the right combination of kick duration and trapping frequency led to a rotation of the phase-space distribution onto to the x-axis.

If we now increase the bias field ($B_{bias} = 5.9$ G) and apply a longer pulse duration $\tau_{dkc} = 500$ μs (green triangles), the rotating phase-space distribution will pass the point of perfect conversion of momentum width into spatial width. Given the schematic in Fig. 4.1 (left), most of the atoms at positions $x > 0$ now have a momentum pointing against the initial direction with $p < 0$ and vice versa. This leads to a focusing of the

I_z [A]	$B_{bias,0}$ [G]	$m_{\delta v}$ [μm /ms $\cdot$ G]
0.6	4.6(3)	-175(9)
0.7	5.3(2)	-220(7)
0.8	6.0(3)	-239(12)
0.9	6.7(3)	-274(10)

Table 4.1: Evaluation of the data given in Fig 4.5. From linear fits to the displacements $z_{at,dkc} - z_{at} \in \{-500\ \mu\text{m}, 500\ \mu\text{m}\}$ for each I_z, one can obtain a value for no additional kick $B_{bias,0}$. Moreover, each slope $m_{\delta v}$ determines an additional velocity kick for a bias field mismatch around $B_{bias,0}$ as $\delta v_{dkc} = m_{\delta v} \cdot (B_{bias} - B_{bias,0})$.

matter wave packet until the ensemble again starts to increase with the time-of-flight (in Fig. 4.6, lines between the green triangles are added to guide the eye).

One has to note, that this method gives just an indication of the cooling effect. The expansion of a condensate under the influence of a time-dependent potential should be properly modeled with the λ-matrix formalism embedded in the QUANTUS-I chip-model [113]. Moreover, the size of the clouds are on the order of the resolution of the imaging system for effective DKC in ground-based measurements. Thus, the expansion temperature on the observable time scales can only be roughly estimated. Again, microgravity is a promising environment to overcome this restriction and to determine expansion temperatures for delta-kick cooled atoms at large timescales.

The next section will present the application of an optimized DKC sequence to thermal atoms and compare the cooling effect with a condensate released from the same initial holding trap.

4.3 DKC sequence optimization and applicability to thermal ensembles

Degenerate sources feature sub-recoil momentum distributions, but nevertheless will profit from additional DKC in extended free fall experiments (see Sec. 5.2). In this environment, some of the major advantages of further cooling have already been discussed at the beginning of this section. For the implementation of a matter wave interferometer, they are mainly dedicated to optimized beam splitter efficiencies, a more homogeneous wavefront due to point source character of the wave packet and larger signal after macroscopic interrogation times in the interferometer.

As a commonly used alternative in atom interferometers, thermal ensembles do not require sophisticated setups such as in BEC experiments. Thermal clouds are generally faster to prepare, and feature higher atom numbers even after molasses phase and state selection (typically about 10^7 atoms [61, 190]). But at least 1D velocity selection processes are necessary to extract a sub-recoil momentum distribution, which is afterwards used in the interferometer [175]. The other atoms are removed with blow-away beams and are lost, which leads to a lower SNR. A much more elegant method to prepare ensembles cooled in 3D without notable losses in atom number after optical molasses is Raman sideband cooling [191, 192]. However, this technique requires additional optical access for an optical lattice and well controlled magnetic field gradients.

DKC with an atom chip might be another method to prepare thermal sources at sub-recoil temperatures as an input for interferometry experiments.

4.3.1 Expansion studies

The influence on the expansion of a thermal ensemble is compared to a Bose-condensed source by measuring the cooling effect in the two visible dimensions. The atomic cloud is released from the steep trapping potential ($\omega_x \approx 2\pi \cdot 350$ Hz) and freely expands for $T_0 = 6$ ms until a delta-kick with a duration of $\tau_{dkc} = 300\ \mu$s is applied. This parameter choice for the DKC trap ($B_{bias} = 5.5$ A, $I_z = 1.15$ A) is a result of a thorough

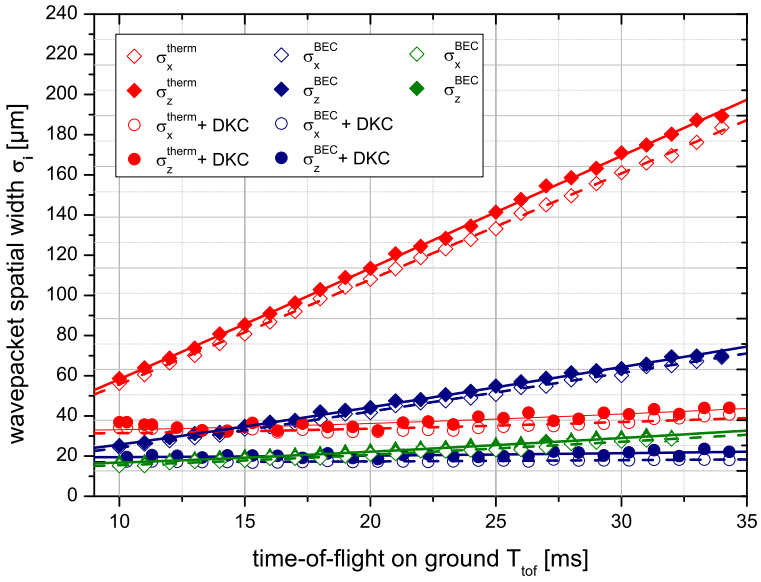

Figure 4.7: Optimized DKC applied on thermal (red symbols) and Bose-condensed (blue symbols) sources released from the same steep trapping potential with $\omega_{rad} \approx 2\pi \cdot 350$ Hz. For comparison, the free expansion of a condensate released from the shallow trap with $\omega_{rad} \approx 2\pi \cdot 50$ Hz is given (green symbols). Details in text.

optimization process based on the presented systematics in Sec. 4.2.2 and 4.2.3. In the following measurements, we show that both visible dimensions (x- and z-direction) can be sufficiently cooled down with one pulse in ground-based measurements, independent of the condensate fraction. The first picture is taken after a time-of-flight of 10.3 ms which is subsequently scanned to a final value of 34.3 ms (see Fig. 4.7).

The results for a purely thermal ensemble (red symbols) and a Bose-condensed cloud (blue symbols) are compared. With application of DKC, the expansion is reduced to a negligible value within the given observation time. As a measure for the spatial width of the wave packets, the rms widths of Gaussian envelopes have been evaluated. Three experimental runs are averaged, the standard deviation is only shown if it exceeds the size of the plotted data points. Additionally, the rms widths of a freely expanding BEC from the shallow trap with $\omega_x \approx 2\pi \cdot 50$ Hz are given (green symbols).

For the thermal case ($\nu_{rf} = 1.9$ MHz, cf. Sec. 2.6.1), the temperature is reduced from $T_x = 330(3)$ nK and $T_z = 296(3)$ nK to final values after DKC of about $T_x \approx 8(2)$ nK and $T_z \approx 5(2)$ nK, respectively. Again, the same concerns as in Sec. 4.2.3 are raised here and finally a detailed chip-model should be used to model the expansion under the influence of DKC. Restrictions due to (i) the limited size of the chip-based IPT for which the harmonic approximation is valid and (ii) trap anharmonicities are not considered in the given approximation. Especially the deformation of the cloud along the z-direction (see Fig. 4.8, (C)) is inadequately fitted by a simple Gaussian distribution. However, using the rms width as a "scaling" for the wave packet width under the influence of this optimized magnetic lens ($B_{bias} = 5.5$ A, $I_z = 1.15$ A), yields a reduced expansion rate by a factor of ~ 50.

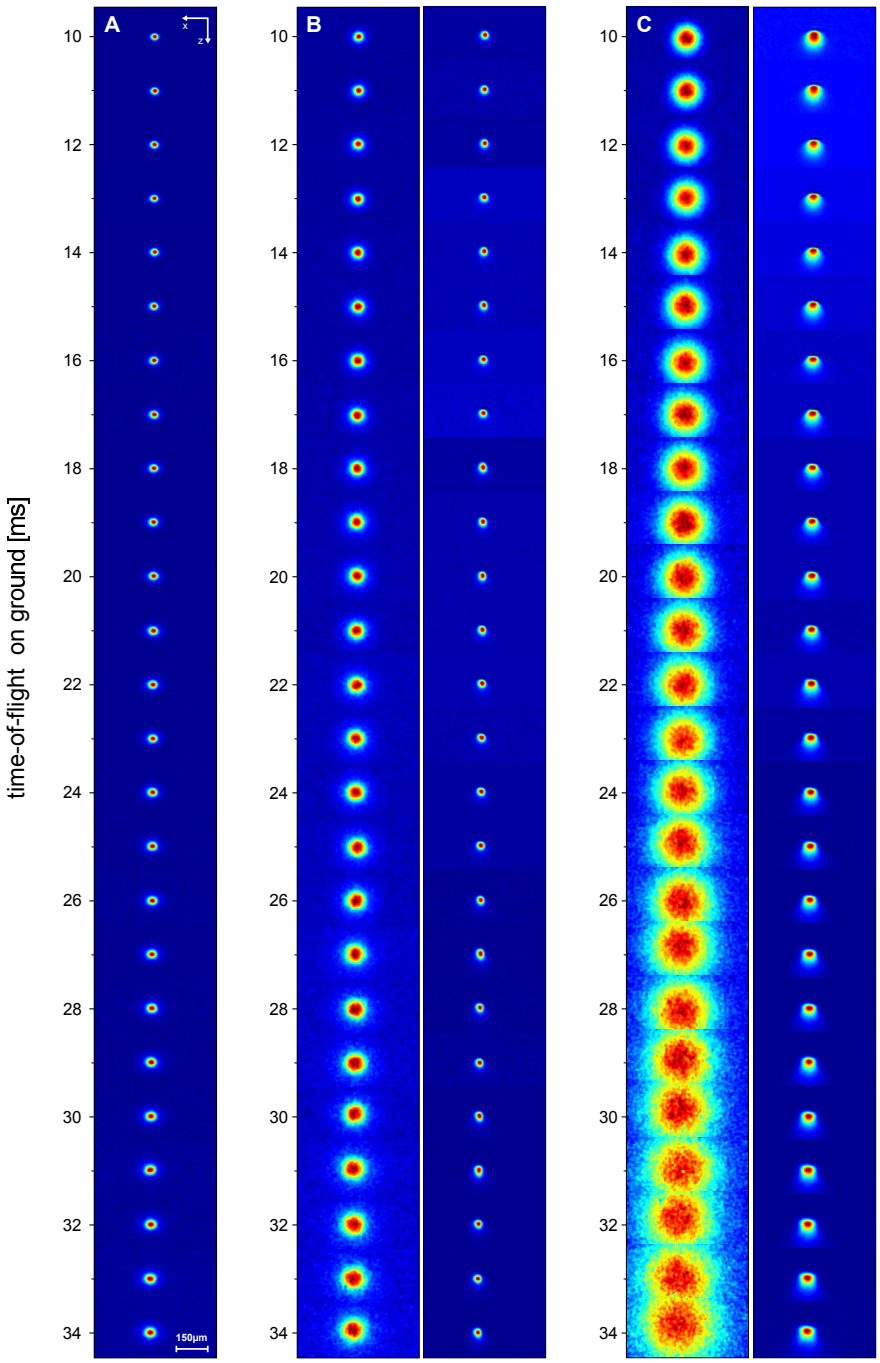

Figure 4.8: Temporal sequence of time-of-flight images for differently prepared matter wave sources on ground. A: Expansion of a BEC released from the shallow trap ($\omega_{rad} \approx 2\pi \cdot 50$ Hz). B: Expansion of a BEC released from the steep trap ($\omega_{rad} \approx 2\pi \cdot 350$ Hz) without (left) and with (right) optimized DKC. C: Expansion of a thermal ensemble released from the steep trap ($\omega_{rad} \approx 2\pi \cdot 350$ Hz) without (left) and with (right) optimized DKC.

A condensate expansion ($\nu_{rf} = 1.835$ MHz, cf. Sec. 2.6.1) is shown for comparison. Without DKC, the expansion of the Gaussian rms widths gives rise to temperatures of $T_x = 42(3)$ nK and $T_z = 45(2)$ nK, respectively. Based on the previously used DKC parameters, we optimized the sequence for a condensate to mostly preserve the same aspect ratio before and after application. As a result, the applied lens had to be slightly adapted ($B_{bias} = 5.3$ A, $I_z = 1.15$ A) but was again applied for $\tau_{dkc} = 300$ μs after $T_0 = 6$ ms of free expansion. The residual wave packet expansion can be associated with temperatures of about $T_x \approx T_z \approx 1$ nK. Compared to the collimated thermal cloud (red symbols), the condensed ensemble after DKC (blue symbos) is only roughly half the size, whereas a freely evolving condensate released from the shallow trap (green symbols) clearly shows a finite momentum width larger than both ensembles manipulated with DKC.

The series of absorption images for the condensed (B) and the thermal (C) ensemble with and without DKC application are depicted in Fig. 4.8. For comparison, the expansion of a condensate released from the shallow trap is given as well (A).

The expansion temperature of ensembles under the influence of DKC can be quantitatively determined with the chip-model and the λ-matrix formalism when using Bose-condensed sources. Here, we presented the experimental demonstration of a collimated matter wave packet and demonstrated the reduction of the expansion rate to nearly zero. In these ground-based measurements, we have been operating at the limit of what is technically measurable. A more reliable analysis of the expansion rate and the full potential of DKC in time-of-flight series can only be evaluated on the extended timescales provided by a microgravity environment (see Sec. 5.2).

Another method to investigate the finite expansion rate of an atomic cloud is given by a measurement of the Bragg diffraction efficiency. Bragg spectroscopy is a reliable method to directly measure the momentum width of freely expanding clouds and therefore allows to reliably quantify the cooling effect.

4.3.2 Beam splitter efficiency

The effect of a reduced momentum width can also be displayed in terms of an enhanced Rabi amplitude. More efficient beam splitters are useful for high-resolution interferometry applications, since any atom loss (e.g. due to imperfect beam splitters) will be directly translated into a loss of the measurement signal,

$$SNR \propto C \cdot \sqrt{N}, \tag{4.19}$$

with contrast C and number of detected atoms N. Since DKC reduces the expansion rate and therefore the momentum spread of the atomic clouds, a higher beam splitter efficiency can be expected for a given Fourier width of the Bragg pulses. We first compare the influence of DKC on the beam splitter efficiency for our already introduced degenerate and purely thermal source. The atomic gases have been released from the same steep trapping potential ($\omega_x \approx 2\pi \cdot 350$ Hz).

In Fig. 4.9, the first-order Bragg diffraction efficiency is shown while scanning the Bragg pulse duration τ from $0 - 400$ μs. To rule out influences of the COM velocity, the detuning of the Bragg lattice has been optimized for all investigated ensembles. It

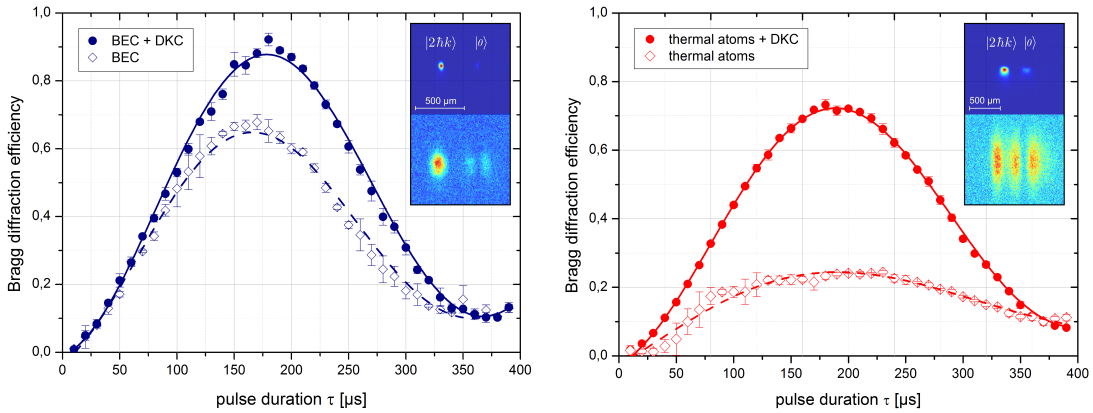

Figure 4.9: Rabi oscillations of a BEC (left) and a purely thermal source of atoms (right) released from the same steep trap ($\omega_x \approx 2\pi \cdot 350$ Hz). The application of DKC reduces the effective momentum spread of the ensembles which leads to an increase of the transfer efficiency (full circles). More details in text.

has to be noted, that the application time of the Bragg pulses has not been adapted to guarantee the same local intensity in the measurements. However, assuming the effect of our optimized DKC on the COM motion to be negligible here, the chosen timings (4 ms and 7 ms after release) correspond to intensity fluctuations of less than 3% (see Sec. 3.4.2). Thus, all measurements have been performed with nearly the same Rabi frequency which has not been optimized for the largest diffraction efficiency here. This exemplary measurement should generally demonstrate the effect of DKC on the cloud's momentum width, thus the Rabi frequency was fixed to a trade-off value to observe a comparably large cooling effect in both ensembles.

The magnetic lens (for explicit parameters see Sec. 4.3.1) has been applied $T_0 = 6$ ms after the release for $\tau_{dkc} = 300\ \mu$s. The Bragg pulse is applied 0.7 ms after DKC followed by a separation phase of $T_{sep} = 28.1$ ms until an absorption image is taken. Three experimental runs have been averaged and the error bars depict the standard deviation. A damped sine function is fitted to the data to extract the duration and efficiency for a π- pulse. For comparison, the absorption images at the measured

	η_π	
	BEC	thermal
w/o DKC	0.65	0.24
w DKC	0.88	0.72
rel. diff.	+35%	+300%

Table 4.2: Diffraction efficiencies η_π for a mirror pulse with Bose-condensed (left rows) and thermal atoms (right rows) released from the steep trapping potential ($\omega_x \approx 2\pi \cdot 350$ Hz). Note, these values have been extracted from exemplary measurements to demonstrate the effect of DKC on the momentum width (see Fig. 4.9). The Rabi frequency has not been optimized for the best diffraction efficiency here.

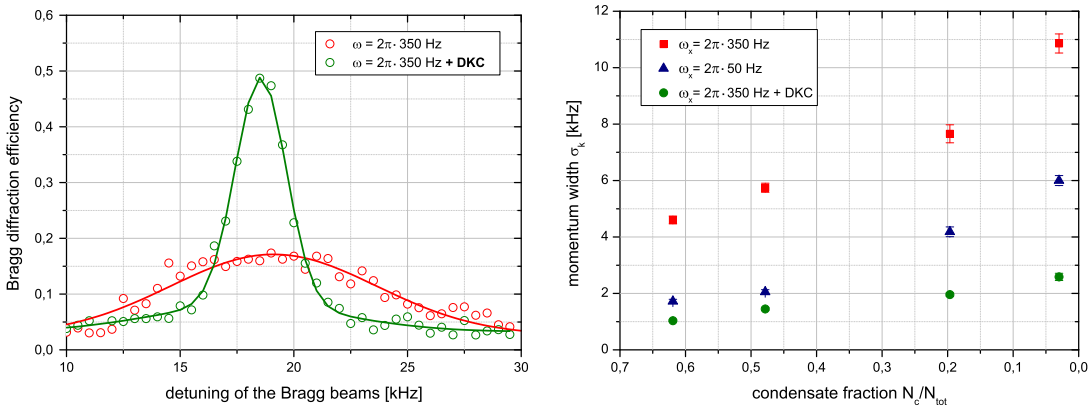

Figure 4.10: Exemplary Bragg spectra for condensates ($N_c/N = 0.62$) released from the steep trap with $\omega_x \approx 2\pi \cdot 350$ Hz (left). Without DKC, a simple Gaussian fit (red line) gives an rms width of $\sigma_{350} = 4.64(53)$ kHz. With DKC, the width of the central peak fitted by a double-Gaussian distribution leads to $\sigma_{350,dkc} = 1.52(12)$ kHz. Bragg spectroscopy measurements of differently prepared ensembles indicate a 4-fold reduction of the momentum width through DKC which is independent of the condensate fraction (right). The momentum width of a condensate released from the shallow trap is given for comparison.

π-pulse duration are given as an inlay.

In this configuration, the efficiency of a mirror pulse η_π using a condensate (Fig. 4.9, left) could be increased by about 35% (η_π from 0.65 to 0.88). The results show, that we can even reach higher diffraction efficiencies for condensates released from the steep trap with DKC compared to a condensate released from the shallow trap without DKC ($\eta_\pi \approx 0.8$, see Fig. 3.4.2). Moreover, with a measured increase of the diffraction efficiency of about 300% (η_π from 0.24 to 0.72), thermal gases profit even more of the delta-kick cooling scheme. The results are summarized in Tab. 4.2.

The increase in diffraction efficiency could not be directly verified by an increase in total atom number of the diffracted part of the wave function. This might be due to the high densities and small sizes of the clouds manipulated with DKC (which leads to an underestimation of the atom number) or loss effects during lens application, which have to be further analyzed.

Bragg spectroscopy

With Bragg spectroscopy (see Sec. 3.4.3), we can directly measure the momentum width of freely expanding clouds with and without the application of DKC. To demonstrate the basic measurement principle, a rectangular-shaped Bragg pulse was applied for a duration of $\tau = 600$ μs which scanned the momentum distribution 9 ms after the release of the steep trap. At first, no DKC was applied and the separation time of the adressed momentum states before imaging was $T_{sep} = 22$ ms. As a measure for the momentum width, a Gaussian was fitted to the data (red circles) and from the fit we obtain an rms width of $\sigma_{350} = 4.64(53)$ kHz (see Fig. 4.10, left).

In the second run, DKC was applied ($I_z = 1.85$ A, $B_{bias} = 6.1$ G) after an expansion

time of 8 ms for a duration of $\tau_{dkc} = 300\ \mu$s. The Bragg pulse was applied 1 ms later. The condensate fraction of only 62% leads to a significant bi-modality which is also present after application of the magnetic lens. Here, a double-Gaussian (green line) was fitted to extract the rms width of the center peak, which in this case is presumably Fourier-limited to about $\sigma_{350,dkc} = 1.52(12)$ kHz. This example already indicates a reduction of the momentum width by at least a factor of 3.

As we already have seen in the expansion measurements and corresponding absorption images, DKC is not only restricted to condensed sources and is even applicable for broader thermal distributions. By adjusting the end-frequency of the forced RF-evaporation (see Sec. 2.6.1), we can determine the temperature of the trapped gas and therefore the condensate fraction. Four different values of the latter have been analyzed via Bragg spectroscopy and the obtained momentum widths are given in Fig. 4.10 (right). The clouds have been released from the steep trap ($\omega_x \approx 2\pi \cdot 350Hz$) and evolved freely for $T_0 = 6$ ms before our optimized DKC trap ($I_z = 1.15$ A, $B_{bias} = 5.3$ G) was applied with a duration of $\tau_{dkc} = 300\ \mu$s. 4 ms later, Bragg pulses with Fourier-limited widths of about 250 Hz and 500 Hz have been applied for an accurate spectroscopy of the ensembles with and without DKC, respectively.

For each of the investigated condensate fractions, the momentum width σ_x of the freely expanding ensemble released from the steep trap (red squares), the ones manipulated with DKC (green squares) and ensembles released from the shallow trap (blue triangles) are given. This graph again underlines, that the application of DKC is not limited to condensed sources only. Specifically, the velocity width after DKC manipulation can be reduced by a factor of ~ 4 independent of the condensate fraction.

DKC allows to create samples which are colder compared to our most shallow trapping potential, we can create them faster since we do not need to evaporate until degeneracy and we do not need to wait for mean-field conversion but rather take a shortcut to adiabaticity [193]. However, regarding enhanced SNR in a matter wave interferometer, this method is only advantageous if the application of DKC does not lead to a reduced contrast (e.g. through disturbed matter wave fronts). Whether the spatial coherence can be preserved during DKC application will be investigated in the next section.

4.4 Delta-kick cooled atoms for matter wave interferometry

DKC was successfully applied to our atom-chip based source of matter waves. The next step is to image the phase evolution and prove the coherence of a delta-kick (DK) cooled ensemble in an open Ramsey-type interferometer (ORI) sequence (for details on the sequence, see Sec. 3.5.1). Therefore, the temporal evolution and contrast of fringe patterns emerging from spatially interfering condensates are investigated for different DKC configurations.

4.4.1 Fringe spacing evolution with time-of-flight

The BECs are released from a steep trapping potential ($I_z = 2\,A$ and $I_{bias} = 1.5\,A$) and expand for $T_0 = 8$ ms. Then a lens with $I_z = 1.3$ A is applied for $\tau_{dkc} = 400\ \mu$s until 4 ms later an ORI sequence with $T_{int} = 260\ \mu$s is applied to samples. For the

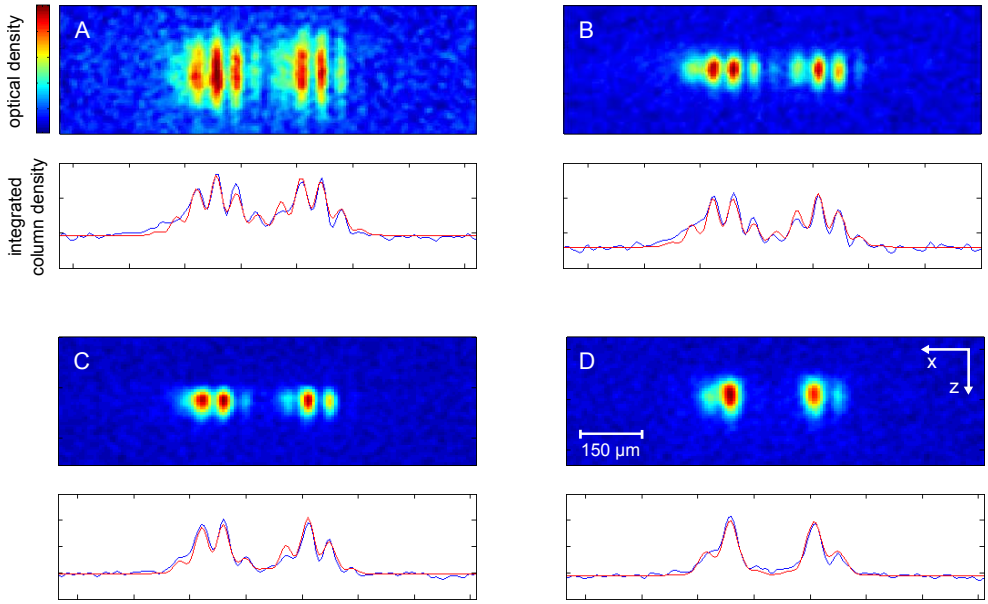

Figure 4.11: Exemplary images of the output ports of an open Ramsey-type interferometer (ORI) with DK-cooled Bose-Einstein condensates. From A-D, the momentum width of the condensate is reduced due to more efficient DKC whereas always the same ORI sequence is applied to the ensembles. The fringe spacing is inversely proportional to the velocity gradient across the cloud (see Sec. 3.5.1), thus it is larger for colder samples. More details in text.

DKC potentials used here, three different bias fields $B_{bias} = (2, 3, 4)\,\mathrm{G}$ have been investigated. The evolution of the fringe spacing is compared to that of a condensate released from the same steep trap but without DKC.

In the chosen configuration, an increasing magnetic bias field means that the position of the lens better coincides with the position of the wave packet at the application time and therefore leads to a smaller momentum width (cf. Sec. 4.2.2). This is depicted in the absorption images (see Fig. 4.11), where each picture corresponds to a total time-of-flight of $T_{tof} = 30.4$ ms. The left picture shows the fringe pattern without the application of DKC, and in the next three pictures B_{bias} is stepwise increased to a final value of $B_{bias} = 4$ G, for which the DKC trap center mostly coincides with the COM position of the condensate which maximizes the cooling effect.

Fig. 4.12 shows the corresponding fringe spacing evolution versus the total time-of-flight on ground. The given error bars are 1σ intervals of the fitted fringe spacing. The evolution of a freely expanding sample without DKC (black squares) coincides with the calculation of the fringe spacing in linear expansion theory (dashed line). With DKC, the evolution of the fringe spacing is still linear in time (fitted with straight lines), but the spacing features an offset which is to be proportional to the DKC strength and therefore to the final momentum width of the clouds after DKC application. The obtained slopes are given in Tab. 4.3 and will be discussed in the next section.

The measured contrast is depicted in Fig. 4.12 (right), where lines between the data points are added to guide the eye. For all configurations, no explicit influence of DKC

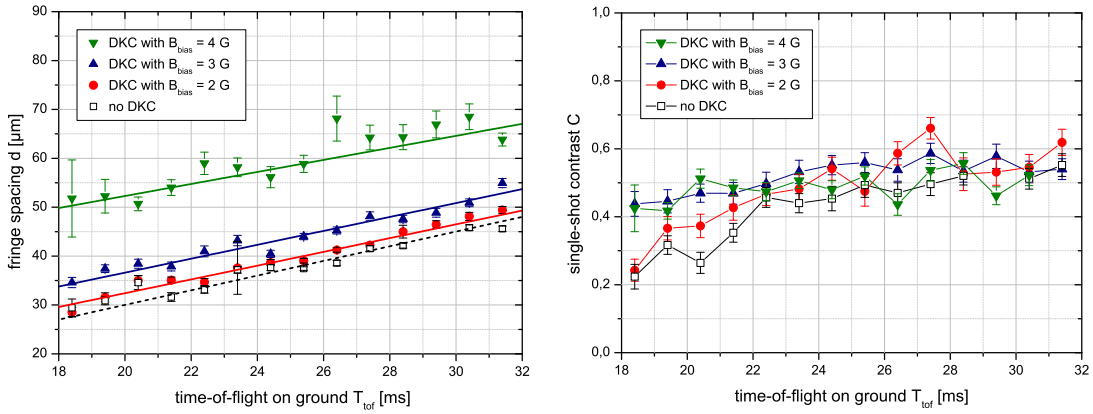

Figure 4.12: Influence of different DKC configurations on the fringe spacing of an ORI sequence (left) and the corresponding evolution of the single-shot contrast (right). Here, an increasing bias field B_{bias} means a more sufficient cooling due to a better overlap between DKC trap center and condensate COM. The slow-down of the wave packet expansion changes the velocity gradient across the cloud and leads to an offset of the observed fringe spacing as $d(t) \sim \lambda/\dot{\lambda}$ (see Eq. 4.20).

can be seen from the data which means that the magnetic manipulation does not necessarily lead to dephasing. The contrast even seems to slightly increase with ongoing time-of-flight T_{tof}, which might be attributed to the vanishing thermal atoms in the background. This was already observed in Sec. 3.5.3.

Scaling law approach for DKC

The spatial evolution of Bose-Einstein condensates manipulated with time-dependent DKC traps can be modeled with the λ-matrix formalism [130]. Based on the numerical results for the scaling factors for size λ_x and expansion $\dot{\lambda}_x$, the fringe spacing dynamics can be predicted as

$$d_{ori}(t) = \frac{2\pi}{\alpha \delta x} = \frac{\lambda_x(t)}{\dot{\lambda}_x(t)} \cdot \frac{h}{m \delta x}, \tag{4.20}$$

with phase curvature α, mass of the atoms m and the initiated separation in the Ramsey-type interferometer δx.

B_{bias} [G]	slope [μm /ms]
0 (no DKC)	1.44 (calculated)
2	1.42(8)
3	1.41(8)
4	1.23(19)

Table 4.3: Slopes and corresponding rms deviations of the linear fits to the experimental data of Fig. 4.12. For $B_{bias} = 0$ G (no DKC), the slope is calculated based on the far-field approximation of the fringe spacing evolution in an ORI (see Sec. 3.5.2).

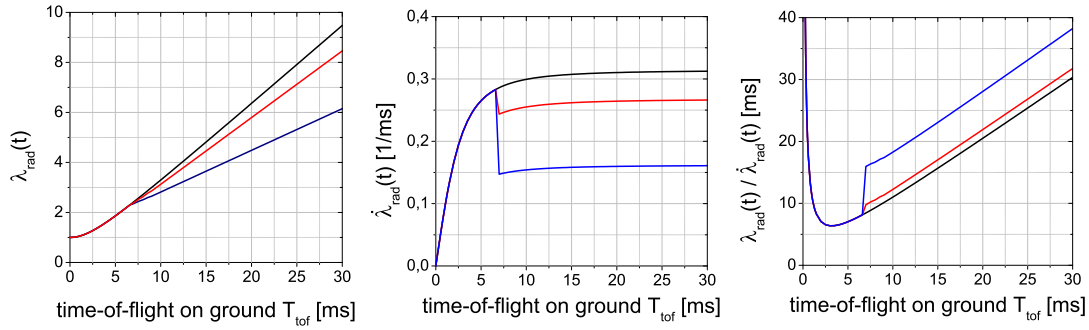

Figure 4.13: Schematic of the temporal evolution of the radial scaling factor $\lambda_{rad}(t)$ (left), the first derivative $\dot{\lambda}_{rad}(t)$ (center) and the fraction of $\lambda_{rad}(t)/\dot{\lambda}(t)$ (right) for free expansion and two artificial DKC operations applied after $T_0 = 7$ ms.

To visualize the general dependencies, however, an example for the evolution of the radial component of a condensate released from an elongated trap is given in Fig. 4.13. Without DKC, the evolution of λ, $\dot{\lambda}$, and the fraction $\dot{\lambda}/\lambda$ can be approximated by the solutions given in Sec. 3.5.2, which are illustrated for comparison (black lines). The application of DKC slows down the expansion rate of the ensemble. This is modeled by artificially reducing the radial scaling factor evolution to 85% (red line) and 50% (blue line) of the freely evolving condensate. Based on this, the derivative $\dot{\lambda}$ and the fraction $\lambda_x/\dot{\lambda}_x$ have been calculated and displayed.

Directly after the DKC, the condensate has roughly the same size as shortly before (left) but the expansion rate $\dot{\lambda}$ gets significantly reduced during the DKC (center). This is the reason for the instantaneous offset in $\lambda_x/\dot{\lambda}_x$ (right), which determines the fringe spacing period (see Eq. 4.20). In this simplified example, the fringe spacing slope is still roughly the same after the kick.

This is indeed what we observed in the experiment. The slopes are comparable within the fit errors (see Tab. 4.3) whereas the intercept continuously increases (See Fig. 4.12, left). One might argue a slight trend of the measured slopes to flatten with increasing B_{bias}. A possible explanation for this observation could be DKC-induced variations of the mean-field energy which have not been considered in the above depicted approximation. Due to the small size and expansion rate of the cloud after DKC application, the density does not decrease as quickly as without DKC which extends the phase of non-linear expansion. This rescales the fringe spacing evolution as previously discussed (see Sec. 3.5.2).

4.4.2 Scan of the DKC strength

The previous interference experiments with DK-cooled atoms showed a linear scaling of the fringe pattern with the time-of-flight and an offset proportional to the cooling effect. The more sufficient the mode overlap between condensate's COM and the DKC trap, the more efficient is the cooling which led to larger fringe spacings.

This is now addressed in another measurement by again investigating the fringe spacing evolution in an ORI. Here, we probe different DKC strengths by scanning the bias field B_{bias} of the previously applied DKC trap. The condensates released from a

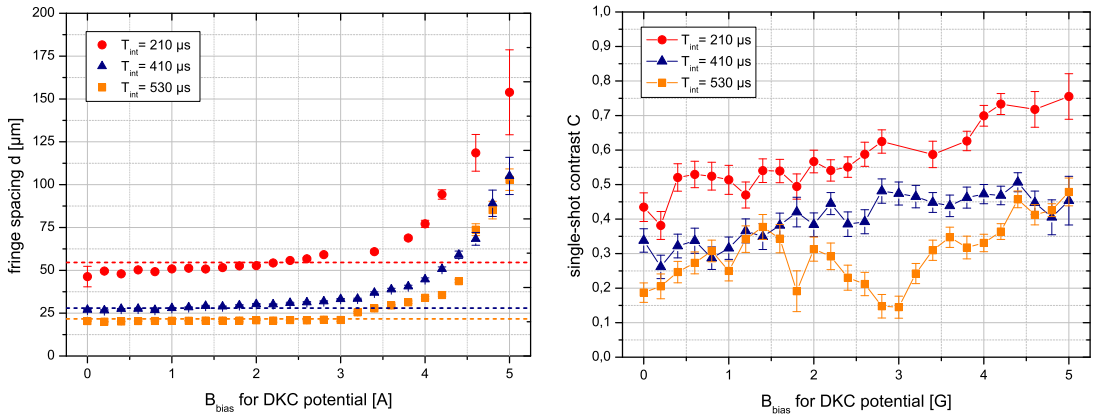

Figure 4.14: Fringe spacing evolution (left) and corresponding single-shot contrast (right) of three different ORI sequences with $T_{int} = (210,\ 410,\ 530)$ ms. The bias field B_{bias} for the DKC trap is subsequently increased which leads to a more narrow momentum width. The modified phase evolution of the DK-cooled wave packets leads to a larger fringe spacing.

steep trap ($I_z = 2\,A$ and $I_{bias} = 1.5\,A$) are manipulated in ORI sequences with three different initiated wave packet separations δx, determined by interrogation times fixed to $T_{int} = (210,\ 410,\ 530)\,\mu$s. DKC with a duration of $\tau_{dkc} = 400\ \mu$s has been applied $T_0 = 8$ ms after release and 4 ms later the ORI was operated. The absorption images have been taken at a total time-of-flight of $T_{tof} = 29.4$ ms. The chip current for the DKC potential was fixed to $I_z = 1.3$ A, whereas B_{bias} was scanned from 0 to 5 G.

For negligible influences of DKC (0 G $< B_{bias} <$ 2 G), the measured fringe spacing corresponds to the far-field approximation which is given as dashed lines for each T_{int} (see Fig. 4.14, left). By continuously moving the DKC center towards the COM position of the condensate (2 G $< B_{bias} <$ 5 G), the cooling gets more efficient. This again reduces the slope of λ and shifts $\dot{\lambda}$ to another offset which changes the fringe spacing to larger values.

The evolution of the contrast confirms earlier observations, that the application of DKC does not reduce the phase coherence of the manipulated sample. One might ascribe even higher contrasts due to the application of stronger DKC which makes it a valuable tool for long baseline atom interferometry.

4.5 Summary

As the third ingredient towards long-term matter wave interferometry at the Bremen drop tower, the on-chip realization of delta-kick cooking (DKC) was demonstrated for the first time. This included the implementation of DKC for condensed and thermal atoms as well as the analysis of relevant error sources affecting the center-of-mass (COM) motion. The net cooling effect was studied by a series of expansion and Bragg spectroscopy measurements.

By the choice of the right DKC trap parameters, the momentum width could be reduced by a factor of 4 (16-fold reduction of temperature). Moreover, these ground-

based results have been proven to be independent of the condensate fraction. This led to the observation of freely expanding samples with approximated expansion temperatures in the lower nK range.

DKC applied on matter waves as an input for light-pulse interferometers showed no additional dephasing on the corresponding timescales. However, DKC changed the phase evolution $\dot{\lambda}/\lambda$ of the expanding clouds. This affected the fringe pattern formation and therefore had to be considered for the specific choice of the interferometer timing parameters and the interpretation of the emerging pattern.

We thus have fulfilled the third requirement to be able to proceed to the drop tower for dedicated measurement campaigns:

Free-fall interferometry with Bose-Einstein condensates in microgravity (see Ch. 5)

- Atom-chip-based source of non-magnetic degenerate gases (see Ch. 2)
- ◇
- Bragg diffraction and open interferometers with degenerate gases (see Ch. 3)
- ◇
- Delta-kick cooling as a tool for long baseline atom interferometry

The next chapter will finally review our most recent results on the microgravity experiments with the QUANTUS-I experiment. After a short description of the drop tower and some basic procedures of a drop campaign, the macroscopic expansion of a Bose-Einstein condensates for up to 2 s of free evolution will be highlighted. After pathfinder experiments with an open Ramsey-type interferometer, we eventually discuss the first realization of an asymmetric Mach-Zehnder interferometer with Bose-Einstein condensates in microgravity.

5 Free-fall interferometry with Bose-Einstein condensates in microgravity

After implementation of an non-magnetic source of matter waves, Bragg interferometry and preparatory ground-based measurements with delta-kick cooling (DKC), this chapter summarizes the most recent experimental results of microgravity campaigns operated with the QUANTUS-I apparatus. The whole apparatus performs quantum gas experiments during free fall at the drop tower microgravity facility at the Center of Applied Space Technology and Microgravity (ZARM) in Bremen [107].

After a short introduction of the drop tower environment and the procedures of a standard drop campaign (see Sec. 5.1), we describe experiments with Bose-Einstein condensates in extended free fall, where the atoms are prepared in a non-magnetic state. In the beginning, we show that magnetic stray fields in the tower do not affect the free expansion of atoms in the $m_F = 0$ state. This suggests that indeed the residual fields are responsible for the anomalous expansion of magnetically polarized atoms as observed in the earlier runs of this experiment [19].

The scaling law for the temporal evolution of the condensate's width is introduced [130], whose prediction coincides with the experimental observations up to a maximum free expansion time of 2 s (see Sec. 5.2). The latter was only possible by application of our delta-kick cooling (DKC) scheme in the microgravity environment and constitutes the second largest free expansion time of a cold quantum object reported so far[1].

First interferometer experiments with degenerate gases in microgravity have been performed with an open Ramsey-type interferometer (see Sec. 5.3). In this configuration, macroscopic interference patterns of overlapping condensates after time-of-flights of 500 ms could be observed. The absence of a thermal background after such long evolution times consequently led to an improved contrast compared to ground-based measurements with our setup.

In an asymmetric Mach-Zehnder interferometer, the temporal evolution of the emerging fringe spacing was investigated with and without the application of DKC (see Sec. 5.4). To this end, contrast and signal-to-noise (SNR) ratio have been analyzed for maximum interrogation time of up to $2T - \delta T = 677$ ms. In this campaign, interference has been observed for quantum objects separated over distances which exceed their size by one order of magnitude. These experiments demonstrate the feasibility of operating an atom-chip-based matter wave interferometer under demanding conditions. They will pave the way for future microgravity-enhanced experiments dedicated to differential acceleration measurements with ultra-cold matter waves.

[1] In [110], a Bose-Einstein condensate is launched in an atomic fountain geometry and imaged after $T_{tof} = 2.6$ s of free expansion.

5.1 The drop tower and standard procedures of a free fall campaign

The drop tower is a microgravity facility of the ZARM (Center of Applied Space technology and Microgravity) at the University of Bremen, Germany. It has a total height of 145 m, of which effectively 110 m can be used as free fall distance. The drop tube, formed by multiple tube segments that are welded together, has to be evacuated to a final pressure below 0.2 hPa before operation. Evacuation is necessary since residual air friction would lead to vibrations and decelerations of the drop capsule in free fall, lowering the level of reduced gravity. Additionally, the deceleration process is based on catching the capsule in a container with polystyrene pellets which in principle could lead to large electromagnetic charges, getting inflamed in combination with oxygen. As a consequence of this evacuation, the quality of microgravity is relatively high compared to, for example, zero-g airplanes [106]. Typically, the drop tower provides $\Delta g/g < 10^{-5}$ for frequencies below 500 Hz [107].

As already shown for the QUANTUS-I experiment in Sec. 2.4, payloads need to be integrated within standardized drop capsules to be approved for drop tower operation. The latter comprises a drop and a catapult mode, which offer microgravity durations of 4.7 s and 9.2 s, respectively.

QUANTUS-I is designed for the drop mode, of which a typical timeline describing the preparatory steps of a campaign will be given in the following section.

5.1.1 Typical timeline of a standard campaign

After switch-on and subsequent verification of the experiment's performance in the lab, the capsule is prepared for handover to the drop tower operators. Together with us as the responsible scientists team, the setup is finally checked (e.g., unfavorable integrated electrical connectors, loose components) and capsule closed (see Fig. 5.1, left). First, an outer shell is pulled over the experiment and fastened with a mechanical buckle, which takes place in the integration hall. Then the experiment is moved into the drop tower, where an upper shell including all relevant interfaces (electrical connectors, thermal-control system (TCS), remote control capability) is fixed at the top (see Fig. 5.1, right). Afterwards, a winding mechanism connected to the upper shell smoothly lifts the capsule to the top of the tower in about 15 min.

After elevation to about 110 m, telemetry and telecommand line are checked and remote control access is established. Additionally, TCS and power supplies are connected to the interface. This allows to test the basic status of the different subsystems (e.g., UHV pressure, laser power and frequency locks) as well as the functionality of the entire experiment. The latter is usually done by operating a standard sequence generating Bose-Einstein condensates. Atom number and temperature of a condensate released from the shallow trapping potential are compared to the values from the aforementioned ground check. If successful, the evacuation of the entire tower is started which typically leads to a typical final pressure of 0.2 hPa in about 1.5 hours of operation.

The long evacuation time is the main reason why the drop tower can be operated with at most 3 drops per day. In the case of any unforeseen problems, either on the

Figure 5.1: Final check of the QUANTUS-I payload by the science team[2], which is usually done in the integration hall before hand-over to the drop tower operators (left). Closing of the capsule with an upper shell and preparation for lift-up with a winding mechanism is done by the operators (right).

scientist's or operator's side, the capsule is safely brought back to the ground via the winding mechanism.

After evacuation, external supply units (DC power and cooling) are disconnected and the drop tower operators assign the approval for the drop to the scientist team. Before and after this disconnection process, we again verify the functionality of the experiment by running our standard BEC sequence, which is particularly important for comparing the performance by switching to accumulators. Moreover, the obtained position of the condensate in these absorption images serves as a reference for evaluating the center-of-mass motion in the following drop experiment. If all tests are successfully passed, we release the experiment and perform our measurements in extended free fall.

In the drop mode, free fall lasts for about 4.7 s during which the capsule accelerates to vertical velocities of about 170 km/h. It is finally caught in a 8 m high deceleration tube containing polystyrene pellets, which act as a viscous fluid smoothly decelerating the capsule. However, the experiment has to withstand peak decelerations of up to 50 g lasting for $\sim$ 100 ms during this impact (see Fig. 5.2, left). Permanent monitoring of the most important parameters (e.g., UHV pressure, temperature, battery voltage, laser power) is implemented, but to actively verify the status of the system after the mechanical shock, we routinely generate a condensate while the capsule is still in the deceleration tube.

Right after the impact, the tower is re-flooded with air. About 45 min later, the capsule will be opened again by the drop tower operators and handed back to the scientists for thorough investigation and preparation of the upcoming drop.

[2]QUANTUS-I science team from left to right: A. Wenzlawski, M. Krutzik and H. Müntinga. Unfortunately, H. Ahlers is missing in these pictures as being the photographer.

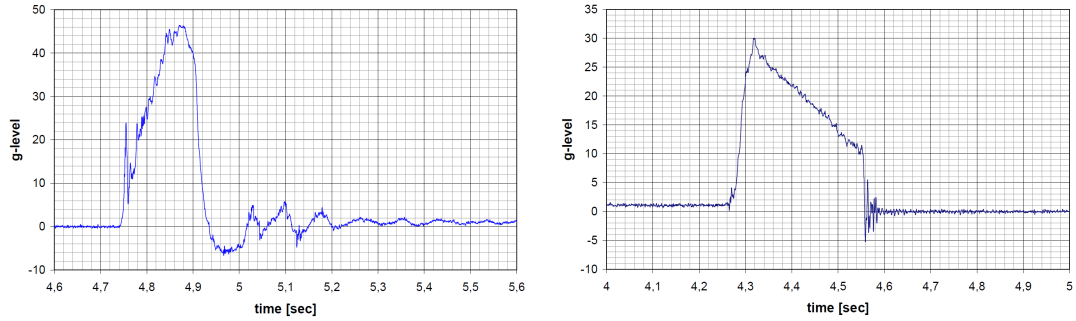

Figure 5.2: Typical decelerations by slowing down a capsule in the polystyrene pool (left) and DC accelerations of a catapult launch (right). Plots taken from [107].

Catapult mode

The QUANTUS-I experiment uses the drop mode only. The successor experiment QUANTUS-II is designed for using the catapult mode of the drop tower, leading to nearly twice the time of free fall.

In the catapult mode, the capsule is launched from the bottom of the tower in a vertical parabola to the top. There are even more demanding requirements on the payloads mass and volume [107]. After the capsule is closed by the operators, it is positioned on a catapult piston. After evacuation and approximately 10 minutes before the launch, supply units (DC power and cooling) are disconnected and the catapult system is armed. The catapult piston is moved down to the final position and from now on a 5 min time window allows the scientists to finally check the system and initiate the launch.

The acceleration is induced by a pneumatic mechanism with an approximate duration of 280 ms and a peak value of 30 g (see Fig. 5.2, right). There is a slight time delay between launch initialization at $T_{ini} = 0$ s and execution, which causes the acceleration peak to be centered around $T_{launch} \approx 4.4$ s. During the free fall parabola, the deceleration chamber is placed exactly at the position of the impact. In this mode, the microgravity experiment time can be extended from 4.7 to about 9.2 s. All interfaces of the catapult capsule are identical to the one used in the normal dropping mode.

We now focus on the results of the QUANTUS-I apparatus probing the coherent evolution of Bose-Einstein condensates in extended free fall.

5.2 Condensate expansion and delta-kick cooling in microgravity

In 2010, the QUANTUS collaboration succeeded in realizing first degenerate quantum gases of ^{87}Rb atoms in microgravity. After optimization of the decompression phase and the adiabatic release, condensates with expansion times of up to 1 s could be detected [17].

However, the observed expansion of the BEC along its weak axes did clearly not correspond to a free evolution. One possible explanation for the anomalous temporal

evolution of the spatial width has been sub-Hertz residual magnetic fields interacting with the atoms during the drop. The drop tower itself is not designed to meet the requirements of magnetically sensitive experiments. It is built out of soldered tubes and metal constructions, potentially leading to static and dynamic stray fields. Another source could have been for instance a residual magnetization of the vacuum chamber. Since the condensate at that time remained in the spin polarized $|F = 2, m_F = 2\rangle$ state after the release, tiny fields could have led to an effective force acting on the atoms even though a single-layer μ-metal shield was used [137].

To circumvent this, we implemented an adiabatic rapid passage (ARP) in microgravity to transfer the atoms in the $m_F = 0$ state (see Sec. 2.7). This Zeeman sublevel is to first order insensitive to magnetic fields and should enormously reduce the effect of present magnetic fields. The first experiments now to be performed in microgravity are dedicated to confirm a free evolution according to the scaling law prediction — or to raise new questions concerning the expansion dynamics of Bose-Einstein condensates in microgravity.

We first discuss a suitable and commonly used theoretical model to describe the free expansion of Bose-Einstein condensates.

5.2.1 Scaling law for time-dependent potentials

In Sec. 2.2.3, the Thomas-Fermi (TF) approximation for a description of the condensate's density distribution in a trap was introduced. This approximation is based on disregarding kinetic energy w.r.t interactions, thus it is not valid to analyze the free expansion of a condensate after release from the trapping potential. Once in free fall, the internal energy is converted into kinetic energy and hence not negligible anymore. First calculations towards the expansion of a condensate by changing the trapping parameters or the external potential U_{ext} have been carried out by numerically solving the Gross-Pitaevskii (GP) equation [128]

$$\left[-\frac{\hbar^2}{2m}\Delta + U_{ext}(\vec{r}) + g\phi^2(\vec{r})\right]\phi(\vec{r}) = \mu\phi(\vec{r}), \tag{5.1}$$

with interaction strength $g = 4\pi\hbar^2 a/m$, chemical potential μ and condensate wave function $\phi(\vec{r})$.

Another approach dedicated to time-dependent potentials was given by Y. Castin and R. Dum, who extended a scaling formalism for isotropic potentials introduced by Kagan [129] to three dimensional, anisotropic harmonic potentials [130]. They motivated a quantum mechanical calculation with a classical ansatz, describing the ballistic motion of the particles within the condensate, released from a potential characterized by a set of time-dependent eigenfrequencies $\omega_i(t)$.

In TF approximation, the density distribution of a Bose-Einstein condensate in an external potential is given by

$$n_{TF}(\vec{r}) = \left|\Phi(\vec{r})^2\right| = \max\left\{\frac{\mu - U_{ext}(\vec{r})}{g}, 0\right\}. \tag{5.2}$$

In a classical model, the effective force acting on every single particle of the ensemble

can be written as

$$\vec{F}(\vec{r},t) = -\nabla(U_{ext}(\vec{r},t) + g \cdot n(\vec{r},t)). \tag{5.3}$$

For time-dependent potentials, we are assuming the shape of the density distribution to remain constant, but the atoms move based on a scaling approach like

$$R_i(t) = \lambda_i(t) R_i(0), \tag{5.4}$$

with the position of atoms in the i-th dimension $R_i(0)$ at time $t = 0$ and the scaling factors λ_i. The entire evolution of the coordinates $R_i(t)$ is then described by Newton's equation of motion $m\ddot{R}_i(t) = F_i(\vec{R}(t), t)$, and we obtain a set of differential equations for the scaling factors [130, 127]

$$m\ddot{\lambda}_i(t) R_i(0) = -(\partial_{r_i} U_{ext})[\vec{R}(t), t] + \frac{1}{\prod_j \lambda_j(t)} (\partial_{r_i} U_{ext})[\vec{R}(t), t]. \tag{5.5}$$

For harmonic potentials with trapping frequencies ω_i, the scaling factors of all three dimensions are proportional to $R_i(0)$ and we get

$$\ddot{\lambda}_i = \frac{\omega_i^2(0)}{\lambda_i \prod_j \lambda_j} - \omega_i^2(t)\lambda_i. \tag{5.6}$$

This expression can be used to calculate the dynamics of the density distribution under modification of the external potential, including instantaneous switch-off. At time $t = 0$ we release the Bose-Einstein condensate from the confining potential and set $\omega_i(t > 0) = 0$. The holding trap in QUANTUS-I can be approximated as an axial symmetric trap ($\omega_x = \omega_z \equiv \omega_{rad} \gg \omega_y$). In this case, Eq. 5.6 can be solved analytically, leading to the following set of coupled differential equations [130, 127]

$$\frac{d^2}{d\tau^2}\lambda_{rad} = \frac{1}{\lambda_{rad}^3}, \tag{5.7}$$

$$\frac{d^2}{d\tau^2}\lambda_y = \frac{(\omega_y/\omega_{rad})^2}{\lambda_{rad}^2 \cdot \lambda_y^2}, \tag{5.8}$$

with a dimensionless variable $\tau = \omega_{rad}(0)t$. The temporal expansion of the width in the radial (W_{rad}) and axial (W_y) direction can now be written as

$$W_{rad}(\tau) = W_{rad}(0)\lambda_{rad}(\tau) = R_{rad}^{tf}\sqrt{1+\tau^2}, \tag{5.9}$$

$$W_y(\tau) = W_y(0)\lambda_y(\tau) = R_y^{tf}\left(1 + \epsilon\left(\tau \arctan\tau - \ln\sqrt{1+\tau^2}\right)\right), \tag{5.10}$$

with the TF radii $R_{rad}^{tf} = \sqrt{2\mu/m\omega_{rad}^2}$, $R_y^{tf} = \sqrt{2\mu/m\omega_y^2}$ and $\epsilon = \omega_y/\omega_{rad}$. Given a series of expansion pictures, we can calculate back the density distribution in the final trapping potential. One can see, that the aspect ratio $\eta = W_{rad}/W_y$ is completely independent from the number of atoms or the chemical potential. In the TF-approximation, the temporal evolution of the aspect ratio depends only on the trapping frequencies

and can be used to verify the existence of a BEC [69, 67, 115].

The detection axis of the QUANTUS-I setup utilized in this thesis coincides with the weak axis of the trap (y-direction), thus a change of the aspect ratio according to Eq. 5.9 and 5.10 cannot be observed[3]. However, we will use the scaling approach for verification of the BEC's free expansion. The evolution of the visible axes will be analyzed in microgravity experiments with time-of-flights of up to 2 s.

5.2.2 Experimental drop tower sequences with QUANTUS-I

Before we describe an experiment in free fall, we first recall the typical situation right before the drop (see Sec. 5.1.1). The capsule is hanging at the top of the drop tower and any external supply units (DC power and cooling) are disconnected. After assignment of approval for the drop and a final test, we start the actual drop sequence by collecting atoms in the MOT while the capsule is still hanging at the top. Once the MOT is saturated ($\sim$ 10 s), we release the capsule. For the particular experimental phases which are now performed in free fall, see Fig. 5.3.

The remaining period of the MOT phase lasts for an additional second, to let any residual vibrations damp out which occur during the release process of the capsule. Subsequently, the atoms are further cooled in a short ($\sim$ 4 ms) molasses phase, optically pumped into the $m_F = 2$ state and transferred into the chip-based Ioffe-Pritchard trap (IPT). After roughly 1.7 s, the atoms are evaporatively cooled down to degeneracy (BEC) and prepared in a final holding trap.

Once in microgravity, no gravitational sag deforms the trapping potential and therefore shallower traps than on ground can be realized [17, 137]. Hence, the condensate is adiabatically decompressed into a holding trap with $I_{bias} = 0.179$ A and trapping frequencies along the principal axes of $\omega_i = 2\pi \cdot (27, 10, 22)$ Hz [17], compared to the most shallow ground configuration ($I_{bias} = 0.36$ A, $\omega_i = 2\pi \cdot (46, 18, 31)$ Hz, see Sec. 2.6).

An optimized delta-kick cooling (DKC) sequence is applied 30 ms after the release. Here, the same holding trap with $2\pi \cdot (27,\ 10,\ 22)$ Hz generated by the atom chip is switched on again for $t_{dkc} = 2$ ms. The experiments in the next sections will specifically compare the free expansion of condensates with and without DKC and their applicability for matter wave interferometry.

In a next step, the BEC is transferred into the $m_F = 0$ state, realized by an ARP lasting for 3.8 ms applied 4 ms after DKC. Efficient RF sweeps have been demonstrated in ground based measurements (e.g., $\nu_{rf} = 7.70 \rightarrow 7.74$ MHz @ 10.5 G, see Sec. 2.7). Due to the magnetic environment in the drop tower, the parameters of the ARP had to be slightly adapted to maintain the same efficiency in microgravity ($\nu_{rf} = 7.71 \rightarrow 7.75$ MHz @ 10.5 G).

After preparation of the matter wave source, approximately 2 s are available for experimental studies of a microgravity-enhanced Bose-Einstein condensate (see Fig. 5.3). We will analyze the temporal evolution of the Thomas-Fermi radius in free expansion (EXP), the fringe spacing and contrast of open Ramsey-type interferometers (ORI) and finally the coherent phase evolution in asymmetric Mach-Zehnder interferometers (AMZI).

[3] In the predecessor setup [17], the camera was oriented along the x-direction.

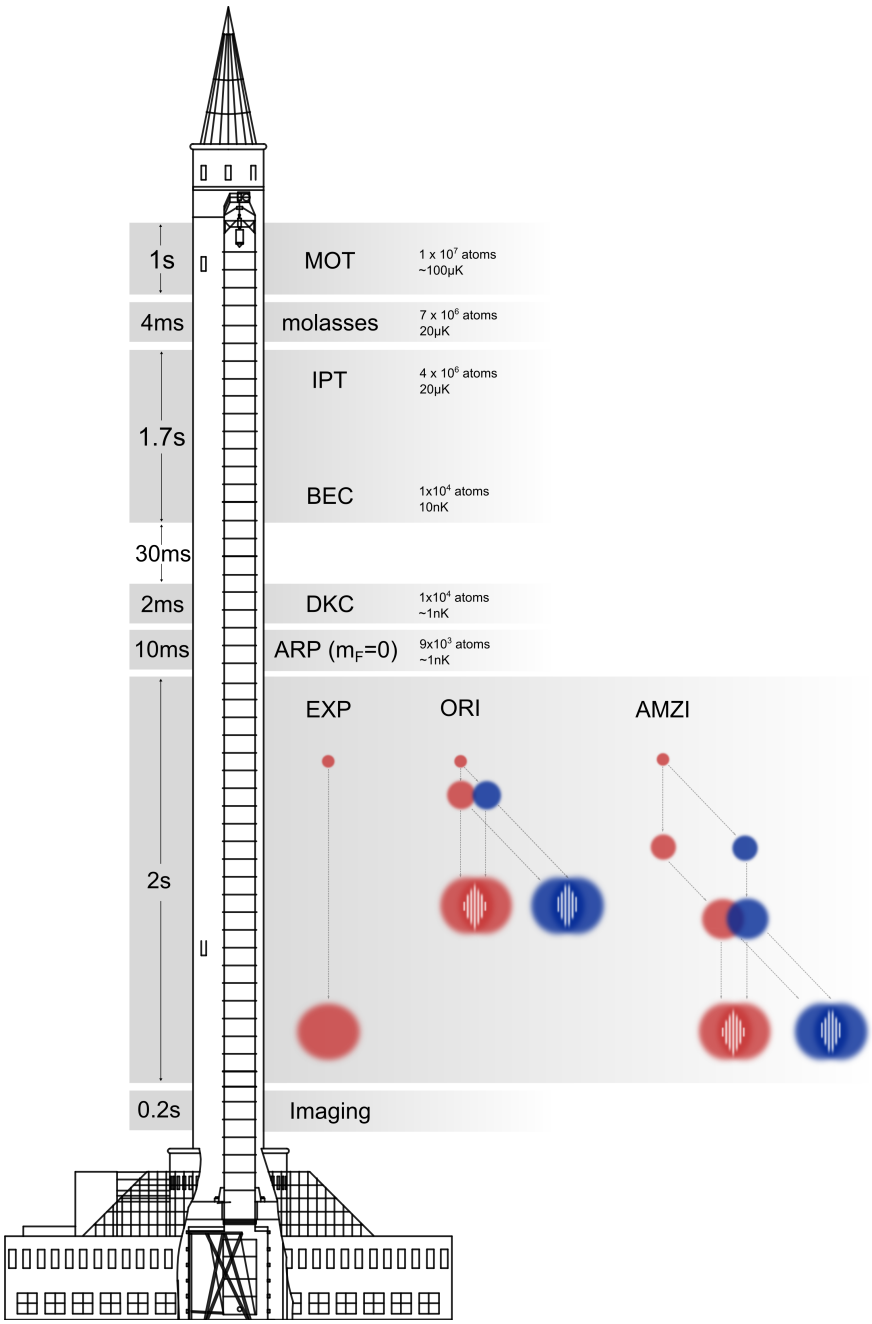

Figure 5.3: Typical timescales, atom numbers and average temperatures for the particular experimental phases of QUANTUS-I in free fall. After preparing cold atoms in a MOT and subsequent molasses phase, they are loaded into an atom-chip-based Ioffe-Pritchard trap (IPT) and evaporatively cooled to degeneracy (BEC). After adiabatic release, the atoms undergo magnetic delta-kick cooling (DKC) and are transferred into the $m_F = 0$ state by means of an adiabatic rapid passage (ARP). The conducted experimental studies comprise free expansion (EXP), an open Ramsey-type interferometer (ORI) and an asymmetric Mach-Zehnder interferometer (AMZI). Shortly before the impact, an absorption image is taken.

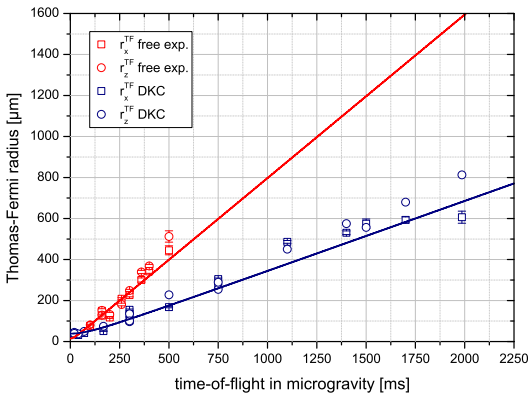

Figure 5.4: Expansion data expressed by Thomas-Fermi radii of freely evolving Bose-Einstein condensates with and without DKC.

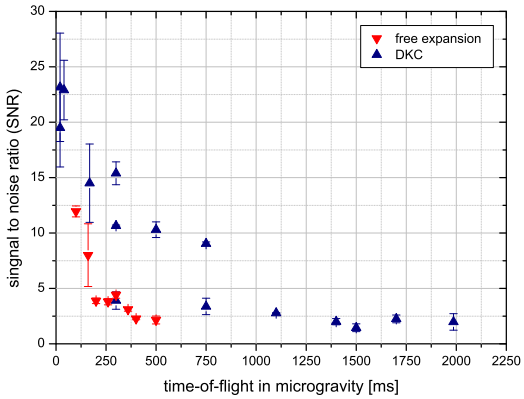

Figure 5.5: Corresponding signal-to-noise ratio (SNR) of the integrated atomic density with and without DKC.

At all times, the atomic cloud or the interferometer output ports are detected after a time-of-flight by means of absorption imaging[4].

5.2.3 Free expansion of a Bose-Einstein condensate for 2 seconds

We will now discuss the results of the drop campaign with BECs in the $m_F = 0$ state.

The expansion of the condensate expressed by the Thomas-Fermi (TF) radii including fitting error is given for up to 500 ms of time-of-flight under microgravity conditions (see Fig. 5.4, red squares). The detection axis points along the weak axis (y-direction) of an trapping potential with $\omega_i = 2\pi \cdot (27, 10, 22)$ Hz. To get an estimation for the condensate expansion dynamics, we say $\omega_x \approx \omega_z \equiv \omega_{rad}$ and fit the averaged condensate widths in x- and z-direction using the scaling approach for elongated traps [130], which predicts the width in the radial direction $R^{rf}_{rad}(t)$ for $\omega_{rad} \gg \omega_y$ as

$$R^{tf}_{rad}(t) = \sqrt{\frac{2\mu}{m\omega^2_{rad}}} \cdot \sqrt{1 + (\omega_{rad} \cdot t)^2}. \tag{5.11}$$

From the fit (solid red line in Fig. 5.4) we extract an effective radial trapping frequency of $\omega_{rad} = 2\pi \cdot 20(3)$ Hz, which is slightly below what we expect from the initial trapping frequencies along the principal axes and simulated data from [137, 17]. In the latter it was argued, that the initially elongated trap is tilted both in the horizontal plane and in the z-direction during adiabatic decompression. Since in this case the principal axes of the condensate in free fall now do not perfectly overlap with the camera axes, one might argue a slight projection error of the Thomas-Fermi radii. This would correspond to the lower value of the trapping frequency obtained by the fit.

Besides this, the observed temporal evolutions correspond to the theoretical predictions based on the scaling approach for unperturbed condensate dynamics in the Thomas-Fermi regime. Based on this analysis in the first $T_{tof} = 500$ ms of free ex-

[4]The detection intensity is increased from $0.2 \cdot I_{sat}$ to well above of the saturation intensity.

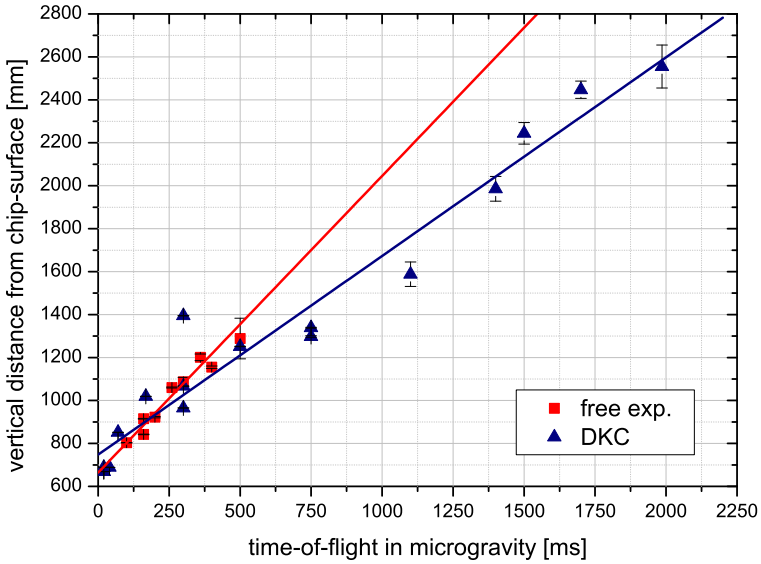

Figure 5.6: Temporal evolution of the center-of-mass (COM) position in z-direction. The distance of the COM w.r.t. the atom chip's surface is depicted for condensates evolving in the $m_F = 0$ state (red squares) and for ensembles previously manipulated with delta-kick cooling (blue triangles). A straight line can be fitted to the data sets which determines a constant velocity in z-direction of $v_z = 1.17(15)$ mm/s and $v_z = 0.93(5)$ mm/s, respectively.

pansion, the radial axis (as an average of the x- and z- direction) shows no obvious deviation from the theoretical prediction. However, the weak axis (y-direction) could not be observed in this geometry. A thorough analysis of the condensate evolution in all three dimensions and the corresponding center-of-mass (COM) motion using a detailed chip model can be found in [113].

The signal-to-noise ratio (SNR) drops rapidly since condensate expansion reduces the atomic density and makes it challenging to detect atoms after 500 ms of free expansion (red triangles in Fig. 5.5). Here, SNR is averaged over both visible dimensions and the error bars depict the corresponding standard deviation. At these timescales, the condensates typically containing $N = 10^4$ atoms usually feature Thomas-Fermi radii of about 500 μm.

The knowledge of the COM position and velocity of the condensate w.r.t. the atom chip surface is important for the upcoming matter wave interferometry experiments. Since both the experimental apparatus and the condensate are in free fall, the COM position should ideally be constant over time, meaning no effective velocity. However, if there is a velocity, one has to distinguish between the two visible dimensions. Slight COM velocities along the beam splitter axis (x-direction) can be equalized by an adjustment of the effective detuning and power broadening of the beams. Vertical accelerations will cause wavefront errors. We only focus on the vertical distance for now.

The position of the condensate is measured w.r.t. the coordinate system of the CCD camera. The accuracy of this method from drop to drop obviously relies on the

stability of the camera position which eventually varies since decelerations of 50 g also affect the camera mounting. In order to compare different drops, either the atom chips surface itself is constituting an absolute reference or the reference pictures right before the drop are used to evaluate the COM position of the condensate in free fall. The first method is obviously only possible if the atom chip is visible in the absorption image. However, the edge is out of focus and the exact position hard to determine. This potentially leads to errors in the estimation of the relative distance of the atomic cloud to the edge.

The estimation of the COM position in the vertical direction is depicted as red squares in Fig. 5.6. The error bars represent fitting errors of the atomic position but do not take errors in the estimation of the atom chip's edge into account. The z-position is not constant over time as a straight line can be fitted to the data which gives rise to a constant velocity of $v_z = 1.17(15)$ mm/s away from the chip surface. This velocity could arise from imperfect switching processes of the magnetic fields or inhomogeneities of the strong bias fields for the ARP. This velocity will again be addressed in the discussion of contrast loss in an asymmetric Mach-Zehnder interferometer (see Sec. 5.4.3).

The transfer of atoms in the $m_F = 0$ state has led to the observation of an unperturbed free evolution along the radial dimension with a finite velocity away from the chip. However, this observations have been limited to free expansion times of $T_{tof} = 500$ ms. To overcome the observed limitations in SNR and to reach even longer free evolution times in microgravity, we have to apply delta-kick cooling (DKC) the atoms get transferred intp the $m_F = 0$ state.

Delta-kick cooling in microgravity

To reduce the kinetic energy and therefore the expansion rate of a condensate, delta-kick cooling (DKC) was implemented in the experimental sequence. The corresponding results of time-of-flight measurements are shown as blue data points in Fig. 5.4 and 5.5. As already mentioned, the BEC is adiabatically released from the holding trap and expands for about $T_0 = 30$ ms. Then, the same trap with trapping frequencies of $\omega_i = 2\pi \cdot (27, 22, 10)$ Hz generated by the atom chip is switched on for $t_{dkc} = 2$ ms. No adaption or further modeling of the DKC trap is necessary. The microgravity environment ensures a high mode overlap of the condensate's wave function with the holding trap, thus the linear approximation of the DKC trap is still valid yielding a position-independent field curvature.

However, the COM position in the z-direction is slightly changing due to the imperfect release process and the interaction of the atoms ($m_F = 2$ state) with residual fields (see Fig. 5.6). Compared to the ground-based experiments with nearly radial-symmetric DKC traps, the anisotropy of the DKC trap in microgravity results in an independent set of optimized parameters for each visible dimension (see Sec. 4.2.2).

Hence, the timing T_0 and the duration τ_{dkc} had to be optimized experimentally to result in the best trade-off between (i) isotropy of the atomic distribution, (ii) cooling effect and (iii) residual COM motion after application [111]. This was done in a similar way as previously shown for ground-based experiments (see Sec. 4.2).

After the kick, the atoms are coherently transferred to the $m_F = 0$ state and detected

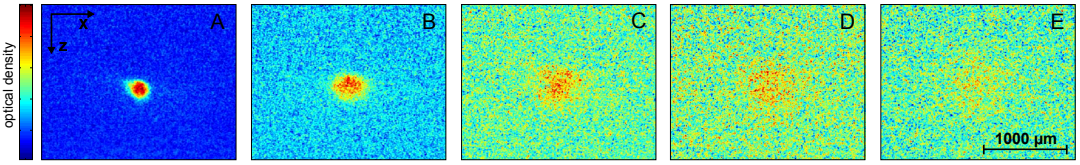

Figure 5.7: Gallery of absorption images of freely expanding BECs in microgravity. The condensates are formed in the $|F = 2, m_F = 2\rangle$ state, manipulated with DKC and afterwards transferred into the $m_F = 0$ state by means of an ARP. The time between initial release and absorption image shown in the pictures is 300 ms (A), 750 ms (B), 1050 ms (C), 1400 ms (D), and 1700 ms (E).

for different time-of-flights T_{tof}. The ARP itself was proven to yield the same transfer efficiency in microgravity, also in combination with DKC.

The expansion rate can be drastically reduced by applying a short magnetic pulse to the atoms (see Fig. 5.4, blue squares). Despite of the anisotropy of the used trap for DKC, the spatial shape of most of the detected clouds can be approximated as isotropic[5]. A quantitative prediction of the evolution of the Thomas-Fermi radii can be given by a numerical simulation based on the λ-matrix formalism for the condensate dynamics in time-dependent traps [130]. As a measure for the reduction of expansion energy, the solution for an elongated trap (Eq. 5.11) is fitted to the averaged Thomas-Fermi radii in both visible dimensions (blue curve). From this, we obtain trapping frequencies and initial condensate sizes which may now be interpreted as trapping parameters, which would lead to the observed expansion without applying DKC. Following that, an adiabatic release from a holding trap with trapping frequencies of about 1 Hz would be necessary to yield a similar expansion rate.

The observed temporal evolution give rise to effective temperatures of ~ 1 nK and clearly demonstrates that DKC leads to a reduced expansion rate. This is accompanied by higher densities of the clouds leading consequently to a higher SNR (see Fig. 5.5, blue triangles). Only with DKC we have been able to observe the BEC via absorption imaging after 2 seconds of free evolution, which is twice as long as in previous experiments [17] and the world's second longest free expansion of a condensate to our knowledge (cf. [110]). A gallery of absorption images for different time-of-flights between 300 ms and 1700 ms is shown in Fig. 5.7. Here, each picture is individually normalized and centered around the cloud's density maximum.

The COM position in z-direction is given in Fig. 5.6 (blue triangles). Compared to the free expansion of atoms in the $m_F = 0$ state, the application of DKC seems to slightly slow down the velocity away from the chip. Fitting a straight line leads to a velocity of $v_z = 0.93(5)$ mm/s, indicating that DKC induces a weak momentum kick in the direction of the atom chip. Taking the ground-based investigations of a mismatch between condensate COM and DKC trap center into account (see Sec. 4.2), this means that the atoms already passed the DKC trap center at the time of application.

We have constituted a predictable source of ultra-cold matter waves in microgravity on timescales clearly superior to the predecessor setup. This was made possible by

[5]However, the slight asymmetry becomes visible for time-of-flight after 1500 ms.

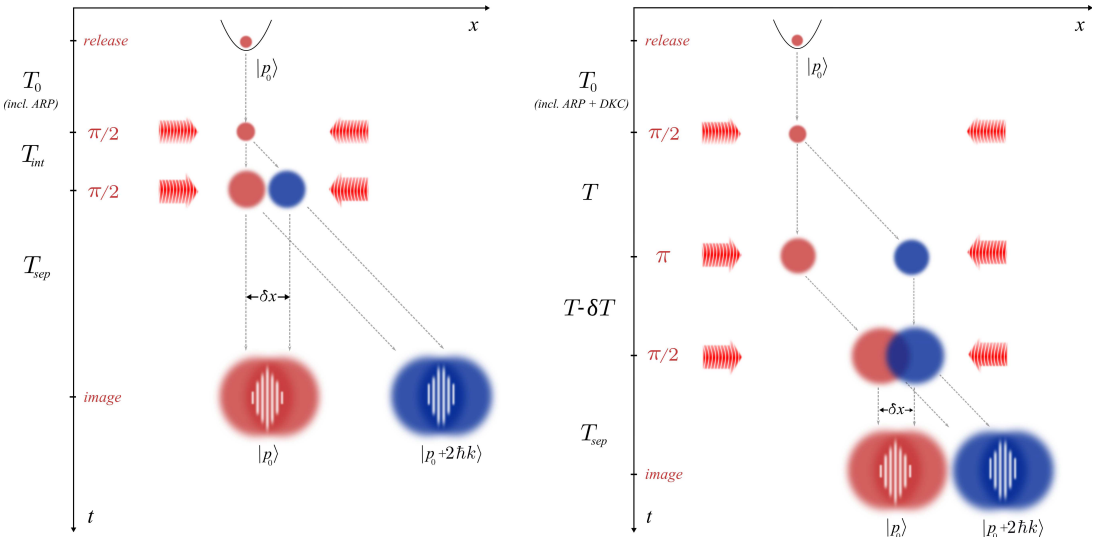

Figure 5.8: Schematic of an open Ramsey-type (ORI, left) and an asymmetric Mach-Zehnder interferometer (AMZI, right) operated in microgravity. For general details on the pulse sequence, see Sec. 3.5.1 and 3.5.4, respectively. The total time-of-flight T_{tof} in each geometry is given by the time between release and imaging. In this schematics, T_0 includes the operation of the adiabatic rapid passage (ARP) and delta-kick cooling (DKC) where applicable.

the use of delta-kick cooling and an adiabatic rapid passage, both implemented on chip. Now, the first interferometry experiments with Bose-Einstein condensates in microgravity will be described.

5.3 Open Ramsey-type interferometer (ORI) in microgravity

The first interference experiments with degenerate gases in extended free fall have been performed with an open Ramsey-type interferometer (ORI). This scheme was already introduced in Sec. 3.5.1 and is based on a freely expanding BEC which is illuminated with two successive $\pi/2$ Bragg pulses, separated by an interrogation time T_{int} (see Fig. 5.8, left). This interferometer geometry generates two output ports with two overlapping parts of the condensate wave function each. The relative distance between the density peaks of the interfering distributions for first-order Bragg diffraction can be calculated to $\delta x = 2v_r \cdot T_{int} \approx 11.77\ \mathrm{mm/s} \cdot T_{int}$.

Interference patterns occur in the overlapping region and the evolution of the corresponding contrast, either in time-of-flight series or in an auto-correlation measurement can be analyzed as an indication for the phase coherence of a matter wave source [163]. Moreover, an ORI can be considered as a double-slit experiment for matter waves [12]. Here, microgravity offers ultra-long evolution times and thus enable the observation of an interference pattern of macroscopic matter wave packets in the far-field. In the first interference experiments with an ORI to be presented in the next section, we do not apply delta-kick cooling (DKC).

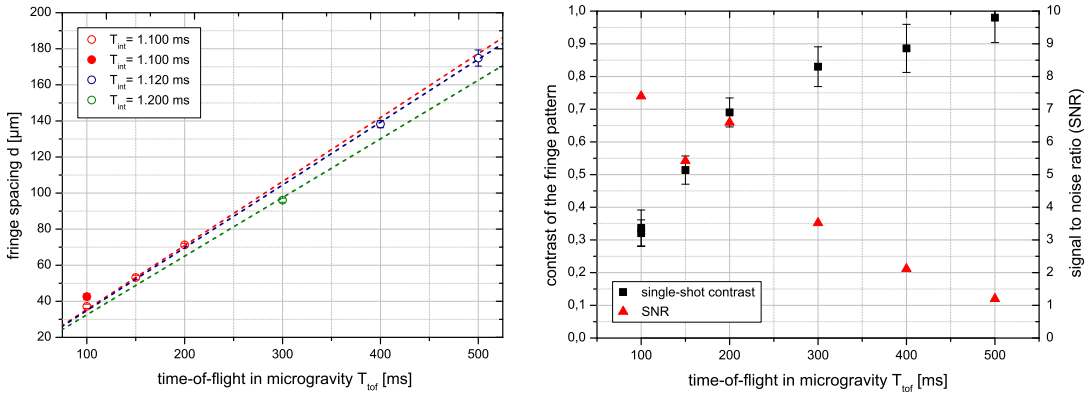

Figure 5.9: The temporal evolution of the fringe spacing in an ORI is probed up to a time-of-flight of $T_{tof} = 500$ ms (left). The applied interrogation times T_{int} (different colors) determine the phase gradient of the interfering wave packets and therefore the slope of the far-field approximation (dashed lines). The absence of thermal atoms for long timescales lead to an increase in contrast, whereas the SNR drops due to the finite expansion of the condensed ensemble (right). More details in text

Temporal evolution of the fringe spacing and far-field approximation

From the presented expansion data, the Thomas-Fermi radii of freely expanding clouds ($m_F = 0$) agree with the predicted evolution of a condensate emerging from a holding trap with trapping frequencies along the principal axes of $\omega_i = 2\pi \cdot (27, 10, 22)$ Hz. We therefore can approximate the ratio of the cloud's expansion rate and width in the direction of the beam splitter, which determines the phase curvature of the expanding ensemble as $\alpha = \lambda_x/\dot{\lambda}_x$ (see Sec. 3.5.1). The interrogation time between two successive Bragg pulses changes the relative distance δx between the interfering wave packets, which defines the fringe spacing period d in the far-field (see Sec. 3.5.2) according to

$$d_{ori} = \frac{2\pi}{\alpha \delta x} = \frac{\lambda_x}{\dot{\lambda}_x} \cdot \frac{h}{m \delta x} \approx \frac{\pi T_{tof}}{k \cdot T_{int}}, \tag{5.12}$$

with mass of the atoms m, total time-of-flight between release and absorption image T_{tof}, wave vector k and interrogation time T_{int}. Based on the prediction of $\lambda_x/\dot{\lambda}_x$, T_{int} was chosen to values around 1 ms to be able to observe about 3-4 local maxima (minima) in the density profile (see Fig. 5.10). This allows for a reliable determination of the characteristic parameters from the fit routines as done in ground-based measurements.

In Fig. 5.9 (left), we show the fringe spacing d of an ORI with varying time-of-flight in microgravity. In this campaign, the Ramsey-type sequences have always been performed with the same pause times between the pulses of $T_p = 1$ ms, but with different $\pi/2$-pulse durations $\tau_{\pi/2}$. The effective interrogation time reads $T_{int} = T_p + \tau_{\pi/2}$ and varies slightly on a daily basis due to intensity drifts of the Bragg laser beams, which results in different durations of $\tau_{\pi/2}$. With this configuration, values for the fringe spacing between $d \approx 40$ μm for $T_{tof} = 100$ ms and $d \approx 160$ μm for the longest possible time-of-flight of $T_{tof} = 500$ ms have been observed.

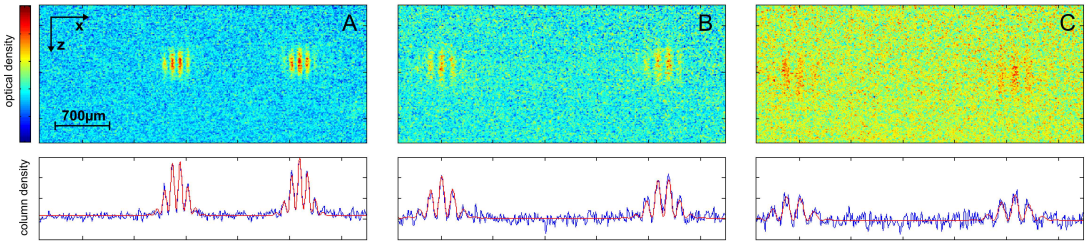

Figure 5.10: Absorption images of the output ports of an ORI in microgravity. The experiments are realized with an interrogation time of $T_{int} \sim 1$ ms, and three different time-of-flights 300 ms, 400 ms, and 500 ms are depicted from left to right (A-C). Note, that the separation time between recombination and detection was not kept constant but varies between $T_{sep} = 126$ ms (A) and $T_{sep} = 226$ ms (B, C).

Each circle represents a single drop experiment, the different colors correspond to the effective interrogation time and the error bars are given by the 1σ confidence intervals of the fitted parameters. The ARP was always applied 4 ms after release with a duration of 4 ms, followed by a 1 ms ramp down of the bias field. Open symbols now represent experiments, for which the initial expansion time T_0 between release and the interferometer is always much larger than the characteristic time $1/\omega_{rad}$, the full symbols instead correspond to an ORI operated for $T_0 \approx 1/\omega_{rad}$.

In the far-field, the temporal evolution of the fringe spacing in an ORI can be safely approximated by Eq. 5.12. These predictions are given as dashed lines for each T_{int} in Fig. 5.9 (left). After sufficiently long times of free expansion $T_0 \gg 1/\omega_{rad}$ before application of the ORI (open circles), the entire mean-field energy of the condensate is converted into kinetic energy and we are operating the interferometer in the ballistic regime. The influence of the non-linear expansion directly after release of the condensate is insignificant. This yields a better agreement between the measured data and the far-field approach compared to ground-based measurements (see Sec. 3.5.1).

The single data point (full circle) at a time-of-flight of $T_{tof} = 100$ ms again visualizes the influence of mean-field acceleration at relatively short free expansion times. Here, the initial expansion time (including ARP) before the interferometer is $T_0 = 9$ ms $\approx 1/\omega_{rad}$. As observed in ground-based measurements, a first interferometer pulse applied in the phase of mean-field driven acceleration reduced the density by half[6] and immediately changes the slope of $\dot{\lambda}/\lambda$.

The change of the phase curvature $\alpha \sim \dot{\lambda}/\lambda$ leads to a discrepancy between far-field approximation and observed fringe spacing. The implications of beam splitter pulses to the evolution of λ and $\dot{\lambda}$ have to be calculated based on the chip-model scaling approach [113], but have not yet been implemented. As an approximation for the single experiment, the offset can be quantified to $\Delta d = 8.4(1.7)$ μm which means a relative error of about 24%.

[6] Additionally, a finite repulsion velocity δv between the separating momentum states is induced (see Sec. 3.5.5 and Sec. 5.4.1). However, the resulting error in δx scales with interrogation time T_{int} and thus might be negligible in case of an ORI.

Contrast and signal-to-noise ratio

In Fig. 5.9 (right), the contrast C of the interference fringes (black squares) and the corresponding signal-to-noise ratio (red triangles) are shown. They are extracted by fitting Eq. 3.73 to the obtained absorption images. If given, error bars depict 1σ confidence intervals of the fitted parameters.

For comparably short time-of-flights of 100 ms, the contrast can be quantified to about $C = 0.3$ and finally increases up to values near $C \approx 1$ for $T_{tof} = 500$ ms. Vice versa, the SNR decreases by a factor of ~ 7. The increase in contrast can be explained by the absence of a non-condensed (thermal) fraction of the atomic cloud, which washes out the interference contrast at comparably short time-of-flights. This was already presented as the main decoherence mechanism in our ground-based measurements (see Sec. 3.5.3). Due to the extended free fall provided by the drop tower environment, we can wait for 500 ms to let the thermal background vanish, which results in a completely modulated interference pattern.

The almost perfect contrast at long timescales leads to the assumption of a coherence length at least just as big as the condensate's width, as expected for purely phase coherent matter waves [163]. However, due to the limited number of atoms in the BEC and the finite expansion rates of about 1 mm/s, the atomic density and the SNR decreases accordingly. This can also be seen in Fig. 5.10, where typical absorption images are shown for three different time-of-flights of 300 ms (A), 400 ms (B), and 500 ms (C). Each picture is individually normalized and depicts the same region of interest. Here, momentum transfer of the Bragg beams occurs in the negative x-direction, that means the right output port represents interfering clouds of momentum class $0\hbar k$. The interfering momentum classes of $2\hbar k$ separate from this stationary output port with twice the recoil velocity until the absorption image is taken. For increasing time-of-flight, the fringe spacing increases due to the finite dispersion of the wave packet which can be seen in the integrated column densities. Note, that the initial expansion time T_0 was not equal in the three pictures. This results in different separation times between wave packet recombination and detection of $T_{sep} = 126$ ms (A) and $T_{sep} = 226$ ms (B, C). Due to a non-perfect release process, the previously analyzed COM velocity of the atoms in the z-direction is additionally visible.

The next section will review the results of an asymmetric Mach-Zehnder interferometer operated with Bose-Einstein condensates in microgravity. This geometry can in principle be used to form matter wave sensors which are extremely sensitive to inertial forces such as accelerations and rotations [20, 110]. The upcoming results indicate the feasibility of this setup for future precision tests of gravity-related effects such as a test of the Universality of the Free Fall (UFF) by means of differential acceleration measurements with ultra-cold matter waves.

5.4 Asymmetric Mach-Zehnder interferometer (AMZI) in extended free fall

Light-pulse atom interferometers rely on the fact, that the phase shift between two interfering paths can be read out by measuring atomic transition probabilities. For

example, the local acceleration a of atoms w.r.t a reference mirror is encoded in the phase difference of a gravimeter [194, 49]. The sensitivity of a quantum projection noise limited single-shot acceleration measurement with N atoms in Mach-Zehnder configuration can be expressed as

$$\delta a \propto \cdot \frac{1}{C\sqrt{N}} \cdot \frac{1}{k_{\mathit{eff}}} \cdot \frac{1}{T^2}, \tag{5.13}$$

with the contrast C, the effective wave-vector k_{eff} , and the interrogation time T. The T^2 scaling is obviously favorable for microgravity conditions, as long as one can assure a measurable contrast C. The population ratio and thus a phase difference can only be determined through a measurable contrast envelope.

To measure contrast, typically a set of multiple experiments with different phases imprinted by, for example, the interferometer beams have to be performed. During a phase scan, contrast may additionally vary from shot-to-shot even in lab-based experiments. Numerous systematic effects [20, 9] introduce noise and bias terms in the phase extraction. Contrast determination with this method gets even more challenging when considering a drop tower experiment with max. 3 drops per day. The current Bragg laser setup does not yet feature an active frequency stabilization of the Bragg lattice, and reproducing exactly the same experimental conditions (e.g., center-of-mass velocity and positions) from drop to drop is challenging and the focus of current investigations.

With an asymmetric Mach-Zehnder interferometer, however, the contrast can be read out by a single shot. As introduced in the ground-based measurements of Sec. 3.5.4, this interferometer scheme applies an asymmetry between the two pulse separation times, therefore resulting in a total interrogation time of $T_{int} = 2T - \delta T$ (see Fig. 5.8, right). The temporal asymmetry directly translates to a spatial displacement of interfering parts of the wave function at the two output ports, $\delta x = 2v_r\delta T$.

In the far-field approximation, the fringe spacing d of an AMZI with effective wave vector k is inversely proportional to the induced displacement δx as

$$d_{amzi} = \frac{\lambda_x}{\dot{\lambda_x}} \cdot \frac{h}{m\delta x} \approx \frac{\pi \cdot T_{tof}}{k \cdot \delta T} = \frac{\pi \cdot (T_0 + 2T - \delta T + T_{sep})}{k \cdot \delta T}, \tag{5.14}$$

with initial expansion time T_0, the interrogation time $2T - \delta T$ and the output port separation time T_{sep}. In contrast to the open Ramsey-type sequence, the pulse duration has not been taken into account for calculating the effective asymmetry δT. The latter is only given by the timing asymmetry between the center of the Bragg pulse envelopes.

5.4.1 Probing the phase evolution of a condensate with an AMZI

To verify the feasibility of our apparatus in performing high-precision interferometry measurements in microgravity, we performed an AMZI campaign operated with Bose-Einstein condensates. They have been released from a shallow Ioffe-Pritchard trap (IPT) with $\omega_i = 2\pi \cdot (27, 10, 22)$ Hz. The ARP was applied 4 ms after release with a duration of 4 ms, and 1 ms later the asymmetric interferometer sequences have been applied.

From the measurements operated with an ORI, we already learned that a beam-splitter induced reduction of mean-field conversion influences the formation of the

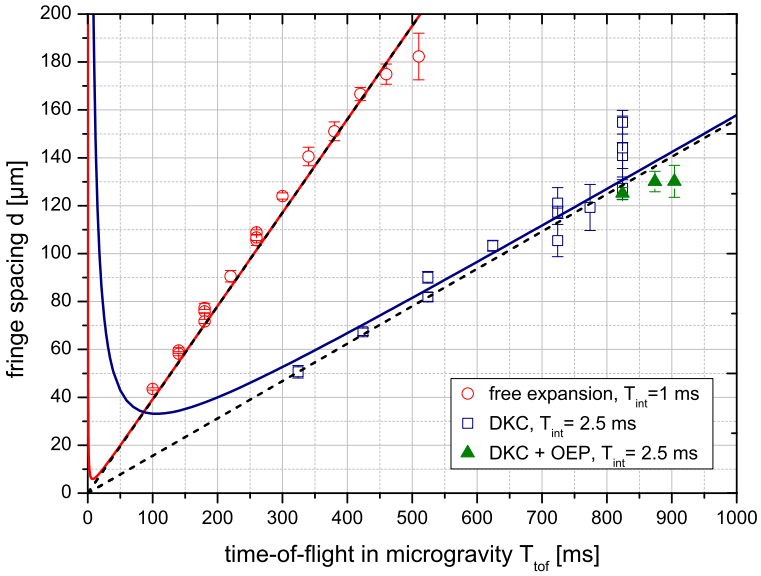

Figure 5.11: Fringe spacing of an asymmetric Mach-Zehnder interferometer (AMZI) in microgravity. Shown here is the temporal evolution of the fringe spacing d for condensates released from a shallow trapping potential (red circles), and condensates additionally manipulated with DKC (blue squares). The solid lines correspond to calculations using the scaling law solution for elongated traps with radial trapping frequencies $\omega_{rad} = 2\pi \cdot 20$ Hz (red line) and $\omega_{rad} = 2\pi \cdot 1$ Hz (blue line) estimated from the expansion data (see Sec. 5.2.3). The black dashed lines represent the far-field approximation for asymmetries of $\delta T = 1$ ms and $\delta T = 2.5$ ms, respectively. More details in text.

fringe pattern (see Sec. 5.3 or 3.5.2). This has to be considered for interferometer pulses applied after free expansion times $T_0 \leq 1/\omega_{rad}$. However, since the available free fall time is limited and we have to consider a sufficiently long separation time to observe the two output ports spatially separated, we had to apply the AMZI as early as possible.

Evolution of the fringe spacing without DKC

Based on the experiments made with the ORI, an asymmetry of $\delta T = 1$ ms was chosen, which means the pause time between the first and the second pulse was slightly longer compared to the time between the second and the third one. For this measurement campaign, the separation time (see Fig. 5.8) was kept constant at $T_{sep} = 52$ ms. This allows for a spatial separation of the output ports on the order of half a millimeter (exceeding a few times the condensates size) before detection.

We observed a linear scaling of the fringe pattern with the total time-of-flight T_{tof}. The evolution of fringe spacing could be measured up to a total interrogation time of $2T - \delta T = 449$ ms (see Fig. 5.11, red circles), where error bars depict 1σ-confident bounds of the fitted parameter. The measured fringe spacings slightly exceeds the scaling law prediction calculated with an approximated radial trapping frequency of

$\omega_{rad} = 2\pi \cdot 20(3)$ Hz (red line). Notably, this calculation coincides with the far-field approximation (dashed line) after some tens of milliseconds[7].

Deviations from measured fringe spacings d_{meas} to the theoretical prediction

$$d_{calc} = \frac{\lambda_x}{\dot{\lambda}_x} \cdot \frac{h}{m\delta x} \tag{5.15}$$

can occur for an erroneous model of the fraction of the condensates size and velocity $\dot{\lambda}/\lambda$, and errors of the assumed wave packet separation δx. A thorough analysis of the fringe spacing evolution is important, since it allows to detect external influences on the wave packet dynamics and thus gives insight to decoherence mechanisms. In the next section, we will qualitatively discuss possible error models which affect the formation of the fringe pattern.

Influences on the fringe spacing evolution in open interferometers with BECs

In the following, some of the major influences on the fringe spacing evolution will be discussed, which have to be considered in Eq. 5.15 for a correct theoretical prediction and interpretation of the fringe pattern:

- **Error in δx (1): Timing asymmetry** δT. The fringe spacing scales as $d \sim 1/\delta x$ and is thus inversely proportional to the temporal asymmetry ($\delta x \sim 2\hbar k/m \cdot \delta T$). For QUANTUS-I, uncertainties in δT are negligible since our timing reference (PulseBlaster DDS-II-300) has a temporal resolution on the order of some tens of ns, which is much smaller than the here applied asymmetry $\delta T = 1$ ms. Moreover, duration and temporal uncertainty of supposedly equally long beam splitter pulses have not to be considered for the effective interrogation time in a Mach-Zehnder configuration.

- **Error in δx (2): Alignment of the Bragg beams**. If we generate the Bragg lattice by the interference of two independent beams enclosing an angle ϑ (see Fig. 3.1), the transferred momentum for resonant atoms is proportional to the sine of the half angle as $p_r(\vartheta) = 2\hbar k \cdot \sin(\vartheta/2)$. Here, $\vartheta = 180°$ for anti-parallel beams. The separation of the interfering wave packets after recombination is described by $\delta x(\vartheta) = 2\hbar k/m \cdot \sin(\vartheta/2) \cdot \delta T$, which affects the evolution of the fringe spacing $d \sim 1/\delta x(\vartheta)$. However, the dimensions of the UHV chamber in QUANTUS-I prohibit large angles between the Bragg beams such that misalignment as a potential error source can be omitted by carefully adjusting the beams. To explain the observed offset, an angle of $\vartheta \approx 140°$ would be necessary, which can safely be excluded.

- **Error in δx (3): Repulsion velocity kick**. As measured in ground-based experiments with an asymmetric Mach-Zehnder interferometer, the application of interferometer pulses in the presence of a strong mean-field will modify the relative COM velocity between both momentum states (see Sec. 3.5.5). The

[7] This is true for all corresponding scaling law calculations within the fitting error of ω_{rad}. These are not shown here for better visibility.

positive scattering length of ^{87}Rb causes an additional phase shift due to mean-field repulsion between the overlapping wave packets, which can be measured as a small repulsion velocity rate δv. Without repulsion kick and $\vartheta = 180°$, the separation after recombination is $\delta x_0 = 2\hbar k/m \cdot \delta T$. An additional COM velocity δv after the first pulse will consequentially lead to a time-dependent spatial displacement of $\delta x(\delta v) = \delta x_0 + \delta v \cdot (2T - \delta T + T_{sep})$, which again affects the fringe spacing as $d(t) \sim 1/\delta x(\delta v)$. The repulsion velocity itself is dependent on the strength of the mean-field and therefore on the condensate preparation before release. Comparably steep traps with $\omega_{rad} \approx 2\pi \cdot 130$ Hz (see Sec. 3.5.5) led to ground-based measurements of δv on the order of μm/s, which can be seen as an upper value for the AMZI campaigns in microgravity. Here, we released the condensate from our most shallow trap ($\omega_{rad} \approx 2\pi \cdot 20\,\text{Hz}$) and the impact on the fringe spacing is estimated in Fig. 5.12.

- **Error in δx (4): Rotations**. Capsule rotations will affect the evolution of fringe spacing d as well as the fringe pattern's read out. We have to distinguish between the three axes (see Fig. 5.17) and always have to keep in mind that the experiment chamber (incl. beam splitter direction) is rotating w.r.t the atomic cloud. Rotations Ω_x along the direction of the beam splitter wave vector (x-direction) will ideally not affect d or the interferometer read out and can thus be neglected. Rotations along directions perpendicular to the wave vector (Ω_y and Ω_z) will lead to more complex fringe spacing dynamics and affect the pattern's read out. For a better understanding, let us first recall the situation of a non-rotating experiment. After recombination in an AMZI, lines of constant phase are perpendicular to the vector $\delta\vec{r}$ between the COM of both wave packets, which in the 1D case of beam splitters along the x-direction is given as $\delta\vec{x}$. The norm $|\delta\vec{x}| = \delta x$ is time-independent and usually used as wave packet separation in Eq. 5.15. Rotations of the beam splitter wave vector will now lead to a rotated COM vector $\delta\vec{r}(t)$ with a time-dependent length. This implies (i) a rotation of the fringe pattern and (ii) smaller fringe spacings compared to the non rotating experiments. Whereas rotations Ω_y in this case will still allow for high-contrast imaging of the fringe pattern, rotations along the z-axis will additionally lead to reduced contrast in the absorption images. Capsule rotations during a drop have been monitored with an inertial measurement unit (IMU) and will be discussed in Sec. 5.4.3.

- **Error in $\dot{\lambda}/\lambda$ (1): Principal axes of the condensate**. It was proven in [137] (and indicated through the analysis of the free expansion in Sec. 5.2.3), that the initially elongated trap is tilted both in the horizontal plane and in the z-direction during adiabatic decompression. Since the principal axes of the condensate after release now do not perfectly overlap with the beam splitter axis, errors will arise due to the assumption of an elongated trapping potential whose fast axis is aligned perpendicular to the beam splitter axis. A detailed chip-model was developed [113] and used for our Bragg interferometer analysis in [12], which properly predicts the scaling of the of the condensate based on the λ-matrix formalism [130] (see Fig. 5.12).

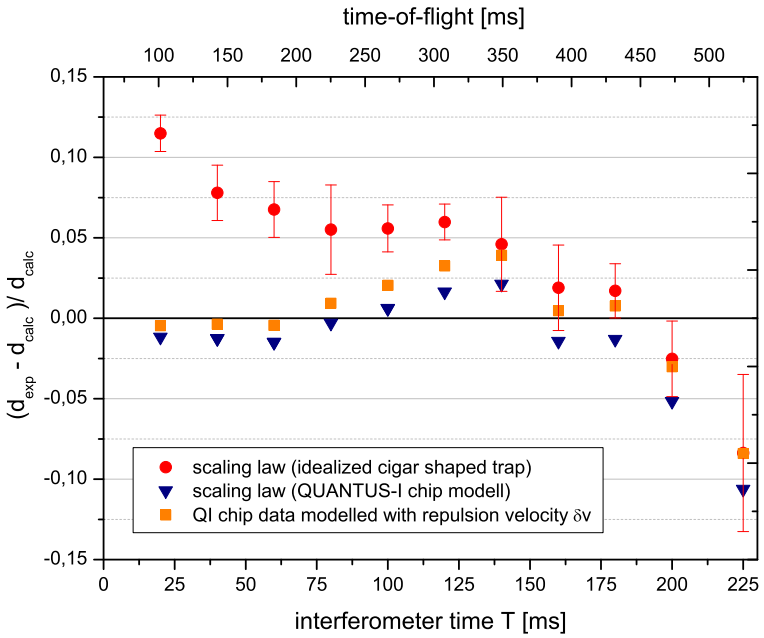

Figure 5.12: Comparison of observed and calculated fringe spacing for three different models. The relative error of the experimentally measured fringe spacing to the prediction of the scaling law with an idealized cigar shaped trap (red circles, $\omega_{rad} \approx 2\pi \cdot 20$ Hz) is compared to the numerical solution of the chip model (blue triangles). Additionally, the latter has been modified with a repulsion velocity δv (orange squares). Details in text.

- **Error in $\dot{\lambda}/\lambda$ (2): Beam-splitter induced reduction of α.** In this AMZI campaign without DKC, the first interferometer pulse is applied 9 ms after release of the condensate from a shallow trapping potential with about $\omega_{rad} \approx 2\pi \cdot 20$ Hz. For this trap, the acceleration of the condensate is still mean-field driven (cf. Fig. 3.16 and 3.17). If now a beam splitter is applied, the wave function is split into a coherent superposition of two momentum states with bisected density. The wave packets expansion rate $\dot{\lambda}$ will reach its asymptotic value earlier and therefore change the slope of $\alpha \sim \dot{\lambda}/\lambda$. An offset arises which was already identified in the context of ORIs in measurements on ground (see Sec. 3.5.2) and in microgravity (see Sec. 5.3).

The relative error between the measured and calculated fringe spacings

$$\frac{d_{meas} - d_{calc}}{d_{calc}} \tag{5.16}$$

using three different models (including some of the aforementioned influences) is given in Fig. 5.12. The relative error is plotted versus the interferometer time T, which is given by the pause time between the first and the second Bragg pulse. Since we kept the initial expansion time T_0 and separation time T_{sep} constant, there is a linear dependence between T and total time-of-flight T_{tof}, which is why the latter is indicated with a second x-axis at the top of the graph.

The red data points correspond to the relative error between experiment and calculation as shown in Fig. 5.11, where the fringe spacing d_{calc} is calculated with Eq. 5.15 by approximating $\omega_x = \omega_z \equiv \omega_{rad}$. The value for ω_{rad} was obtained by fitting the expansion data (see Sec. 5.4). The error bars of $(d_{meas} - d_{calc})/d_{calc}$ correspond to the fitting error of the experimentally observed fringe spacing. For short timescales, the measured fringe spacing exceed the prediction by up to 10%, but incrementally approach the zero line (coincidence of measurement and model) until they finally fall below it. This simple model is obviously not suitable for a correct fringe spacing prediction.

In [12], we simulated the fringe spacing based on a chip-model (CM) which considers the tilt of the condensate and induced rotations of the principal axes. The blue data points correspond to the relative deviation of the observed data to this model, which fit quite well to the data[6].

Additional influences on the evolution of $\dot{\lambda}/\lambda$ due to the reduction of α (error in $\dot{\lambda}/\lambda$ (2)) cannot account for the observed behavior since they would only lead to a positive offset. However, for large interferometer times, the error still increases since the experimental fringe spacing is smaller than the prediction. This might be assigned to the relative big error in fitting the fringe spacing but could also be an indication of an error in δx (e.g., repulsion velocity kick or rotations).

As one example for a linear phase factor, we modeled the CM with an additional repulsion velocity. For that, we took $\delta v = 10\ \mu$s/s which was measured previously in ground based measurements for a comparably tight trap ($\omega_{rad} \approx 2\pi \cdot 130$ Hz). This should serve as an upper value for δv. The results are depicted as orange squares[6]. The additional linear phase term shifts the fringe spacing but could also not explain the tendency observed for the last two data points.

The long-term evolution of the fringe spacing should be analyzed in further drop campaigns since all contributions to the phase evolution have to be perfectly understood and considered in a dedicated model to perform high-precision measurements. Due to the long time-of-flight available, microgravity experiments with interfering condensates at long timescales are sensitive to even the slightest perturbations in position and velocity.

Evolution of the contrast without DKC

The observed contrast for AMZI with condensates in the $m_F = 0$ state is plotted versus the interferometer time $2T - \delta T$ (see Fig. 5.13). This is the time the atoms spend in the interferometer and contrast is expected to scale with this characteristic time. The contrast typically exceeds $C = 0.5$ (see red circles in Fig. 5.13), which is less than compared to the measurements with an ORI, which featured about the same separation δx. This indicates decoherence mechanisms which will be analyzed at the end of this section.

The SNR dropped rapidly and prohibited longer interrogation times (see red circles in Fig. 5.14). These have only become accessible by applying delta-kick cooling prior to the ARP and the subsequent AMZI sequences.

[6] The errors remain on the same scale as shown for the red data, but are omitted here for better visibility.

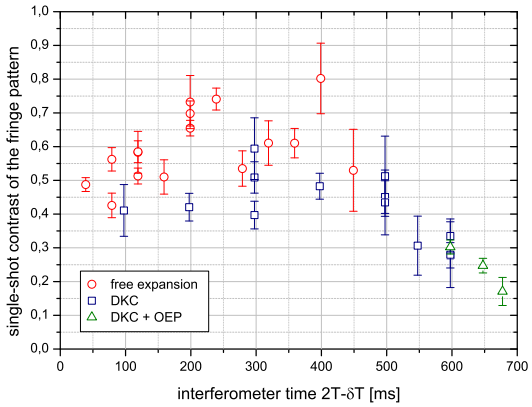

Figure 5.13: Contrast of the evolving interference pattern versus the total interferometer time $2T - \delta T$.

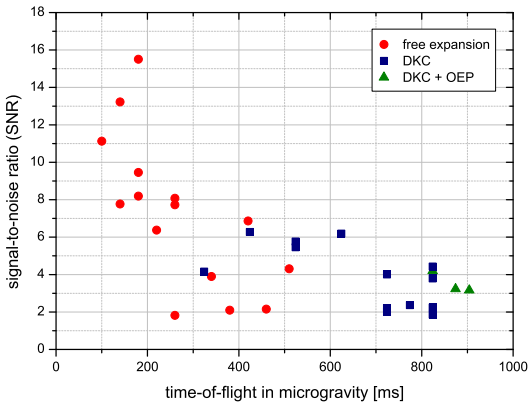

Figure 5.14: Signal-to-noise ratio (SNR) extracted from the fits to the integrated column density data.

5.4.2 An AMZI with delta-kick cooled condensates

By applying the delta-kick cooling (DKC) technique, we could extend the observation of contrast to an interrogation time $2T - \delta T = 677$ ms. In our experimental sequence, this corresponds to a total time-of-flight of $T_{tof} = T_0 + 2T - \delta T + T_{sep} = 960$ ms (blue squares in Fig. 5.11 - 5.14).

The BEC is released from the shallow trap with $\omega_i = 2\pi \cdot (27, 10, 22)$ Hz and expands for 30 ms. Then, we applied DKC by means of a 2 ms lasting magnetic trap with the same trapping frequencies as the holding trap. The ARP was applied 4 ms after DKC with a duration of 4 ms. After ramp down of the offset field within 1 ms, the cloud freely expands for 164 ms until the interferometer sequence is applied. We therefore assume to operate in the ballistic regime. Since DKC effectively slows down the expansion rate, we changed the asymmetry to a slightly larger value $\delta T = 2.5$ ms to preserve the number of visible fringes along the now much narrower condensate. This is the reason for the rescaling of the fringe spacing's slope, which follows quite well the interaction-free far-field approximation (black dashed line).

In Sec. 5.2.3, the spatial evolution of a delta-kick cooled ensemble was modeled with a virtual trapping potential. Indeed, to realize a cloud with an expansion rate comparable to that observed with DKC, an initial trap with $\omega_{rad} = 2\pi \cdot 1.4(1)$ Hz would be necessary. Compared to our method, this would require longer preparation times (adiabatic opening of the trap) and has another major disadvantage. For such a shallow trapping potential, mean-field conversion would slow down and affect the evolution of the phase profile even on timescales available in microgravity. As an example, the calculation of the fringe pattern evolution with $\omega_{rad} = 2\pi \cdot 1.4$ Hz is shown as a blue line in Fig. 5.11. With the help of DKC, we can prepare ultra-cold ensembles without mean-field driven accelerations.

The contrast is not as high as the AMZI operated without DKC, which in part can be explained by the larger asymmetry (See Sec. 3.5.3). However, it still exceeds $C = 0.4$ for interrogation times up to $2T - \delta T \approx 500$ ms. Due to the larger signal after employing DKC, we are able to detect interference fringes until a maximum interrogation time

of 596 ms. Here, contrast and SNR both decrease with the interrogation time of the AMZI and generally with the expansion time of the BEC.

Our currently largest interferometer (green triangles in Fig. 5.11 - 5.14) is made possible by carefully adjusting the separation time T_{sep} between recombination through the last $\pi/2$ pulse and detection. In this method, both output ports are not completely spatially separated for imaging. The timing is chosen such that the output ports are separated by a distance which is equal to half a fringe spacing. The pattern of the two exit ports now overlap, ideally leading to the same contrast with an increased absorption signal. This allowed for an AMZI with a maximum interrogation time of $2T - \delta T = 677$ ms.

5.4.3 Limitations in contrast and signal-to-noise ratio

The output of our open interferometers are spatially interfering parts of condensed matter waves. Thus, the contrast of each shot can be inferred from the modulation depth of the fringe pattern. The contrast itself depends on various external influences, noise sources as well as on the atomic cloud properties itself (e.g., coherence length, see Sec. 3.5.3).

For an AMZI with DKC, contrast typically exceeds $C = 0.4$ but fades away for increasing T. The observed reduction is non-exponential in time and uniform over the cloud [12]. The SNR drops as the clouds expand, which leads to a lower signal for long time-flights. This limitation can in principle be overcome by using other detection methods or condensates with more atoms as in the successor experiment[7]. However, decoherence mechanisms will still lead to significant loss of contrast and thus ultimately limit the precision of matter wave interferometry experiments in microgravity. We will now qualitatively discuss three important systematics which can be attributed to decoherence in drop experiments.

Influence of residual fields

In [17], the QUANTUS-I experiment observed anomalous expansion of a condensate in the microgravity environment of the drop tower. The cloud of condensed atoms was prepared in a magnetic sensitive state $|F = 2, m_F = 2\rangle$, and the corresponding data indicates the presence of magnetic stray fields. The expansion could be modeled with an artificial sub-Hertz residual field [137]. With an interferometer, we now have another possibility to directly verify the presence of electro-magnetic stray fields.

With an adiabatic rapid passage, we now have a tool to compare interferometers with atoms in $|F = 2, m_F = 2\rangle$ and $|F = 2, m_F = 0\rangle$ state, without affecting the clouds' temperatures or center-of-mass motion to first order. On the timescales of our ground-based measurements ($T_{tof} = 32$ ms), we could not observe loss of contrast by using magnetically polarized atoms.

In 5.15, two absorption images are shown for exactly the same interferometer sequence operated with differently polarized atoms in microgravity. They have been taken after a total time-of-flight of 260 ms and in case of atoms in the $m_F = 2$ state

[7] In the QUANTUS-II experiment, condensates with about $N = 3 \cdot 10^5$ atoms can be generated within a cycle time of less than two seconds [195].

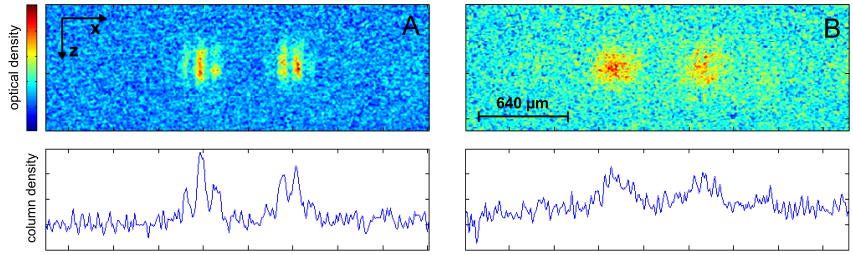

Figure 5.15: Comparison of the influence of residual fields on the free propagation of matter waves. An AMZI is used to study the coherence of differently polarized ensembles in two consecutive measurements ($m_F = 0$ (A) vs. $m_F = 2$ (B)). In both cases, the sequence is performed with $2T - \delta T = 199$ ms and the absorption images are taken after a total time-of-flight of 260 ms. The contrast drops from $C = 0.64$ ($m_F = 0$) to $C \approx 0$ ($m_F = 2$).

(B) no interference pattern occurs, whereas interfering condensate copies in the $m_F = 0$ state show a fringe pattern with a contrast of $C = 0.64$ (A). This is a clear evidence for residual magnetic fields which influence the evolution of $\dot{\lambda}/\lambda$. Another result is shown in Fig. 5.16, where a 50/50 mixture of atoms in the $m_F = 0$ and $m_F = -1$ state has been prepared as an input state for an AMZI with $2T - \delta T = 99$ ms. After recombination, the interferometer output ports of the different m_F states are spatially separated in a Stern-Gerlach experiment. After application of a strong magnetic gradient, the isolated interferometer with $m_F = 0$ atoms could be detected with a contrast of $C = 0.69$ whereas no fringes are observed in case of the $m_F = -1$ sub-ensemble.

However, the discussed measurements of an AMZI in microgravity in this thesis have been operated with atoms in the $m_F = 0$ state during interferometry. They are to first order insensitive to magnetic fields. Nevertheless, the quadratic Zeeman shift

$$\Delta E_{quad}(m_F) = (4 - m_F^2)\hbar\omega_{quad}/4 \tag{5.17}$$

with $\omega_{quad} = 286$ Hz/G^2 [150] still leads to perturbations of the free evolution. Compared to the linear shift, the quadratic one is small but might accumulate to finite COM displacements of the wave packets as well as disturbances of the phase evolution, which cause a loss of contrast for extended free fall times. This will be implemented in the next version of the chip model.

Capsule rotations

Capsule rotations will affect the evolution of the fringe spacing d as well as the fringe pattern's read out. They will lead to (i) a rotation of the fringe pattern and (ii) a smaller fringe spacing compared to the non rotating experiments. As already discussed in Sec. 5.4.1, rotations Ω_x and Ω_y can be neglected as a source of contrast loss. However, the contrast of an absorption image suffers from the projection of a rotated fringe pattern along the z-axis.

To quantify the rotation rate of the capsule during a drop, an inertial measurement unit (IMU) was installed which measured the rates independently for all three dimen-

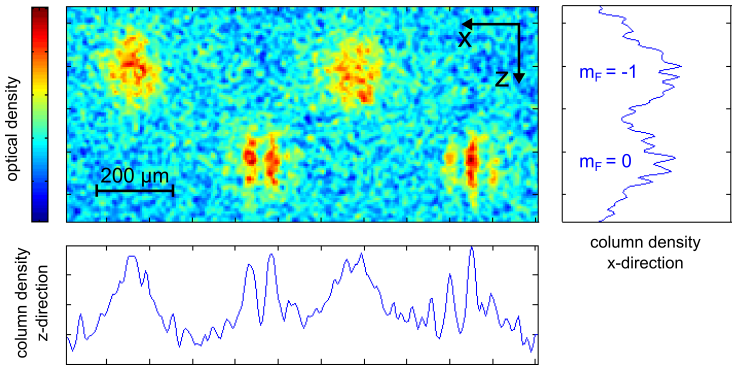

Figure 5.16: Absorption image of an AMZI operated with spinor gases to probe residual fields. An equally populated mixture of atoms in the $m_F = 0$ and $m_F = -1$ state is prepared with the adiabatic rapid passage. This mixture is then used as an input state for an AMZI with $2T - \delta T = 99$ ms. After recombination, the output states are spatially separated with a magnetic field gradient. The isolated interferometer wit $m_F = 0$ atoms shows a contrast of $C = 0.69$ whereas no contrast is observed in case of the $m_F = -1$ sub-ensemble.

sions. A typical result is shown in Fig. 5.17. The largest rotation rates ($\Omega_x = 0.17°/s$ and $\Omega_y = 0.12°/s$) have been measured along the x- and y-direction, which both will not contribute to a loss in contrast. Rotations along z-direction can be quantified to about $\Omega_z = 0.03°/s$, which cannot explain a complete loss of contrast on the investigated timescales [112].

Beam splitter alignment and wavefront distortions

Since the atoms have a finite COM motion perpendicular to the wave vector of the Bragg beams and the wave function itself spreads over macroscopic distances of half a millimeter (see Sec. 5.2.3), the quality of the interferometer beams will play a significant role regarding the interferometer contrast. Wavefront curvatures and aberrations are one of the main sources of decoherence and phase estimation errors in high-precision atom interferometers.

In a uniform gravitational field, the measured phase difference in a Mach-Zehnder interferometer is dependent on the phase of the Bragg beams imprinted on the atomic wave function. At the different times t_1, t_2, t_3 of the beam splitter pulses, the atomic wave function of the i-th atom with positions $\vec{r}_i$ in the lattice beam accumulates a total phase shift of

$$\Delta_i \Phi = \phi_1(\vec{r}_i, t_1) - 2 \cdot \phi_2(\vec{r}_i, t_2) + \phi_3(\vec{r}_i, t_3), \tag{5.18}$$

We now have an atomic distribution, which in case of a nK cold BEC is small compared to thermal sources at μK temperatures. However, in microgravity experiments with extended free fall time, even the condensate's expansion has to be taken into account.

The first pulse of the AMZI with DKC is applied 194 ms after release. Here, the

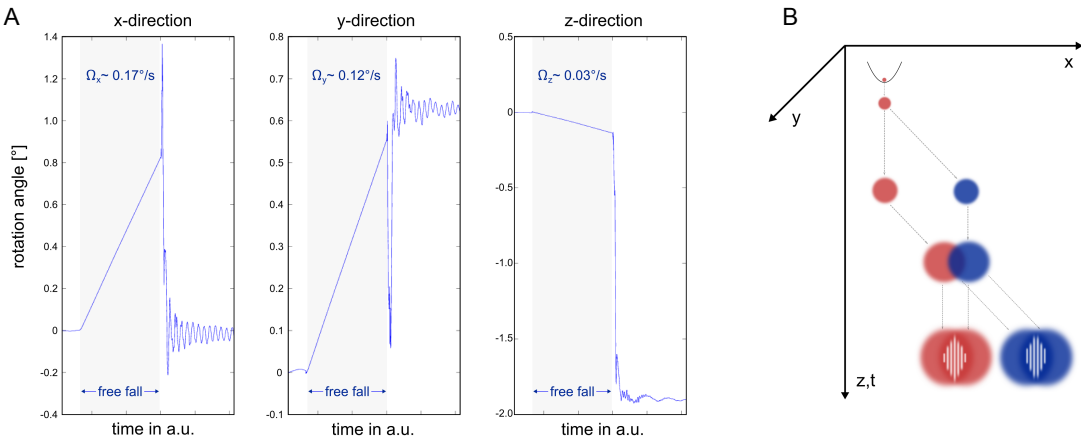

Figure 5.17: Typical rotations of the QUANTUS-I capsule during a drop experiment (A). An inertial measurement unit (IMU) monitored the rotation along the three principal axes while being in free fall. This period is colored in each graph. For convenience, the geometry of the AMZI is given in (B).

condensate has a spatial extension of about 100 μm in the radial direction, and is displaced from the atom chip's surface by about 800 μm. Ideally, a Gaussian intensity profile can be assumed for the Bragg lattice, which itself has a planar wavefront only in the focal plane. In QUANTUS-I, self-built telescopes collimate the light to a FWHM of 6.5 mm and have not been optimized to the full extend w.r.t to a perfect wavefront. More critical, imperfections of all traversed optics (e.g., lenses, waveplates, windows) and additional reflections at the HR-coated chip surface will presumably lead to a perturbed wavefront. In the setup presented here, both Bragg beams are collimated via two separated sets of telescopes and enter the UHV chamber via opposite non AR-coated entry windows. The imprinted phase on the atoms suffers from wavefront inhomogeneities over the clouds width.

For our longest interferometer, the last pulse is applied at $2T-\delta T = 677$ ms, which is 882 ms after release from the holding trap. Here, the condensate has evolved to a radial size of about 300 μm. Assuming the Bragg laser beams only to cause 1D momentum transfer along the x-direction, the condensate's COM position changes over 800 μm in the z-direction mainly due to the imperfect release process and the interaction with the magnetic lens (see Sec. 5.2.3).

The imprinted phase difference now changes from pulse to pulse due to (i) the finite expansion and (ii) the COM velocity in an arbitrary wavefront. Finally, one can not assure that even the orientation of both interferometer telescopes w.r.t. each other and the atom chip is the same for each drop.

The influence of imperfect wavefronts and the role of the HR-coated chip surface as a reflector has to be analyzed in future drop campaigns. The arising systematics are of importance for the next-generation drop capsule experiments which aim for precision measurements of differential accelerations at timescales exceeding QUANTUS-I. Ultimately, space-borne sensors will offer even longer microgravity times and wavefront errors will be a major limitation in the phase estimation.

6 Summary and outlook

The central results of this thesis constitute an important step towards operating precision interferometry experiments based on ultra-cold atoms in weightlessness. Despite the fact that there is still a long way to go for space-borne applications, this work demonstrated necessary scientific techniques and tools for free-fall interferometry on extended time scales. Specifically, it proved the general feasibility of microgravity-enhanced quantum sensors with an atom-chip-based source of Bose-Einstein condensates in the Bremen drop tower.

The achieved results with QUANTUS-I (Q-I) can be assigned to two consecutive working phases: ground-based implementation of experimental techniques for unperturbed matter wave interferometry including preparatory studies, and the adaption of all techniques for microgravity application and subsequent combination to demonstrate the first BEC interferometer in extended free fall:

Free-fall interferometry with Bose-Einstein condensates in microgravity (see Ch. 5)
- Atom-chip-based source of non-magnetic degenerate gases (see Ch. 2)
- ◇
- Bragg diffraction and open interferometers with degenerate gases (see Ch. 3)
- ◇
- Delta-kick cooling as a tool for long baseline atom interferometry (see Ch. 4)

6.1 Results of the preparatory ground-based studies

As a first major upgrade compared to earlier setups of Q-I [17], the on-chip generation of (to first order) magnetic insensitive Bose-Einstein condensates with an RF-induced adiabatic rapid passage (ARP) has been demonstrated. Typically, up to 90% of the atomic ensemble were coherently transferred into the $m_F = 0$ state.

A compact and robust Bragg laser system based on a distributed feedback (DFB) diode laser was built and qualified for drop tower operation. After integration into the Q-I payload, matter wave beam splitters and combiners based on two-photon transitions between two internal momentum states have been implemented.

The phase evolution of chip-based Bose-Einstein condensates has been probed with open light-pulse interferometer geometries. The temporal evolution of contrast and

fringe spacing of interfering condensates in an open Ramsey-type interferometer (ORI) has been investigated and compared with the theoretical predictions. We explored the border to the non-linear expansion regime as we analyzed the influence of residual mean-field energy on the quadratic and linear term of the condensate's phase. This was done in ORI geometries as well as with an asymmetric Mach-Zehnder interferometer (AMZI), the latter of which was finally used to probe the phase coherence of the condensate in our drop experiments.

As the third experimental requirement towards long-term matter wave interferometry, the on-chip realization of delta-kick cooling (DKC) has been presented for the first time. This included the implementation of DKC for condensed and thermal sources as well as the analysis of relevant error sources affecting the center-of-mass (COM) motion. By the choice of the right DKC trap parameters, the momentum width could be reduced by a factor of 4 (16-fold reduction of temperature), independent of the condensate fraction. This led to the observation of freely expanding samples with approximated expansion temperatures in the lower nK range.

6.2 Results of the microgravity campaigns

After the preparatory ground-based studies and the implementation of relevant tools for unperturbed matter wave interferometry in microgravity, dedicated drop campaigns with the Q-I payload have been performed. In more than 250 free fall experiments operated at the drop tower in Bremen, the first demonstration of a matter wave interferometer with degenerate gases in extended free fall has been realized. To this end, a well-planned drop strategy including the following intermediate steps has rigorously been followed:

- Implementation of the ARP in microgravity and verification of the free expansion of atoms in the $m_F = 0$ state to follow the scaling law. These results suggested that indeed residual magnetic fields in the tower have been responsible for anomalous expansion of magnetically polarized atom as observed in the earlier runs of this experiment [17, 137].

- Operation of ORI sequences to demonstrate the basic tools for matter wave interferometry in microgravity. The resulting interference pattern was similar to the one in the far-field of a double-slit and we could verify the spatial coherence of condensates after free expansion times of up to 500 ms. The absence of thermal background atoms led to an improved contrast of nearly $C = 1$ and indicated a coherence length at least as large as the condensate width.

- First demonstration of on-chip DKC in microgravity. This technique allowed us to observe the free evolution of a $\sim$ 1 nK cold quantum object after 2 s, which constitutes the second largest free expansion time of a cold quantum object reported so far [110]. For comparison, an adiabatic release from a holding trap with trapping frequencies of about 1 Hz would be necessary to yield the same expansion rate.

- First application of DKC as a tool for long baseline matter wave interferometry. The feasibility of an inertial sensitive geometry has been proven by the realization of an AMZI with interrogation times of up to $2T - \Delta T = 677$ ms [12]. Here, the contrast usually exceeded 40% but faded away for longer timescales.

Conclusion and next steps with QUANTUS-I

It still has to be evaluated why the contrast is decreasing and what mitigation strategies can be deployed. Generally, the related interferometer sequences are throughout operated in the linear expansion regime and collisions with thermal background atoms (typical condensate fraction $\sim 60\%$) may be excluded since ORI experiments indicated an increasing contrast for timescales up to 500 ms. Moreover, it was shown that the application of DKC per se did not lead to dephasing and contrast loss.

We discussed the possible impact of capsule rotations, which affect the direction of the beam splitter wave vector and therefore the effective trajectories of the wave packets in the rotating framework. We measured the rotation rate with an inertial measurement unit (IMU) and a first analysis shows that the residual rotations in the contrast-sensitive direction ($\Omega_z \approx 0.03°/\mathrm{s}$) are indeed too small to completely explain the observations in our AMZI drop tower campaign [112].

The application of an ARP minimizes the influence of residual fields since atoms in the $m_F = 0$ state are to first order insensitive to magnetic fields. However, to rule out that higher order terms of the magnetic interaction can be accounted for the contrast loss on macroscopic timescales, they should be included in the Q-I chip model.

Wavefront distortions and imperfect beam splitter alignment are obvious candidates to explain the contrast loss. Reflections of the Gaussian tails of the Bragg beams at the highly reflecting coating of the atom chip surface cause optical interferences in the vicinity of it. Additionally, imperfections of all traversed optics (e.g., wave plates, lense, non-coated entry windows of the UHV chamber) and scattered light in general lead to a perturbed wavefront at the atoms position. Due to the finite width and COM velocity of the condensate, the imprinted phase profile on the atoms suffers from beam splitter to beam splitter and we suspect this wavefront inhomogeneities over the cloud's spatial extension as the main reason for global dephasing.

In principle, this assumption can be investigated in a series of dedicated drop experiments. Therefore, a controlled mechanism to move the BEC further away from the chip surface is needed, which would allow for systematic studies of the interferometer contrast in dependance of the z-position. A variable spatial displacement of the COM position can also be used to improve beam splitter efficiencies (shorter pulses and homogenous intensity), since the Gaussian peak of the Bragg beams is centered about 5 mm below the position of the atom chip. It could be realized with a COM kick during the adiabatic release and subsequent stop with an appropriately designed magnetic lens pulse. Here, the atom chip gives us control over shape and position of the DKC trap.

A more convenient method might be given by a series of two successive Bragg beam splitter pulses reflected at the surface of the atom chip. Whereas the first possibility is technically challenging and requires indeed some drops to find the right parameters, the second method comes at the prize of 50% atom loss at least. In microgravity,

two identical but counter propagating traveling waves will lead to simultaneous Bragg diffraction in two opposing directions. One cloud will be accelerated towards the chip, the other away from the surface. Thus 50% atom loss cannot be prohibited, which is a challenge for achieving ultra-long expansion time with typical atom numbers of Q-I ($N \sim 10^4$).

Upcoming drop experiments with Q-I might also be used to further explore the fundamental limits of DKC. Better control over the COM motion of the released condensate and the application of Multi-DKC sequences might lead to even colder sources and potentially enable a more symmetric cooling of the condensate along both visible directions. In general, on-chip magneto-optics for matter waves (e.g. multi-lens matter wave telescopes) is a promising tool for a versatile wave packet preparation in phase-space. Spatial extension, momentum width and COM velocity can be adapted to prepare a source which accurately features the desired properties for a specific experiment. For example, this could be point-like sources mostly insensitive to wave front curvatures for atom interferometry on ultra-long time scales. Macroscopic quantum samples with tunable spatial extensions instead are beneficial for the study of long-range order effects [14, 35] or even quantum reflection [196, 19].

Q-I is a pathfinder experiment which greatly demonstrated the technical feasibility of an atom-chip-based source of degenerate gases as well as matter wave interferometers on ultra-long timescales. It's unquestioned that operating Q-I in microgravity will still bring in new ideas and insights to important questions of microgravity-enhanced quantum science. Examples of running experimental investigations on a proof-of-principle level are rotation-insensitive interferometer topologies, double-Bragg diffraction topologies and compact chip-based gravimeter setups. However, Q-I was not inherently designed for precision measurements.

Quantitative analyses of the contrast loss and global dephasing as well as multi-sequential DKC have to be carefully considered with the limited number of available drops at the drop tower. For a number of technical reasons, it might be more appropriate to address these issues with the successor drop tower experiments. They are specifically designed for precision interferometry experiments in extended free fall and amongst others will be reviewed in the following outlook.

6.3 Outlook on future experiments and advanced laser system technology

To extend the reader's picture of what the corresponding community (with its numerous collaborations) is planning for the near future, we now review a selection of upcoming microgravity experiments and missions with an emphasis on the already used or proposed laser system technology[1].

The success of QUANTUS-I (and previously ATKAT, which demonstrated the first MOT in microgravity [197]) led to two other drop tower experiments: QUANTUS-II and PRIMUS (see Sec. 6.3.1). They aim for the the demonstration of dual-species mat-

[1] Conception, assembly and qualification of laser systems for quantum gas experiments aboard sounding rockets and space-borne instruments was the second main focus of my work during my time as a Ph.D. student at Humboldt-University. The results will be published elsewhere.

ter wave interferometry with rubidium-potassium (Rb-K) mixtures and first quantum-based tests of the universality of the free fall (UFF) in a microgravity environment.

As a next major stepping stone towards space-applicability and proof of quantum technological maturity, several sounding rocket experiments and missions are planned (see Sec. 6.3.2). These comprise (i) the MAIUS mission which constitutes the third generation of QUANTUS experiments to be operated as a single payload on an own sounding rocket vehicle and (ii) technology-related experiments (e.g. FOKUS) for tests of the laser heritage which has been developed in the framework of the LASUS project[2].

The achieved results of the drop tower and sounding rocket experiments as well as related system studies constituted the baseline of the German contribution to a proposal for a satellite mission based on ultra-cold quantum gases. STE-QUEST (Space-time explorer and quantum equivalence principle space test) was a medium-size (M3) candidate satellite mission in the scope of ESA's Cosmic Vision program (see Sec. 6.3.3). In this context, a European consortium proposed a satellite-borne instrument which consists of a dual-species atom interferometer operated with different rubidium isotopes (^{85}Rb and ^{87}Rb) to test the weak equivalence principle in space.

6.3.1 Quantum tests of the UFF at the drop tower

The verification of the universality of the free fall (UFF) with quantum objects is one of the major scientific goals of the QUANTUS collaboration[3]. QUANTUS-I (Q-I) is only capable of single species condensate generation whereas the next-generation experiment QUANTUS-II (Q-II) is designed for on-chip dual-species quantum gas operation with ultra-cold rubidium and potassium atoms (see Tab. 6.1 and [43]). As another ultra-cold quantum gas experiment to be operated at the drop tower, PRIMUS [4] is also aiming at testing the UFF with rubidium and potassium degenerate mixtures. Both are designed for the catapult mode of the drop tower, which offers a microgravity time of up to 9.2 s. (see Sec. 5.1). The main difference between them is given by the technological approach to generate the degenerate matter wave mixture, since PRIMUS will use an optical dipole trap [198, 44].

In this context, UFF-violating measurements aim for a direct determination of the Eötvös ratio η based on the quantum nature of particles,

$$\eta = \frac{|a_{Rb} - a_K|}{g}, \tag{6.1}$$

determining the normalized differential acceleration of two matter wave packets associated with supposedly individual accelerations a_{Rb} and a_K. By anticipating shot-noise

[2]LASUS is a collaboration of the groups of A. Peters (HU Berlin), A. Wicht (Leibniz-Institut, Ferdinand-Braun Institut für Höchstfrequenztechnik), E.M. Rasel (LU Hannover) and K. Sengstock (U Hamburg).

[3]QUANTUS is a collaboration of the groups of E.M. Rasel (LU Hannover), K. Bongs (U Birmingham), C. Lämmerzahl (ZARM / U Bremen), A. Peters (HU Berlin/ Leibniz-Institut, Ferdinand-Braun Institut für Höchstfrequenztechnik), A. Wicht (Leibniz-Institut, Ferdinand-Braun Institut für Höchstfrequenztechnik), K. Sengstock (U Hamburg), R. Walser (TU Darmstadt), and W.P. Schleich (U Ulm)

[4]PRIMUS is a collaboration of the groups of S. Herrmann/C.Lämmerzahl (ZARM / U Bremen) and E.M. Rasel (LU Hannover).

	QUANTUS-II	QUANTUS-I
payload volume	300 l	500 l
payload mass	180 kg	240 kg
total capsule mass	480 kg	590 kg
microgravity time	9.2 s	4.7 s
atomic species	^{87}Rb and ^{39,40,41}K	^{87}Rb
atom source flux (Rb only)	10^9 at/s	$5 \cdot 10^6$ at/s
condensate atom number (Rb only)	10^5	10^4
cycle time (Rb only)	typ. 1 s	10 - 15 s

Table 6.1: Comparison of the QUANTUS-II catapult-capable experiment versus the QUANTUS-I pathfinder. Mass and volume budgets are approximated values based on [199, 19]. The total capsule mass includes payload, platforms, base structure (incl. battery platform), four stringers, nose cone, pressurized cover and top lid plate [107].

limited detection in the microgravity environment, the only noise source contributing to the measurement sensitivity is quantum projection noise [62]. The sensitivity to accelerations for a single-species measurement in Mach-Zehnder configuration can thus be approximated as

$$\delta a \sim \frac{1}{C\sqrt{N}} \cdot \frac{1}{k_{\mathit{eff}}} \cdot \frac{1}{T^2}, \tag{6.2}$$

with contrast C, atom number N, effective wave vector k_{eff} and interrogation time T. As an example, given our results with the Q-I experiment reported in [12] and the achieved atom numbers and anticipated performance of the Q-II apparatus [199] (see also Tab. 6.1), a single-shot sensitivity enhancement (assuming the same contrast and beam splitter wave vector) of about

$$\frac{[\Delta a]_{\mathrm{Q-II}}}{[\Delta a]_{\mathrm{Q-I}}} = \frac{(2.5\ \mathrm{s})^2 \cdot \sqrt{10^5}}{(0.34\ \mathrm{s})^2 \cdot \sqrt{10^4}} \approx 160 \tag{6.3}$$

seems feasible. With a more conservative approach ($T = 1$ s), the attainable single-shot sensitivity with Q-II ($\Delta a \approx 10^{-10}\, g$) combined with a high degree of common-mode suppression of residual vibrations in a differential measurement scheme [52, 60] might allow for a measurement of the Eötvös factor of better than $\eta \leq 5 \cdot 10^{-11}$ [44]. Since the drop tower environment only allows for a repetition rate of three drops a day, the most promising method to extract the differential acceleration phase from the interferometric signal is Bayesian estimation [42].

Ultimately, these experiments might pave the way for space based instruments such as STE-QUEST (see Sec. 6.3.3), that in principle could achieve an overall sensitivity at the 10^{-15} level, based on a single-shot resolution of the differential acceleration of about $\sigma_{\Delta a} = 10^{-12}\,\mathrm{g}$ [9, 31] with $T = 5\,s$ and $N = 10^6$. In the end, this is comparable to the level of accuracy targeted by proposed space tests based on classical bulk matter [32, 33, 34]. As it was motivated in the beginning of this thesis, these

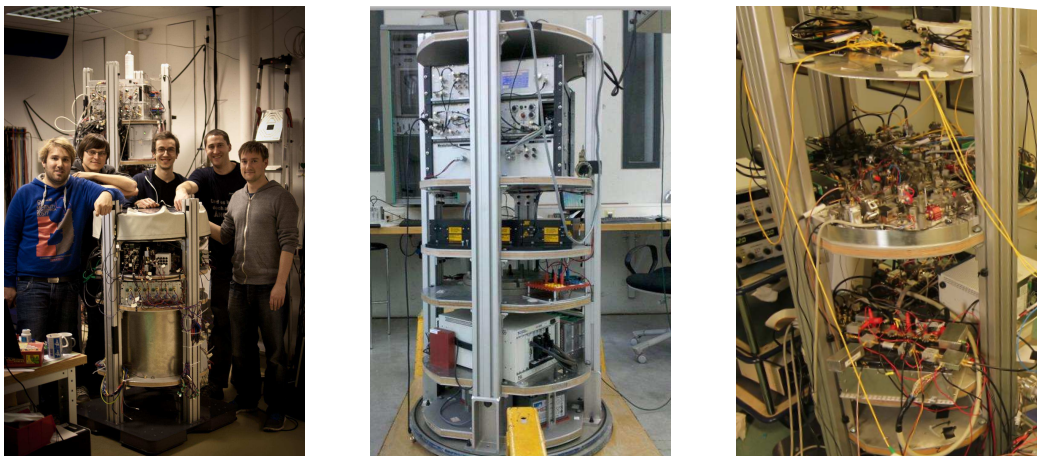

Figure 6.1: Photograph of the QUANTUS-II team[5] arrival in Bremen (left), the PRIMUS frequency comb (center) and laser system test capsule (right).

so far unmatched precision measurements in the classical and in the quantum domain would consequently set new limits to the validity of the equivalence principle in mutual agreement or, probably more interesting, find contradictory results.

QUANTUS-II

The second generation experiment Q-II outperforms the predecessor Q-I in many technical aspects and allows for dual-species operation (see Tab. 6.1). The budgets of a capsule eligible for catapult operation are defined by the ZARM Fallturmbetriebsgesellschaft (FAB) [107]. They show even more stringent limitations compared to a capsule for drop mode in terms of total length (2094 mm vs. 2860 mm) as well as total mass including all platforms and the outer shell (400 kg vs. 500 kg). With a net payload mass of less than 161.5 kg (including capsule platforms) and a volume of 0.3 m^3, Q-II impressively demonstrated the realization of the world's most compact dual-species quantum gas machine [199].

The heart of the experiment is a multi-layer atom chip, loaded in combination of a $2D^+$ [200] and 3D MOT which are separated by a differential pumping stage. Multiple layers of current carrying wires on the chip allow for the generation of various trapping potentials, including large volume traps for efficient MOT operation as well as ultra-steep harmonic potentials for fast evaporation. The flexibility in the attainable trap configurations are also promising for the optimization of DKC. First results of corresponding simulations indicate the possibility of reaching temperatures in the sub-nK regime [201]. With this setup, the full span between large single-species ^{87}Rb condensates (a few 10^5 atoms) and fast cycle times (repetition rate of up to 0.5 Hz) has already been proven in ground-based experiments. More technical details on the physics package and the performance can be found in [199]. In December 2013, the payload was transported to the Bremen drop tower (see Fig. 6.1, left) and the team is currently expecting a first drop in June 2014.

[5]From left to right: A. Grothe, W. Herr, Ch. Grzeschik, T. Sternke and J. Rudolph.

As one of the key elements for the successful Q-II operation in microgravity, a robust and miniaturized laser system for dual-species laser cooling of and atom interferometry with rubidium and potassium quantum gases is required. For this purpose, a catapult-capable laser system was developed in our group [202, 203, 204, 205] which ensures sufficient functionality even after DC shocks of about 30 g during launch and 50 g during recapture (see Sec. 5.1).

Exploiting the full potential of the Q-II atom-chip-based setup in terms of loading rate and atomic flux [199] requires high output powers on the order of a few hundreds of mW for $2D^+$ and 3D MOT. Therefore, micro-integrated master-oscillator, power amplifier (MOPA) modules are operated as light sources which have been developed specifically for this purpose at the Ferdinand-Braun Institut, Leibniz-Institut für Höchstfrequenztechnik in context of the QUANTUS project. They are based on a distributed feedback (DFB) diode laser whose emission is fed into a rich-waveguide (RW) mode filter/ preamplifier and subsequently amplified in a tapered amplifier section (see Fig. 6.2). Commercial-of-the-shelf thermo-electric coolers (TEC) are mounted between module and heatsink to regulate the temperature for reliable operation using on-module NTC sensors. With typical FWHM linewidths on the order of a few hundreds of kHz for 780 nm emission [206], this micro-integrated MOPA technology is capable to provide at least 1 W optical output power [207]. Detailed results on the electro-optical performance and first atom-optical applications of corresponding modules for 780/767 nm are currently prepared for publication [208].

The MOPA modules are the central devices of the Q-II dual-species laser system, which consists of two nearly congruent parts (Rb and K), segmented into four functional units each (see Fig. 6.3). These are interconnected with polarization maintaining single-mode optical fibers and comprise:

- **Reference laser module**. Miniaturized DFB diode laser based frequency reference, for technical details see [205].
- **MOPA module**. Houses the three MOPA modules and self-made, high-rigidity miniaturized opto-mechanics (titanium grade 5) together with commercially available passive (e.g., optical isolator, fiber-collimators) components to fiber-couple and subsequently guide the light to the other units.
- **Light distribution and switching module**. Capable of $2D^+$/3D switching, selection of Raman- or Bragg beam splitter operation. Besides obligatory optics and catapult-capable opto-mechanics, it additionally features active components for reliable and fast light switching (e.g., acousto-optical modulators, shutters).
- **Raman laser module**. Coherent manipulation of the atomic cloud with beam splitters of Raman-type. Information on these systems can be found it [203, 204].

The final overlap between potassium and rubidium light and the distribution towards the physics package is done by fiber-optical splitter systems. Including the 5 cm thick honey-comb aluminum base plate, the entire laser system (without control and driver electronics) for dual-species operation fits within a volume of less than 50 l and features a mass budget of about 35 kg.

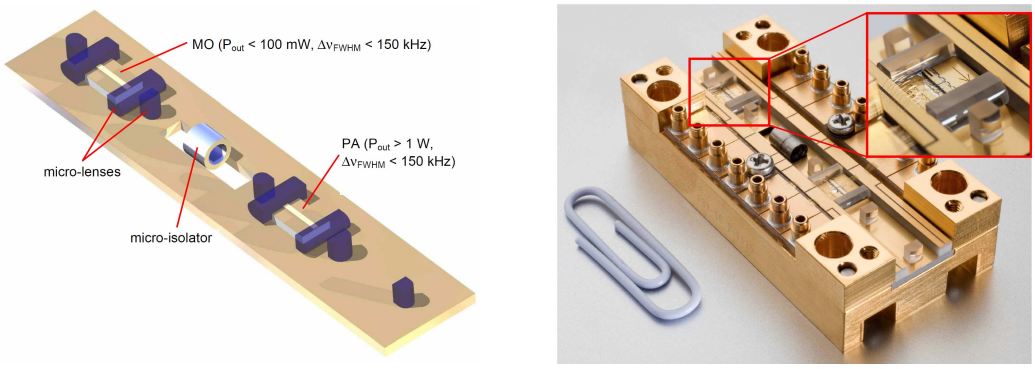

Figure 6.2: Schematic (left) and picture (right) of a 2nd generation micro-integrated master-oscillator, power-amplifier (MOPA) module. The oscillator (MO) and the amplifier chip (PA) are mounted onto a gold-coated aluminum-nitride (AlN) sub-mount which serves as a heat spreader. The sub-mounts are soldered onto a micro-optical bench (in-between, micro-optics are assembled with adhesive bonding techniques), which itself is clamped on a copper heat sink for better handling and contacting. To prevent optical feedback, a micro-isolator is placed between MO and PA section. The microbench features a net size of only 10 x 50 mm^3, the entire module is smaller than 25 x 50 x 15 mm^3. Adapted from [209].

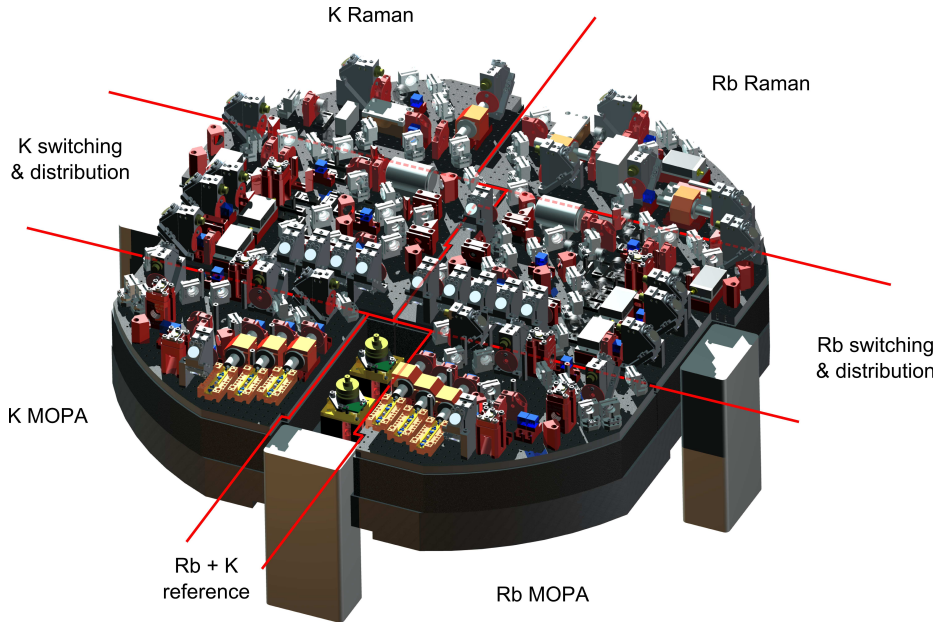

Figure 6.3: CAD drawing of the Q-II catapult capable laser system for dual-species interferometry with ultra-cold Rb and K quantum gas mixtures [202]. It consists of two nearly congruent parts (for Rb and K), segmented into four functional units each. With a total mass budget of less than 35 kg (without electronics), the entire system fits on a capsule platform with a diameter of about 700 mm only.

The rubidium part of the laser system is operable and already integrated in the Q-II catapult payload. Prior to integration, the mechanical stability and basic performance of the frequency stabilization has been separately tested in dedicated drop- and catapult campaigns. Currently, the potassium part is being assembled and will presumably complete the laser system in mid of 2015[6].

PRIMUS

The PRIMUS experiment complements the drop tower related research towards dual-species interferometry with a different technological approach. Here, the source for degenerate gases will be a crossed optical dipole trap [198, 44]. Once trapped in such a potential, both atomic species can be simultaneously cooled down to degeneracy by simply lowering the optical power of the two beams for forced evaporative cooling [210]. Additionally, a crossed optical dipole trap or dipole forces in general may be interesting for the implementation of DKC. In principle, the waist can be tuned to generate larger trapping volumes and highly symmetric configurations can be accessed due to the Gaussian beam profile. The DKC strength is adjustable via the total optical power and the absolute frequency detuning [211].

A striking advantage of this setup lies in the accessibility of Feshbach resonances. They allow to (i) tune the interaction strength to favorable values for efficient evaporation and lower losses due to two- and three body collisions [212, 213] as well as (ii) adjust the mixture to remain in a miscible phase during the measurements.

Currently, the subsystems are being assembled and integrated to achieve all-optical Bose-Einstein condensation in ground-based measurements, which is scheduled for late 2014 [214]. A picture of the PRIMUS payload comprising laser system, batteries, control computer and basic capsule infrastructure is shown in Fig. 6.1 (right).

The PRIMUS laser system (excl. dipole trap laser) is mostly based on the Q-II laser technology but relies on another approach concerning the laser source type. Here, the Raman lasers are drop tower capable, micro-integrated extended cavity diode laser (ECDL) modules. These ECDLs have become available due to the on-going developments at the Ferdinand-Braun Institut, Leibniz-Insitut für Höchstfrequenztechnik in context of the LASUS project (see Fig. 6.4, top). They provide sufficiently narrow short-term FWHM linewidhts of less than 100 kHz (100 μs) and an output power on the order of a few tens of mW. In preparation of the sounding rocket missions (see Sec. 6.3.2), they have been qualified in vibration tests (8.1 g_{RMS} and 21.4 g_{RMS} 20-2000 kHz) and mechanical shock tests (1500 g) where no degradation of the electro-optical performance was observed [215].

Since the dual-species interferometer will operate with beam splitter lasers at different wavelengths of 780 nm and 767 nm, it ultimately may be necessary to provide a phase link between the two laser systems to obtain an accurate estimate of the differential phase. In PRIMUS, this will be achieved by means of a femtosecond frequency comb (Menlo Systems), which has been tested separately in various drop campaigns (see Fig. 6.1, center).

[6] This point in time mainly depends on the concerted Q-II drop campaign strategy and corresponding preparatory experiments on ground.

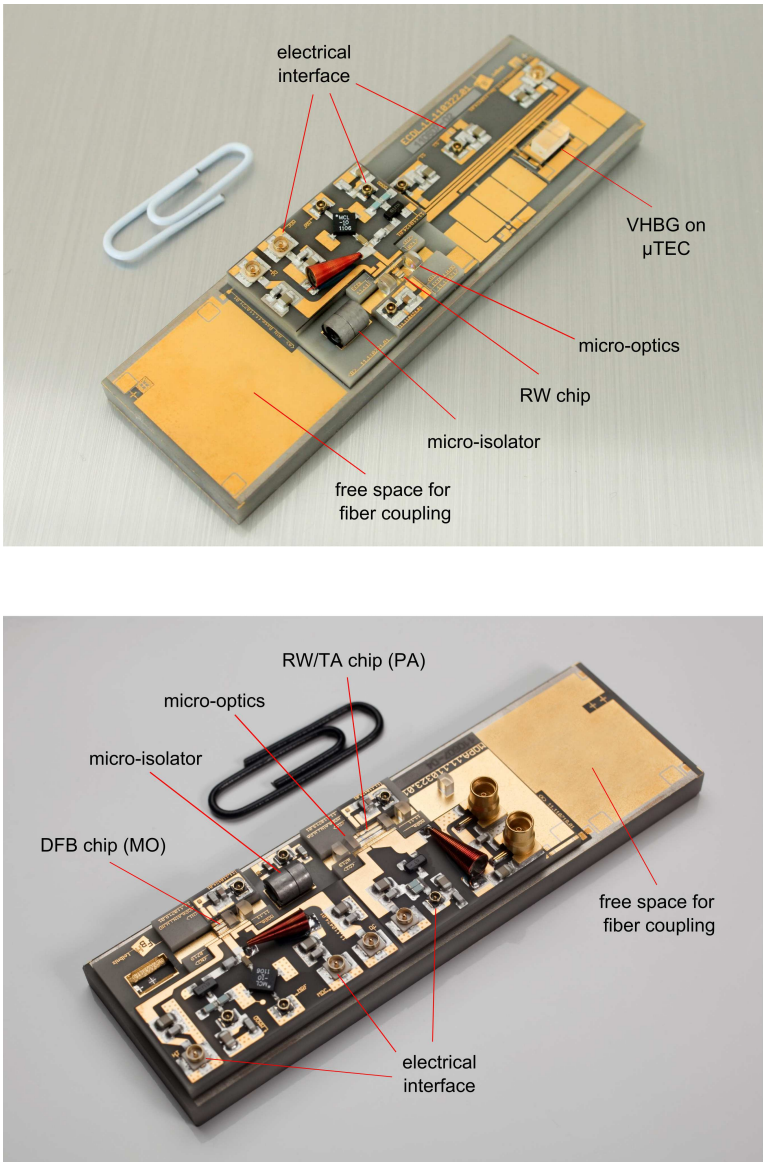

Figure 6.4: Photographs of micro-integrated ECDL (top) and MOPA (bottom) modules of the 3rd generation (© Ferdinand-Braun Institut, Leibniz-Institut für Höchstfrequenztechnik). They are based on a versatile platform comprising the GaAs semiconductor chip(s), micro-optics and electronic interfaces altogether assembled onto a structured aluminum-nitride (AlN) ceramic plate with a footprint of 80 x 25 mm^2. Including the electrical interface, it takes up a volume of 30 cm^3 only with mass budget of 40 g [215].

For laser cooling of rubidium, DFB-MOPA modules based on the same technology platform [216] (see Fig. 6.4, bottom) are used whereas in case of the comparably dense D_2-level structure of potassium, again ECDLs are foreseen which will be subsequently fed into a macroscopic TA section to achieve the relevant output power levels. The light switching, overlapping and distribution modules are mostly based on Q-II heritage which comprises free-space laser beam manipulation with high-rigidity, self-made opto-mechanics assembled onto a honey-comb baseplate (cf. Fig. 6.3).

6.3.2 Sounding rocket experiments and missions

The drop tower is an excellent test-bed for pathfinder experiments in extended free fall. In return, this microgravity platform already imposes demanding requirements on the payload key technologies in terms of mechanical and thermal robustness, long-term reliability, remote control capability, and miniaturization.

As the next step towards space-borne application and consecutive experiments, sounding rockets are commonly used. They offer a reduced gravity environment (remaining accelerations below 10^{-5} g after heights of 80 - 100 km) with a duration of about six minutes during a free fall parabola in the thermosphere [217, 218]. The height of the apex depends on the specific motor combination and the payload mass, but typically yields 250-300 km. The comparably strong requirements in mechanical stability of sounding rocket payloads manifest the necessity of quantum technological maturity and sufficiently high technology-readiness-level (TRL):

- **Mechanical loads**. During the burning phase of the motors, the sounding rocket will spin up to about 3 Hz and high accelerations (up to 20 g), vibrations (8.1 g_{RMS} @ 20-2000 Hz, typ. qualification level for a double-stage sounding rocket of VSB-30 type) as well as DC shocks ($\sim$ 50 g) will affect the payload. Accordingly, the components and the subsystems as well as the entire instrument need to successfully pass all corresponding test procedures.

- **Temperature gradients**. Air friction heats up the outer hull to approx. 200°C during the ascent and additionally the flight electronics, laser sources and other accompanying active components will locally raise the temperature. During approximately 7 min of operational time (incl. ascent), a thermal-control-system (TCS) has to guarantee an acceptable thermal environment for the subsystems to operate reliably.

- **Maintenance-free instrument**. The entire experiment cannot be accessed after integration into the rocket, which is typically done more than half a year prior to launch[7]. After final integration, the instrument will be operating in its commissioning phase to optimize the measurement sequences and the over-all performance. All components and subsystems need to be reliably operating and must not show a critical degradation until launch. In case of any unexpected circumstances, this pre-flight phase might easily add up to more than a year.

[7] Some experiments require late access, for example short-living biological probes. In this case, the outer structure might be equipped with late access hatches. But considering a highly integrated and thermally system with delicate fiber optics, small hatches have not been considered as an advantageous option.

All of the above mentioned aspects have to be tackled by dedicated technology programs targeting at compact and robust solutions for each subsystem. The LASUS project led to design, assembly and qualification of diode laser systems for quantum gas operation aboard sounding rockets. In this context, a reference laser system for rubidium spectroscopy based on a micro-integrated DFB diode laser has been developed. It will fly as a piggy-back payload of the FOKUS experiment. Additionally, an entire laser system for laser cooling, state preparation, Bragg interferometry and detection of condensed rubidium atoms has been developed, assembled and qualified. This work was done in context of the MAIUS mission.

FOKUS experiment on TEXUS-51

Optical atomic clocks and atom interferometers in space would both benefit from an optical reference with high accuracy and precision such as a frequency comb [82, 219]. Since this technology is still comparably large and complex, the FOKUS project aimed for a compact, robust and maintenance-free solution for space applications.

In this context, a rocket-borne frequency comb has been developed by Menlo Systems and the MPQ [82]. The comb system is stabilized onto a chip-scale atomic clock (CSAC), comprises an Erbium-doped fiber laser emitting at 1560 nm in combination with an all-fibered optical amplifier. Approximately 100 mW are used for carrier-envelope-offset (CEO) beat detection in a f-2f interferometer [220] and 50 mW are frequency doubled to 780 nm in a waveguide-based second harmonic generation (SHG) module. This light can be used for absolute frequency comparisons of the comb oscillator with an additional laser system running at 780 nm, which is referenced to, for example, an optical transition of rubidium.

Within the LASUS project, a robust and miniaturized 780 nm reference laser system was developed which will operate together with the fiber comb on the TEXUS-51 mission. A schematic (left) as well as a picture (right) of the piggy-back payload are given in Fig. 6.5. The laser source comprises a DFB laser diode which is micro-integrated onto a structured AlN micro-bench. The latter corresponds to the 3rd generation of diode laser modules developed at the Ferdinand-Braun Institut, Leibniz-Institut für Höchstfrequenztechnik (cf. Fig. 6.4).

After passing a micro-isolator (OI), the light exiting the front facet is coupled into a polarization-maintaining single-mode fiber by means of a Zerodur [221] based fiber in-coupler[8] (INC). This in-coupler is glued onto a dedicated free-space area on the microbench. The laser module is placed onto a precision manufactured copper mount with a maximum bow of less than 10 μm with respect to a total length of 104 mm, and three clamps with a line contact fix the module in position [222]. This mount is then attached to a thermo-electric cooler (TEC), used for temperature stabilization with on-module NTC sensors next to the laser chip.

The fiber-coupled light is partially guided to a rubidium spectroscopy cell unit based on free-space optical bench technology[8] (B). Zerodur was chosen as the base material, comprising high rigidity and excellent thermal characteristics [221, 223]. On this board, one path is used for monitoring the Doppler-broadened signal (single pass, PD1),

[8]Developed and assembled in the framework of the LASUS project at the University of Hamburg

while the second path is designed in a double-pass configuration, allowing to detect a Doppler-free spectroscopy signal for frequency stabilization (PD2). The main part of the fiber-coupled light of the DFB master laser is being overlapped with frequency-doubled light of the frequency comb for subsequent beat detection (PD3). After electronic bandpass filtering, the beat frequency will be monitored during the mission which allows for on-flight frequency comparison.

The entire FOKUS experiment payload including the rubidium reference module (see Fig. 6.6) has a mass of about 23 kg, fits into a pressurized dome of 30 cm diameter and 35 cm height and needs about 80 W electrical power for operation [82]. The final vibration test was passed on qualification level (8.1 g_{RMS} @ 20-2000 Hz) for 120 s each axis. Immediately after the vibration phase the system is automatically mode-locked and then phase-stabilized. In addition, the 780 nm reference module was tested separately and remained stabilized to the atomic transition even during the vibration test. Moreover, a flight simulation test (switched-off cooling) verified all locks to remain in their locking range for at least 15 min of operation.

FOKUS should fly as part of the TEXUS-51 mission with a first scheduled launch date of April 2013. However, the mechanical guidance system of the specific launch tower at ESRANGE (European Space and Sounding Rocket Range) showed a critical degradation which would have led to unpredictable sounding rocket trajectories. The responsible safety board thus decided to cancel the campaign. Currently, the launch of the FOKUS experiment as part of the TEXUS-51 mission is scheduled for late 2014.

MAIUS mission

The MAIUS missions shall demonstrate the technological readiness of delicate quantum gas experiments for space applications by realizing the first rubidium Bose-Einstein condensate (BEC) and matter wave interferometer aboard a sounding rocket. Moreover, the experiment team will try to operate the system in a parameter regime (e.g. free evolution time), which is beyond the state-of-the-art accessible at the drop tower or in zero-g airplanes.

The physics package comprises a $2D^+$/3D-MOT atomic source combined with a multi-layer atom chip, both based on an enhanced Q-II design. The laser system technology and miniaturized electronics for the whole payload have been developed within the LASUS project. The mechanical and thermal engineering of the entire sounding rocket instrument was mainly done by DLR-RY and the stability tests have been carried out at the ZARM. The MAIUS experiment is currently in its integration phase and scheduled for a launch in late 2014. A scheme of the 11.8 m long sounding rocket vehicle with its subsystems (A-F) and a CAD drawing of the scientific payload (a-e) are shown in Fig. 6.7.

As one of the key subsystems, the laser system is based on a hybrid approach, combining free-space optical bench technology with fiber-integrated distribution systems. Laser sources are micro-integrated semiconductor laser modules which have been developed for precision measurement applications aboard sounding rockets (cf. Fig. 6.4) [216]. The functionality of the system comprises the operation of a $2D^+$/3D MOT for rubidium atoms, optical pumping, interferometry based on Bragg beam splitters and absorption imaging of the ultra-cold atomic cloud. Besides a total number of 8

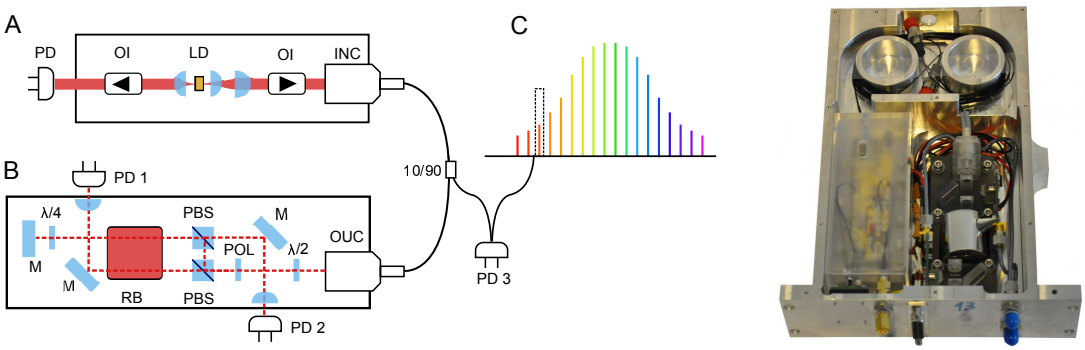

Figure 6.5: Schematic (left) and photograph (right) of the DFB-based reference laser module as a piggy-back payload developed for the FOKUS experiment. The outer dimensions of the assembled module are 215 x 170 x 48 mm^3. The GaAs semiconductor chip is soldered onto a submount, integrated on a 3rd generation microbench and collimated via micro-optics (**A**). The main output is fiber-coupled, guided to a spectroscopy module (**B**) and combined with the frequency doubled light of the frequency comb (**C**) for on-flight beat measurements. Abbreviations: photodiode (PD), optical isolator (OI), laser diode (LD), fiber in-coupler (INC), fiber out-coupler (OUC), half waveplate ($\lambda/2$), quarter waveplate ($\lambda/4$), mirror (M), dichroic polarizer (P), polarizing beam splitter (PBS), vapor cell (RB).

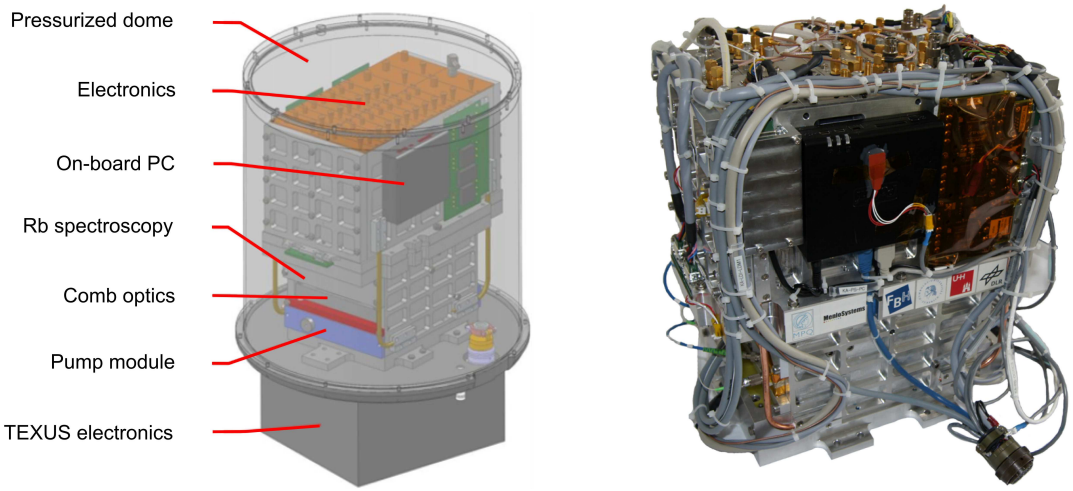

Figure 6.6: Design (left) and photograph (right) of the FOKUS overall system, ready for integration into the sounding rocket. The payload will be flown in a pressurized dome, with an inner diameter of 35 cm and a height of 35 cm. The total power consumption of the system is about 80 W, the total flight mass adds up to less than 25 kg. Figure adapted from [82].

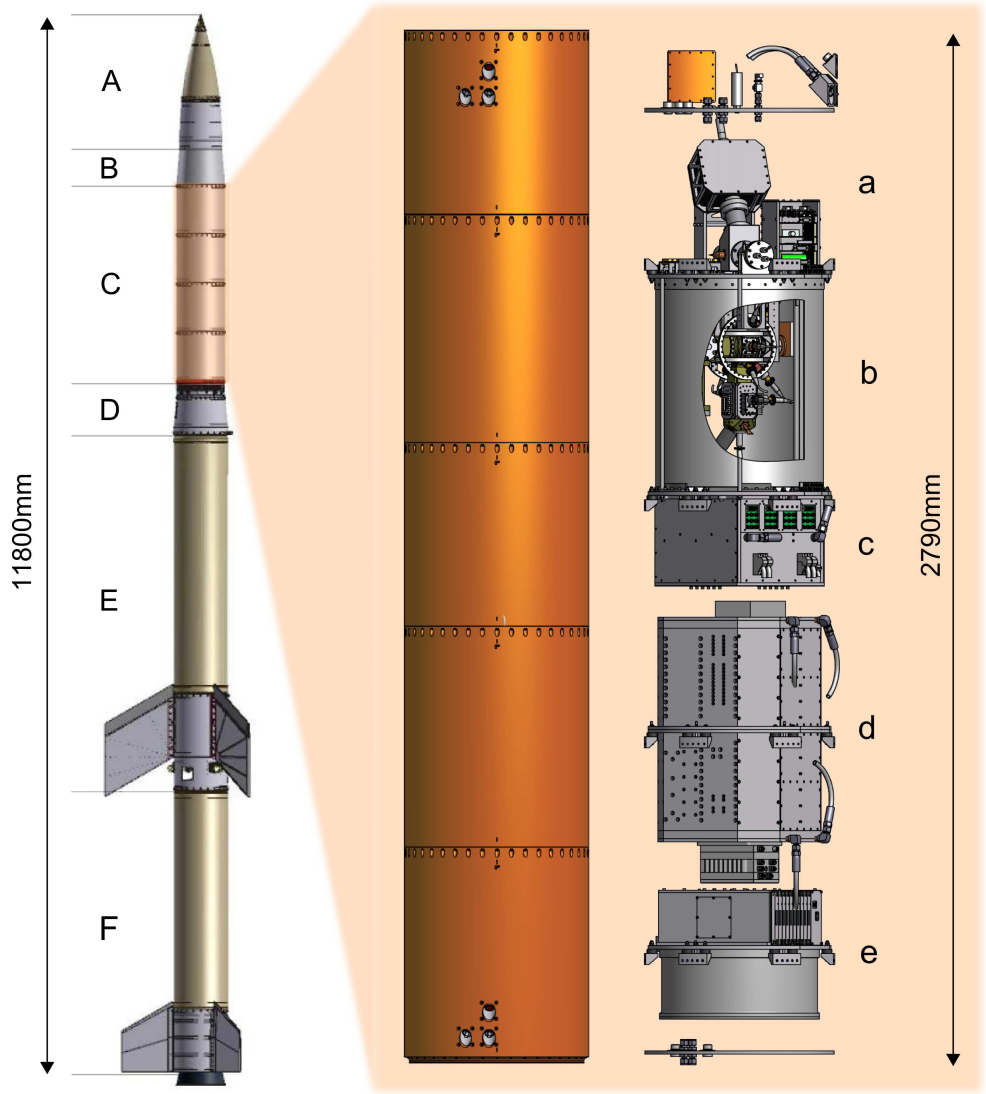

Figure 6.7: Overview of the sounding rocket experiment MAIUS-I [218]. The vehicle consists of a European recovery system (A), service system and rate-control system (B), the scientific payload (C), motor adapter and de-spin system (D), S30 motor incl. fin assembly (E), and the S31 motor incl. fin assembly (F). The payload consists of the vacuum pump section (a), the μ-metal shielded UHV chamber section with atomic source (b), the laser system (c), control electronics (d) and the power supply (e) [224].

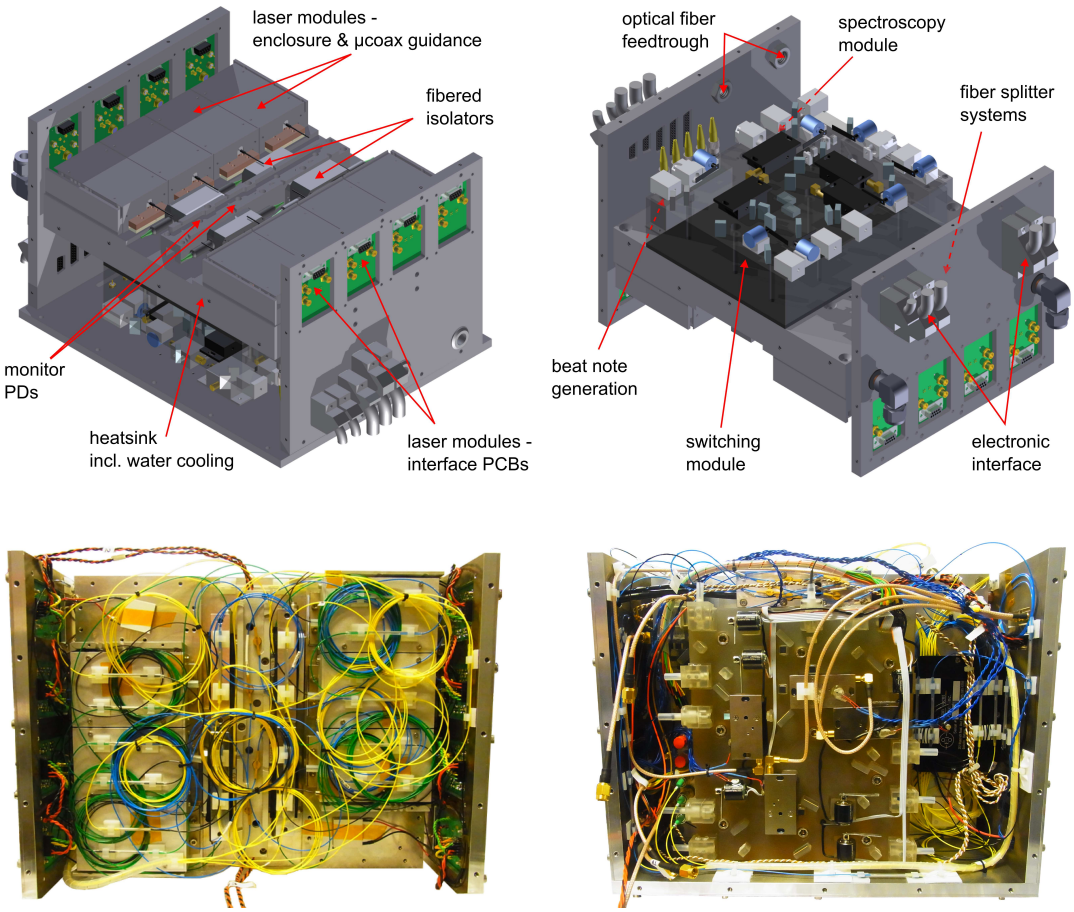

Figure 6.8: CAD drawing of the MAIUS laser system (top) and pictures of the integrated flight model (FM) laser system (bottom). The two-level design features a laser source part and a switching and distribution part both mounted onto opposite sides of a water cooled heat sink. On the left, the packaged laser modules, the PCB interfaces, fiber-optical isolators and PD-monitoring capability are shown. The right side comprises the Zerodur-based switching and spectroscopy module, the beat module and the fiber-splitter systems for distribution. The dimensions of the assembled FM laser system are 274 x 340 x 227 mm^3 and it features a total flight mass of about 27 kg.

micro-integrated laser modules, a Zerodur based switching and spectroscopy module, a beat module and fiber-optical splitter systems have been integrated together with extensive monitoring capabilities (e.g., power, frequency, temperature). Moreover, a basic redundancy architecture has been forseen[8].

Within a volume of less than 25 l and a mass of 27 kg (without control and driver electronics), the entire laser system successfully passed the final vibration test on acceptance level (5.4 g_{RMS} @ 20-2000Hz, 60 s each axis) in October 2013 and is now being integrated with the flight electronics and subsequently with the physics package. A CAD drawing and pictures of the integrated laser system are given in Fig. 6.8.

All electrical, thermal and optical interfaces of the laser system are summarized in the corresponding section of the Interface Control Document (ICD), see [225]. Detailed information on design, (sub-)system assembly, vibration test (qualification and acceptance level) and overall performance of the MAIUS laser system will be published elsewhere.

6.3.3 Towards satellite-borne quantum sensors

The STE-QUEST mission [226] proposal is a response to the call for medium-size (M-class) satellite missions by ESA's Cosmic Vision plan with launch opportunity between 2022 and 2024. It was recommended by the ESA advisory structure and finally selected for an assessment study (phase A).

The proposed satellite is operated in a highly elliptical orbit and hosts a dual-species atom interferometer (ATI) with two different isotopes of rubidium [227]. With the planned instrument, a measurement of the differential acceleration between ^{85}Rb and ^{87}Rb and therefore a space-based test of the weak equivalence principle (WEP) can be carried out. The specific choice of these isotopes as quantum test matter is justified by the high common-mode rejection for the differential acceleration [30, 9] and the technological heritage [12, 228, 46] as well as ground-based demonstration experiments [23].

As a source for coherent matter waves, Bose-Einstein condensates are generated in a hybrid trap setup, consisting of a multi-layer atom chip and a crossed optical dipole trap. After adiabatic release and optical delta-kick cooling, the matter wave mixture will be simultaneously interrogated by a $2T = 10$ s lasting, symmetric double-diffraction interferometer sequence to extract the differential acceleration [229, 230].

In particular, STE-QUEST is designed to measure for 0.5 hours during the perigee pass ($\sim$ 600 km) of the highly elliptical orbit with a total duration of about 16 hours (see Fig. 6.9), since the proximity to Earth maximizes a possible violation signal. The satellite's orientation is actively controlled with an inertial pointing mode which avoids the use of compensation strategies to maintain a sufficient measurement signal, such as co-rotating mirrors [231]. The proposed mission duration of 5 years enables a determination of the Eötvös ratio (net integration of 1.5 years) to an accuracy of

[8] Two DFB-MOPA modules are implemented as redundancy units, which will be connected to a redundant set of driver electronics. In case of any malfunction or critical degradation, the optical fiber of the defect device will be disconnected from the system and subsequently spliced to the output of the redundancy laser. This allows to restore the laser system's operative condition without major modifications.

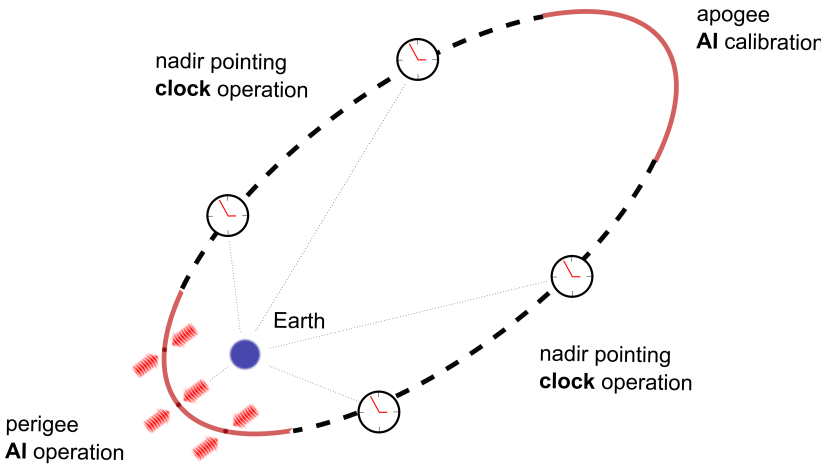

Figure 6.9: Schematic of the highly elliptical orbit initially chosen for clock comparison tests with STE-QUEST. The matter wave interferometer will operate for 0.5 hours during the perigee pass ($\sim$ 600 km).

2×10^{-15} [30]. This is four orders of magnitude more accurate than the proposed drop tower experiments (see Sec. 6.3.1) and beyond state-of-the-art precision achieved by lunar laser ranging [28, 232] and torsion balances [29]. Parameter optimization and re-calibration is operated and controlled during the apogee phase ($\sim$ 50000 km).

A cesium cold atomic clock is foreseen as an optional payload and would be operating in between apogee and perigee to be exposed to the largest possible variation of the gravitational potential. Using the clock on the satellite in comparison with a highly accurate ground-based network of clocks enables Earth and Sun gravitational redshift tests with fractional uncertainties of 1×10^{-7} and 2×10^{-6}, respectively [227].

The dual-species atom interferometer payload as the main instrument can be subdivided into three functional units: physics package, laser system, and electronics module. The physics package consists of a magnetically shielded UHV vacuum chamber which comprises the atomic source ($2D^+/3D$ MOT assembly), the hybrid trap of atom chip and optical dipole trap, the high-quality retro-reflecting mirror for the interferometer beams and the detection system. The laser system provides all necessary frequencies to operate a dual-species interferometer. Both, the physics package as well as the laser system require complex driver and control electronics unit. A detailed description of the payload is given in [233].

Including 20% component contingency, a total mass budget of 221 kg, a peak power level below 815 W (608 W in average) and a volume of 470 l are allocated for the entire STE-QUEST payload. Corresponding system studies showed that the payload would well fit on a satellite launched with a Soyuz rocket [233].

Laser system for the STE-QUEST dual-species atom interferometer

For STE-QUEST, a hybrid system is proposed comprising a reference and optical dipole trap laser based on telecom technology and frequency doubling techniques with

micro-integrated, high power diode laser modules. The complex switching procedures of all laser beams (excl. dipole trap) as well as the precise and controlled distribution of the laser light to the physics package is realized with a Zerodur optical bench setup combined with a fiber optical splitter system.

In particular, this design approach is the result of a delta-study of the technological key components and subsystems carried out in the consortium's work of phase A. The proposed system (see Fig. 6.10.) can be divided into three functional units:

- **Reference and optical dipole trap laser (ROL)**. Includes the frequency stabilized reference laser and generates the laser beams for optical dipole trap operation. This unit is mostly based on telecommunication components and frequency doubling waveguide technologies. All-fibered components developed in the telecom field naturally supply miniaturized and robust solution, whose technological maturity has also been demonstrated within several projects in the area of inertial quantum sensors [46, 45, 234]

- **Micro-integrated diode laser package (DLP)**. Micro-integrated diode laser modules are the sources for laser cooling (in a $2D^+/3D$ MOT configuration), internal state preparation, coherent manipulation and detection of the ^{87}Rb and ^{85}Rb quantum gas mixture. They are built on either already space qualified or space compatible technologies and constitute the 4th generation of micro-integrated diode laser modules (cf. 2nd gen. in Sec. 6.3.1 and 3rd gen. in Sec. 6.3.2) developed at the Ferdinand-Braun Institut, Leibniz-Institut für Höchstfrequenztechnik[9]. The laser modules are hermetically sealed in a housing made of Kovar, filled with a technical gas and have a size of 128 x 78.2 x 22.5 mm^3 [227, 233]. The STE-QUEST concept features a narrow linewidth, extended cavity diode laser module (μECDL module) as a master oscillator and a separate high power amplifier (μPA module) unit interconnected with a polarization maintaining single-mode optical fiber. This two-module strategy provides a small linewidth (< 100 kHz) and a high fiber-coupled output power (1000 mW) with improved thermal stability.

- **Switching and distribution module (SDM)**. Switching module based on Zerodur optical bench technology in combination with a fiber-optical distribution module. Switching and intensity control is realized with a combination of acousto-optical modulators (AOMs) and mechanical shutters assembled onto the optical bench. Details on the SDM can be found in [111]

Each of the subsystems is integrated within a separate mechanical structure with optimized thermal budgets and adapted for specific characteristics in spatial dimensions [233]. The general requirements on the laser system performance and additional information can be found in [227].

In the end, however, STE-QUEST has not been selected for a M3 mission since the technological readiness of the instrument could not yet compete with more established

[9] Developed in the framework of the MILAS project (Mikrointegration von Lasersystemen für den Weltraumeinsatz).

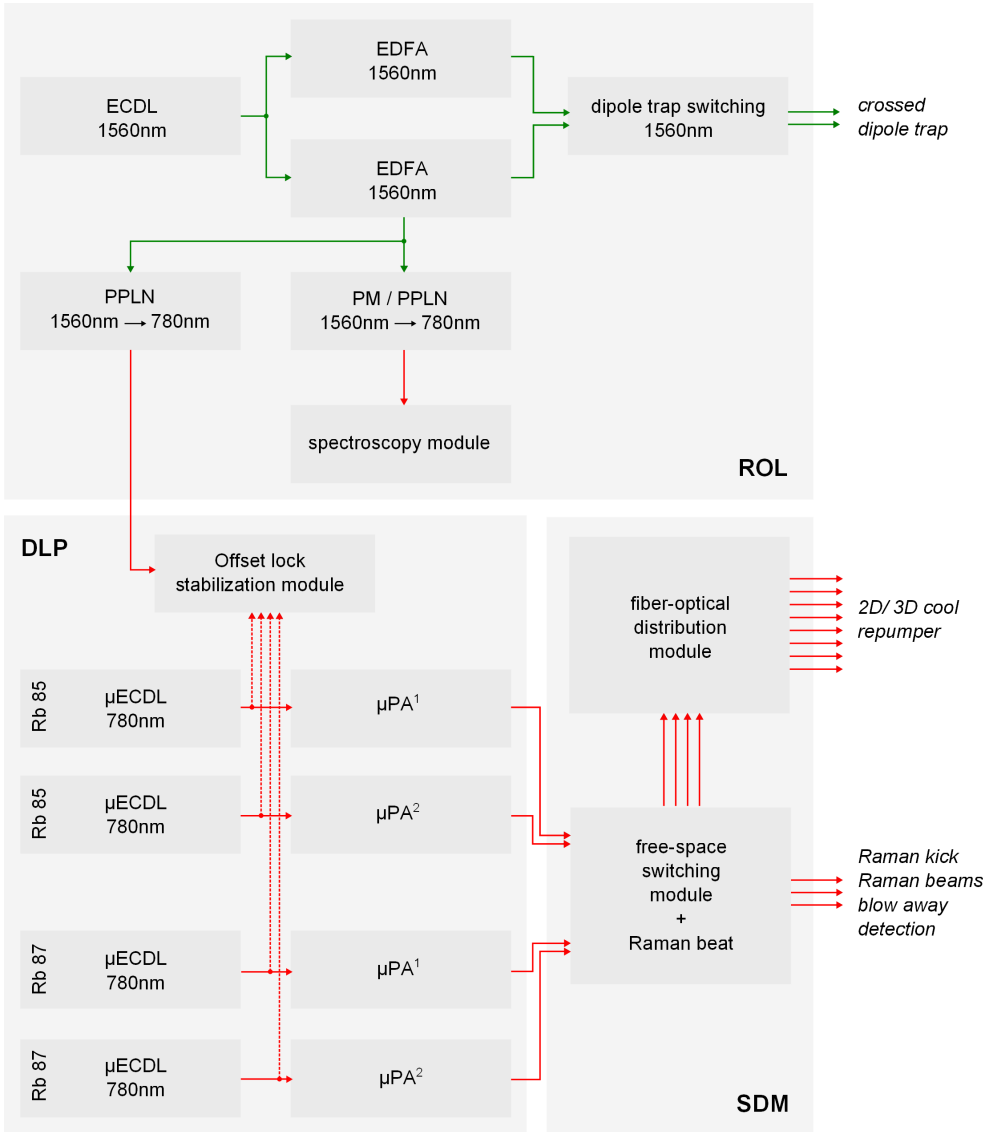

Figure 6.10: Overall schematic of the laser system for STE QUEST ATI. The laser system is divided into three subsystems: The reference laser and optical dipole trap module (ROL), the diode laser package module (DLP) and the switching and distribution module (SDM). All interfaces shown here are pm single mode optical fibers. Abbreviations: Extended cavity diode laser (ECDL), Erbium-doped fiber amplifier (EDFA), phase modulator (PM), periodically poled Lithium-Niobate (PPLN), micro-integrated extended cavity diode laser (μECDL), micro-integrated power amplifier (μPA). [1]Laser modules used for 2D$^+$/3D MOT operation and as one beam of the Raman laser pair. [2]Laser modules used for repumping and as the other beam of the Raman laser pair.

technologies as proposed for payloads in the other mission scenarios. The science case had nevertheless received a positive evaluation and the consortium already discusses the immediate next steps to be prepared for upcoming calls on suitable satellite missions [235].

A Light-pulse levitation and a bouncing condensate gravimeter

By dropping bodies and timing their free-fall, one can derive a value for the local gravitational acceleration. The timing presented here is based on repetitive optical levitation of atoms with acceleration-induced first-order Bragg diffraction off a standing light wave.

Usually, levitation in cold atomic physics is referred to as magnetic fields interacting with paramagnetic atoms. The magnetic moment of the atoms interacts with magnetic fields which results in an effective force when using gradients as

$$\vec{F} = g m_F \mu_B \nabla \vec{B}, \tag{A.1}$$

with magnetic quantum number m_F, Landé factor g, Bohr magneton μ_B and the magnetic field gradient $\nabla \vec{B}$. For example, this force could be used for continuous levitation of atoms against gravity. By doing so, cold atom experiments could for example profit from extended measurement times, the possibility to realize ultra-shallow trapping potentials and optimizations of the evaporation efficiency due to the compensation of the gravitational sag [19]. So far, magnetic levitation is restricted to a small volume only and requires numerous of bias fields for precise control [63]. The levitating potential is inherently affected by noise of the current sources driving the magnetic coils, which might disturb the free evolution of the atomic wave function. Moreover, magnetic levitation can be optimized for one atomic species or isotope only, since the magnetic force is independent of the mass, which obviously is not the case for gravity.

Another method for levitation is given by repetitive optical pulses based on Bragg diffraction. Let us assume an atomic cloud in free fall which has a certain COM position and velocity. After some time, it gets diffracted by a standing light wave whose effective wave vector points anti-parallel to gravity. If the transferred beam splitter momentum is larger than the momentum of the atoms before the pulse, the diffracted part bounces off the light wave, changes the direction of motion and ideally follows a classical 1D parabola. The atomic trajectory will pass its apex and at some point reach again position and velocity at the time of the first pulse. Here, we can apply another beam splitter and repeat this operation for a number of carefully timed Bragg pulses to keep the atoms "suspended" against gravity.

Using an atom chip with HR-coating simplifies such a setup enormously (see Fig. A.1, left), since besides the cold atoms themselves just one single-frequency laser beam reflected at the chip surface with μs timing is sufficient for basic operation[1]. The atoms will accelerate under the influence of the gravitational field which causes a

[1] In our experiment, an additional beam perpendicular to the Bragg beam is used for absorption imaging

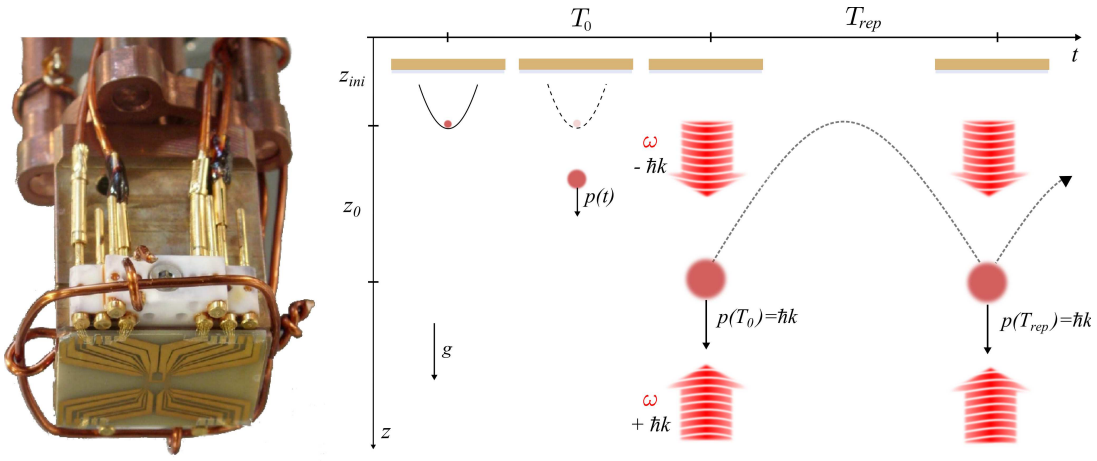

Figure A.1: Picture of the QUANTUS-I atom chip (left) and schematic of a chip-based acceleration measurement with repetitive Bragg diffraction (right). After release from the holding trap, the condensate is accelerated towards Earth. We wait for an expansion time $T_0 = \hbar k/mg$ until a standing light wave pulse is created by retro-reflection of a single frequency beam at the atom chip's HR-coated surface. In the moving frame of the atoms, the beams are Doppler-shifted to fulfill the condition for first-order Bragg diffraction. Subsequently, a fraction of atoms gets diffracted and can ideally be suspended against gravity if the pulses are applied with a repetition rate of $T_{rep} = 2\hbar k/mg$.

standing light wave to be Doppler-shifted in the moving frame of the atoms. With the right timing of the pulse, the Doppler-induced frequency difference between the incident and reflected beam fulfills the condition for Bragg diffraction (see Sec. 3.2.2).

If the beam splitting process does not affect the expansion of the atoms perpendicular to the wave vector (e.g., plane wave fronts, ideal mirror pulses), we can artificially extend the effective free expansion time in these directions. Additionally, the local gravitational acceleration can be derived from the optimized timing between subsequent Bragg pulses to achieve the best suspension efficiency. In principle, this method is applicable in rather compact setups without the need for large UHV chambers.

A.1 Proof-of-principle experiment

The described method can be used to demonstrate an extremely compact, atom-chip-based device for measuring the acceleration of the atoms induced by gravity. This was already demonstrated in similar setups [236, 237]. We start the experiment by creating a BEC in our chip-based Ioffe-Pritchard trap (IPT), which is adiabatically expanded into the weak trapping potential ($\omega_i = 2\pi \cdot (46, 18, 31)$). After the holding trap is switched off, the cloud expands due to mean-field repulsion whereas the center-of-mass (COM) is accelerated towards Earth.

In a one dimensional treatment (see Fig. A.1, right), the position of the COM as a function of time is given by $z(t) = z_{ini} + v_{ini}t - 1/2gt^2$, the corresponding momentum is $p(t) = m \cdot (v_{ini} - gt)$, with the initial velocities v_{ini} and positions z_{ini}. For simplicity,

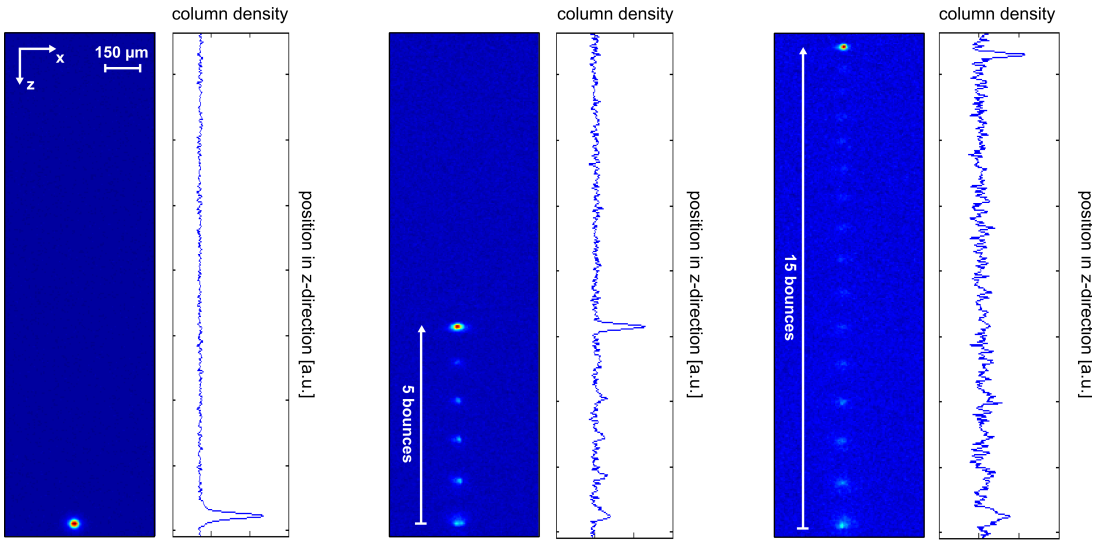

Figure A.2: Absorption images for different numbers of light-pulse levitation pulses. The BEC is released from the shallow trap ($\omega_i = 2\pi \cdot (46, 18, 31)$) and expands for about $T_0 = 580\,\mu$s. Then, an optical lattice is generated by retro-reflecting a single-frequency Gaussian beam at the HR-coated chip surface. From left to right, absorption images for 0, 5 and 15 subsequent first-order Bragg pulses are depicted. These are always taken after the same time-of-flight $T_{tof} = 32$ ms, which results in shifted COM positions of the bounced atoms in the z-direction since a fraction of atoms is suspended at a constant altitude. Next to each image, the corresponding column density profile is given.

we set $v_{ini} = z_{ini} = 0$ and after a free-fall time of T_0, the atoms will have momentum of $p(T_0) = mg \cdot T_0 \equiv \hbar k$. For ^{87}Rb, this yields $T_0 \approx 0.6$ ms[2].

At this time, we manipulate the atoms with a pulsed optical standing wave, reflected at the HR coated surface of the atom chip. In the end, about 10 mW have been used for the Bragg laser beam and the frequency was $\Delta = 640$ MHz red-detuned with respect to the $5S_{1/2} \rightarrow 5P_{3/2}$ cooling transition of ^{87}Rb. The light for the Bragg lattice was coupled into one polarization maintaining single mode optical fiber and guided to a telescope which is pointing towards the atom chip's surface (negative z-direction).

The telescope is of the same type as used for Bragg diffraction experiments described in this thesis so far. It is based on a single lens design with a FWHM of 0.65 cm. The angle of incidence at the atom chip's surface and therefore optimal overlapping of the incident and retro-reflected beam can be adjusted with three external screws. The optimization was done by maximizing the back-coupling efficiency.

After an expansion time T_0, the pulsed standing optical light wave will be Doppler-shifted in the moving frame of the atoms. T_0 can be chose such that the condition for first-order Bragg diffraction is fulfilled. In this way, a fraction of falling atoms with a COM momentum of $p(T_0) = \hbar k$ will be addressed by the beam splitter and afterwards

[2] In the real experiment, the atoms additionally get a slight momentum kick due to an imperfect release process. However, this can be compensated with the timing T_0 of the first beam splitter pulse.

feature an upward pointing momentum with $p(T_0 + \tau) = -\hbar k$ (see Fig. A.1, right). The corresponding beam splitter operation for a coherent superpostion can be written as

$$|\hbar k\rangle \rightarrow \frac{1}{\sqrt{2}} \left(|\hbar k\rangle - i|\hbar k\rangle \right), \tag{A.2}$$

and by carefully adjusting pulse duration and intensity, a pulse area of $\Omega \cdot \tau = \pi$ would ideally allow for bouncing-off the hole sample of atoms (see Sec. 3.2.2). In our experiment, however, Gaussian shaped beam splitter pulses have been applied with a duration of $\tau = 70$ μs which led to diffraction efficiencies of about 80%. Gravity again forces the atoms to change their direction at the apex of the parabola. After a time

$$T_{rep} = 2\hbar k/mg, \tag{A.3}$$

the momentum state $-|\hbar k\rangle$ evolves back into $|\hbar k\rangle$ due to the COM motion under the influence of gravity. For ^{87}Rb atoms, this time is approx. $T_{rep} \approx 1.2$ ms [150]. By now applying beam splitters with a timing interval of T_{rep}, we can suspend a fraction of atoms at a constant altitude.

In an exemplary measurement, both the time before the first pulse T_0 and the time between the repetitive pulses T_{rep} were varied to maximize the number of suspended atoms. In Fig. A.2, typical absorption images are shown which correspond to 0, 5 and 15 subsequent beam splitter operations. Since the absolute time-of-flight T_{tof} in these images was kept constant, the repetitive application of Bragg pulses results in a shifted COM position. The timing between the pulses T_{rep} was first estimated by using a common value for local gravity ($g = 9.81$ m/s^2), but afterwards optimized in terms of transition probability to achieve the best suspension efficiency for a certain number of bounces. The results of such an optimization are shown in Fig. A.3, where the accumulated diffraction efficiency for 12 subsequent beam splitter operations is plotted versus the separation time T_{sep}. A double-Gaussian was fitted to the data to extract the value for T_{sep} for the central peak (red line) in presence of the thermal background (dashed line), which results in the largest diffraction efficiency. The obtained cycle time $T_{sep} = 1198.6(7)$ μs determines the acceleration of the atoms due to gravity as

$$g = \frac{2\hbar k}{mT_{rep}} = 9.819(6) \text{ m/s}^2, \tag{A.4}$$

with the mass of the atoms m and the wave vector of the standing light wave $k = 2\pi/\lambda$. Here, the uncertainties are given by the fitting error of the central peak of the double-Gaussian fit. If we could have applied more beam splitters, the central peak would have become sharper and more pronounced. In our proof-of-principle measurement, the latter seems to be slightly off-centered w.r.t. thermal background (see Fig. A.3). This indicates that the timing of our pulses is still slightly incorrect. Moreover, the absolute value is arguable, since the atoms in the measurement have been in a state with non-zero magnetic moment ($m_F = 2$) and the direction of the effective wave vector (e.g. the orientation of the entire drop capsule) has not been optimized to the full extend along the direction of gravity.

Timing errors in T_{rep} cause a Doppler-induced frequency difference of the traveling

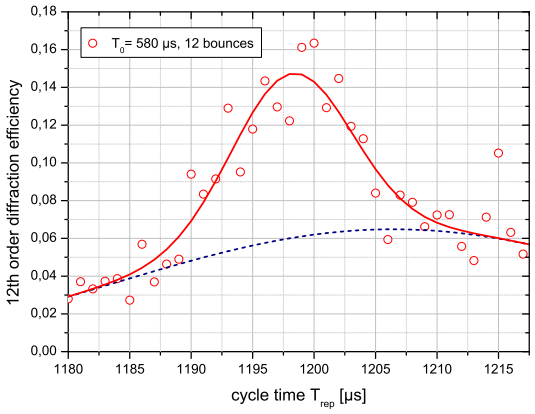

Figure A.3: Optimization of the cycle time T_{rep} to achieve the best suspension efficiency for 12 subsequent Bragg pulses.

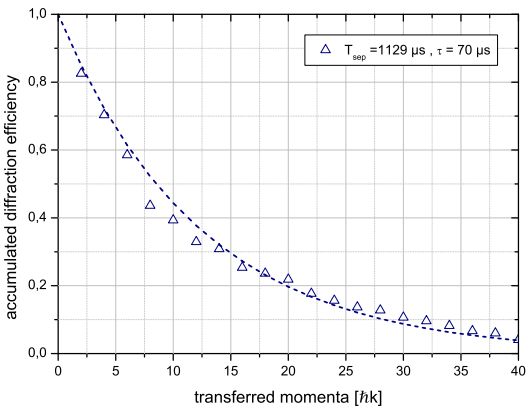

Figure A.4: Measurement of the decay of the accumulated diffraction efficiency for up to 23 repetitive Bragg pulses.

wave which does not correspond to twice the recoil frequency of ^{87}Rb. This mismatch will increase over time. Together with losses due to spontaneous emission and the non-linear expansion of the condensate due to mean-field acceleration (see Sec. 3.5.1), this mainly leads to a reduction in the repeatability and therefore fidelity of this optical levitation process. Single-pulse operation was measured to transfer about $\eta = 83\%$ of the atoms into the desired momentum state $-|\hbar k\rangle$ and populates adjacent states with the remaining atoms (see Fig. A.2). The experimentally observed decay rate for the application of up to 23 subsequent Bragg pulses (corresponds to $46\hbar k$ transferred momenta) is depicted as blue triangles in Fig. A.4. The blue dashed line is the calculation which considers an exponential decay.

Without optical levitation, the free fall time in our ground-based measurements is limited to about 32 ms. The atoms will then leave the detection volume and finally hit the ground of the chamber. With the method presented here, this observation time could be extended by $\Delta T = N_{bounce} \cdot T_{sep} \approx 23 \cdot 1.2\,\text{ms} = 27.6\,\text{ms}$, which efficiently results in a doubled time-of-flight of about $T_{max} \approx 59.6$ ms. With some technical improvements on the beam splitter efficiency and the transfer of the atoms into a magnetically insensitive state prior to the beam splitter pulses, this technique might be generally able to achieve suspension times on the order of $\Delta T > 100$ ms. This comes along with a more precise determination of the repetition rate T_{rep}, which might lead to a gravimetric precision as achieved with freely falling atom interferometers, but in a much more compact volume [236, 237].

B Rubidium D_2 line data

The properties of ^{87}Rb and ^{85}Rb given here are relevant to the calculations and approximations made in this thesis. All data is adapted from [148, 150], which to the full extend can be accessed by `http://steck.us/alkalidata`.

Rubidium 87 D_2 line ($5^2S_{1/2} \rightarrow 5^2P_{3/2}$) optical properties

parameter	symbol	value
frequency	ω_0	$2\pi \cdot 384.230\,484\,468\,5(62)$ THz
transition energy	$\hbar\omega_0$	1.589 049 462(38) eV
wavelength (vacuum)	λ	780.241 209 686(13) nm
wave number (vacuum)	$k/2\pi$	12 816.549 389 93(21) cm^{-1}
natural linewidth (FWHM)	Γ	$2\pi \cdot 6.0666(18)$ MHz
recoil velocity	v_r	5.8845 mm/s
recoil energy	ω_r	$2\pi \cdot 3.7710$ kHz
recoil temperature	T_r	361.96 nK
doppler temperature	T_D	145.57 μK

Rubidium 85 D_2 line ($5^2S_{1/2} \rightarrow 5^2P_{3/2}$) optical properties

parameter	symbol	value
frequency	ω_0	$2\pi \cdot 384.230\,406\,373(14)$ THz
transition energy	$\hbar\omega_0$	1.589 049 139(38) eV
wavelength (vacuum)	λ	780.241 368 271(27) nm
wave number (vacuum)	$k/2\pi$	12 816.546 784 96(45) cm^{-1}
natural linewidth (FWHM)	Γ	$2\pi \cdot 6.0666(18)$ MHz
recoil velocity	v_r	6.0230 mm/s
recoil energy	ω_r	$2\pi \cdot 3.8597$ kHz
recoil temperature	T_r	370.47 nK
doppler temperature	T_D	145.57 μK

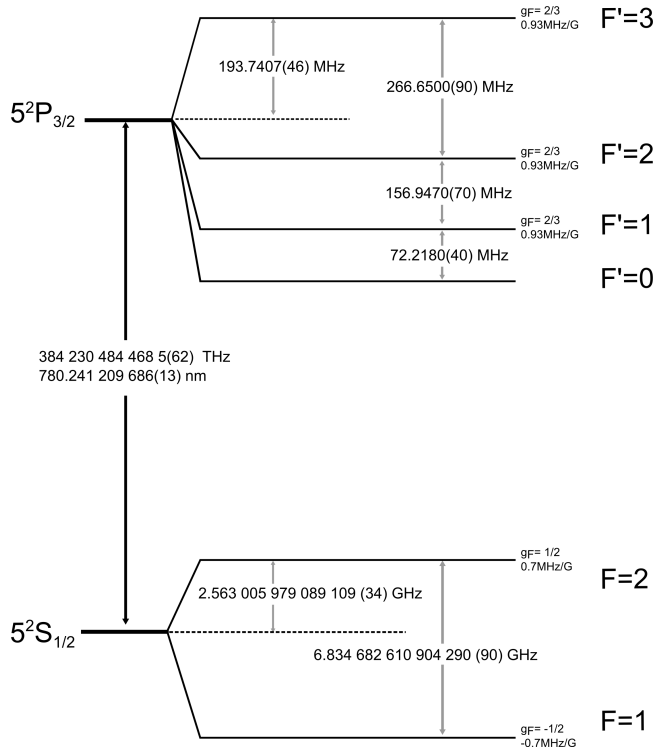

Figure B.1: ^{87}Rb D_2 transition hyperfine structure, with frequency splittings between the hyperfine energy levels, adapted by [150].

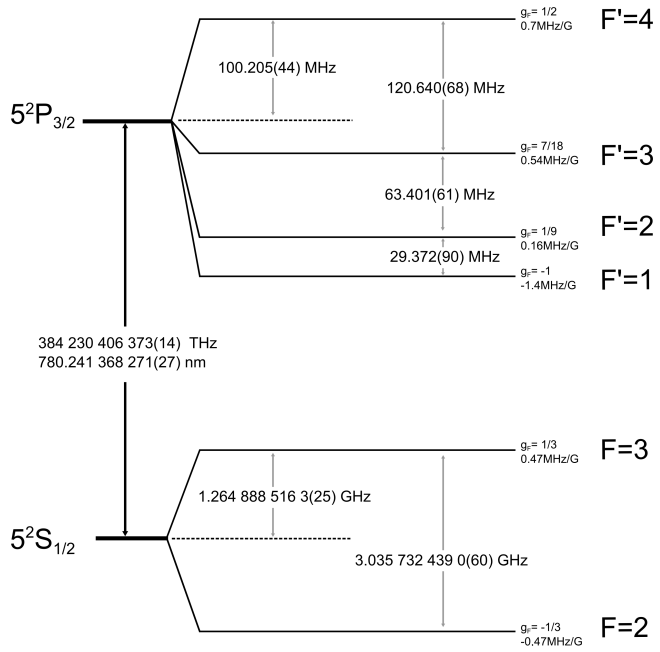

Figure B.2: ^{85}Rb D_2 transition hyperfine structure, with frequency splittings between the hyperfine energy levels, adapted by [148].

C Abbreviations

The abbreviations used in this thesis are explained here.

ACES	Atomic clock ensemble in space
AI	Atom interferometer
AlN	Aluminum-nitride
AMZI	Asymmetric Mach-Zehnder interferometer
AOM	Acousto-optic modulator
ARP	Adiabatic rapid passage
BEC	Bose-Einstein condensate
CAL	Cold atom laboratory
CCD	Charge-coupled device
CCP	Conductively cooled package
CHAMP	Challenging mini-satellite payload
CM	Chip model
COM	Center-of-mass
COTS	Commercial-off-the-shelf
DDS	Direct digital synthesizer
DFB	Distributed feedback
DKC	Delta-kick-cooling
DLP	Diode laser package module
ECDL	Extended cavity diode laser
μECDL	Micro-integrated extended cavity diode laser
EDFA	Erbium-doped fiber amplifier
EEP	Einstein's Equivalence Principle
EOM	Electro-optic modulator
FC	Fiber coupler
FFT	Fast Fourier transform
FMS	Frequency modulation spectroscopy
FOKUS	Faserlaserbasierter optischer Kammgenerator unter Schwerelosigkeit
FPGA	Field-programmable gate array
GOCE	Gravity field and steady-state ocean circulation explorer
GP	Gross-Pitaevskii
GPS	Global positioning system
GRACE	Gravity recovery and climate experiment
GR	General Relativity
GW	Gravitational waves
HYPER	Hyper-precision cold-atom interferometry in space
ICE	Interférométrie cohérente pour l'Espace
IMU	Inertial measurement unit

IPT	Ioffe-Pritchard trap
ISS	International Space Station
KALEXUS	Kalium-Laserexperimente unter Schwerelosigkeit
LASUS	Entwicklung von neuartigen Diodenlasersystemen für Präzisionsexperimente unter Schwerelosigkeit
LD	Laser diode
LLI	Local Lorentz Invariance
LO	Local oscillator
LPI	Local Position Invariance
MAIUS	Materiewellen-Interferometer unter Schwerelosigkeit
MILAS	Mikrointegration von Lasersystemen für den Weltraumeinsatz
MOPA	Master-oscillator-power-amplifier
MORABA	Mobile Raketen Basis
MOT	Magneto-optical trap
MTS	Modulation transfer spectroscopy
OI	Optical isolator
OPLL	Optical phase lock loop
ORI	Open Ramsey-type interferometer
μPA	Micro-integrated power amplifier
PBS	Polarizing beam splitter
PD	Photo diode
PFD	Phase-frequency detector
PHARAO	Projet d'horloge atomique par refroidissement d'atomes en orbite
PPLN	Periodically poled Lithium-Niobate
PRIMUS	Präzisionsinterferometrie unter Schwerelosigkeit
QED	Quantum electrodynamics
QUANTUS	Quantengase unter Schwerelosigkeit
QWEP	Quantum test of the weak equivalence principle
RF	Radio frequency
ROL	Reference and optical dipole trap laser
SDM	Switching and distribution module
SHG	Second harmonic generation
SHM	Space hydrogen maser
SME	Standard-model extension
SNR	Signal-to-noise ratio
STE-QUEST	Space time explorer and quantum equivalence space test
TA	Tapered amplifier
TCS	Thermal control system
TEC	Thermo-electric cooler
TEXUS	Technologische Experimente unter Schwerelosigkeit
TF	Thomas-Fermi
TOF	Time-of-flight
TRL	Technology-readiness-level
UFF	Universality of the Free Fall
UHV	Ultra-high vacuum

Acknowledgment

In the last years, I have received support and encouragement from a great number of people. It is to them that I owe my deepest gratitude. I would like to thank...

my advisor Achim Peters for giving me the opportunity to work in his group. His in-depth knowledge, continuous enthusiasm and commitment to the highest standards inspired and motivated me throughout the entire thesis. He gave me the confidence and the necessary academic freedom to participate in a broad range of exciting projects.

Ernst Maria Rasel for leading the hopefully further growing QUANTUS collaboration, for many valuable discussions during the meetings and his thoughtful guidance of the experiment.

The experiment team of QUANTUS-I for all the time in and around the lab: Hauke Müntinga, Holger Ahlers, and André Wenzlawski.

Holger Müller for a wonderful and stimulating research period at UC Berkeley, and especially my collegues Mike Hohensee and Shau-Yu Lan there.

Wojtek Lewoczko-Adamzczyk, Sven Herrmann and Max Schiemangk for not only proofreading the manuscript, but also for helpful discussions and advises.

Thorsten Rausche and his team of the mechanical workshop for professional and constant support. Without them, most of my constructions would have led to serious problems.

The bunch of people I had the opportunity to work with in the innumerable projects and collaborations: QUANTUS, LASUS, MAIUS, STE-QUEST, KALEXUS, FOKUS,... It was a pleasure and I learned a lot from you guys - but I can hardly list you all here.

All colleagues of the QOM and NANO groups here at Humboldt-University as well as the laser metrology group coordinated by Andreas Wicht at the Ferdinand-Braun-Institute. Especially: Ahmad Bawamia, Heike Christoher, Aline Dinkelacker, Klaus Döringshoff, Christian Freier, Christoph Grzeschik, Matthias Hauth, Anja Kohfeldt, Christian Kürbis, Matthias Leifgen, Moritz Nagel, Andreas Schell, Vladimir Schkolnik.

My family and friends.

Kim.

Bibliography

[1] C. Kiefer. *Quantum Gravity*, volume 155. International Series of Monographs on Physics - Third Edition, 2012.

[2] N. Yu, J.M. Kohel, J.R. Kellogg, and L. Maleki. Development of an atom-interferometer gravity gradiometer for gravity measurement from space. *Appl. Phys. B*, 84(4):647–652, 2006.

[3] J.D. Prestage and G.L. Weaver. Atomic clocks and oscillators for deep-space navigation and radio science. *Proceedings of the IEEE*, 95(11):2235–2247, 2007.

[4] L. Cacciapuoti and Ch. Salomon. Space clocks and fundamental tests: The ACES experiment. *The European Physical Journal Special Topics*, 172(1):57–68, 2009.

[5] G. Seeber. *Satellite geodesy: foundations, methods, and applications*. Walter de Gruyter, 2003.

[6] C.-W. Chou, D.B. Hume, T. Rosenband, and D.J. Wineland. Optical clocks and relativity. *Science*, 329(5999):1630–1633, 2010.

[7] J.M. Hogan, D.M.S. Johnson, S. M. Dickerson, T. Kovachy, A. Sugarbaker, S.-W. Chiow, W. Graham, M.A. Kasevich, B. Saif, S. Rajendran, P. Bouyer, B.D. Seery, L. Feinberg, and R. Keski-Kuha. An atomic gravitational wave interferometric sensor in low earth orbit (AGIS-LEO). *General Relativity and Gravitation*, 43 (7):1953–2009, 2011.

[8] S. Dimopoulos, P.W. Graham, J.M. Hogan, and M. A. Kasevich. Testing general relativity with atom interferometry. *Phys. Rev. Lett.*, 98(11):111102, 2007.

[9] C. Schubert, J. Hartwig, H. Ahlers, K. Posso-Trujillo, N. Gaaloul, U. Velte, A. Landragin, A. Bertoldi, B. Battelier, P. Bouyer, F. Sorrentino, G.M. Tino, M. Krutzik, A. Peters, S. Herrmann, C. Lämmerzahl, L. Cacciapouti, E. Rocco, K. Bongs, W. Ertmer, and E.M. Rasel. Differential atom interferometry with ^{87}Rb and ^{85}Rb for testing the UFF in STE-QUEST. *arXiv:1312.5963*, 2013.

[10] H. Dittus, C. Lämmerzahl, and S.G. Turyshev. *Lasers, clocks and drag-free control: exploration of relativistic gravity in space*, volume 349. Springer, 2009.

[11] S.A. Fulling. Nonuniqueness of canonical field quantization in Riemannian space-time. *Physical Review D*, 7(10):2850, 1973.

[12] H. Müntinga, H. Ahlers, M. Krutzik, A. Wenzlawski, S. Arnold, D. Becker, K. Bongs, H. Dittus, H. Duncker, N. Gaaloul, C. Gherasim, E. Giese, C. Grzeschik, T. W. Hänsch, O. Hellmig, W. Herr, S. Herrmann, E. Kajari,

S. Kleinert, C. Lämmerzahl, W. Lewoczko-Adamczyk, J. Malcolm, N. Meyer, R. Nolte, A. Peters, M. Popp, J. Reichel, A. Roura, J. Rudolph, M. Schiemangk, M. Schneider, S.T. Seidel, K. Sengstock, V. Tamma, T. Valenzuela, A. Vogel, R. Walser, T. Wendrich, P. Windpassinger, W. Zeller, T. van Zoest, W. Ertmer, W.P. Schleich, and E.M. Rasel. Interferometry with Bose-Einstein condensates in microgravity. *Phys. Rev. Lett.*, 110:093602, 2013.

[13] J. Collins, A. Perez, D. Sudarsky, L. Urrutia, and H. Vucetich. Lorentz invariance and quantum gravity: an additional fine-tuning problem? *Physical review letters*, 93(19):191301, 2004.

[14] C. Lämmerzahl. The search for quantum gravity effects I. *Applied Physics B*, 84 (4):551–562, 2006.

[15] G. Amelino-Camelia, C. Lämmerzahl, A. Macias, and H. Müller. The search for quantum gravity signals. *arXiv preprint gr-qc/0501053*, 2005.

[16] D. Colladay and V.A. Kosteleckỳ. Lorentz-violating extension of the standard model. *Physical Review D*, 58(11):116002, 1998.

[17] T. van Zoest, N. Gaaloul, Y. Singh, H. Ahlers, W. Herr, S.T. Seidel, W. Ertmer, E.M. Rasel, M. Eckart, E. Kajari, S. Arnold, G. Nandi, W.P. Schleich, R. Walser, A. Vogel, K. Sengstock, K. Bongs, W. Lewoczko-Adamczyk, M. Schiemangk, T. Schuldt, A. Peters, T. Koenemann, H. Müntinga, C. Lämmerzahl, H. Dittus, T. Steinmetz, T.W. Haensch, and J. Reichel. Bose-Einstein condensation in microgravity. *Science*, 328(5985):1540–1543, 2010.

[18] A. Vogel, M. Schmidt, K. Sengstock, K. Bongs, W. Lewoczko, T. Schuldt, A. Peters, T. van Zoest, W. Ertmer, E.M. Rasel, T. Steinmetz, J. Reichel, T. Könemann, W. Brinkmann, E. Goeklue, C. Lämmerzahl, H.J. Dittus, G. Nandi, W.P. Schleich, and R. Walser. Bose-Einstein condensates in microgravity. *Appl. Phys. B*, 84(4):663–671, 2006.

[19] T. van Zoest. *Realisierung erster quantenentarteter Gase unter Schwerelosigkeit.* PhD thesis, Leibniz-Universität Hannover, 2008.

[20] A. Peters, K.Y. Chung, and S. Chu. High-precision gravity measurements using atom interferometry. *Metrologia*, 38(1):25–61, 2001.

[21] S. Merlet, Q. Bodart, N. Malossi, A. Landragin, F. Pereira Dos Santos, O. Gitlein, and L. Timmen. Comparison between two mobile absolute gravimeters: optical versus atomic interferometers. *Metrologia*, 47(4):L9–L11, 2010.

[22] S. Fray and M. Weitz. Atom-based test of the equivalence principle. *Space Science Reviews*, 148(1-4):225–232, 2009.

[23] A. Bonnin, N. Zahzam, Y. Bidel, and A. Bresson. Simultaneous dual-species matter-wave accelerometer. *Phys. Rev. A*, 88:043615, 2013.

[24] D. Schlippert, J. Hartwig, H. Albers, L.L. Richardson, C. Schubert, A. Roura, W.P. Schleich, W. Ertmer, and E.M. Rasel. Quantum test of the universality of free fall. *Phys. Rev. Lett.*, 112:203002, 2014.

[25] S.M. Dickerson, J. Hogan, A. Sugarbaker, T. Kovachy, S.-W. Chiow, and M.A. Kasevic. Atomic test of the equivalence principle in a 10-meter tower. In *43rd Annual Meeting of the APS Division of Atomic, Molecular and Optical Physics Volume 57, Number 5*, 2012.

[26] P. Hamilton, T. Barter, G. Kim, B. Mukherjee, and H. Mueller. Progress towards a test of the universality of free fall using a ^{6}Li-^{7}Li atom interferometer. In *43rd Annual Meeting of the APS Division of Atomic, Molecular and Optical Physics Volume 57, Number 5*, 2012.

[27] M.A. Hohensee, S. Chu, A. Peters, and H. Müller. Equivalence principle and gravitational redshift. *Phys. Rev. Lett.*, 106:151102, 2011.

[28] J.G. Williams, S.G. Turyshev, and D.H. Boggs. Lunar laser ranging tests of the equivalence principle. *Classical and Quantum Gravity*, 29(18):184004, 2012.

[29] T.A. Wagner, S. Schlamminger, J.H. Gundlach, and E.G. Adelberger. Torsion-balance tests of the weak equivalence principle. *Classical and Quantum Gravity*, 29(18):184002, 2012.

[30] D. Aguilera, H. Ahlers, B. Battelier, A. Bawamia, A. Bertoldi, R. Bondarescu, K. Bongs, P. Bouyer, C. Braxmaier, L. Cacciapuoti, et al. STE-QUEST – Test of the universality of free fall using cold atom interferometry. *accepted for publication in Class. Quantum Grav.*, 2014.

[31] G.M. Tino, F. Sorrentino, D. Aguilera, B. Battelier, A. Bertoldi, Q. Bodart, K. Bongs, P. Bouyer, C. Braxmaier, L. Cacciapuoti, N. Gaaloul, N. Gürlebeck, M. Hauth, S. Herrmann, M. Krutzik, A. Kubelka, A. Landragin, A. Milke, A. Peters, E.M. Rasel, E. Rocco, C. Schubert, T. Schuldt, K. Sengstock, and A. Wicht. Precision gravity tests with atom interferometry in space. *Nuclear Physics B - Proceedings Supplements*, 243-244:203 – 217, 2013.

[32] P. Touboul, G. Métris, V. Lebat, and A. Robert. The MICROSCOPE experiment, ready for the in-orbit test of the equivalence principle. *Classical and Quantum Gravity*, 29(18):184010, 2012.

[33] J. Overduin, F. Everitt, P. Worden, and J. Mester. STEP and fundamental physics. *Classical and Quantum Gravity*, 29(18):184012, 2012.

[34] A.M. Nobili, M. Shao, R. Pegna, G. Zavattini, S.G. Turyshev, D.M. Lucchesi, A. De Michele, S. Doravari, G.L. Comandi, T.R. Saravanan, F. Palmonari, G. Catastini, and A. Anselmi. 'Galileo Galilei' (GG): space test of the weak equivalence principle to 10^{-17} and laboratory demonstrations. *Classical and Quantum Gravity*, 29(18):184011, 2012.

[35] S. Herrmann, E. Göklü, H. Müntinga, A. Resch, T. Zoest, H. Dittus, and C. Lämmerzahl. Testing fundamental physics with degenerate quantum gases in microgravity. *Microgravity Science and Technology*, 22(4):529–538, 2010.

[36] E. Joos. *Decoherence and the appearance of a classical world in quantum theory.* Springer, 2003.

[37] M. Arndt, A. Ekers, W. von Klitzing, and H. Ulbricht. Focus on modern frontiers of matter wave optics and interferometry. *New Journal of Physics*, 14(12):125006, 2012.

[38] R. Kaltenbaek, G. Hechenblaikner, N. Kiesel, O. Romero-Isart, K. Schwab, U. Johann, and M. Aspelmeyer. Macroscopic quantum resonators (MAQRO). *Experimental Astronomy*, 34(2):123–164, 2012.

[39] M. Doser and the Aegis collaboration. AEGIS: An experiment to measure the gravitational interaction between matter and antimatter. *Journal of Physics: Conference Series*, 199(1):012009, 2010.

[40] A. Kellerbauer, Y. Allkofer, C. Amsler, A.S. Belov, G. Bonomi, P. Bräunig, J. Bremer, R.S. Brusa, G. Burghart, L. Cabaret, C. Canali, F. Castelli, K. Chlouba, S. Cialdi, D. Comparat, G. Consolati, L. Dassa, L. Di Noto, A. Donzella, M. Doser, A. Dudarev, T. Eisel, R. Ferragut, G. Ferrari, A. Fontana, P. Genova, M. Giammarchi, A. Gligorova, S.N. Gninenko, S. Haider, J.P. Hansen, F. Haug, S.D. Hogan, L.V. Jørgensen, T. Kaltenbacher, D. Krasnický, V. Lagomarsino, S. Mariazzi, V.A. Matveev, F. Merkt, F. Moia, G. Nebbia, P. Nédélec, T. Niinikoski, M.K. Oberthaler, D. Perini, V. Petráek, F. Prelz, M. Prevedelli, C. Regenfus, C. Riccardi, J. Rochet, O. Røhne, A. Rotondi, M. Sacerdoti, H. Sandaker, M. Špaek, J. Storey, G. Testera, A. Tokareva, D. Trezzi, R. Vaccarone, F. Villa, U. Warring, S. Zavatarelli, and A. Zenoni. The AEGIS experiment at CERN. In *EXA 2011*, pages 43–49. Springer Netherlands, 2012.

[41] P. Hamilton, A. Zhmoginov, F. Robicheaux, J. Fajans, J.S. Wurtele, and H. Müller. Antimatter interferometry for gravity measurements. *Physical review letters*, 112(12):121102, 2014.

[42] G. Varoquaux, R.A. Nyman, R. Geiger, P. Cheinet, A. Landragin, and P. Bouyer. How to estimate the differential acceleration in a two-species atom interferometer to test the equivalence principle. *New J. Phys.*, 11:113010, 2009.

[43] J. Rudolph, N. Gaaloul, Y. Singh, H. Ahlers, W. Herr, T. Schulze, S.T. Seidel, C. Rode, V. Schkolnik, W. Ertmer, E.M. Rasel, H. Müntinga, T. Könemann, A. Resch, S. Herrmann, C. Lämmerzahl, T. van Zoest, H. Dittus, A. Vogel, A. Wenzlawski, K. Sengstock, N. Meyer, K. Bongs, M. Krutzik, W. Lewoczko-Adamczyk, M. Schiemangk, A. Peters, M. Eckart, E. Kajari, S. Arnold, G. Nandi, W.P. Schleich, R. Walser, T. Steinmetz, T.W. Hänsch, and J. Reichel. Degenerate quantum gases in microgravity. *Microgravity Science and Technology*, 23(3):287–292, 2011.

[44] S. Herrmann, H. Dittus, C. Lämmerzahl, QUANTUS, and PRIMUS teams. Testing the equivalence principle with atomic interferometry. *Classical and Quantum Gravity*, 29(18):184003, 2012.

[45] G. Stern, B. Battelier, R. Geiger, G. Varoquaux, A. Villing, F. Moron, O. Carraz, N. Zahzam, Y. Bidel, W. Chaibi, F. Pereira Dos Santos, A. Bresson, A. Landragin, and P. Bouyer. Light-pulse atom interferometry in microgravity. *Eur. Phys. J. D*, 53(3):353–357, 2009.

[46] R. Geiger, V. Menoret, G. Stern, N. Zahzam, P. Cheinet, B. Battelier, A. Villing, F. Moron, M. Lours, Y. Bidel, A. Bresson, A. Landragin, and P. Bouyer. Detecting inertial effects with airborne matter-wave interferometry. *Nat Commun*, 2:474, 2011.

[47] S.T. Seidel. MAIUS − A rocket-borne atom optical experiment. *Proceedings of the 63rd International Astronautical Congress, Naples*, 2013.

[48] L. Altenbuchner, J. Ettl, M. Hörschgen, W. Jung, R. Kirchhartz, A. Stamminger, and P. Turner. MORABA—Overview on DLR's mobile rocket base and projects. *SpaceOps 2012 conference proceedings*, 2012.

[49] A. Peters, K.Y. Chung, and S. Chu. Measurement of gravitational acceleration by dropping atoms. *Nature*, 400(6747):849–852, 1999.

[50] G. Tackmann, P. Berg, C. Schubert, S. Abend, M. Gilowski, W. Ertmer, and E.M. Rasel. Self-alignment of a compact large-area atomic sagnac interferometer. *New Journal of Physics*, 14(1):015002, 2012.

[51] A. Gauguet, B. Canuel, T. Lévèque, W. Chaibi, and A. Landragin. Characterization and limits of a cold-atom sagnac interferometer. *Phys. Rev. A*, 80:063604, 2009.

[52] J.M. McGuirk, G.T. Foster, J.B. Fixler, M. J. Snadden, and M.A. Kasevich. Sensitive absolute-gravity gradiometry using atom interferometry. *Phys. Rev. A*, 65:033608, 2002.

[53] H. Müller, S.-W. Chiow, S. Herrmann, S. Chu, and K.-Y. Chung. Atom-interferometry tests of the isotropy of post-newtonian gravity. *Phys. Rev. Lett.*, 100:031101, 2008.

[54] R. Bouchendira, P. Cladé, S. Guellati-Khélifa, F. Nez, and F. Biraben. State of the art in the determination of the fine structure constant: test of quantum electrodynamics and determination of h/m. *Annalen der Physik*, 525(7):484–492, 2013.

[55] S. Gupta, K. Dieckmann, Z. Hadzibabic, and D. E. Pritchard. Contrast interferometry using Bose-Einstein Condensates to measure h/m and α. *Phys. Rev. Lett.*, 89:140401, 2002.

[56] J.B. Fixler, G.T. Foster, J.M. McGuirk, and M.A. Kasevich. Atom interferometer measurement of the newtonian constant of gravity. *Science*, 315(5808):74–77, 2007.

[57] G. Lamporesi, A. Bertoldi, L. Cacciapuoti, M. Prevedelli, and G. M. Tino. Determination of the newtonian gravitational constant using atom interferometry. *Phys. Rev. Lett.*, 100(5):050801, 2008.

[58] S.Y. Lan, P.C. Kuan, B. Estey, D. English, J.M. Brown, M.A. Hohensee, and H. Müller. A clock directly linking time to a particle's mass. *Science*, 339(6119): 554–557, 2013.

[59] M. Kasevich and S. Chu. Atomic interferometry using stimulated Raman transitions. *Phys. Rev. Lett.*, 67(2):181–184, 1991.

[60] S.W. Chiow, S. Herrmann, S. Chu, and H. Müller. Noise-immune conjugate large-area atom interferometers. *Phys. Rev. Lett.*, 103:050402, 2009.

[61] M. Hauth, C. Freier, V. Schkolnik, A. Senger, M. Schmidt, and A. Peters. First gravity measurements using the mobile atom interferometer gain. *Applied Physics B*, 113(1):49–55, 2013. ISSN 0946-2171.

[62] W.M. Itano, J.C. Bergquist, J.J. Bollinger, J.M. Gilligan, D.J. Heinzen, F.L. Moore, M.G. Raizen, and D.J. Wineland. Quantum projection noise: Population fluctuations in two-level systems. *Phys. Rev. A*, 47:3554–3570, 1993.

[63] A.E. Leanhardt, T.A. Pasquini, M. Saba, A. Schirotzek, Y. Shin, D. Kielpinski, D.E. Pritchard, and W. Ketterle. Cooling Bose-Einstein condensates below 500 picokelvin. *Science*, 301(5639):1513–1515, 2003.

[64] H. Ammann and N. Christensen. Delta kick cooling: A new method for cooling atoms. *Phys. Rev. Lett.*, 78:2088–2091, 1997.

[65] S.H. Myrskog, J.K. Fox, H.S. Moon, J.B. Kim, and A.M. Steinberg. Modified "δ-kick cooling" using magnetic field gradients. *Phys. Rev. A*, 61:053412, 2000.

[66] M.A. Hohensee and H. Müller. Precision tests of general relativity with matter waves. *Journal of Modern Optics*, 58(21):2021–2027, 2011.

[67] M.H. Anderson, J.R. Ensher, M.R. Matthews, C.E. Wieman, and E.A. Cornell. Observation of Bose-Einstein condensation in a dilute atomic vapor. *Science*, 269(5221):198–201, 1995.

[68] C.C. Bradley, C.A. Sackett, J.J. Tollett, and R.G. Hulet. Evidence of Bose-Einstein condensation in an atomic gas with attractive interactions. *Phys. Rev. Lett.*, 75:1687–1690, 1995.

[69] K.B. Davis, M.-O. Mewes, M.R. Andrews, N.J. van Druten, D.S. Durfee, D.M. Kurn, and W. Ketterle. Bose-Einstein condensation in a gas of sodium atoms. *Phys. Rev. Lett.*, 75:3969–3973, 1995.

[70] S.S. Szigeti, J.E. Debs, J.J. Hope, N.P. Robins, and J.D. Close. Why momentum width matters for atom interferometry with Bragg pulses. *New Journal of Physics*, 14(2):023009, 2012.

[71] C. Gross, T. Zibold, E. Nicklas, J. Esteve, and M.K. Oberthaler. Nonlinear atom interferometer surpasses classical precision limit. *Nature*, 464(7292):1165–1169, 2010.

[72] M.F. Riedel, P. Böhi, Y. Li, T.W. Hänsch, A. Sinatra, and P. Treutlein. Atom-chip-based generation of entanglement for quantum metrology. *Nature*, 464 (7292):1170–1173, 2010.

[73] HYPER mission summary. *Science in perspective, ESA*, 2000.

[74] NASA's Cold Atom Laboratory (CAL) mission homepage, http://coldatomlab.jpl.nasa.gov/, 02/11/2014.

[75] M. Schmidt. *A mobile high-precision gravimeter based on atom interferometry*. PhD thesis, Humboldt-Universität zu Berlin, 2011.

[76] Ch. Reigber, H. Lühr, and P. Schwintzer. CHAMP mission status. *Advances in Space Research*, 30(2):129–134, 2002.

[77] B.D. Tapley, S. Bettadpur, M. Watkins, and Ch. Reigber. The gravity recovery and climate experiment: Mission overview and early results. *Geophysical Research Letters*, 31(9), 2004.

[78] M.R. Drinkwater, R. Floberghagen, R. Haagmans, D. Muzi, and A. Popescu. GOCE: ESA's First Earth Explorer Core Mission. In *Earth Gravity Field from Space — From Sensors to Earth Sciences*, volume 17 of *Space Sciences Series of ISSI*, pages 419–432. Springer Netherlands, 2003.

[79] N. Sneeuw, J. Flury, and R. Rummel. Science requirements on future missions and simulated mission scenarios. *Earth Moon Planets*, 94(1-2):113–142, 2004.

[80] D.S. Weiss, B.C. Young, and S. Chu. Precision measurement of $\hbar/m_{Cs}$ based on photon recoil using laser-cooled atoms and atomic interferometry. *Applied physics B*, 59(3):217–256, 1994.

[81] H. Müller, S.-W. Chiow, Q. Long, Ch. Vo, and S. Chu. A new photon recoil experiment: towards a determination of the fine structure constant. *Applied Physics B*, 84(4):633–642, 2006.

[82] T. Wilken, M. Lezius, T.W. Hänsch, A. Kohfeldt, A. Wicht, V. Schkolnik, M. Krutzik, H. Duncker, O. Hellmig, P. Windpassinger, et al. A frequency comb and precision spectroscopy experiment in space. In *CLEO: Applications and Technology*, pages AF2H–5. Optical Society of America, 2013.

[83] A. Wicht, J.M. Hensley, E. Sarajlic, and S. Chu. A preliminary measurement of the fine structure constant based on atom interferometry. *Physica scripta*, 2002 (T102):82, 2002.

[84] L.I. Schiff. Motion of a gyroscope according to Einstein's theory of gravitation. *Proceedings of the National Academy of Sciences of the United States of America*, 46(6):871, 1960.

[85] R. Giacomo. History of the attempts to measure orbital frame-dragging with artificial satellites. *Central European Journal of Physics*, 11(5):531–544, 2013.

[86] C.W.F. Everitt, D.B. DeBra, B.W. Parkinson, J.P. Turneaure, J.W. Conklin, M.I. Heifetz, G.M. Keiser, A.S. Silbergleit, T. Holmes, J. Kolodziejczak, M. Al-Meshari, J.C. Mester, B. Muhlfelder, V.G. Solomonik, K. Stahl, P.W. Worden, W. Bencze, S. Buchman, B. Clarke, A. Al-Jadaan, H. Al-Jibreen, J. Li, J.A. Lipa, J.M. Lockhart, B. Al-Suwaidan, M. Taber, and S. Wang. Gravity Probe B: Final results of a space experiment to test general relativity. *Phys. Rev. Lett.*, 106:221101, 2011.

[87] Hyper-precision cold-atom interferometry in space (HYPER)*, ESA assement study report*, 2000.

[88] BICEP2 Collaboration. BICEP2 I: Detection of b-mode polarization at degree angular scales. *arXiv:1403.3985*, 2014.

[89] S. Dimopoulos, P.W. Graham, J.M. Hogan, M.A. Kasevich, and S. Rajendran. Gravitational wave detection with atom interferometry. *Phys. Lett. B*, 678(1): 37–40, 2009.

[90] K. Danzmann. LISA − An ESA cornerstone mission for the detection and observation of gravitational waves. *Advances in Space Research*, 32(7):1233–1242, 2003.

[91] B.P. Abbott, R. Abbott, R. Adhikari, P. Ajith, B. Allen, G. Allen, R.S. Amin, S.B. Anderson, W.G. Anderson, M.A. Arain, et al. LIGO: The laser interferometer gravitational-wave observatory. *Reports on Progress in Physics*, 72(7): 076901, 2009.

[92] G. Modugno, G. Ferrari, G. Roati, R.J. Brecha, A. Simoni, and M. Inguscio. Bose-Einstein condensation of potassium atoms by sympathetic cooling. *Science*, 294(5545):1320–1322, 2001.

[93] Cold Atom Laboratory (CAL) - *Workshop report*, 2012.

[94] M. Greiner, O. Mandel, T. Esslinger, T.W. Hänsch, and I. Bloch. Quantum phase transition from a superfluid to a mott insulator in a gas of ultracold atoms. *Nature*, 415(6867):39–44, 2002.

[95] L.E. Sadler, J.M. Higbie, S.R. Leslie, M. Vengalattore, and D.M. Stamper-Kurn. Spontaneous symmetry breaking in a quenched ferromagnetic spinor Bose–Einstein condensate. *Nature*, 443(7109):312–315, 2006.

[96] Ph. Laurent (CNES) – *private communication.*

[97] Ph. Laurent, M. Abgrall, Ch. Jentsch, P. Lemonde, G. Santarelli, A. Clairon, I. Maksimovic, S. Bize, Ch. Salomon, D. Blonde, et al. Design of the cold atom PHARAO space clock and initial test results. *Applied Physics B*, 84(4):683–690, 2006.

[98] N.F. Ramsey. Experiments with separated oscillatory fields and hydrogen masers. *Rev. Mod. Phys.*, 62:541–552, 1990.

[99] Atomic Clock Ensemble in Space (ACES) — *Factsheet ESA-HSO-COU-020 (Rev. 2.0).*

[100] I. Moric and Ph. Laurent. Status of the flight model of the cold atoms space clock pharao. In *European Frequency and Time Forum International Frequency Control Symposium (EFTF/IFC), 2013 Joint*, pages 967–972, 2013.

[101] D. Hils and J.L. Hall. Improved Kennedy-Thorndike experiment to test special relativity. *Physical review letters*, 64(15):1697, 1990.

[102] Office of Science and Technology Policy website, http://www.whitehouse.gov, 01/15/2014.

[103] International Space Station User's guide. *Release 2.0*, 2010.

[104] NASA website, www.nasa.gov, 03/02/2014.

[105] Novespace website, http://www.novespace.fr, 02/22/2014.

[106] Novespace A300 Zero-G rules and guidelines, 2009.

[107] Zarm Drop Tower Bremen User Manual, 2012.

[108] FAI website, http://www.fai.org, 03/02/2014.

[109] Swedish Space Corporation website, http://www.sscspace.com/esrange-space-center-3.

[110] S.M. Dickerson, J.M. Hogan, A. Sugarbaker, D.M.S. Johnson, and M.A. Kasevich. Multiaxis inertial sensing with long-time point source atom interferometry. *Phys. Rev. Lett.*, 111:083001, 2013.

[111] A. Wenzlawski. *Matter-wave optics in microgravity: Laser technology and applications.* PhD thesis, Universität Hamburg, 2014.

[112] H. Müntinga. *Realisierung eines Materiewelleninterferometers unter Schwerelosigkeit.* PhD thesis, Universität Bremen, 2014.

[113] H. Ahlers. *Atomoptik und Interferometrie mit quantendegenerierten Gasen unter den Bedingungen des ausgedehnten freien Falles.* PhD thesis, Leibniz-Universität Hannover, 2014.

[114] F. Dalfovo, S. Giorgini, L.P. Pitaevskii, and S. Stringari. Theory of Bose-Einstein condensation in trapped gases. *Rev. Mod. Phys.*, 71:463–512, 1999.

[115] W. Ketterle, D.S. Durfee, and D.M. Stamper-Kurn. Making, probing and understaunder Bose-Einstein condensates. *Proceedings of the International School of Physics "Enrico Fermi", Course CXL, edited by M. Inguscio, S. Stringari and C.E. Wieman (IOS Press, Amsterdam)*, pages 67 –176, 1999.

[116] C.J. Pethick and H. Smith. *Bose-Einstein condensation in dilute gases*. Camebridge University Press, 2002.

[117] S.N. Bose. Plancks Gesetz und Lichtquantenhypothese. *Z. Phys*, 26:178, 1924.

[118] A. Einstein. Quantentheorie des einatomigen idealen Gases. *Sitzungsber. Kgl. Preuss. Akad. Wiss.*, 261, 1924.

[119] M. Planck. Über das Gesetz der Energieverteilung im Normalspektrum. *Annalen der Physik*, 5:553, 1901.

[120] L. de Broglie. Ondes et Quanta. *Compt. Ren.*, 177:507, 1923.

[121] T.W. Hänsch and A.L. Schawlow. Cooling of gases by laser radiation. *Optics Communications*, 13(1):68–69, 1975.

[122] A. Ashkin. Trapping of atoms by resonance radiation pressure. *Physical Review Letters*, 40:729–733, 1978.

[123] W.D. Phillips and H. Metcalf. Laser deceleration of an atomic beam. *Physical Review Letters*, 48(9):596, 1982.

[124] S. Chu, L. Hollberg, J.E. Bjorkholm, A. Cable, and A. Ashkin. Threedimensional viscous confinement and cooling of atoms by resonance radiation pressure. *Phys. Rev. Lett.*, 55(1):48–51, 1985.

[125] E.L. Raab, M. Prentiss, A. Cable, S. Chu, and D.E. Pritchard. Trapping of neutral sodium atoms with radiation pressure. *Physical Review Letters*, 59(23): 2631, 1987.

[126] D.J. Wineland, R.E. Drullinger, and F.L. Walls. Radiation-pressure cooling of bound resonant absorbers. *Physical Review Letters*, 40(25):1639, 1978.

[127] L.P. Pitaevskii and S. Stringari. *Bose-Einstein condensation*. Number 116. Oxford University Press, 2003.

[128] P.A. Ruprecht, M.J. Holland, K. Burnett, and M. Edwards. Time-dependent solution of the nonlinear Schrödinger equation for Bose-condensed trapped neutral atoms. *Phys. Rev. A*, 51:4704–4711, 1995.

[129] Yu. Kagan, E.L. Surkov, and G.V. Shlyapnikov. Evolution of a Bose-condensed gas under variations of the confining potential. *Phys. Rev. A*, 54:R1753–R1756, 1996.

[130] Y. Castin and R. Dum. Bose-Einstein condensates in time dependent traps. *Phys. Rev. Lett.*, 77:5315–5319, 1996.

[131] P. Cheinet, F. Pereira Dos Santos, T. Petelski, J. Le Gouët, J. Kim, K.T. Therkildsen, A. Clairon, and A. Landragin. Compact laser system for atom interferometry. *Applied Physics B*, 84(4):643–646, 2006.

[132] W. Petrich, M.H. Anderson, J.R. Ensher, and E.A. Cornell. Stable, tightly confining magnetic trap for evaporative cooling of neutral atoms. *Phys. Rev. Lett.*, 74:3352–3355, 1995.

[133] Y.V. Gott, M.S. Ioffe, and V.G. Telkovskii. *Nuclear Fusion Suppl.*, 3:1045, 1962.

[134] D.E. Pritchard. Cooling neutral atoms in a magnetic trap for precision spectroscopy. *Phys. Rev. Lett.*, 51:1336–1339, 1983.

[135] V.S. Bagnato, G.P. Lafyatis, A. G. Martin, E. L. Raab, R.N. Ahmad-Bitar, and D.E. Pritchard. Continuous stopping and trapping of neutral atoms. *Phys. Rev. Lett.*, 58:2194–2197, 1987.

[136] J. Reichel and V. Vuletic. *Atom Chips*. John Wiley & Sons, 2010.

[137] W. Lewoczko-Adamczyk. *Bose-Einstein condensation in microgravity*. PhD thesis, Humboldt-Universität zu Berlin, 2009.

[138] J. Reichel, W. Hänsel, P. Hommelhoff, and T.W. Hänsch. Applications of integrated magnetic microtraps. *Applied Physics B*, 72(1):81–89, 2001.

[139] R. Folman, P. Krüger, D. Cassettari, B. Hessmo, T. Maier, and J. Schmiedmayer. Controlling cold atoms using nanofabricated surfaces: Atom chips. *Phys. Rev. Lett.*, 84:4749–4752, 2000.

[140] R. Folman, P. Krüger, J. Schmiedmayer, J. Denschlag, and C. Henkel. Microscopic atom optics: from wires to an atom chip. *Advances in Atomic Molecular and Optical Physics*, 48:263–356, 2002.

[141] W. Hänsel, P. Hommelhoff, T.W. Hänsch, and J. Reichel. Bose-Einstein condensation on a microelectronic chip. *Nature*, 413(6855):498–501, 2001.

[142] A. Günther, S. Kraft, C. Zimmermann, and J. Fortágh. Atom interferometer based on phase coherent splitting of Bose-Einstein condensates with an integrated magnetic grating. *Phys. Rev. Lett.*, 98:140403, 2007.

[143] W. Hänsel, J. Reichel, P. Hommelhoff, and T. W. Hänsch. Magnetic conveyor belt for transporting and merging trapped atom clouds. *Phys. Rev. Lett.*, 86: 608–611, 2001.

[144] S. Hofferberth, I. Lesanovsky, B. Fischer, J. Verdu, and J. Schmiedmayer. Radiofrequency-dressed-state potentials for neutral atoms. *Nat Phys*, 2(10):710–716, 2006.

[145] T. Schumm, S. Hofferberth, L.M. Andersson, S. Wildermuth, S. Groth, I. Bar-Joseph, J. Schmiedmayer, and P. Kruger. Matter-wave interferometry in a double well on an atom chip. *Nat Phys*, 1(1):57–62, 2005.

[146] Y. Shin, C. Sanner, G.-B. Jo, T.A. Pasquini, M. Saba, W. Ketterle, D.E. Pritchard, M. Vengalattore, and M. Prentiss. Interference of Bose-Einstein condensates split with an atom chip. *Phys. Rev. A*, 72:021604, 2005.

[147] J. Denschlag, D. Cassettari, and J. Schmiedmayer. Guiding neutral atoms with a wire. *Phys. Rev. Lett.*, 82:2014–2017, 1999.

[148] D.A. Steck. *Rubidium 85 D Line Data – revision 2.1.6*, 2008.

[149] J.H. Shirley. Modulation transfer processes in optical heterodyne saturation spectroscopy. *Opt. Lett.*, 7(11):537–539, 1982.

[150] D.A. Steck. *Rubidium 87 D Line Data – revision 2.0.1*, 2008.

[151] W.D. Phillips. Nobel lecture: Laser cooling and trapping of neutral atoms. *Rev. Mod. Phys.*, 70:721–741, 1998.

[152] O.J. Luiten, M.W. Reynolds, and J.T.M. Walraven. Kinetic theory of the evaporative cooling of a trapped gas. *Phys. Rev. A*, 53:381–389, 1996.

[153] H.F. Hess. Evaporative cooling of magnetically trapped and compressed spin-polarized hydrogen. *Phys. Rev. B*, 34:3476–3479, 1986.

[154] H. Ott, J. Fortagh, G. Schlotterbeck, A. Grossmann, and C. Zimmermann. Bose-Einstein condensation in a surface microtrap. *Physical Review Letters*, 87(23): 230401, 2001.

[155] R. Jáuregui. Nonperturbative and perturbative treatments of parametric heating in atom traps. *Phys. Rev. A*, 64:053408, 2001.

[156] S.T. Seidel. Manipulation von Bose-Einstein-Kondensaten unter Schwerelosigkeit. Diploma thesis, Leibniz-Universität Hannover, 2009.

[157] W. Lewozcko-Adamczyk (HUB) – *private communication.*

[158] A.D. Cronin, J. Schmiedmayer, and D.E. Pritchard. Optics and interferometry with atoms and molecules. *Reviews of Modern Physics*, 81(3):1051, 2009.

[159] P. Meystre. *Atom optics*, volume 33. Springer, 2001.

[160] M. Kozuma, L. Deng, E.W. Hagley, J. Wen, R. Lutwak, K. Helmerson, S.L. Rolston, and W.D. Phillips. Coherent splitting of Bose-Einstein condensed atoms with optically induced Bragg diffraction. *Phys. Rev. Lett.*, 82:871–875, 1999.

[161] H. Müller, S.-W. Chiow, and S. Chu. Atom-wave diffraction between the Raman-Nath and the Bragg regime: Effective Rabi frequency, losses, and phase shifts. *Phys. Rev. A*, 77:023609, 2008.

[162] S.-W. Chiow, T. Kovachy, H.-C. Chien, and M.A. Kasevich. $102\hbar k$ large area atom interferometers. *Phys. Rev. Lett.*, 107:130403, 2011.

[163] F. Gerbier, J. H. Thywissen, S. Richard, M. Hugbart, P. Bouyer, and A. Aspect. Momentum distribution and correlation function of quasicondensates in elongated traps. *Phys. Rev. A*, 67:051602, 2003.

[164] Y. Torii, Y. Suzuki, M. Kozuma, T. Sugiura, T. Kuga, L. Deng, and E.W. Hagley. Mach-Zehnder Bragg interferometer for a Bose-Einstein condensate. *Phys. Rev. A*, 61:041602, 2000.

[165] S. Bernet, M.K. Oberthaler, R. Abfalterer, J. Schmiedmayer, and A. Zeilinger. Coherent frequency shift of atomic matter waves. *Phys. Rev. Lett.*, 77:5160–5163, 1996.

[166] M. Kozuma, Y. Suzuki, Y. Torii, T. Sugiura, T. Kuga, E.W. Hagley, and L. Deng. Phase-coherent amplification of matter waves. *Science*, 286(5448):2309–2312, 1999.

[167] G. Birkl, M. Gatzke, I.H. Deutsch, S.L. Rolston, and W.D. Phillips. Bragg scattering from atoms in optical lattices. *Physical review letters*, 75(15):2823, 1995.

[168] J. Stenger, S. Inouye, A.P. Chikkatur, D.M. Stamper-Kurn, D.E. Pritchard, and W. Ketterle. Bragg Spectroscopy of a Bose-Einstein Condensate. *Phys. Rev. Lett.*, 82:4569–4573, 1999.

[169] M. Hugbart, J.A. Retter, F. Gerbier, A.F. Varón, S. Richard, J.H. Thywissen, D. Clément, P. Bouyer, and A. Aspect. Coherence length of an elongated condensate. *The European Physical Journal D - Atomic, Molecular, Optical and Plasma Physics*, 35(1):155–163, 2005.

[170] W. Friedrich, P. Knipping, and M. Laue. Interferenzerscheinungen bei Röntgenstrahlen. *Annalen der Physik*, 346(10):971–988, 1913.

[171] W.L. Bragg. The specular reflection of x-rays. *Nature*, 90:410, 1912.

[172] P.J. Martin, B.G. Oldaker, A.H. Miklich, and D.E. Pritchard. Bragg scattering of atoms from a standing light wave. *Phys. Rev. Lett.*, 60:515–518, 1988.

[173] I. Bloch. Licht-Atom Wechselwirkung im Zwei-Niveau System. *Vorlesungsskript, Atomphysik WS2003/2004, Johannes-Gutenberg-Universität*, 2004.

[174] T. Petelski. *Atom Interferometers for Precision Gravity Measurements.* PhD thesis, Università degli studi di Firenze, 2005.

[175] M. Kasevich, D.S. Weiss, E. Riis, K. Moler, S. Kasapi, and S. Chu. Atomic velocity selection using stimulated Raman transitions. *Phys. Rev. Lett.*, 66(18): 2297–2300, 1991.

[176] P. Cheinet. *Conception et Réalisation d'un Gravimètre à Atomes Froids.* PhD thesis, Université Paris VI, 2006.

[177] D.M. Giltner, R.W. McGowan, and S.A. Lee. Atom interferometer based on Bragg Scattering from standing light waves. *Phys. Rev. Lett.*, 75:2638–2641, 1995.

[178] E.W. Hagley, L. Deng, M. Kozuma, M. Trippenbach, Y.B. Band, M. Edwards, M Doery, P.S. Julienne, K. Helmerson, S.L. Rolston, and W.D. Phillips. Measurement of the coherence of a Bose-Einstein condensate. *Phys. Rev. Lett.*, 83: 3112–3115, 1999.

[179] J. Steinhauer, R. Ozeri, N. Katz, and N. Davidson. Excitation spectrum of a Bose-Einstein condensate. *Phys. Rev. Lett.*, 88:120407, 2002.

[180] P.B. Blakie, R.J. Ballagh, and C.W. Gardiner. Theory of coherent Bragg spectroscopy of a trapped Bose-Einstein condensate. *Phys. Rev. A*, 65:033602, 2002.

[181] J.-C. Diels and W. Rudolph. *Ultrashort laser pulse phenomena.* Academic press, 2006.

[182] P.L. Gould, G.A. Ruff, and D.E. Pritchard. Diffraction of atoms by light: The near-resonant Kapitza-Dirac effect. *Phys. Rev. Lett.*, 56:827–830, 1986.

[183] EYP-DFB-0780-00080-1500-TOC03-0000*, Datasheet, Eagleyard.*

[184] P.B. Blakie and R.J. Ballagh. Mean-field treatment of Bragg scattering from a Bose-Einstein condensate. *Journal of Physics B: Atomic, Molecular and Optical Physics*, 33(19):3961, 2000.

[185] M.R. Andrews, C.G. Townsend, H.-J. Miesner, D.S. Durfee, D.M. Kurn, and W. Ketterle. Observation of interference between two Bose condensates. *Science*, 275(5300):637–641, 1997.

[186] J.E. Simsarian, J. Denschlag, Mark Edwards, Charles W. Clark, L. Deng, E.W. Hagley, K. Helmerson, S. L. Rolston, and W.D. Phillips. Imaging the phase of an evolving Bose-Einstein condensate wave function. *Phys. Rev. Lett.*, 85: 2040–2043, 2000.

[187] K. Bongs, S. Burger, G. Birkl, K. Sengstock, W. Ertmer, K. Rzazewski, A. Sanpera, and M. Lewenstein. Coherent evolution of bouncing Bose-Einstein condensates. *Phys. Rev. Lett.*, 83:3577–3580, 1999.

[188] E.A. Burt, R.W. Ghrist, C.J. Myatt, M.J. Holland, E.A. Cornell, and C.E. Wieman. Coherence, correlations, and collisions: What one learns about Bose-Einstein condensates from their decay. *Phys. Rev. Lett.*, 79:337–340, 1997.

[189] T. Aoki, T. Kato, Y. Tanami, and A. Morinaga. Delta-kick cooling using the Ioffe-Pritchard potential. In *International Quantum Electronics Conference*, page ITuI24. Optical Society of America, 2004.

[190] M. Hauth (HUB) – *private communication.*

[191] V. Vuletić, Ch. Chin, A.J. Kerman, and S. Chu. Degenerate Raman sideband cooling of trapped cesium atoms at very high atomic densities. *Phys. Rev. Lett.*, 81:5768–5771, 1998.

[192] A.J. Kerman, V. Vuletić, Ch. Chin, and S. Chu. Beyond optical molasses: 3D Raman sideband cooling of atomic cesium to high phase-space density. *Phys. Rev. Lett.*, 84:439–442, 2000.

[193] J.-F. Schaff, P. Capuzzi, G. Labeyrie, and P. Vignolo. Shortcuts to adiabaticity for trapped ultracold gases. *New Journal of Physics*, 13(11):113017, 2011.

[194] M. Kasevich and S. Chu. Measurement of the gravitational acceleration of an atom with a light-pulse atom interferometer. *Appl. Phys. B*, 54(5):321–332, 1992.

[195] Ch. Grezschik (HUB) – *private communication.*

[196] T.A. Pasquini, M. Saba, G.-B. Jo, Y. Shin, W. Ketterle, D.E. Pritchard, T.A. Savas, and N. Mulders. Low velocity quantum reflection of Bose-Einstein condensates. *Phys. Rev. Lett.*, 97:093201, 2006.

[197] T. Könemann, W. Brinkmann, E. Göklü, C. Lämmerzahl, H. Dittus, T. Van Zoest, E.M. Rasel, W. Ertmer, W. Lewoczko-Adamczyk, M. Schiemangk, et al. A freely falling magneto-optical trap drop tower experiment. *Applied Physics B*, 89(4):431–438, 2007.

[198] C. Vogt, S. Kulas, A. Resch, and S. Herrmann. Towards a test of the universality of free fall of atoms in microgravity. In *Verhandl. DPG (VI), GR5.1*, 2014.

[199] W. Herr. *Eine kompakte Quelle quantenentarteter Gase hohen Flusses für die Atominterferometrie unter Schwerelosigkeit.* PhD thesis, Leibniz-Universität Hannover, 2013.

[200] K. Dieckmann, R.J.C. Spreeuw, M. Weidemüller, and J.T.M. Walraven. Two-dimensional magneto-optical trap as a source of slow atoms. *Phys. Rev. A*, 58: 3891–3895, 1998.

[201] H. Ahlers (LUH) – *private communication.*

[202] M. Schiemangk. *Ein kompaktes Lasersystem zur Manipulation von Quantengasen unter Schwerelosigkeit.* PhD thesis, Humboldt-Universität zu Berlin, 2014.

[203] Ch. Grzeschik. *Aufbau eines Rubidium-Ramanlasersystems für Atominterferometrie unter Schwerelosigkeit.* Diploma thesis, Humboldt-Universität zu Berlin, 2010.

[204] A.-L. Geyssel. *Realisierung eines katapulttauglichen Ramanlasersystems für Atominterferometrie mit Kalium unter Schwerelosigkeit.* Diploma thesis, Humboldt-Universität zu Berlin, 2011.

[205] K. Lampmann. *Design, Aufbau und Test von Schlüsselkomponenten eines Lasersystems für Experimente mit Quantengasen auf einer Forschungsrakete.* Diploma thesis, Humboldt-Universität zu Berlin, 2012.

[206] T.-P. Nguyen, M. Schiemangk, S. Spießberger, H. Wenzel, A. Wicht, A. Peters, G. Erbert, and G. Tränkle. Optimization of 780 nm DFB diode lasers for high-power narrow linewidth emission. *Applied Physics B*, 108(4):767–771, 2012.

[207] Ch. Grzeschik, M. Schiemangk, K. Lampmann, M. Krutzik, and A. Peters. A state of the art diode laser system for matter wave interferometry in microgravity. In *CLEO: 2013*, page CM1N.6. Optical Society of America, 2013.

[208] M. Schiemangk, K. Lampmann, M. Krutzik, S. Spiessberger, A. Sahm, A. Wicht, G. Erbert, G. Tränkle, and A. Peters. 3W microintegrated laser systems at 767 nm and 780 nm. *in prep.*

[209] S. Spießberger, M. Schiemangk, A. Sahm, A. Wicht, H. Wenzel, A. Peters, G. Erbert, and G. Tränkle. Micro-integrated 1 Watt semiconductor laser system with a linewidth of 3.6 kHz. *Opt. Express*, 19(8):7077–7083, 2011.

[210] S. Ospelkaus, C. Ospelkaus, R. Dinter, J. Fuchs, M. Nakat, K. Sengstock, and K. Bongs. Degenerate K–Rb Fermi–Bose gas mixtures with large particle numbers. *Journal of Modern Optics*, 54(5):661–673, 2007.

[211] R. Grimm, M. Weidemüller, and Y.B. Ovchinnikov. Optical dipole traps for neutral atoms. *arXiv preprint physics/9902072*, 1999.

[212] A. Simoni, F. Ferlaino, G. Roati, G. Modugno, and M. Inguscio. Magnetic control of the interaction in ultracold K-Rb mixtures. *Physical review letters*, 90(16): 163202, 2003.

[213] G. Roati, M. Zaccanti, C. D'Errico, J. Catani, M. Modugno, A. Simoni, M. Inguscio, and G. Modugno. ^{39}K Bose-Einstein condensate with tunable interactions. *Phys. Rev. Lett.*, 99:010403, 2007.

[214] S. Herrmann (ZARM) – *private communication.*

[215] E. Luvsandamdin, Ch. Kürbis, M. Schiemangk, A. Sahm, A. Wicht, A. Peters, G. Erbert, and G. Tränkle. Micro-integrated extended cavity diode lasers for precision potassium spectroscopy in space. *Opt. Express*, 22(7):7790–7798, 2014.

[216] A. Kohfeldt, M. Schiemangk, S. Spiessberger, A. Wicht, A. Peters, G. Erbert, and G. Tränkle. Micro-integrated, high power, narrow linewidth master oscillator power amplifier for precision quantum optics experiments in space. In *Conference on Lasers and Electro-Optics 2012*, page JW3C.2. Optical Society of America, 2012.

[217] TEXUS-48 Pre-Flight Report. DLR-RB-MR, Issue 1.2, 2010.

[218] MAIUS User Manual v 1.1. Deutsches Zentrum für Luft- und Raumfahrt e.V., 2012.

[219] T. Steinmetz, T. Wilken, C. Araujo-Hauck, R. Holzwarth, T.W. Hänsch, L. Pasquini, A. Manescau, S. D'Odorico, M.T. Murphy, T. Kentischer, et al.

Laser frequency combs for astronomical observations. *Science*, 321(5894):1335–1337, 2008.

[220] Th. Udem, R. Holzwarth, and T.W. Hänsch. Optical frequency metrology. *Nature*, 416(6877):233–237, 2002.

[221] ZERODUR - Zero Expansion Glass Ceramic*, Datasheet, SCHOTT AG.*

[222] Ferdinand-Braun-Insitut für Höchstfrequenztechnik Leibniz-Institut. *Micro-integrated master oscillator power amplifier manual – hardware version MOPA.12 (release 05.01)*, 2013.

[223] K.F. Middleton, C. Killow, C. Braxmaier, G. Heinzel, V. Wand, U. Johann, D. Robertson, M.E. Caldwell, R. Edeson, H. Ward, et al. Prototype optical bench instrument in the interferometer for the LISA–Pathfinder space mission. *Optical Engineering*, 45(12):125601–125601, 2006.

[224] J. Grosse (DLR-RY) – *private communication.*

[225] Interface Control Document MAIUS. *Release v1.0.* Deutsches Zentrum für Luft- und Raumfahrt e.V., 2013.

[226] STE-QUEST mission homepage, http://sci.esa.int/ste-quest, 12/20/2013.

[227] STE-QUEST team. STE-QUEST Assesment Study Report (Yellow Book), ESA. 2013.

[228] F. Sorrentino, K. Bongs, P. Bouyer, L. Cacciapuoti, M. de Angelis, H. Dittus, W. Ertmer, J. Hartwig, M. Hauth, S. Herrmann, K. Huang, M. Inguscio, E. Kajari, T. Könemann, C. Lämmerzahl, A. Landragin, G. Modugno, F. Pereira dos Santos, A. Peters, M. Prevedelli, E.M. Rasel, W.P. Schleich, M. Schmidt, A. Senger, K. Sengstock, G. Stern, G.M. Tino, T. Valenzuela, R. Walser, and P. Windpassinger. The space atom interferometer project: status and prospects. *Journal of Physics: Conference Series*, 327(1):012050, 2011.

[229] N. Malossi, Q. Bodart, S. Merlet, T. Lévèque, A. Landragin, and F. Pereira Dos Santos. Double diffraction in an atomic gravimeter. *Phys. Rev. A*, 81:013617, 2010.

[230] E. Giese, A. Roura, G. Tackmann, E. M. Rasel, and W. P. Schleich. Double bragg diffraction: A tool for atom optics. *Phys. Rev. A*, 88:053608, 2013.

[231] S.-Y. Lan, P.-C. Kuan, B. Estey, P. Haslinger, and H. Müller. Influence of the coriolis force in atom interferometry. *Phys. Rev. Lett.*, 108:090402, 2012.

[232] J. Müller, F. Hofmann, and L. Biskupek. Testing various facets of the equivalence principle using lunar laser ranging. *Classical and Quantum Gravity*, 29(18): 184006, 2012.

[233] T. Schuldt, Ch. Schubert, M. Krutzik, L.G. Bote, N. Gaaloul, et al. Design of a dual species atom interferometer for space. *submitted for publication in Exp. Astronomy*, 2014.

[234] T. Lévèque, L. Antoni-Micollier, B. Faure, and J. Berthon. A laser setup for rubidium cooling dedicated to space applications. *Applied Physics B*, pages 1–8, 2014.

[235] N. Gaaloul (LUH) – *private communication*.

[236] K.J. Hughes, J.H.T. Burke, and C.A. Sackett. Suspension of atoms using optical pulses, and application to gravimetry. *Phys. Rev. Lett.*, 102:150403, 2009.

[237] F. Impens, P. Bouyer, and C.J. Bordé. Matter-wave cavity gravimeter. *Applied Physics B*, 84(4):603–615, 2006.

List of Figures

List of Tables

Selbständigkeitserklärung

Hiermit erkläre ich, die vorliegende Arbeit selbständig und nur unter Verwendung der angegebenen Quellen und Hilfsmittel angefertigt zu haben. Ich habe mich anderweitig nicht um einen Doktorgrad beworben und besitze einen solchen auch nicht. Die dem Verfahren zugrunde liegende Promotionsordnung der Mathematisch-Naturwissenschaftlichen Fakultät der Humboldt-Universität zu Berlin habe ich zur Kenntnis genommen.

Berlin, den 10.06.2014 Markus Krutzik